

Multi-Physics Driven Electromigration Study: Multi-Scale Modeling and Experiment

Cui, Z.

DOI

[10.4233/uuid:839e79d1-ea4b-4440-9077-d6fb2df4c086](https://doi.org/10.4233/uuid:839e79d1-ea4b-4440-9077-d6fb2df4c086)

Publication date

2021

Document Version

Final published version

Citation (APA)

Cui, Z. (2021). *Multi-Physics Driven Electromigration Study: Multi-Scale Modeling and Experiment*. [Dissertation (TU Delft), Delft University of Technology]. <https://doi.org/10.4233/uuid:839e79d1-ea4b-4440-9077-d6fb2df4c086>

Important note

To cite this publication, please use the final published version (if applicable).
Please check the document version above.

Copyright

Other than for strictly personal use, it is not permitted to download, forward or distribute the text or part of it, without the consent of the author(s) and/or copyright holder(s), unless the work is under an open content license such as Creative Commons.

Takedown policy

Please contact us and provide details if you believe this document breaches copyrights.
We will remove access to the work immediately and investigate your claim.

**MULTI-PHYSICS DRIVEN
ELECTROMIGRATION STUDY: MULTI-SCALE
MODELLING AND EXPERIMENT**

MULTI-PHYSICS DRIVEN ELECTROMIGRATION STUDY: MULTI-SCALE MODELLING AND EXPERIMENT

Dissertation

for the purpose of obtaining the degree of doctor
at Delft University of Technology
by the authority of the Rector Magnificus Prof.dr.ir. T.H.J.J. van der Hagen
chair of the Board for Doctorates
to be defended publicly on
Monday, 20 December 2021 at 12:30 o'clock

by

Zhen CUI

Master of Engineering in Solid Mechanics, Tianjin University, China
born in Shanxi, China

This dissertation has been approved by the promotor.

Composition of the doctor committee:

Rector Magnificus	chairperson
Prof.dr. G.Q. Zhang	Delft University of Technology, promotor
Prof.dr. X.J. Fan	Lamar University, USA, promotor
Dr.ir. S. Vollebregt	Delft University of Technology, copromotor

Independent members:

Prof.dr. C.J. Bailey	University of Greenwich, UK
Prof.dr.ir. W.D. van Driel	Delft University of Technology
Prof.dr.ir. J.M.J. den Toonder	Eindhoven University of Technology
Prof.dr. R. Ross	Delft University of Technology
Prof.dr.ir. P.M. Sarro	Delft University of Technology, reserve member



Keywords: Electromigration Simulation, Multiphysics, Multiscale, Accelerated Measurement, Stress-Migration, Self-Diffusion, Thermomigration, Molecular Dynamic Simulation, Finite Element Simulation

Printed by: Ipskamp printing

Cover design by Z. Cui

Copyright © 2021 by Z. Cui

An electrical version of this dissertation is available at

<http://repository.tudelft.nl/>

Contents

LIST OF ABBREVIATIONS	XI
1. Introduction	1
1.1. Background	1
1.2. Electromigration	3
1.2.1. Theoretical Model.....	5
1.2.2. Electromigration Accelerated Test.....	6
1.3. Objectives.....	7
1.4. Organization of Dissertation	9
References	11
2. Literature Review of Multi-Physics Model of Electromigration.....	15
2.1. Introduction.....	16
2.2. Black's Model	16
2.3. Mass Transport Equation of Electromigration.....	18
2.4. Electromigration and Mechanical Stress.....	21
2.5. Thermomigration during Electromigration	29
2.6. Summary and Outlook	30
References	30
3. General Coupling Model of Electromigration.....	35
3.1. Introduction.....	36
3.2. General Coupling Model of Electromigration	37
3.3. Governing Equation for One-Dimensional Solution.....	40
3.4. Numerical Results.....	42
3.5. Revisiting Blech's Theory.....	49
3.6. Conclusion	51

References	51
4. Volume Relaxation of Vacancy: a Molecular Dynamic Study	55
4.1. Introduction.....	56
4.2. Methodology	57
4.2.1. Basic Equations.....	57
4.2.2. Simulation Method	58
4.3. Results and Discussion.....	60
4.3.1 Vacancy Volume Relaxation Factor in Al.....	60
4.3.2. Empirical Formula of Vacancy Volume Relaxation Factor.....	64
4.4. Diffusion-Induced Strain and Stress.....	66
4.5. Conclusion	70
References	70
5. Effects of Mechanical Stress and Self-Diffusion: Experiment and Simulation.....	75
5.1. Introduction.....	76
5.2. Experiment Procedure	77
5.2.1. Electromigration Testing Wafer Design	77
5.2.2. Sample Preparation and Process	78
5.2.3. Electromigration Test Setup	79
5.2.4. Overview of Testing Plan	80
5.3. Experimental Results and Discussion	81
5.3.1. SWEAT vs. Blech Structure	81
5.3.2. Size Effects.....	82
5.3.3. In Vacuum vs. In Air.....	84
5.3.4. Effect of Annealing.....	85
5.3.5. Effects of Passivation	87
5.3.6. Effect of Temperature	90
5.3.7. Effect of Current Density	90

5.4. Fully-Coupled Theory and Governing Equation	92
5.4.1. Multi-physics Driven Fully-coupled Model.....	92
5.4.2. Governing Equation for 1D Case.....	93
5.4.3. Overview of the Simulation Procedure	96
5.4.4. Determination of Diffusivity and Critical Atomic Concentration	97
5.5. Numerical Results and Comparison with Experiment	99
5.5.1. Stress-Free Metal Line	99
5.5.2. Passivated Metal Line.....	104
5.5.3. Molecular Dynamic Simulation	108
5.6. Conclusion	110
References	111
6. Thermomigration Accompanying Electromigration: Experiment and Simulation	115
6.1. Introduction.....	116
6.2. Experiment Procedure.....	117
6.3. Experimental Results.....	118
6.3.1. Blech Structure.....	118
6.3.2. SWEAT Structure.....	121
6.4. Numerical Solutions	124
6.4.1. Governing Equation.....	124
6.4.2. Numerical Results.....	125
6.5. Molecular Dynamic Simulation of Thermomigration.....	135
6.6. Conclusions.....	136
References	137
7. Implementation of General Coupling Model in ANSYS and COMSOL	143
7.1. Introduction.....	144
7.2. Implementation of the General Coupling Model in ANSYS	145
7.2.1. Current Practice of Electromigration Modelling in ANSYS.....	145

7.2.2. General Coupling Model	148
7.2.3. Method of Implementation in ANSYS	150
7.3. Implementation of the General Coupling Model in COMSOL	150
7.3.1. Weak Form of the General Coupling Model	150
7.3.2. Method of Implementation in COMSOL	152
7.4. Case Study	156
7.4.1. Totally Fixed Metal Line	156
7.4.2. Stress-Free Metal Line	159
7.5. Conclusions	161
References	161
8. Calculation of Atomic Diffusivity in Polycrystalline Al	165
8.1. Introduction	166
8.2. Methodology	168
8.2.1. Molecular Dynamic Simulation Details	168
8.2.2. Experiment to Estimate Diffusivity	171
8.3. Results and Discussion	172
8.3.1. Atomic Diffusion along the Grain Boundary	172
8.3.2. Atomic Diffusion in Grains	175
8.3.3. Effective Diffusivity of Polycrystals	176
8.3.4 MD-Based Model for Effective Diffusivity	179
8.4. Experimental Results and Comparison	179
8.5. Conclusions	182
References	183
9. Conclusion and Recommendations	187
Appendix A	193
Appendix B	199
Appendix C	205

Appendix D	209
SUMMARY	211
ACKNOWLEDGEMENT	219
CURRICULUM VITAE.....	221
LIST OF PUBLICATIONS	222

LIST OF ABBREVIATIONS

A	Cross-section area, m^2
B	Appropriate modulus, N/m^2
C	Lattice concentration, m^{-3}
C_0	Initial lattice concentration, m^{-3}
C_a	Atomic concentration, m^{-3}
C_v	Vacancy concentration, m^{-3}
C_{a0}	Initial atomic concentration, m^{-3}
$C_{a,\text{void}}$	Atomic concentration for void formation, m^{-3}
$C_{a,\text{hillock}}$	Atomic concentration for hillock formation, m^{-3}
C_{v0}	Initial vacancy concentration, m^{-3}
C_{ve}	Vacancy concentration at stress free condition, m^{-3}
c_p	Specific heat capacity of material, $\text{J/kg}\cdot\text{K}$
D_a	Atomic diffusivity, m^2/s
D_v	Vacancy diffusivity, m^2/s
d_{grain}	Average diameter of the grains, m
\mathbf{E}	Electric field tensor
E	Young's modulus, N/m^2
EM	Electromigration
E_a	Activation energy, eV
e	Electron charge, C
e_{ij}	Total strain tensor
e_{ij}^M	Elastic strain tensor
e_{ij}^{diff}	Diffusion strain tensor
e_{ij}^T	Thermal strain tensor

F	Resultant force vector
f	Vacancy volume relaxation factor
f'	$1 - f$
J_a	Atomic flux tensor
J_v	Vacancy flux tensor
j	Current density tensor, A/m ²
j_c	Threshold current density, A/m ²
K	Bulk modulus, N/m ²
k	Thermal conductivity of material, W/m·K
k_B	Boltzmann constant, J/K or eV/k
L	Total thickness or total length of material, m
L_{void}	Void size, m
MTF	Median time to failure
m	Mass, kg
Q^*	Heat of transport, kJ/mol or eV
\dot{q}	Heat rate per unit volume, W/m ³
q_0	Heat flux at heat source location, W/m ²
R	Electrical resistance, ohm
R_0	Reference electrical resistance, ohm
S	Entropy
T	Temperature, K or °C
TM	Thermomigration
T_0	Reference temperature, K or °C
t	Time, s
t_f	Time to failure, s
t_n	Nucleation time
t_g	Time of void growth
u	Displacement vector
u	Displacement in x -direction, m
V	Electric potential tensor; mass velocity vector
V_0	Reference volume, m ³

V_e	Electric potential, V
v	Displacement in y-direction, m
v_{drift}	Drift velocity, ms
w	Displacement in z-direction, m
Z^*	Effective charge number
α	Thermal expansion factor, m ² /s
δ_{ij}	Kronecker delta
φ	Ratio between Young's Moduli of conductor and passivation layer
ν	Poisson's ratio
Ω	Atomic volume, m ³
θ	Total volumetric strain
ρ	Electrical resistivity of material, ohm-m
σ	Hydrostatic stress, N/m ²
σ_{cr}	Critical stress, N/m ²
σ_n	Threshold tensile stress, N/m ²
ΔC_a	Difference in atomic concentration, m ⁻³

1

1

INTRODUCTION

1.1. Background

In 1969, the world was inspired and awestruck by the image of man walking on the Moon. The moment has been forever memorialized through the powerful quote from Neil Armstrong when he stepped off the lunar module, ‘That’s one small step for a man, one giant leap for mankind’ [1]. The role of the semiconductor in this feat of engineering should absolutely be recognized. Integrated circuits (ICs), invented in 1962, went into the design of the Apollo Lunar Landing Module’s computer. Texas Instruments, Fairchild Semiconductor, and Motorola were among the IC suppliers. In June of 2021, China successfully launched the Tianzhou-2 cargo spacecraft to the Tiangong space station in an orbit around the Earth, opening the door for building the new space station. After fifty years of development, electronics and semiconductor technology are used for many applications in addition to computer design. From ASIC/FPGA/SRAM to intelligent control platforms, from mechanical arms to sensor systems, nearly every aspect of spacecrafts and space stations has implemented microelectronics and semiconductor technologies.

From the 1960s to the 2020s, the rapid development of microelectronics has driven intelligentize and informationalization in all walks of life. Researchers have succeeded tremendously billions of transistors into integrated circuits (the number of transistors in a dense integrated circuit (IC) doubles about every two years). This is known as ‘Moore’s law’ [2]. However, as the Moore’s Law is coming to an end, thus alternative routes and solutions are required to work together ideally to promote the technology progress, as illustrated in Figure 1.1 [3]. Multi-domain (ICs, 3D packages and boards) and potential materials with

enhanced properties (thermal, optical, electrical and mechanical) need to be co-designed and optimized concurrently. Shortage in any parts of electronics, material technologies, and designs will affect the development of the whole system. Among the parts, the reliability of the interconnects is one of critical concerns in microelectronics from nano-scale ICs to micro-level system packages.

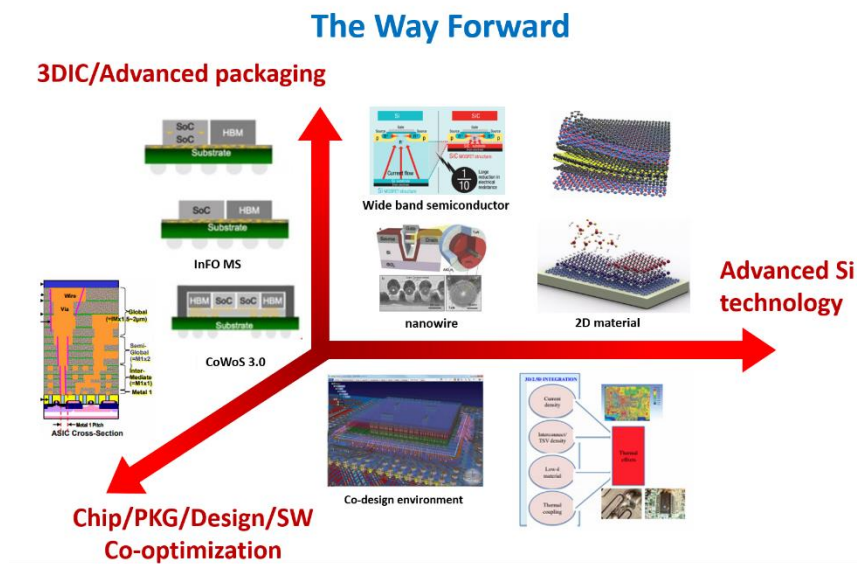


Figure 1.1 Three directions to continued semiconductor innovation (source: ISSCC 2021)

When disassembling any electronic systems, i.e., transistors, diodes, passive circuit elements, microelectromechanical systems (MEMS), etc., we observe that they consist of two parts: the basic components and the highly complex interconnects linking them. The combination of basic circuit elements with multiple 2D-interconnect planes is considered a 2D structure, such as an integrated circuit or a printed circuit board. Connections between planes are then realized through various means, such as through silicon vias (TSVs), pillars, pins and solder balls (Figure 1.2). These interconnects allow the stacking of basic electronic components in the third dimension. However, the continued scaling down of electrical devices and increasing density of components narrows the size of interconnects, which inevitably increases the current density and exacerbates the risk of deterioration in interconnects due to electromigration.

ICs, Components, Devices ...

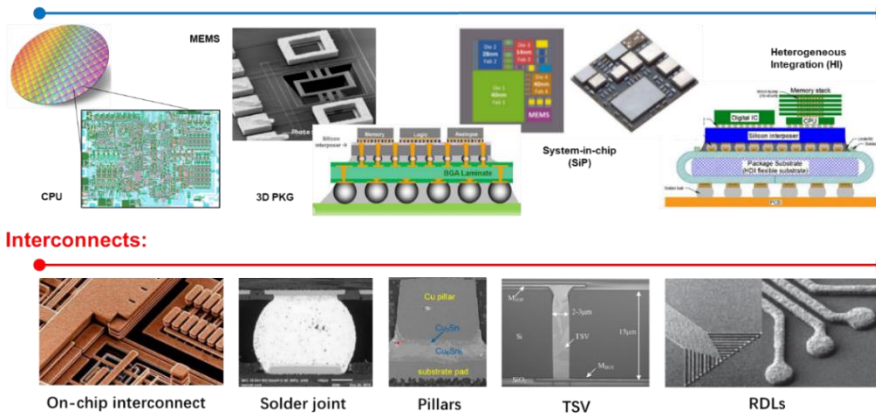


Figure 1.2. Various interconnect structures used in microelectronic devices.

1.2. Electromigration

Electromigration is the phenomenon of mass transport in the conducting metal under an electrical current. The earliest observation can be traced back to 1861 when Gerardin observed electromigration in lead [4]. Subsequently, Huntington *et al.* [5, 6] conducted a series of studies in 1961 on the electromigration process. By observing the motion of surface markers on metal, the authors concluded that the mass transport was caused by the high current density due to the momentum exchange between free electrons and atoms, as illustrated in Figure 1.3 (a). The force to push atoms' movements was vividly described as 'electron wind force'.

In the late 1960s, electromigration began to attract interest from industries because IBM, Fairchild, Motorola and Texas Instruments observed electromigration failure in ICs at approximately the same time. At the time, Al-based metallisation was the first choice for interconnections owing to its low resistivity, good adhesion with SiO_2 and Si, low cost, etc. Black conducted a series of electromigration experiments on Al-based metallisation [7-9]. It was found that the electromigration degradation follows the increasing current density and Arrhenius relationship with temperature. Therefore, a semi-empirical equation for the median time to failure of a conductor was formulated. Shortly after this series of studies, a dielectric passivation layer on top of the Al metallisation layer was reported to potentially improve electromigration reliability compared to bare metallisation [10]. Electromigration lifetime as a function of the thickness of the passivation layer was also later observed [11, 12].

In 1976, Blech *et al.* [13-16] discovered that the mass transport induced by electromigration disappears when the conductor length is below a certain value, as shown in Figure 1.3 (b). The ‘back flow’ of atoms opposite to the electron flow due to the presence of a stress gradient was proposed to explain this phenomenon. Meanwhile, voids and hillocks were observed near the cathode and anode, respectively, in various electromigration experiments. Gradually, two failure modes due to electromigration in interconnects were broadly identified, namely open circuits and short circuits due to the formation of voids and hillocks, respectively.

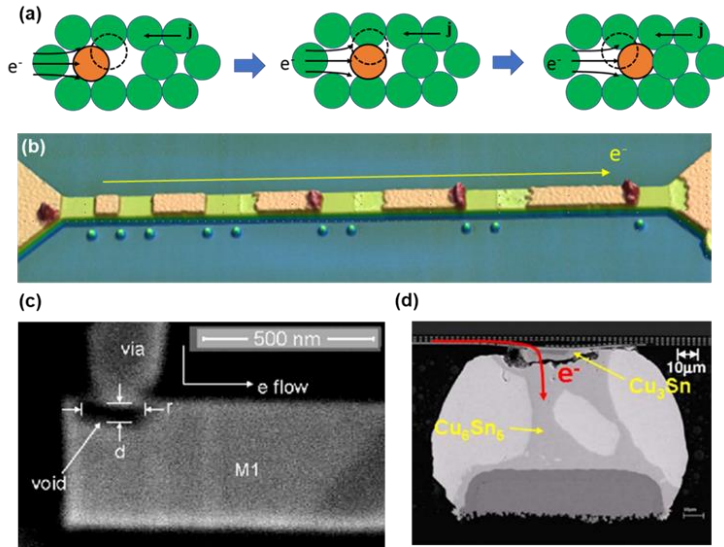


Figure 1.3 (a) Schematic illustration of driving force of electromigration. (b) Typical electromigration failure in Blech structure. (c) Typical electromigration failure in TSV. (d) Typical electromigration failure in solder joint [17].

With the ongoing miniaturisation of electronic devices, Al-based interconnects with small cross-sections were unable to meet the requirements (around the late 1990s). Subsequently, copper, which has the lowest resistivity besides silver, was proposed as a replacement. The early electromigration test using Cu showed that the activation energy for Cu atoms is ~ 2.3 eV [18], which is obviously better than the activation energy of ~ 0.7 eV in Al [19]. Both advantages of Cu encouraged the use of Cu-based interconnect to replace Al-based interconnects.

In chip-level, the fabrication process for Al- and Cu-based interconnections is significantly different. Al-based metallization is patterned by using fluorine base chemistry on the Al thin

film, whereas Cu-based metallization is patterned by creating trench in the dielectric and depositing Cu electrochemically in the trench, known as the damascene process [36–38]. This processing difference is mainly because copper fluoride is non-volatile in nature while Al fluoride is volatile. Moreover, the TSV structure was developed to enable vertical stacking of interconnects. The top surface of Cu metallization which has a chemical-mechanically polished surface, is normally capped by a dielectric barrier layer such as SiN, SiC, etc., of typically 50 nm thick. This dielectric barrier layer protects Cu diffusion into the active area of the chip and acts as etch stop layer. However, the studying of dual damascene structures showed that the Cu/cap interface acts as the dominant diffusing path, causing void formation at the interface between the via and the line (Figure 1.3 (c)). This is believed to be due to the defects generated on the top surface of Cu during chemical–mechanical polishing (CMP) [20–22].

In packaging-level, the heterogeneous integration requires flip-chip technology with submicron solder bumps, wherein electromigration has a different diffusion mechanism than that in pure Cu interconnect. For example, a typical Cu_6Sn_5 joint connects two Cu pads at the top and bottom. Under electromigration at approximately $2 \times 10^5 \text{ A/cm}^2$ and 150°C , the Cu atoms at the top pad could interstitially diffuse into Sn. This could cause phase transfer of solder joint from Cu_6Sn_5 to Cu_3Sn and void formation near the Cu/solder interface, as shown in Figure 1.3 (d) [17]. Notably, the interstitial diffusivity of Cu atoms in Sn is approximately 10^{12} times higher than the self-diffusivity of Sn in Sn. Hence, electromigration in solder joint appears to be a more complex and critical issue compared to that in Cu interconnects.

1.2.1. Theoretical Model

To understand the electromigration process, various mathematical models have been developed over the past decades. One well-known model is Black's equation (Black 1967, 1969)[7–9, 23], which follows the Arrhenius equation and indicates that the electromigration lifetime has an exponential relationship with the current density. Thus, this model is suitable for accelerated tests of electromigration. However, the diffusion process and failure mechanisms are not reflected in Black's equation. Based on Fick's laws of diffusion, Attardo and Rosenberg proposed an early diffusion model to describe the vacancy concentration variations under self-diffusion and an electron wind force [24]. In this model, voids are considered to nucleate at locations with high vacancy supersaturation.

Circa 1976, Blech published a series of papers implying that there is another force that balances the electron wind force [13–16]. This force, discussed to be the tensile stress at the

cathode and the compressive stress at anode, forms a stress gradient. Subsequently, several models were proposed to evaluate the stress build-up during electromigration, including Kirchheim's model (1992) [25], Korhonen's model (1993) [26], Clement and Thompson's model (1995, 1997) [27, 28], Sarychev's model (2000) [29], Suo's model (2004) [30] and Sukharev's model (2004, 2007) [31, 32]. Additionally, the temperature gradient is the other driving force for the mass transport during electromigration. Hence, Basaman's model (2005) [33], Sukharev's model (2007) and Tu's energy model (2019) [34] considered the thermal field equation and thermomigration in the diffusion model.

With further study of electromigration, researchers observed that the microstructure of interconnects plays a significant role in electromigration. This is because it introduces a variety of diffusion paths and local mechanical properties (Young's modulus and Poisson's ratio depend on the crystal orientation in each grain). However, the microstructure itself cannot be completely controlled by process technology. Namely, the locations of grain boundaries, the angles at which they meet the interfaces, etc., cannot be designed. Therefore, several statistical models (Ho *et al.* (2016)[35], Ceric *et al.* (2009) [36]) of electromigration were developed recently to consider the effect of the statistical distribution of grains and grain boundaries on electromigration.

1.2.2. Electromigration Accelerated Test

The required interconnect electromigration lifetime at normal operating conditions exceeds 10 years. Thus, an accelerated test is required to evaluate the electromigration performances of interconnects. There are several aspects in accelerated tests:

1. Circuit structure: Electromigration testing requires precise resistance measurement; therefore, it is necessary to use a Kelvin connection to avoid including the contact resistance in the resistance measurement.
2. Testing structures: There are various types of test structures. The simplest EM test structure is the 'Blech structure'. The standard wafer-level electromigration acceleration test (SWEAT) structure and the National Institute of Standards and Technology (NIST) test structure are also typical single-level planar metallization used in EM test. The line-via test structures and the solder bump structures were designed for the requirements of multilevel metallisation.
3. Resistivity calibration: While performing an electromigration test, the failure criteria is the % change in the resistance of an interconnect. The actual temperature of the interconnect plays an important role in its time to failure. Thus, an accurate

measurement of the resistivity as a function of temperature, $R(T)$, is important. Common electrical measurement for obtaining $R(T)$ is performed before the electromigration test when the oven temperature rises from room temperature to test temperature. During this period, the sample resistance is measured by sending a small (in magnitude) current pulse for at least three different temperatures (excluding the room temperature resistance measurement).

4. Failure analysis: The physical failure analysis (FA) is conducted to check the sample that had undergone current stressing. The FA is performed using various tools, such as optical microscopy, FIB, SEM, etc., to investigate the root cause, failure location, fast diffusion path, etc. TEM is also used in the FA, especially for samples of line-widths below $0.2\text{ }\mu\text{m}$ and when resolutions higher than those in SEM is desired. Using X-rays is another technique for FA that can be used to measure the deformation of interconnects during electromigration. However, to test the lattice expansion/shrinkage induced by electromigration, synchrotron x-ray microscopy is required.

1.3. Objectives

While the general description of the electromigration phenomenon is well established, several unsolved issues and challenges remain:

1. Many mathematical models in literature have been developed to evaluate the stress build-up during electromigration, such as Kirchheim's model, Korhonen's model, Sarcheve's model, Suo's model and Suckareve's model. However, variations between these models raise confusion and there remain some unsolved problems.
2. Thermomigration has increasingly become a potential concern in 2.5D or 3D packaged devices. Using Si interposers has been reported to enhance the lateral heat transfer along it; however, it has caused unexpected thermomigration failures. To completely understand thermomigration coupled with electromigration, both experimental testing and numerical simulation are required.
3. Electromigration strongly depends on the microstructure of materials and the bonding strength between the interconnects and the capping layer. Unfortunately, most of the simulation studies on electromigration are only based on continuum theory, which cannot provide a fundamental understanding of the aforementioned mechanisms. The accurate determination of material properties, such as the atomic diffusivity along grain boundaries, effective charge number and vacancy relaxation factor, are critical to the simulation of electromigration. However, such parameters

are difficult to be determined via traditional experimental methods.

Considering the issues and challenges above, the primary objective of this study is to advance the fundamental knowledge and understanding of electromigration, establishing a multi-physics and fully coupled electromigration model. Our objectives are as follows:

1. Establish a fully coupled multi-physics theory of electromigration, solving several long-standing questions in the formulation of electromigration.
2. Conduct electromigration experiments and characterizations to investigate various influential factors on electromigration. We also intend to compare the fully coupled simulation results with experimental data to validate the new theory developed in this dissertation.
3. Apply atomistic modelling to the study of electromigration, such as calculating parameters used in continuum modelling and the fundamental understanding of the properties for different atomistic configurations.
4. Implement the developed multi-physics theory in commercial finite element software ANSYS and COMSOL, providing a convenient way for its application in industries.

To further illustrate the objectives and investigations presented in this dissertation, a technology roadmap is plotted in Figure 1.4.

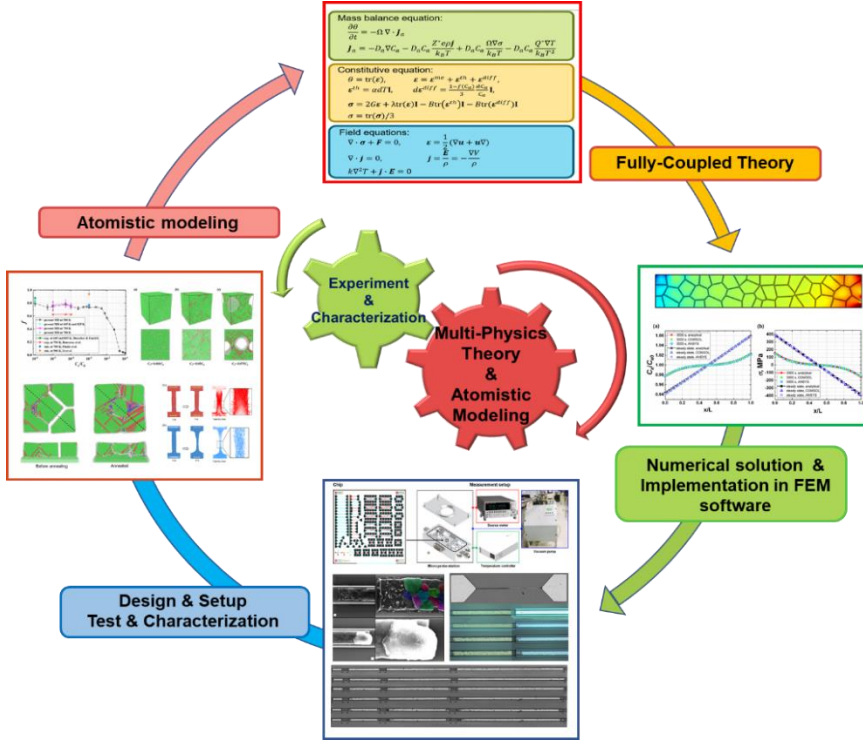


Figure 1.4 Illustration of roadmap of this dissertation.

1.4. Organization of Dissertation

This dissertation is separated into nine chapters beginning with Chapter 1, the introduction. Chapter 2 reviews several electromigration models that have been proposed over the past decades. One-dimensional (1D) numerical solutions obtained using different electromigration models are presented and compared. Following which, in Chapter 3, we propose a 3D general coupling model for electromigration. Several long-standing conundrums in the physical formulas of electromigration are solved. Numerical solutions for the 1D problem are provided to illustrate the differences between our model and existing models in literature.

Chapter 4 calculates a key parameter, the vacancy volume relaxation factor. To quantitatively determine the diffusion-induced strain and stress in electromigration, it is necessary to determine this parameter accurately. Hence, large-scale molecular dynamic (MD) models are constructed for different vacancy concentration levels. A uniform empirical equation for the vacancy volume relaxation factor at different concentration levels is obtained. Hydrostatic

stresses and diffusion strain obtained from MD simulations are compared with a commonly used stress-vacancy equation.

In Chapter 5, electromigration experiments are conducted. A full wafer with various testing structures is designed and fabricated. The electromigration measurement setup is established. Various influential factors, such as conductor length, current density, annealing or non-annealing, temperature, passivation condition and sample structures, are experimentally investigated. Moreover, based on the developed fully coupled model of electromigration, numerical solutions for the 1D dielectric-covered metal line and stress-free metal line are obtained to determine the effects of mechanical stress and self-diffusion on electromigration.

Chapter 6 investigates the thermomigration accompanying electromigration through experiments and simulations. The effects of the current density, conductor length and sample structures on thermomigration are investigated. In the simulations, by using the developed fully coupled electromigration model, the numerical solutions of a 1D metal line with perfectly blocking conditions and constant atomic concentration at both sides are obtained and compared with the experimental results. The coupling relationship between thermomigration and electromigration and its effect on mass transport, void formation and breaking locations are determined.

In Chapter 7, the general coupling theory of electromigration is implemented in ANSYS and COMSOL. The theory is implemented in ANSYS by using the ANSYS build-in multi-physics theory. Similarly, it is implemented in COMSOL by using the weak form in partial differential equation (PED) modulus. Case studies of 1D fully fixed metal lines and stress-free metal lines are provided as benchmark problems.

Chapter 8 demonstrates an MD simulation-based methodology to calculate the effective diffusivity in polycrystalline metals. Atomic diffusivities along grain boundaries and grains are calculated. The effective diffusivity determined based on the MD results is obtained, which is then compared with that determined from electromigration experiments.

Chapter 9 concludes the dissertation, summarises the contributions and proposes a few novel ideas for future research.

References

1. "Journey to the Moon, H.o.t.A.G.C., Eldon Hall, page 79.
2. "Cramming More Components onto Integrated Circuits", G.M., pp 114 – 117, Electronics, 19 April 1965.
3. Liu, M., *Unleashing the Future of Innovation*. IEEE International Solid-State Circuits Conference, 2021: p. 9-16.
4. Puttlitz, K.J. and K.A. Stalter, *Handbook of lead-free solder technology for microelectronic assemblies*. 2004: CRC Press.
5. Huntington, H. and A. Grone, *Current-induced marker motion in gold wires*. Journal of Physics Chemistry of Solids, 1961. **20**(1-2): p. 76-87.
6. Huntington, H., *Effect of driving forces on atom motion*. Thin Solid Films, 1975. **25**(2): p. 265-280.
7. Black, J.R., *Electromigration failure modes in aluminum metallization for semiconductor devices*. Proceedings of the IEEE, 1969. **57**(9): p. 1587-1594.
8. Black, J.R., *Electromigration—A brief survey and some recent results*. IEEE Transactions on Electron Devices, 1969. **16**(4): p. 338-347.
9. Black, J.R. *Mass transport of aluminum by momentum exchange with conducting electrons*. in *6th Annual Reliability Physics Symposium (IEEE)*. 1967. IEEE.
10. Spitzer, S. and S. Schwartz, *The effects of dielectric overcoating on electromigration in aluminum interconnections*. IEEE Transactions on Electron Devices, 1969. **16**(4): p. 348-350.
11. Lloyd, J., *Electromigration in Al-Cu thin films with polyimide passivation*. Thin Solid Films, 1982. **91**(2): p. 175-182.
12. Lloyd, J. and P. Smith, *The effect of passivation thickness on the electromigration lifetime of Al/Cu thin film conductors*. Journal of Vacuum Science Technology A: Vacuum, Surfaces, Films, 1983. **1**(2): p. 455-458.
13. Blech, I.A., *Electromigration in thin aluminum films on titanium nitride*. Journal of applied physics, 1976. **47**(4): p. 1203-1208.
14. Blech, I. and E. Kinsbron, *Electromigration in thin gold films on molybdenum surfaces*. Thin Solid Films, 1975. **25**(2): p. 327-334.
15. Blech, I. and K. Tai, *Measurement of stress gradients generated by electromigration*. Applied Physics Letters, 1977. **30**(8): p. 387-389.
16. Blech, I. and C. Herring, *Stress generation by electromigration*. Applied Physics Letters, 1976. **29**(3): p. 131-133.

17. Chen, H.-Y., C. Chen, and K.-N. Tu, *Failure induced by thermomigration of interstitial Cu in Pb-free flip chip solder joints*. Applied Physics Letters, 2008. **93**(12): p. 122103.
18. Grone, A., *Current-induced marker motion in copper*. Journal of Physics Chemistry of Solids, 1961. **20**(1-2): p. 88-93.
19. Schreiber, H.-U., *Activation energies for the different electromigration mechanisms in aluminum*. Solid-State Electronics, 1981. **24**(6): p. 583-589.
20. Hu, C.-K. and J. Harper, *Copper interconnections and reliability*. Materials Chemistry Physics, 1998. **52**(1): p. 5-16.
21. Wang, H., C. Bruynseraede, and K. Maex. *The influence of surface fluctuations on early failures in single-damascene Cu wires: a weakest link approximation analysis*. in *2004 IEEE International Reliability Physics Symposium. Proceedings*. 2004. IEEE.
22. Gan, D., et al., *Isothermal stress relaxation in electroplated Cu films. I. Mass transport measurements*. Journal of Applied Physics, 2005. **97**(10): p. 103531.
23. PR Bourassa, D.L., DA Blackburn, *Effect of High Pressure on the Thermoelectric Power and Electrical Resistance of Aluminum and Gold*. Physical Review, 1968. **165**(3).
24. Attardo, M. and R. Rosenberg, *Electromigration damage in aluminum film conductors*. Journal of Applied Physics, 1970. **41**(6): p. 2381-2386.
25. Kirchheim, R., *Stress and electromigration in Al-lines of integrated circuits*. Acta Metallurgica et Materialia, 1992. **40**(2): p. 309-323.
26. Korhonen, M., et al., *Stress evolution due to electromigration in confined metal lines*. Journal of Applied Physics, 1993. **73**(8): p. 3790-3799.
27. Clement, J. and C. Thompson, *Modeling electromigration - induced stress evolution in confined metal lines*. Journal of applied physics, 1995. **78**(2): p. 900-904.
28. Clement, J., *Vacancy supersaturation model for electromigration failure under dc and pulsed dc stress*. Journal of applied physics, 1992. **71**(9): p. 4264-4268.
29. Sarychev, M., et al., *General model for mechanical stress evolution during electromigration*. Journal of Applied Physics, 1999. **86**(6): p. 3068-3075.
30. He, J., et al., *Electromigration lifetime and critical void volume*. Applied Physics Letters, 2004. **85**(20): p. 4639-4641.

31. Sukharev, V. and E. Zschech, *A model for electromigration-induced degradation mechanisms in dual-inlaid copper interconnects: Effect of interface bonding strength*. Journal of Applied Physics, 2004. **96**(11): p. 6337-6343.
32. Sukharev, V., E. Zschech, and W.D. Nix, *A model for electromigration-induced degradation mechanisms in dual-inlaid copper interconnects: Effect of microstructure*. Journal of Applied Physics, 2007. **102**(5): p. 053505.
33. Lin, M. and C. Basaran, *Electromigration induced stress analysis using fully coupled mechanical–diffusion equations with nonlinear material properties*. Computational Materials Science, 2005. **34**(1): p. 82-98.
34. Tu, K.-N. and A. Gusak, *A unified model of mean-time-to-failure for electromigration, thermomigration, and stress-migration based on entropy production*. Journal of Applied Physics, 2019. **126**(7): p. 075109.
35. Kraatz, M., et al., *A model for statistical electromigration simulation with dependence on capping layer and Cu microstructure in two dimensions*. Computational Materials Science, 2016. **120**: p. 29-35.
36. De Orio, R., H. Ceric, and S.J.M.R. Selberherr, *Physically based models of electromigration: From Black's equation to modern TCAD models*. 2010. **50**(6): p. 775-789.

2

2

LITERATURE REVIEW OF MULTI-PHYSICS MODEL OF ELECTROMIGRATION

Mathematical modelling is an important tool for understanding electromigration and predicting failure. In this chapter, we review several electromigration models that have been proposed over the past decades. We begin with Black's equation and end at a very simple one-dimensional model that only considers self-diffusion and electromigration. We then proceed to more complex models incorporating the effects of mechanical stress, sink/source terms and thermomigration. Several unsolved issues and conundrums in literature are discussed. To illustrate the differences between these models, corresponding one-dimensional numerical solutions are obtained and compared with each other.

2.1. Introduction

Electromigration is a mass transport process attributed to the electron wind force due to the momentum transfer between conducting electrons and metal atoms. Typically, voids are formed and grow in the region where atoms are depleted, causing a significant increase in resistance and leading to line breaking. Hillocks are generated in the region where atoms are accumulated, causing short circuits. While electromigration is induced by the electron wind force, it is not the only driving force at work. The balance of other forces, such as stress migration, concentration gradient and thermal migration, determines the diffusive motion of atoms.

Over the past decades, different approximate approaches to the mathematical formulation and solution have appeared in literature. These significantly contribute to the understanding of electromigration failure mechanisms. Nowadays, mathematical modelling is not only used to explain experimental observations but has also become an important tool to design interconnects. However, variations between these physical models and mathematical modelling caused several issues. In this chapter, we will present a review of the physical models of electromigration in a somewhat chronological order. Different influential factors on electromigration are introduced by reviewing the studies from the very simple one-dimensional model to complex three-dimensional models. Several unsolved issues and confusion in literature are presented and discussed.

2.2. Black's Model

In 1969, a simple equation was developed by Black [1-3] to predict the lifetimes of metal lines subjected to electromigration. He considered that the mean time to failure (MTTF) is related to the rate of mass transfer and the conductor cross area as follows:

$$MTTF = \frac{Fwh}{R} \quad (2.1)$$

where F is a constant, and w and h are the width and thickness of the conductor, respectively, R is the rate of mass transport, which is proportional to the electron momentum (P), the number density of conducting electrons (n_e), and the density of activated ions (N_a). Thus, R is expressed using the following equation.

$$R = n_e P N_a \quad (2.2)$$

The momentum transfer (P) is assumed to be related to the electric field (E), diffusion length (l) and average velocity (v) according to the following equation.

$$P = eE \frac{l}{v} = e\rho j \frac{l}{v} \quad (2.3)$$

where e is the charge of an electron, ρ is the electrical resistivity and j the current density. Additionally, the density of conducting electrons (n_e) in Eq. (2.2) is related to the current density (j). Therefore,

$$n_e = j/e. \quad (2.4)$$

The activated ions in the conductor follow the Arrhenius equation; therefore,

$$N_a = N_{a0} \exp\left(-\frac{E_a}{kT}\right) \quad (2.5)$$

where E_a is the activation energy, k is the Boltzmann's constant and T is the temperature. Applying Eqs. (2.2)–(2.5) to Eq. (2.1), we can obtain the following equation

$$\frac{Fwt}{MTTF} = (e\rho j \frac{l}{v}) \left(\frac{j}{e}\right) N_{a0} \exp\left(-\frac{E_a}{kT}\right) \quad (2.6)$$

The MTTF can be then derived as follows:

$$MTTF = \frac{A}{j^2} \exp\left(-\frac{E_a}{kT}\right) \quad (2.7)$$

where A is a constant that depends on several physical properties and geometrical features of interconnects. Eq. (2.7) indicates that the failure time of electromigration is inversely proportional to the square of the current density. However, not all experimental results followed this law [4, 5]. In subsequent studies, Black's equation was modified to the following equation.

$$MTTF = \frac{A}{j^n} \exp\left(-\frac{E_a}{kT}\right) \quad (2.8)$$

In Eq. (2.8), the parameters A , E_a and n can be determined by fitting the experimental results. The reported n -value in literature varies as follows: $1 < n < 2$ [6-8], $n = 4$ [9, 10], $n = 4.5$ [11], $n = 4.9$ [12], $n = 5$ [13] or n as high as 10 [14]. Several studies [15, 16] conclude that the current exponent, n , in Black's equation equals to 2 for lifetimes controlled by void nucleation and equals to 1 for lifetimes limited by void growth. In a recent publication, Lloyd *et al.* [17] discussed significant errors that Black's equation may cause because the determination of the parameters above does not consider the details of the failure process and the underlying physics behind the electromigration behaviour. Therefore, more sophisticated physically based models are required.

2.3. Mass Transport Equation of Electromigration

The total atomic transport of electromigration is controlled by a combination of interplayed driving forces with different physical mechanisms. Furthermore, because atomic migration occurs via a vacancy exchange mechanism, the material transport can be described in terms of a vacancy flux via Fick's 1st law. The total vacancy flux is typically written as [18-22]

$$J_v = -D_v(\nabla C_v - \frac{Z^*}{kT} C_v \mathbf{E} - \frac{Q^*}{kT^2} C_v \nabla T + \frac{f\Omega}{kT} C_v \nabla \sigma) \quad (2.9)$$

where D_v is the vacancy diffusivity, C_v is the vacancy concentration, Z^* is the effective charge number ($Z^* > 0$), \mathbf{E} is the electric field and Q^* is the heat of transport. Ω is the atomic volume, σ is the hydrostatic stress, k is Boltzmann's constant and T is the temperature. This equation contains all the important driving forces during electromigration, namely, the driving force for self-diffusion (gradient of the vacancy concentration), electron wind force and the driving forces due to the gradients of temperature and mechanical stress.

In 1986, Shatzkes and Lloyd [23] employed Fick's 2nd law to describe the vacancy evolution during electromigration while considering the influences of self-diffusion and electromigration as follows:

$$\frac{\partial C_v}{\partial t} = D_v \left(\frac{\partial^2 C_v}{\partial x^2} - \frac{Z^* e \rho j}{kT} \frac{\partial C_v}{\partial x} \right) \quad (2.10)$$

For a finite line with blocking boundary conditions at both ends

$$J_v(0, t) = J_v(L, t) = 0 \quad (2.11)$$

where L is the line length. The solution of Eq. (2.10) was obtained as follows:

$$\frac{C_v(x, t)}{C_{v0}} = A_0 - \sum_{n=1}^{\infty} A_n \exp \left(-B_n \frac{D_v}{L^2} t + \frac{\alpha x}{2L} \right) \quad (2.12)$$

where

$$A_0 = \frac{\alpha}{1 - \exp(-\alpha)} \exp \left(\alpha \frac{x}{L} \right) \quad (2.13)$$

$$A_n = \frac{16n\pi\alpha^2(1 - \exp(\alpha/2))}{(\alpha^2 + 4n^2\pi^2)^2} \left[\sin \left(n\pi \frac{x}{L} \right) + \frac{2n\pi}{\alpha} \cos \left(n\pi \frac{x}{L} \right) \right] \quad (2.14)$$

$$B_n = n^2\pi^2 + \alpha^2/4 \quad (2.15)$$

$$\alpha = \frac{Z^* e \rho j L}{kT} \quad (2.16)$$

Using the parameters listed in Table 2.1, the evolution of the vacancy concentration with time in a 50 μm long line was obtained, as plotted in Figure 2.1. The vacancy migrates along the direction of the current density, causing vacancy accumulation and deletion at the cathode and anode, respectively. However, results showed that the vacancy concentration at the cathode saturated at ~ 1 s (see Figure 2.1 (b)). This is a very short time compared to the failure time in the order of several hours obtained from experiments.

Table 2.1 Parameters used in the calculations.

Material properties	Value
Length of metal line (L)	50 μm
Temperature (T)	500 K
Atomic diffusivity (D_a)	$3 \times 10^{-16} \text{ m}^2/\text{s}$
Vacancy diffusivity (D_v)	$3 \times 10^{-9} \text{ m}^2/\text{s}$
Atomic volume (Ω)	$1.66 \times 10^{-29} \text{ m}^3$
Electrical resistivity (ρ)	$4.88 \times 10^{-8} \text{ Ohm}\cdot\text{m}$
Current density (j)	$10^{10} \text{ A}/\text{m}^2$
Electrical charge (e)	$1.6 \times 10^{-19} \text{ C}$
Charge number (Z^*)	3.5
Boltzmann's constant (k)	$1.38 \times 10^{-23} \text{ J/K}$
Young's modulus (E)	70 GPa
Poisson's ratio (ν)	0.3

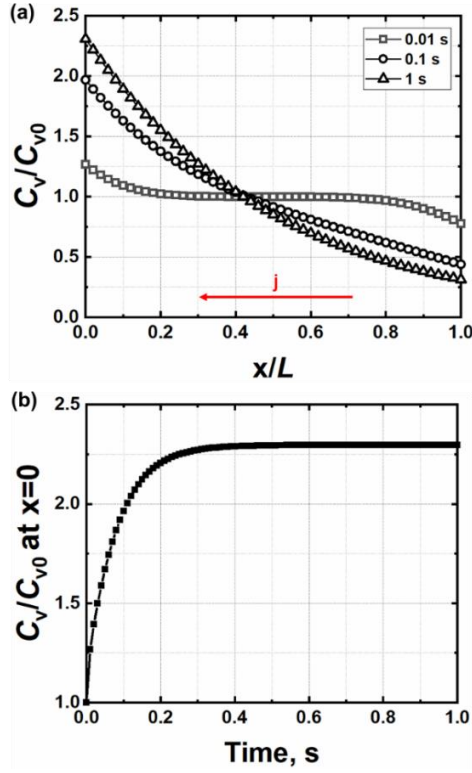


Figure 2.1. (a) Vacancy concentration distribution along the length of the metal line under blocking boundary conditions. (b) Vacancy concentration evolution at $x = 0$.

On further investigation, researchers realized that such a short time scale for failure is due to the absence of a sink/source term. The electromigration model proposed by Kirchheim *et al.* [24, 25] includes the sink/source term as follows:

$$\frac{\partial C_v}{\partial t} = -\frac{\partial J_v}{\partial x} - \frac{C_v - C_{ve}}{\tau} \quad (2.17)$$

where C_{ve} is the equilibrium vacancy concentration, which depends on the stress level in the metal line. τ is the characteristic vacancy relaxation time. The last term on the right-hand side of Eq. (2.17) represents a source function that models vacancy annihilation and generation. This term implies that vacancies are either annihilated or produced depending on whether their concentrations are larger or smaller, respectively, than the equilibrium value. Subsequently, a somewhat simplified model was proposed by Korhonen *et al.* [26], which considered the rate of change of lattice concentration as the sink/source term

$$\frac{\partial C_v}{\partial t} = -\frac{\partial J_v}{\partial x} + \frac{\partial C_L}{\partial t} \quad (2.18)$$

where C_L is the lattice concentration. Assuming $\frac{\partial C_v}{\partial t} \ll \frac{\partial C_L}{\partial t}$, Eq. (2.18) becomes

$$\frac{\partial C_L}{\partial t} = \frac{\partial J_v}{\partial x} \quad (2.19)$$

Furthermore, Korhonen considered that the change in lattice concentration (C_L) could induce a volume strain as follows [26]:

$$\frac{dC_L}{C_L} = d\varepsilon = d\varepsilon_{xx} + d\varepsilon_{yy} + d\varepsilon_{zz} \quad (2.20)$$

Thus, Eq. (2.19) can be rewritten as follows:

$$\frac{\partial \varepsilon^T}{\partial t} = \Omega \frac{\partial J_v}{\partial x} \quad (2.21)$$

A similar mass transport equation is provided in the study conducted by He *et al.* [27].

$$\frac{\partial \theta}{\partial t} = \Omega \frac{\partial J_v}{\partial x} \quad (2.22)$$

where θ is the total volumetric strain of the metal line during electromigration. To solve Eqs. (2.17), (2.21) and (2.22), additional relationships with regards to hydrostatic stress were introduced in the studies conducted by Kirchheim [25], Korhonen [26] and He [27]. As discussed below, this mechanical stress plays an important role in electromigration and extensive studies have been published to discuss the coupling relationship between mechanical stress and electromigration.

2.4. Electromigration and Mechanical Stress

From 1976, Blech published a series of short papers to explain the origin of mechanical stress, commonly called ‘back stress’ [28], during electromigration [29-31]. In his experiments, aluminium (Al) stripes of different lengths were patterned onto a thin TiN layer, as shown in

Figure 2.2 (a). Al is a better conductor than TiN; therefore, the current would detour from TiN and pass through the Al stripes. As expected, electromigration failures were observed in the Al stripes with depletions or void formations at the cathode end and the growth of hillocks at the anode end. Blech also determined that the longer the stripe, the greater the depletion. Moreover, no damage was observed in very short stripes, as shown in Figure 2.2 (b).

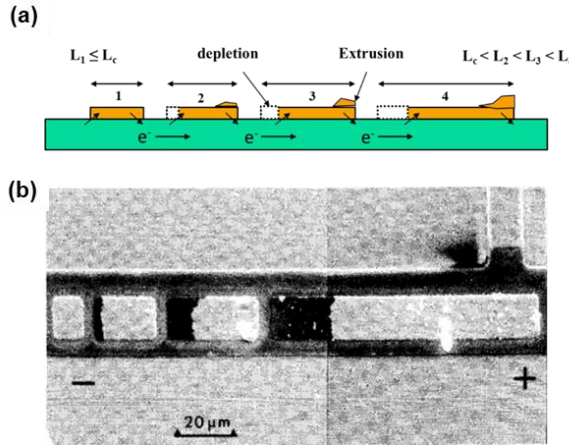


Figure 2.2. (a) Schematic diagram of Blech's experiment. (b) SEM image of Al stripes of different lengths after passage of 3.7×10^5 A/cm² for 15 h. [29]

To explain this phenomenon, Blech suggested that electromigration can be fully stopped when the driving force from the stress gradient exactly equals the electron wind force, as shown in the following equation.

$$Z^* e \rho j + \Omega \frac{\Delta \sigma}{\Delta x} = 0 \quad (2.23)$$

where Δx is defined as the critical length of the stripe, below which there is no electromigration failure. Integrating Eq. (2.23) over the length of the metal line and assuming that the critical failure condition is the maximum stress that the metal line can withstand (σ_{th}) [29], a critical product of the metal line length and the current density can be obtained as follows:

$$(jL)_c = \frac{(\sigma_{th} - \sigma_0) \Omega}{Z^* e \rho} \quad (2.24)$$

From Eq. (2.24), for a given current density, j , we can determine a critical line length.

$$L_B = \frac{(\sigma_{th} - \sigma_0)\Omega}{Z^*ej} \quad (2.25)$$

This is known as the ‘Blech length’. The equation above implies that a shorter interconnect would not fail because σ would be below the critical stress. Based on Blech’s theory, electromigration failure is a mechanical failure. Although Blech provides a useful insight into electromigration failure mechanisms, it does not present a thorough understanding of the underlying physical behaviours of mechanical stress in electromigration at both transient and steady states. As mentioned in section 2, Kirchhiem *et al.* [24, 25], Korhonen *et al.* [26] and He *et al.* [27] connected the rate of stress generation to electromigration. Furthermore, Sharchev *et al.*, Sukharev *et al.* and Maniatty *et al.* also established different models to evaluate the stress build-up during electromigration. Among them, Korhonen’s model, one of the most widely used ones, includes three parts to consider the mechanical stress in electromigration.

Firstly, Korhonen *et al.* [26] added the driving force of hydrostatic stress in the vacancy flux.

$$J_v = D_v C_v \frac{Z^*ej}{kT} - D_v C_v \frac{\Omega}{kT} \frac{\partial \sigma}{\partial x} \quad (2.26)$$

Secondly, the equilibrium vacancy concentration was related to the mechanical stress via the following equation [32, 33].

$$C_v = C_{v0} \exp\left(\frac{\Omega \sigma}{kT}\right) \quad (2.27)$$

where C_{v0} is the initial vacancy concentration.

Thirdly, for a metal line confined in a dielectric, the author considered that the volumetric strain induced by the change in the lattice concentration produces stress according to Hooke’s law.

$$d\sigma = -B d\varepsilon^T = -B \frac{dC_L}{C_L} \quad (2.28)$$

where B is the effective modulus of the material. With the above-mentioned considerations about mechanical stress, Eq. (2.21) becomes

$$\frac{\partial \sigma}{\partial t} = \frac{\partial}{\partial x} \left[\frac{D_a B \Omega}{kT} \left(\frac{\partial \sigma}{\partial x} - \frac{Z^* e \rho j}{\Omega} \right) \right] \quad (2.29)$$

Clement *et al.* [34] studied Eq. (2.21) under similar conditions; however, they described it in terms of vacancy concentration as follows:

$$\frac{\partial C_v}{\partial t} = \frac{D_a B \Omega}{kT} \left(\frac{\partial^2 C_v}{\partial x^2} - \frac{Z^* e \rho j}{kT} \frac{\partial C_v}{\partial x} \right) \quad (2.30)$$

According to Korhonen's equation (2.29), using the boundary condition in Eq. (2.11) and parameters from Table 2.1, Figure 2.3 shows the stress development with time at $x=0$. Notably the time scale of stress build-up is in the order of several hours rather than a few minutes. This is because the sink source term and mechanical stress were considered in the continuity equation. Figure 2.4 shows the vacancy concentrations and stress distributions along the line length at different times. At a steady state, the stress varies linearly, as predicted by Blech [29]. Maximum hydrostatic stress can develop in the interconnect for void nucleation. Clement *et al.* [34], Kirchheim *et al.* [26] and He *et al.* [27] presented similar results.

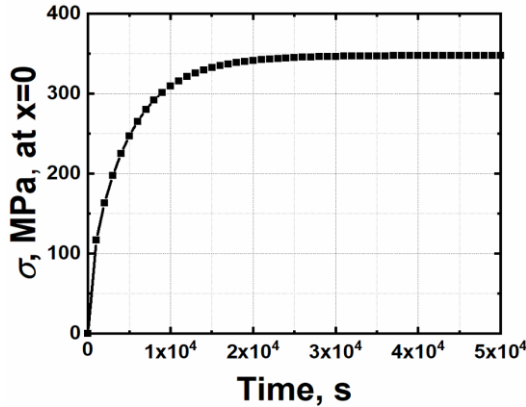


Figure 2.3. Hydrostatic stress at $x = 0$ for Eq. (29) under blocking boundary condition.

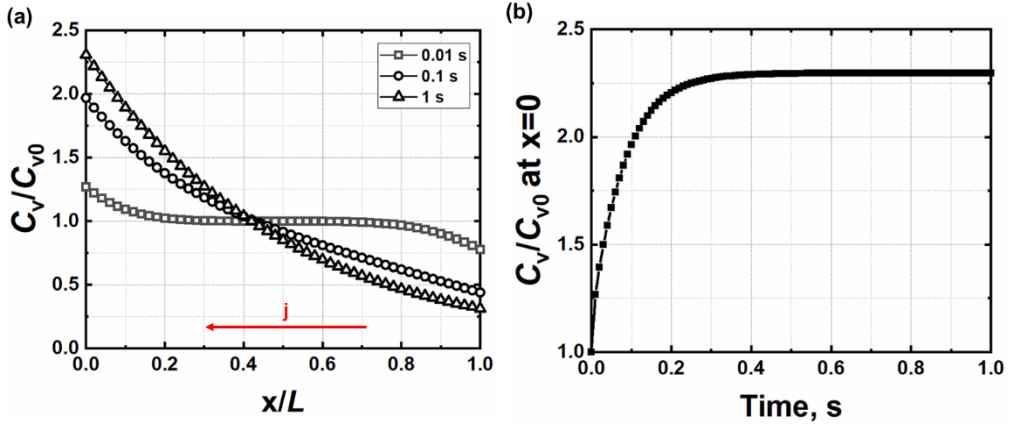


Figure 2.4. (a) Vacancy concentration distribution along the metal line under blocking boundary conditions obtained by solving Eq. (29). (b) Hydrostatic stress distribution along the metal line.

Subsequently, Sarychev *et al.*[35] proposed a set of three-dimensional (3D) equations for the evolution of stress during electromigration. In this model, the inelastic strains (ε_{ij}^i) due to vacancy migration (ε_{ij}^m) and generation/annihilation (ε_{ij}^g) were proposed.

$$\frac{\partial \varepsilon_{ij}^i}{\partial t} = \frac{\partial \varepsilon_{ij}^m}{\partial t} + \frac{\partial \varepsilon_{ij}^g}{\partial t} \quad (2.31)$$

$$\frac{\partial \varepsilon_{ij}^m}{\partial t} = \frac{1}{3} f \Omega (\nabla \cdot \mathbf{J}_v) \delta_{ij} \quad (2.32)$$

$$\frac{\partial \varepsilon_{ij}^g}{\partial t} = \frac{1}{3} (1 - f) f \Omega G \delta_{ij} \quad (2.33)$$

where f is a parameter denoting the vacancy volume relaxation and δ_{ij} is the Kronecker delta. If the metal line deforms elastically,

$$\sigma_{ij} = \lambda \varepsilon_{kk} \delta_{ij} + 2G \varepsilon_{ij} - B \varepsilon_{kk}^i \delta_{ij} \quad (2.34)$$

where G and λ are Lamé constants ($2G = E/(1 + \nu)$ and $\lambda = 2G\nu/(1 - 2\nu)$), E is Young's modulus, ν is Poisson's ratio and $B = \lambda + 2G/3$ is the bulk modulus. Based on the stress equilibrium equation,

$$\frac{\partial \sigma_{ij}}{\partial x_j} = 0 \quad (2.35)$$

and under a small displacement approximation,

$$\varepsilon_{ij} = \frac{1}{2} \left(\frac{\partial u_i}{\partial x_j} + \frac{\partial u_j}{\partial x_i} \right) \quad (2.36)$$

The deformation of the line as a function of the inelastic strain due to electromigration can be calculated using

$$2G \nabla^2 u_i + (\lambda + 2G) \frac{\partial}{\partial x_i} (\nabla \cdot u) = B \frac{\partial}{\partial x_i} \text{tr}(\varepsilon_{ij}^i) \quad (2.37)$$

A significant contribution of Sarychev's model is the coupling of mechanical stress with electromigration by using the constitutive equation and the stress equilibrium equation. In this manner, the impact of the interconnect geometry and imposed boundary conditions on the stress evolution can be considered. However, the 1D governing equation and the numerical solution obtained based on Sarychev's model were not available to compare with the previous results.

With the understanding of electromigration, researchers determined that the mass transport along the grain boundary plays an important role in electromigration. To consider the effects of different diffusion paths on electromigration, Sukharev *et al.* [21, 22] considered the fast diffusivity paths and specific vacancy annihilation/generation rates at different sites. The continuity equations for the bulk matter and the interfaces are separately provided as follows,

$$\frac{\partial C_v^{bulk}}{\partial t} = -\nabla \cdot \mathbf{J}_v^{bulk} \quad (2.38)$$

$$\frac{\partial C_v^{int}}{\partial t} = -\nabla \cdot \mathbf{J}_v^{int} + G_{int} \quad (2.39)$$

where the interfaces generally refer to the grain boundaries. The fluxes along the bulk matter and the interfaces are identical to those in Eq. (2.7); however, D_v is replaced by the corresponding diffusion coefficient. Thus, the vacancy flux along each path is characterised by its own diffusivity. Additionally, each interface that acts as a vacancy sink/source can be described by a specific vacancy annihilation/generation rate. Furthermore, Sukharev *et al.*

[22] suggested that the exchanged locations between vacancies and atoms may produce a diffusion strain.

$$\varepsilon_{ij}^e = \Omega[-(1-f)(C_v - C_{v0}) + (C_a - C_{a0})]\delta_{ij} \quad (2.40)$$

where C_{a0} is the plated atom concentration at the zero-stress condition. Subsequently, while considering the diffusion and thermal strains (ε_{kk}^T), Sukharev *et al.* [21] provided the equation for hydrostatic stress as follows:

$$\sigma = \frac{E(\varepsilon_{kk} - \varepsilon_{kk}^T - \varepsilon_{kk}^e)}{3(1-2\nu)} \quad (2.41)$$

For a metal line embedded into the rigid confinement while considering mechanical stress as shown in Eqs. (2.27) (2.28) and the vacancy flux,

$$J_v = -D_v \frac{\partial C_v}{\partial x} + D_v C_v \frac{Z^* e \rho j}{kT} - D_v C_v \frac{\Omega}{kT} \frac{\partial \sigma}{\partial x} \quad (2.42)$$

Sukharev provided the analytical solutions for vacancy concentration, atomic concentration and hydrostatic stress at the steady state as follows:

$$C_v = C_{v0} \exp \left[-\frac{Z^* e \rho j}{2kT} \left(x - \frac{L}{2} \right) \right] \quad (2.43)$$

$$C_a = C_{a0} + \frac{Z^* e \rho j}{2\Omega B} \left(x - \frac{L}{2} \right) + C_{v0}(1-f) \left[\exp \left(-\frac{Z^* e \rho j}{2kT} \left(x - \frac{L}{2} \right) \right) - 1 \right] \quad (2.44)$$

$$\sigma = -\frac{Z^* e \rho j}{2\Omega} \left(x - \frac{L}{2} \right) \quad (2.45)$$

Using the parameters listed in Table 2.1, Figures 2.5 and 2.6 plot the distributions of C_v , C_a and σ along the metal line at the steady state. The obtained stress level is noticeably lower than Korhonen's result (Figure 2.4 (b)) primarily because self-diffusion, i.e., the concentration gradient, is considered in the calculation. This is consistent with the study conducted by Cui *et al.*, where the concentration gradient plays an important role in resisting electromigration. This can reduce the stress level produced in the metal line. Moreover, the distribution of atomic concentration clearly depicts material depletion and accumulation at the cathode and anode, respectively. However, the variations in atomic and vacancy

concentrations likely do not meet the requirements for substitutional diffusion, $C_v + C_a = C_L$. Sukharev *et al.* [21, 22] also explained that the failure mechanism dramatically changes according to the dominant diffusivity path. When the copper/capping layer interface is the dominant diffusivity path, failure typically occurs because of a void, which forms at this interface, migrates to the cathode end of the line and grows.

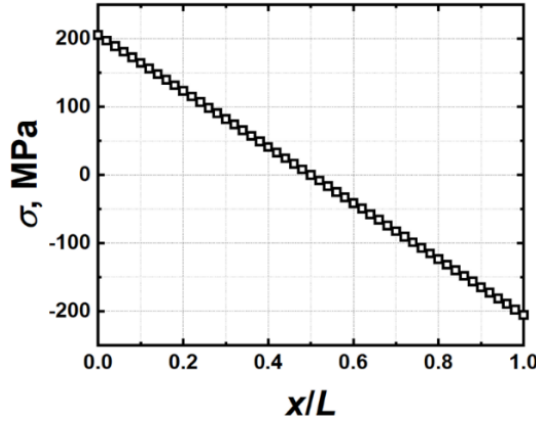


Figure 2.5. Hydrostatic stress distribution along the metal line at steady state based on Sukharev's model.

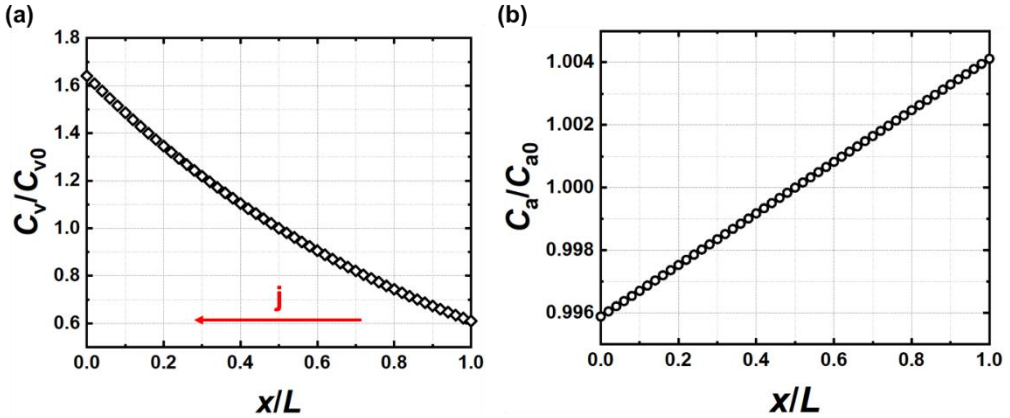


Figure 2.6. (a) Vacancy concentration distribution along the metal line at steady state based on Sukharev's model.

(b) Atomic concentration distribution at steady state.

2.5. Thermomigration during Electromigration

Temperature gradient-induced thermomigration is an increasingly important influential factor in electromigration. For instance, when flip-chip joints are subjected to an elevated electric current, a higher temperature due to Joule heating is generated at the chip side than the substrate side owing to the unique packaging shape and current crowding. Additionally, heat is generally dissipated from the surface of the chip module by the heat sink, resulting in a large temperature gradient between the surface of the module and the interior [36]. Owing to the larger temperature gradient and faster atomic diffusion in flip-chip joints, thermomigration becomes one of the most crucial reliability issues. The atomic flux driven by the temperature gradient can be written as [37]

$$J_a = \frac{D_a C_a}{kT} \frac{Q^*}{T} \left(-\frac{\partial T}{\partial x} \right) \quad (2.46)$$

where Q^* is the heat of transport. Certain materials, e.g. Cu, Al, Pb, etc., migrate from hot to cold regions; thus, the Q^* would be positive. However certain other materials, i.e. Sn, migrate from cold to hot regions; thus, the Q^* would be negative.

According to the study conducted by Tu *et al.* [38], for a temperature difference of 1 °C between the two ends of a 10 µm solder joint, the temperature gradient could reach 1000 °C/cm. Across an atom of diameter 3×10^{-10} m, the ΔT due to a 1000 °C/cm temperature gradient is approximately 3×10^{-5} K. The change in thermal energy across an atom is

$$3k\Delta T = 3 \times 1.38 \times 10^{-23} (J/K) \times 3 \times 10^{-5} K \approx 1.3 \times 10^{-27} J \quad (2.47)$$

For comparison, Tu *et al.* [38] considered the driving force, F , of electromigration at a current density of 1×10^4 A/cm² while considering the parameter listed in Table 2.1. The work done by the electrical force in an atomic distance is

$$W = Z^* e j \Delta d = 3.5 \times 1.6 \times 10^{-19} C \times 4.88 \times 10^{-8} \Omega m \times \frac{10^{10} A}{m^2} \times 3 \times 10^{-10} m = 4.8 \times 10^{-27} J \quad (2.48)$$

Using this simple calculation, Tu *et al.* [36] concluded that if a current density of 10^4 A/cm² can induce electromigration in a solder joint, a temperature gradient of 1000 °C/cm would induce thermomigration in a solder joint.

The theoretical study of thermomigration occurred after the study of stress-migration. The physical models, including Korhonen's, Kirchheim's and Sarchev's models, were devoted to describing the variation in mechanical stress during electromigration while neglecting the influence of the temperature gradient. Until recently, based on Sharchev's model, Bassama *et al.* [39, 40] included the effect of temperature on mechanical stress and considered the effect of the temperature gradient on mass transport equations. The heat transfer equation was used to calculate the temperature distribution. Subsequently, Liu *et al.* [41] extended Basama's study to 3D problems and calculated the influence of temperature on the lifetime of the solder structure using the finite element method. Furthermore, in the study conducted by Sukharev *et al.* [21, 22], the authors developed a 3D coupling model that couples the thermal field with electromigration. However, the authors neglected the temperature gradient in all cases studies without any explanation. Precise modelling using fully-coupled theory to investigate the role of thermomigration in electromigration process is lacking.

2.6. Summary and Outlook

In this chapter, we discussed a wide variety of electromigration models that have been proposed since the electromigration phenomenon was first identified. We began with the early basic derivation of Black's equation and gradually presented the development of the models as they became increasingly complete. A variety of factors that affect electromigration, from the mass transport equation to mechanical stress and thermomigration, were gradually understood. 1D solutions based on Shatzkes and Lloyd's model, Korhonen's model and Sukharev's model were obtained and compared with each other to illustrate the effects of the sink/source term, mechanical stress and self-diffusion on electromigration modelling. Moreover, confusion and several drawbacks among the different models were presented. As a summary, physical electromigration modelling has allowed significant understanding of electromigration. On the other hand, we believe that improvements in this area are crucial for a sound reliability prediction.

References

1. Black, J.R., *Electromigration failure modes in aluminum metallization for semiconductor devices*. Proceedings of the IEEE, 1969. **57**(9): p. 1587-1594.
2. Black, J.R., *Electromigration—A brief survey and some recent results*. IEEE Transactions on Electron Devices, 1969. **16**(4): p. 338-347.

3. Black, J.R. *Mass transport of aluminum by momentum exchange with conducting electrons*. in *6th Annual Reliability Physics Symposium (IEEE)*. 1967. IEEE.
4. Hofman, G.L. and H. Breitling, *On the current density dependence of electromigration in thin films*. Proceedings of the IEEE, 1970. **58**(5): p. 833-833.
5. Huntington, H. and A. Grone, *Current-induced marker motion in gold wires*. Journal of Physics Chemistry of Solids, 1961. **20**(1-2): p. 76-87.
6. Hauschildt, M., et al. *Electromigration early failure void nucleation and growth phenomena in Cu and Cu (Mn) interconnects*. in *2013 IEEE International Reliability Physics Symposium (IRPS)*. 2013. IEEE.
7. Gardner, D.S., J.D. Meindl, and K.C. Saraswat, *Interconnection and electromigration scaling theory*. IEEE Transactions on Electron Devices, 1987. **34**(3): p. 633-643.
8. Hu, C.-K., et al. *Scaling effect on electromigration in on-chip Cu wiring*. in *Proceedings of the IEEE 1999 International Interconnect Technology Conference (Cat. No. 99EX247)*. 1999. IEEE.
9. Hemmert, R. and M. Costa. *Electromigration-induced compressive stresses in encapsulated thin-film conductors*. in *IEEE Proc. Int. Reliab. Phys. Symp.* 1991.
10. Tezaki, A., et al. *Measurement of three dimensional stress and modeling of stress induced migration failure in aluminium interconnects*. in *28th Annual Proceedings on Reliability Physics Symposium*. 1990. IEEE.
11. Kraft, O. and E. Arzt, *Current density and line width effects in electromigration: A new damage-based lifetime model*. Acta materialia, 1998. **46**(11): p. 3733-3743.
12. Yuzuriha, T. and S. Early. *Failure mechanisms in a 4 micron pitch 2-layer gold IC metallization process*. in *IEEE VLSI MIC Conference*. 1986.
13. Bo/rgesen, P., et al. *Stress - induced voiding and electromigration*. in *AIP Conference Proceedings*. 1992. American Institute of Physics.
14. Ho, P.S. and T. Kwok, *Electromigration in metals*. Reports on Progress in Physics, 1989. **52**(3): p. 301.
15. Gambino, J.P., et al. *Reliability challenges for advanced copper interconnects: Electromigration and time-dependent dielectric breakdown (TDDB)*. in *2009 16th IEEE International Symposium on the Physical and Failure Analysis of Integrated Circuits*. 2009. IEEE.
16. Filippi, R., et al., *Implications of a threshold failure time and void nucleation on electromigration of copper interconnects*. Journal of Applied Physics, 2010. **107**(10): p. 103709.

17. Lloyd, J., *Black's law revisited-Nucleation and growth in electromigration failure*. Microelectronics reliability, 2007. **47**(9-11): p. 1468-1472.
18. De Orio, R., H. Ceric, and S.J.M.R. Selberherr, *Physically based models of electromigration: From Black's equation to modern TCAD models*. 2010. **50**(6): p. 775-789.
19. Cui, Z., X. Fan, and G. Zhang, *General coupling model for electromigration and one-dimensional numerical solutions*. Journal of Applied Physics, 2019. **125**(10): p. 105101.
20. Antonova, E.E. and D.C. Looman. *Finite elements for electromigration analysis*. in *2017 IEEE 67th Electronic Components and Technology Conference (ECTC)*. 2017. IEEE.
21. Sukharev, V. and E. Zschech, *A model for electromigration-induced degradation mechanisms in dual-inlaid copper interconnects: Effect of interface bonding strength*. Journal of Applied Physics, 2004. **96**(11): p. 6337-6343.
22. Sukharev, V., E. Zschech, and W.D. Nix, *A model for electromigration-induced degradation mechanisms in dual-inlaid copper interconnects: Effect of microstructure*. Journal of Applied Physics, 2007. **102**(5): p. 053505.
23. Shatzkes, M. and J. Lloyd, *A model for conductor failure considering diffusion concurrently with electromigration resulting in a current exponent of 2*. Journal of applied physics, 1986. **59**(11): p. 3890-3893.
24. Kirchheim, R. and U. Kaeber, *Atomistic and computer modeling of metallization failure of integrated circuits by electromigration*. Journal of applied physics, 1991. **70**(1): p. 172-181.
25. Kirchheim, R., *Stress and electromigration in Al-lines of integrated circuits*. Acta Metallurgica et Materialia, 1992. **40**(2): p. 309-323.
26. Korhonen, M., et al., *Stress evolution due to electromigration in confined metal lines*. Journal of Applied Physics, 1993. **73**(8): p. 3790-3799.
27. He, J., et al., *Electromigration lifetime and critical void volume*. Applied Physics Letters, 2004. **85**(20): p. 4639-4641.
28. Lloyd, J., *Electromigration failure*. Journal of Applied Physics, 1991. **69**(11): p. 7601-7604.
29. Blech, I.A., *Electromigration in thin aluminum films on titanium nitride*. Journal of applied physics, 1976. **47**(4): p. 1203-1208.
30. Blech, I. and K. Tai, *Measurement of stress gradients generated by electromigration*. Applied Physics Letters, 1977. **30**(8): p. 387-389.

31. Blech, I. and C. Herring, *Stress generation by electromigration*. Applied Physics Letters, 1976. **29**(3): p. 131-133.
32. Balluffi, R., *Grain boundary diffusion mechanisms in metals*. Metallurgical transactions B, 1982. **13**(4): p. 527-553.
33. Balluffi, R. and A.J.D.i.s. Granato, *Dislocations, vacancies and interstitials*. 1980. **4**: p. 1-133.
34. Clement, J. and C. Thompson, *Modeling electromigration - induced stress evolution in confined metal lines*. Journal of applied physics, 1995. **78**(2): p. 900-904.
35. Sarychev, M., et al., *General model for mechanical stress evolution during electromigration*. Journal of Applied Physics, 1999. **86**(6): p. 3068-3075.
36. Zhang, P., S. Xue, and J. Wang, *New challenges of miniaturization of electronic devices: Electromigration and thermomigration in lead-free solder joints*. Materials and Design, 2020: p. 108726.
37. Tu, K.-N., Y. Liu, and M. Li, *Effect of Joule heating and current crowding on electromigration in mobile technology*. Applied Physics Reviews, 2017. **4**(1): p. 011101.
38. Chen, C., et al., *Thermomigration in solder joints*. Materials Science Engineering: R: Reports, 2012. **73**(9-10): p. 85-100.
39. Basaran, C. and M. Lin, *Damage mechanics of electromigration induced failure*. Mechanics of Materials, 2008. **40**(1-2): p. 66-79.
40. Lin, M. and C. Basaran, *Electromigration induced stress analysis using fully coupled mechanical-diffusion equations with nonlinear material properties*. Computational Materials Science, 2005. **34**(1): p. 82-98.
41. Liu, Y., et al., *Prediction of electromigration induced voids and time to failure for solder joint of a wafer level chip scale package*. 2010. **33**(3): p. 544-552.

3

GENERAL COUPLING MODEL OF ELECTROMIGRATION

Although existing physical models in literature have contributed to significant understandings of electromigration failure mechanisms, there still exists several errors among these models. In this chapter, a new 3D general coupling model for electromigration is developed, which introduces the coupling of the mass conservation equation with the volumetric strain due to electromigration, thermal strain and mechanical deformation. The flux terms that include the concentration gradient, electron wind force, stress migration and thermal migration are considered. The constitutive equation for the diffusion strain is derived, and subsequently, the governing equations for 1D metal lines are obtained for both totally fixed and stress-free mechanical boundary conditions. The numerical results reveal that the hydrostatic stress is significantly lower than the results predicted in the existing literature for the totally fixed configuration. Extensive discussions are presented to provide explanations for such differences. The vacancy concentration gradient plays an important role in formulating electromigration problems. The current-driven flux can be entirely balanced by the concentration gradient that acts as an opposing force during electromigration under a stress-free condition in a steady-state. In addition, the new solutions of the critical threshold jL , the product of the current density and the metal line length are obtained in terms of the vacancy concentration. Electromigration is eventually determined by the void growth; therefore, the critical vacancy concentration is used to reanalyse Blech's experiment data. Lastly, the theoretical predictions are consistent with the experimental observations.

3.1. Introduction

Electromigration is a mass transport process controlled by interplayed driving forces, such as electron wind force, self-diffusion (concentration gradient), the mechanical stress gradient and the temperature gradient [1-3]. To describe this process accurately, these influential factors must be fully coupled in a self-consistent manner. In Chapter 2, we had reviewed several important multi-physics models of electromigration proposed over the past few decades. Although these studies contribute to significant understandings of electromigration failure mechanisms, there still exist several questions and errors among the models, as summarized in Table 3.1. Neglecting any influential factors could produce significant differences in the predictions of electromigration, as the 1D numerical results presented in Chapter 2.

Table 3.1. Summary of several physical models in literature

Physical models	Self-diffusion	Stress-migration	Thermo-migration	Sink/Source term	Constraint condition	Stress equilibrium	Diffusion strain
Shatzkes <i>et al.</i> (1986)[4]	✓	✗	✗	✗	N/A	N/A	N/A
Kirchheim <i>et al.</i> (1992)[5]	✗	✓	✗	✓	✗	✗	✗
Korhonen <i>et al.</i> (1993)[6]	✗	✓	✗	✓	✗	✗	✗
Clement <i>et al.</i> (1995) [7]	✗	✓	✗	✓	✗	✗	✗
Suo <i>et al.</i> (2003) [8]	✗	✓	✗	✓	✗	✗	✗
Sarychev <i>et al.</i> (2000)[9]	✓	✓	✗	✓	N/A	✓	✓
Sukharev <i>et al.</i> (2004, 2007) [10, 11]	✓	✓	✓	✓	✗	✓	✓
Maniatty <i>et al.</i> (2016) [12]	✗	✓	✗	✓	N/A	✓	✓
Cui <i>et al.</i> (2019)[1]	✓	✓	✓	✓	✓	✓	✓

In this chapter, we present a new 3D general coupling model for electromigration [1] wherein all the significant questions listed in Table 3.1 are resolved. In Section 3.2, basic equations of the general coupling model are introduced. The mass conservation equation is used to describe the dynamic process of electromigration. Herein, not only the interacting driving forces of the electron wind, atomic/vacancy concentration, temperature and mechanical stress are considered but also the sink/source term is inherently included in the coupled volumetric

strain. The constitutive equation with the migration strain is derived. The stress equilibrium is satisfied as a part of the whole set of equations to obtain the relationships between the vacancy concentration and stress. In Section 3.3, the numerical solutions for the 1D confined metal line are obtained with perfectly blocking boundary conditions at both ends. The results are then compared with the existing results in literature. Furthermore, a ‘stress-free’ configuration is considered to provide insight into the role of self-diffusion in electromigration. In Section 3.4, we consider the solutions at a steady state and revisit Blech’s theory, developing a new threshold criterion for electromigration failure.

3.2. General Coupling Model of Electromigration

A. Mass Conservation Equation

We use the mass conservation equation proposed in He *et al*’s study [8] to describe the electromigration process. Assuming that metal atoms migrate via a vacancy exchange mechanism, the fluxes of the metal atoms and the vacancies are equal and opposite i.e. $\mathbf{J}_a = -\mathbf{J}_v$. Thus, the mass conservation equation can be expressed as

$$\frac{\partial \theta}{\partial t} = -\Omega \nabla \cdot \mathbf{J}_a \quad (3.1)$$

The total vacancy flux of the vacancies is given as follows [13]:

$$\mathbf{J}_v = -D_v (\nabla C_v - \frac{Z^* e \rho \mathbf{j}}{kT} C_v - \frac{Q^*}{kT^2} \nabla T C_v + \frac{f \Omega}{kT} \nabla \sigma C_v) \quad (3.2)$$

where D_v is the vacancy diffusivity, C_v is the vacancy concentration, Z^* is the effective charge number ($Z^* > 0$), ρ is the electrical resistivity, \mathbf{j} is the current density, Q^* is the heat of transport. Ω is the atomic volume, σ is the hydrostatic stress, k is Boltzmann’s constant and T is the temperature.

B. Constitutive Equation

The volumetric strain, θ , in Eq. (3.1) is the trace of the total strain $\boldsymbol{\varepsilon}$ that can be decomposed into the sum of the elastic strain $\boldsymbol{\varepsilon}^m$, thermal strain $\boldsymbol{\varepsilon}^{th} = \alpha \Delta T \mathbf{I}$ (α is the coefficient of thermal expansion and \mathbf{I} is the unit tensor) and diffusion strain $\boldsymbol{\varepsilon}^{diff}$.

$$\theta = \text{tr}(\boldsymbol{\varepsilon}), \quad (3.3)$$

$$\boldsymbol{\varepsilon} = \boldsymbol{\varepsilon}^m + \boldsymbol{\varepsilon}^{th} + \boldsymbol{\varepsilon}^{diff}, \quad (3.4)$$

where the ϵ^{diff} describes the volumetric strain due to local concentration variations during electromigration. Therefore, ϵ^{diff} is dependent on C_v . A general function $g(C_v)$ is introduced as follows:

$$\epsilon^{diff} = \frac{1}{3} g(C_v) I \quad (3.5)$$

Considering that the material is linearly elastic and isotropic, the stress-strain relation can be determined by applying Hooke's law as follows:

$$\sigma = 2G\epsilon + \lambda \text{tr}(\epsilon)I - B \text{tr}(\epsilon^{th})I - B \text{tr}(\epsilon^{diff})I, \quad (3.6)$$

$$\sigma = \text{tr}(\sigma)/3, \quad (3.7)$$

where G and λ are Lamé constants ($2G=E/(1+\nu)$ and $\lambda=2G\nu/(1-2\nu)$), E is Young's modulus, ν is Poisson's ratio, $B=\lambda+2G/3$ is the bulk modulus and σ is the hydrostatic stress.

C. Constitutive Equation for Diffusion Strain

Considering a fully fixed configuration with a uniform distribution of vacancy concentration, the total volumetric strain in the absence of temperature change is

$$\theta = \epsilon_{kk} = \epsilon_{kk}^m + \epsilon_{kk}^{diff} = 0. \quad (3.8)$$

Meanwhile, a vacancy equilibrium equation related to the hydrostatic stress is provided in many electromigration studies [5-7, 10, 11].

$$C_v = C_{v0} \exp\left(\frac{\sigma\Omega}{kT}\right) \quad (3.9)$$

Eq. (3.9) can be rewritten as follows:

$$\sigma = \frac{kT}{\Omega} \ln\left(\frac{C_v}{C_{v0}}\right) \quad (3.10)$$

Based on Hooke's law, the elastic strain is

$$\epsilon_{kk}^m = \frac{\sigma}{B} \quad (3.11)$$

According to Eqs. (3.8), (3.10) and (3.11), the diffusion strain can be obtained as follows:

$$\varepsilon_{kk}^{diff} = g(C_v) = -\varepsilon_{kk}^m = -\frac{kT}{B\Omega} \ln\left(\frac{C_v}{C_{v0}}\right) = -A \ln\left(\frac{C_v}{C_{v0}}\right) \quad (3.12)$$

$$A = \frac{kT}{B\Omega} \quad (3.13)$$

where A is defined as the coefficient of diffusion strain, whose typical values for different materials are listed in Table 3.2. The minus sign in Eq. (3.12) indicates that an increase in the vacancy concentration would decrease the volumetric strain.

Table 3.2 The coefficient of diffusion strain (A) for various materials.

Material	B (GPa)	Ω (m ⁻²⁹)	A
Al	58.0	1.66	0.0071
Cu	110	0.62	0.0122
Sn	50.0	2.41	0.0069
Au	79.0	1.07	0.0098
Ag	83.0	1.19	0.0084

D. Other Field Equations

The vacancy transport equation is coupled with stress, electric and temperature fields; thus, the above equations must be solved together with the governing field equations of stress, displacement, strain, electric field and temperature. These equations are given below.

$$\nabla \cdot \boldsymbol{\sigma} + \mathbf{F} = 0 \quad (3.14)$$

$$\boldsymbol{\varepsilon} = \frac{1}{2}(\nabla \mathbf{u} + \mathbf{u} \nabla) \quad (3.15)$$

$$\nabla \cdot \mathbf{j} = 0 \quad (3.16)$$

$$\mathbf{j} = \frac{\mathbf{E}}{\rho} = -\frac{\nabla V}{\rho} \quad (3.17)$$

$$\nabla \cdot (k \nabla T) + \mathbf{j} \cdot \mathbf{E} = 0 \quad (3.18)$$

where F is the body force, u is the displacement vector, E is the electric field, V is the electrical voltage and k is the thermal conductivity. Only the steady state is considered in Eqs. (3.14)–(3.18) because the process of electromigration in Eqs. (3.1) and (3.2) is on a time scale of a different order compared to the temperature, electric and stress fields.

3.3. Governing Equation for One-Dimensional Solution

A. Totally Fixed Configuration

We first study a thin and narrow interconnect line covered in a dielectric passivation layer, as considered by Korhonen *et al.*[6] and Clement and Thompson.[7] For the 1D problem, the constant current density, j , passing through the line is along the negative x -axis, as illustrated in Figure 1. For simplicity, Joule heating is neglected in this study, and thus, no temperature gradient exists.

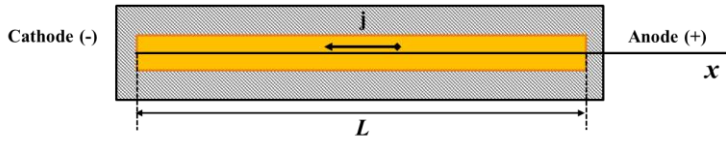


Figure 3.1. Schematic diagram for the 1D metal line with the totally fixed mechanical boundary condition.
The atomic flux is blocked at both ends.

Owing to the 1D assumption and the metal line being totally fixed by rigid passivation, we have the mechanical boundary condition.

$$\varepsilon_y = \varepsilon_z = \varepsilon_{xy} = \varepsilon_{yz} = \varepsilon_{xz} = 0 \quad (3.19)$$

$$u(0) = u(L) = 0 \rightarrow \int_0^L \varepsilon_x dx = 0 \quad (3.20)$$

Eq. (3.20) implies that the volumetric strain is not necessarily zero at all points; however, the entire deformation in the x -direction is equal to zero. Moreover, based on the stress equilibrium condition, the stress along the x -axis is constant.

$$\frac{d\sigma_x}{dx} = 0 \rightarrow \sigma_x = \sigma_0 \quad (3.21)$$

Applying Eqs. (3.19)–(3.21) to Eqs. (3.6) and (3.7), we can obtain the following equations for mechanical stresses.

$$\sigma_x = -\frac{EA}{3(1-2\nu)L} \int_0^L \ln\left(\frac{C_v}{C_{v0}}\right) dx \quad (3.22)$$

$$\sigma = \frac{2EA}{9(1-\nu)} \left[\ln\left(\frac{C_v}{C_{v0}}\right) + \frac{1+\nu}{2(1-2\nu)L} \int_0^L \ln\left(\frac{C_v}{C_{v0}}\right) dx \right] \quad (3.23)$$

$$\theta = -\frac{1+\nu}{3(1-\nu)} \left[\ln\left(\frac{C_v}{C_{v0}}\right) - \frac{1}{L} \int_0^L \ln\left(\frac{C_v}{C_{v0}}\right) dx \right] \quad (3.24)$$

Finally, the governing equations based on the general formulation in Eqs. (3.1)–(3.18) are reduced to an equation in terms of the vacancy concentration C_v .

$$\frac{\partial C_v}{\partial t} - \frac{1}{L} \int_0^L \frac{\partial C_v}{\partial t} dx = \frac{3(1-\nu)D_v C_v \Omega}{(1+\nu)A} \left[\frac{Z^* e \rho j}{kT} \frac{\partial C_v}{\partial x} + \frac{\partial^2 C_v}{\partial x^2} + \frac{2E\Omega A}{9(1-\nu)kT} \frac{\partial^2 C_v}{\partial x^2} \right] \quad (3.25)$$

The blocking diffusion boundary condition at both ends are as follows:

$$J_v(0, t) = \frac{Z^* e \rho j}{kT} C_v(0, t) + \left(1 + \frac{2E\Omega A}{9(1-\nu)kT} \right) \frac{\partial C_v(0, t)}{\partial x} = 0 \quad (3.26)$$

$$J_v(L, t) = \frac{Z^* e \rho j}{kT} C_v(L, t) + \left(1 + \frac{2E\Omega A}{9(1-\nu)kT} \right) \frac{\partial C_v(L, t)}{\partial x} = 0$$

and the initial condition is

$$C_v(x, 0) = C_{v0}. \quad (3.27)$$

B. Stress-Free Configuration

Electromigration occurs either along the grain boundary or the interface of the interconnect. Therefore, electromigration is typically combined with mechanical stress owing to the confined condition. However, we present a model here for a stress-free condition—an extreme case where the EM is free from the surrounding constraints, as shown in Figure 3.2. In this case, all stress components are zero.

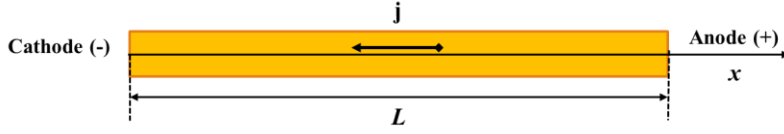


Figure 3.2. Schematic diagram for a 1D stress-free metal line. The atomic flux is blocked at both ends.

Using Eqs. (3.1)–(3.18), we obtain

$$\frac{\partial C_v}{\partial t} = \frac{D_v C_v \Omega}{A} \left(\frac{Z^* e \rho j}{kT} \frac{\partial C_v}{\partial x} + \frac{\partial^2 C_v}{\partial x^2} \right) \quad (3.28)$$

$$\sigma = 0 \quad (3.29)$$

The blocking diffusion boundary conditions at both ends are given below

$$\begin{aligned} J_v(0, t) &= \frac{Z^* e \rho j}{kT} C_v(0, t) + \frac{\partial C_v(0, t)}{\partial x} = 0 \\ J_v(L, t) &= \frac{Z^* e \rho j}{kT} C_v(L, t) + \frac{\partial C_v(L, t)}{\partial x} = 0 \end{aligned} \quad (3.30)$$

and the initial condition is

$$C_v(x, 0) = C_{v0} \quad (3.31)$$

3.4. Numerical Results

To compare with previous results, we use the material parameters and physical properties of the Al line in the study conducted by Clement and Thompson [7], as shown in Table 3.3. The atomic diffusivity (D_a) is $3 \times 10^{-16} \text{ m}^2/\text{s}$ and the concentration ratio C_v/C_a is typically in the order of 10^{-6} at 500 K. By applying the relationship between the vacancy and atomic diffusions, $D_v C_v = D_a C_a$, the vacancy diffusivity (D_v) can be determined as $3.0 \times 10^{-9} \text{ m}^2/\text{s}$.

In the following subsections, the numerical results obtained by using the formulations of Clement and Thompson [7] (see Eq. (2.30) in Chapter 2) are used for comparison and discussion. In fact, Korhonen *et al.* [6], Kirchheim and Kaeber [14], Clement and Thompson

[7] and He [8] all presented similar results and conclusions. In this chapter, all numerical results were obtained by using the partial differential mode in Matlab.

Table 3.3 Parameters used in the calculations.

Material properties	Value
Length of metal line (L)	50 μm
Temperature (T)	500 K
Atomic diffusivity (D_a)	$3 \times 10^{-16} \text{ m}^2/\text{s}$
Vacancy diffusivity (D_v)	$3 \times 10^{-10} \text{ m}^2/\text{s}$
Atomic volume (Ω)	$1.66 \times 10^{-29} \text{ m}^3$
Electrical resistivity (ρ)	$4.88 \times 10^{-8} \text{ Ohm}\cdot\text{m}$
Current density (j)	10^{10} A/m^2
Electrical charge (e)	$1.6 \times 10^{-19} \text{ C}$
Charge number (Z^*)	3.5
Boltzmann's constant (k)	$1.38 \times 10^{-23} \text{ J/K}$
Young's modulus (E)	70 GPa
Poisson ratio (ν)	0.3

A. Totally Fixed Configuration

Figure 3.3 plots the solutions of the normalized vacancy concentration and hydrostatic stress along the length of the metal line compared to those of the formulation of Clement and Thompson. Figure 3.3 (a) shows the accumulation and decrease of vacancies on the cathode and anode sides, respectively, indicating the atomic transport opposite to the direction of the current density. Figure 3.3 (b) shows the tensile stress on the cathode side due to the depletion of atoms and the compressive stress on the anode side for both solutions. However, the results of this study are significantly different from previous ones, particularly in terms of the magnitude of hydrostatic stress. In the solution presented here, at the steady state, the maximum hydrostatic stress is significantly lower than that in the existing solution (110 MPa vs. 400 MPa). The maximum vacancy concentration is also lower than that in the existing solution. There are several reasons for such differences, which will also resolve the issues listed in Table 3.1.

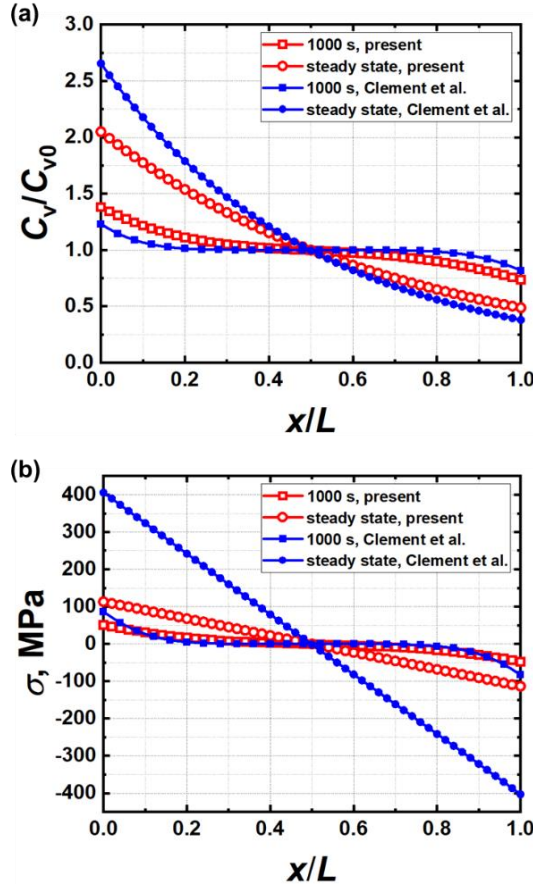


Figure 3.3. (a) Vacancy concentration along the line length under the 1D totally fixed condition. (b) Hydrostatic stress along the line length under the 1D totally fixed condition.

Firstly, uncertainties regarding the constrain condition: As reviewed in Chapter 2, Clement *et al.* considered the metal line at each point as totally confined, such that the volumetric strain (θ) is zero anywhere. As a result, the following equation was applied [6].

$$\frac{dC_L}{C_L} = -\frac{d\sigma}{B'} \quad (3.32)$$

where C_L is the concentration of the lattice sites and B_0 is the effective modulus that considers the metal line as an inclusion in an elastic dielectric passivation. This modulus is given by Eshelby. Eq. (3.32) produces a higher hydrostatic stress owing to the over-constrained

condition. As shown in Eq. (3.20), the total volumetric strain varies along the line and is not zero; however, the integral over the entire length is zero for the given boundary condition. This is because when the electrical current passes through the metal line, the electron wind force causes atomic transport along the electron direction, which can induce a non-uniform distribution of the volumetric strain along the length of the line.

Secondly, uncertainties regarding the vacancy-stress relation: Eq. (3.9) for the equilibrium relation between the hydrostatic stress σ and the vacancy concentration C_v has been used in many previous studies, including Clement's study. However, this equation applies only to a specific condition when the domain has a uniform change in the vacancy concentration under the totally confined configuration. In this study, we have derived an exact vacancy concentration-hydrostatic stress equation, as shown in Eq. (3.23), which satisfies both the equilibrium equation and the mechanical boundary condition. To illustrate the difference between Eqs. (3.9) and (3.23), Figure 3.4 plots their numerical results. The end point of each curve in Figure 3.4 represents the steady-state solution. Evidently, our solutions yield a significantly lower hydrostatic stress and a lower vacancy concentration.

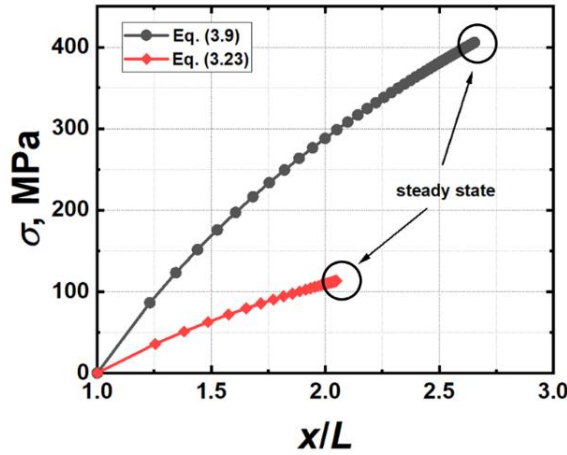


Figure 3.4. Comparison between vacancy concentration-hydrostatic stress relationships.

Thirdly, uncertainties regarding the stress equilibrium condition: According to Eq. (3.21), σ_x must remain constant (no gradient over the line length) owing to the equilibrium requirement in the 1D configuration. Meanwhile, σ varies along the line, as shown in Eq. (3.23). Figure 3.5 plots both σ_x and σ at 3000 s. σ_x has a very small magnitude and remains constant along the line length, while σ generates the gradient, which acts as a counter driving

force against the electron wind force. However, the σ_x obtained in Clement's solution varies along the line, which does not meet the requirement of the stress equilibrium condition.

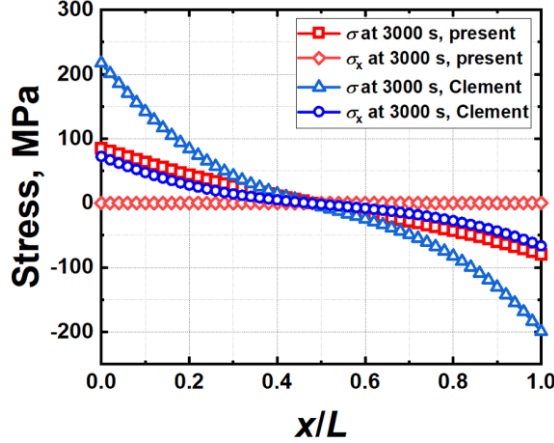


Figure 3.5. σ_x and hydrostatic stress σ along the length of the line.

Fourthly, flux of self-diffusion: Both the Korhonen *et al.* and Clement and Thompson models ignored self-diffusion, i.e. the concentration gradient. From Eq. (3.2), the total vacancy flux is the sum of the driving forces induced by the electric current, concentration gradient, stress gradient and temperature gradient. In the absence of the temperature gradient considered here, there still exist three flux terms, including the concentration gradient. To illustrate the effect of each flux, we introduce the following normalised parameters.

$$\beta_1 = \frac{F_E(\frac{L}{2}, t)}{F_{E0}}, \quad \beta_2 = \frac{F_S(\frac{L}{2}, t)}{F_{E0}}, \quad \beta_3 = \frac{F_C(\frac{L}{2}, t)}{F_{E0}} \quad (3.33)$$

where

$$F_E = -\frac{Z^* e \rho j}{kT} D_v C_v, \quad F_S = -\frac{\Omega}{kT} \frac{\partial \sigma}{\partial x} D_v C_v, \quad F_C = D_v \frac{\partial C_v}{\partial x} \quad (3.34)$$

β_1 , β_2 and β_3 represent the normalized fluxes due to the electron wind force, stress migration and self-diffusion, respectively. Figure 3.6 shows the evolutions of β_1 , β_2 and β_3 at $x = 0.5L$ over time. β_1 consistently remains a positive constant, exerting a constant driving force during electromigration. β_2 (stress gradient) and β_3 (vacancy concentration gradient) are both negative, indicating that both the mechanical stress gradient and the vacancy concentration gradient act as the opposing forces to balance the electron wind force during electromigration. β_2 and β_3 begin at zero at time zero and increase negatively over time. At the steady state, the

sum of the fluxes induced by the stress and concentration gradients is balanced by the electric flux ($\beta_1 + \beta_2 + \beta_3 = 0$). In Figure 3.6, the fluxes from the stress and vacancy concentration gradients are approximately 30% and 70%, respectively, of the total current-driven flux at the steady state. This implies that self-diffusion plays a significant role in electromigration, which is another reason for the difference between our solutions and existing ones.

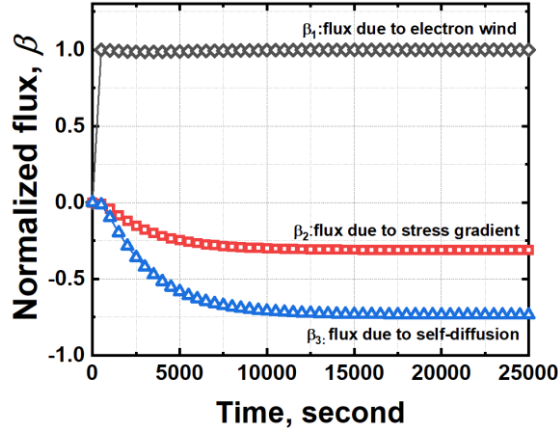


Figure 3.6. The evolution of normalized fluxes at $x = 0.5L$ over time.

B. Stress-Free Configuration

Shatzkes and Lloyd [4] presented a 1D solution without considering the effect of the stress gradient, however, self-diffusion was considered (see Eq. (2.12) in Chapter 2). As a result, the time to failure for electromigration is 5 orders less than the solutions of Clement and Thompson. Such a comparison appears to prove that mechanical stress is a dominant factor affecting electromigration. In this study, we present a self-consistent and complete solution for a stress-free configuration [Eqs. (3.28) and (3.29)]. The vacancy concentration at $x=0$ as a function of time in a stress-free condition is plotted in comparison with the totally fixed configuration in Figure 3.7. Without the mechanical stress, at the early stage of electromigration ($t < 5000$ s), the magnitude of the vacancy accumulation is very close to the solution of the totally fixed configuration. This indicates that, in spite of zero mechanical stress, electromigration continues to be resisted by the counter force due to the concentration gradient. Moreover, the vacancy concentrations under both configurations evolve on the same time scale. When time increases further, a greater vacancy concentration is developed in the stress-free condition. This implies that voids may grow faster under the stress-free condition, compared to that under the totally fixed condition.

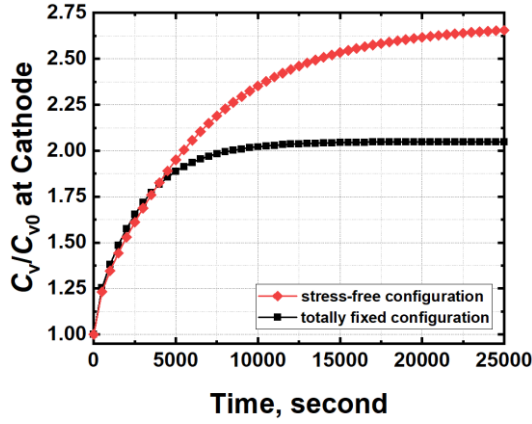


Figure 3.7. Vacancy concentration at $x = 0$ as a function of time for both configurations.

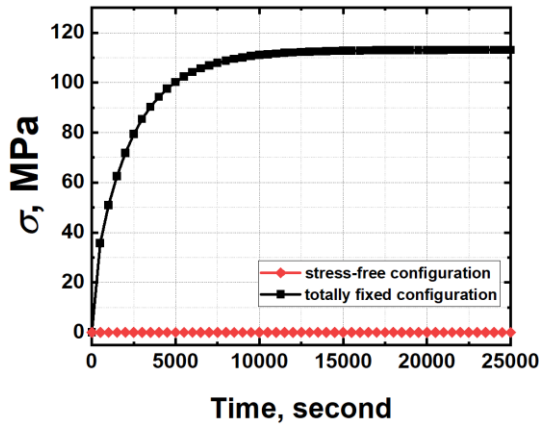


Figure 3.8. Hydrostatic stress at $x = 0$ as a function of time for both configurations.

For comparison, the hydrostatic stresses at $x = 0$ for the stress-free and totally fixed configurations are shown in Figure 3.8. In the totally fixed configuration, a tensile hydrostatic stress of 110 MPa is attained at the steady state. However, for the stress-free configuration, all the stress components during EM are zero over the entire time period; thus, no stress gradient-induced flux exists. The stress-free condition is a hypothetical and extreme condition where the atomic transport has no mechanical constraint. The results indicate that the vacancy concentration gradient plays a more important role to counter balance the electron wind force for electromigration.

3.5. Revisiting Blech's Theory

The governing equations for both the totally fixed and stress-free configurations at the steady-state (Eqs. (3.23) and (3.28)) are reduced to the following equations.

$$\left(1 + \frac{2EA\Omega}{9(1-\nu)kT}\right) \frac{\partial^2 C_v}{\partial x^2} + \frac{Z^* e \rho j}{kT} \frac{\partial C_v}{\partial x} = 0 \quad (\text{Totally fixed condition}), \quad (3.35)$$

$$\frac{\partial^2 C_v}{\partial x^2} + \frac{Z^* e \rho j}{kT} \frac{\partial C_v}{\partial x} = 0 \quad (\text{Stress-free condition}). \quad (3.36)$$

In the paper published by Blech and Herring [15], the effect of the concentration gradient is ignored; thus, the electromigration flux is entirely balanced by the stress-induced counter flux. They found that the stress is linear with the line length, with the maximum and minimum stresses as the tensile and compressive stresses, respectively, at either side. The critical product, jL , namely, the Blech product, is determined by the maximum stress that the metal line can withstand, as shown in the following equation.

$$(jL)_c = \frac{(\sigma_{max} - \sigma_{min})\Omega}{Z^* e \rho} \quad (3.27)$$

If jL is below the critical product, there is no electromigration failure because σ is below the critical stress. In another experiment conducted by Blech [16], the threshold of the product was determined as ~ 2000 A/cm for Al at 200 °C. Under this condition, the maximum tensile hydrostatic stress to induce electromigration failure was obtained as 165 MPa from Eq. (3.27). Similarly, we can solve Eqs. (3.35) and (3.36) to obtain the product jL in terms of the maximum (at $x = 0$) and minimum (at $x = L$) vacancy concentrations as follows:

$$(jL)_c = \left(1 + \frac{2EA\Omega}{9(1-\nu)kT}\right) \frac{kT}{Z^* e \rho} \ln \left(\frac{C_{v,max}}{C_{v,min}}\right) \quad (\text{Totally fixed condition}), \quad (3.38)$$

$$(jL)_c = \frac{kT}{Z^* e \rho} \ln \left(\frac{C_{v,max}}{C_{v,min}}\right) \quad (\text{Stress-free condition}). \quad (3.39)$$

Equations (3.38) and (3.39) consider the effects of both the stress and concentration gradients. In addition, the exact relationships between the stress and concentration (Eq. (3.23) for the totally fixed condition and Eq. (3.29) for the stress-free condition) are used. The threshold

product jL can be determined in terms of the maximum vacancy concentration. Electromigration is eventually determined by the void growth characterised by the vacancy concentration; therefore, the critical vacancy concentration can be calculated from Blech's experiment data. [16] Using Blech's experimental data of 2000 A/cm as a critical condition for the totally fixed condition, we obtain the critical vacancy concentration $C_{v,max}/C_{v0} = 1.33$. Figure 3.9 shows the threshold product curves for the totally fixed and stress-free conditions obtained using Eqs. (3.38) and (3.39), respectively. The total fixed metal line can sustain a higher current density than that under the stress-free condition at the same length. In Blech's experiment [16], the measured threshold product for the uncovered metal line is lower than that for the confined metal line. The experimental results are consistent with the existing theoretical predictions discussed above because the uncovered metal line generates less mechanical stress.

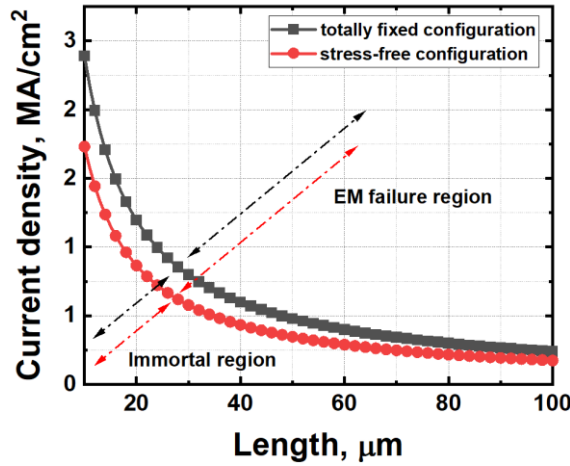


Figure 3.9. Curves of the threshold products for the totally fixed and stress-free configurations.

According to Blech's theory, if the hydrostatic stress rises to a critical value, the conductor line fails because of void formation. As Lloyd discussed [17], the arguments above do not necessarily describe void formation. In fact, in one of Blech's early experiments [18], failure was due to achieving the threshold for extrusion and not that for void formation. This implies that the model study presented here provides a new criterion based on the maximum vacancy concentration, or hillock formation based on the maximum decrease in the vacancy concentration.

3.6. Conclusion

This chapter presents a new 3D general coupling model for electromigration, wherein the mass conservation equation is introduced to describe the atomic/vacancy transport. The constitutive equation for the electromigration-induced volumetric strain is derived. 1D solutions of a metal line with both totally fixed and stress-free boundary conditions are obtained. The numerical results show that the hydrostatic stress is significantly lower than those in the solutions presented in existing literature under the totally fixed configuration. This is because we used the exact vacancy concentration-stress relationship that satisfies both the equilibrium equation and the mechanical boundary condition. We also demonstrate the significance of the concentration gradient in electromigration. The results obtained under the stress-free condition shows that, in spite of zero mechanical stress, the electromigration due to the electron wind force is resisted by the concentration gradient flux. As a result, the time to reach the critical vacancy concentration in the stress-free configuration is in the same order as that under the totally fixed condition. For the steady-state solution, both stress and concentration gradients are considered and the new solutions for the threshold product jL are derived in terms of the vacancy concentration. This is a departure from the well-known Blech's theory, wherein the current-driven flux is entirely balanced by the stress gradient flux. We have reanalysed Blech's experimental data, and the theoretical predictions of electromigration are consistent with the experimental observations.

References

1. Cui, Z., X. Fan, and G. Zhang, *General coupling model for electromigration and one-dimensional numerical solutions*. Journal of Applied Physics, 2019. **125**(10): p. 105101.
2. Ho, P.S. and T. Kwok, *Electromigration in metals*. Reports on Progress in Physics, 1989. **52**(3): p. 301.
3. Tan, C.M. and A. Roy, *Electromigration in ULSI interconnects*. Materials Science and Engineering: R: Reports, 2007. **58**(1-2): p. 1-75.
4. Shatzkes, M. and J. Lloyd, *A model for conductor failure considering diffusion concurrently with electromigration resulting in a current exponent of 2*. Journal of applied physics, 1986. **59**(11): p. 3890-3893.
5. Kirchheim, R., *Stress and electromigration in Al-lines of integrated circuits*. Acta Metallurgica et Materialia, 1992. **40**(2): p. 309-323.

6. Korhonen, M., et al., *Stress evolution due to electromigration in confined metal lines*. Journal of Applied Physics, 1993. **73**(8): p. 3790-3799.
7. Clement, J. and C. Thompson, *Modeling electromigration - induced stress evolution in confined metal lines*. Journal of applied physics, 1995. **78**(2): p. 900-904.
8. He, J., et al., *Electromigration lifetime and critical void volume*. Applied Physics Letters, 2004. **85**(20): p. 4639-4641.
9. Sarychev, M., et al., *General model for mechanical stress evolution during electromigration*. Journal of Applied Physics, 1999. **86**(6): p. 3068-3075.
10. Sukharev, V. and E. Zschech, *A model for electromigration-induced degradation mechanisms in dual-inlaid copper interconnects: Effect of interface bonding strength*. Journal of Applied Physics, 2004. **96**(11): p. 6337-6343.
11. Sukharev, V., E. Zschech, and W.D. Nix, *A model for electromigration-induced degradation mechanisms in dual-inlaid copper interconnects: Effect of microstructure*. Journal of Applied Physics, 2007. **102**(5): p. 053505.
12. Maniatty, A.M., et al., *Effect of microstructure on electromigration-induced stress*. Journal of Applied Mechanics, 2016. **83**(1).
13. De Orto, R., H. Ceric, and S.J.M.R. Selberherr, *Physically based models of electromigration: From Black's equation to modern TCAD models*. 2010. **50**(6): p. 775-789.
14. Kirchheim, R. and U. Kaeber, *Atomistic and computer modeling of metallization failure of integrated circuits by electromigration*. Journal of applied physics, 1991. **70**(1): p. 172-181.
15. Blech, I. and C. Herring, *Stress generation by electromigration*. Applied Physics Letters, 1976. **29**(3): p. 131-133.
16. Blech, I.A., *Electromigration in thin aluminum films on titanium nitride*. Journal of applied physics, 1976. **47**(4): p. 1203-1208.
17. Lloyd, J., *Electromigration failure*. Journal of Applied Physics, 1991. **69**(11): p. 7601-7604.
18. Blech, I. and E. Kinsbron, *Electromigration in thin gold films on molybdenum surfaces*. Thin Solid Films, 1975. **25**(2): p. 327-334.

4

4

VOLUME RELAXATION OF VACANCY AND DIFFUSION- INDUCED STRAIN: A MOLECULAR DYNAMIC STUDY

Mechanical stress development during electromigration is closely related to the volume expansion or contraction of the interconnect. One of the major sources of such a deformation is the volume relaxation or expansion due to vacancy accumulation or depletion, respectively. In this chapter, a large-scale MD simulation is performed to investigate the vacancy volume relaxation. The vacancy volume relaxation factor changes as a function of the vacancy concentration and is nearly constant at a low to mid-vacancy concentration level, i.e. from 10^{-6} to 10^{-3} of the lattice concentrations. However, the volume of the vacancies would collapse at high vacancy concentrations. The simulation results agree well with the existing data from both experiments and simulations in literature. A uniform empirical equation is developed to obtain the vacancy volume relaxation factor. Furthermore, this chapter discusses the relationship between the vacancy volume relaxation and the diffusion strain. The hydrostatic stresses obtained from a MD-based vacancy volume relaxation under a constrained condition are also compared to a commonly used stress-vacancy equation. Lastly, the use of the new formula for diffusion strain in the fully coupled theory is issued.

4.1. Introduction

To produce mechanical stress during electromigration, there must be a volume expansion or contraction of the interconnect [1]. In Chapter 3, we obtained a constitutive equation for the diffusion strain (Eq. (3.12)) from a commonly used stress-vacancy equation to describe the deformation induced by vacancy concentration variations. Corresponding numerical solutions show that the vacancy concentration at the cathode can reach saturation at $\sim 2C_{v0}$. Although this value falls in the $1.5C_{v0} \sim 10C_{v0}$ range shown in many previous studies [2-5], further investigation of material failure due to vacancy accumulation revealed that this value of vacancy concentration is on a very small scale to cause material failure. In solid crystals, the initial vacancy concentration is typically in the order of 10^{-6} of the lattice concentration at 250 °C [6], and it will be lower at room temperature. Thus, $10 C_{v0}$ implies the existence of a few vacancies in millions of atoms, which is insufficient to cause critical material failure, even in the presence of mechanical stress.

It is generally accepted that mass transport in pure metals occurs via exchanging the locations of vacancies and atoms, namely, substitutional diffusion. Replacing an atom with a vacancy tends to produce a volume relaxation in the surrounding lattice; thus, the volume occupied by a vacancy (Ω_v) would become a fraction of the atomic volume (Ω_a).

$$\Omega_v = f\Omega_a \quad (4.1)$$

where f is called the vacancy volume relaxation factor that varies between 0 and 1, i.e. $0 < f < 1$ [7]. Conceivably, the accumulation of vacancies would lead to a local volume contraction. In turn, the depletion of vacancies would produce a local volume expansion. Importantly, to quantitatively determine the diffusion-induced strain, it is necessary to determine the vacancy volume relaxation factor accurately.

Measuring the vacancy volume relaxation factor is not a straightforward and easy task [8]. Using the classical technique of differential dilatometry [9], the values of f in Au and Ni were found to be approximately 0.45 [10] and 0.6~0.74 [7], respectively. Utilizing a Bridgman press and angular correlation counting techniques, Dickman *et al.* [11] measured $f = 0.6$ in indium. Buescher and Emrick [12] quenched Al wires at high pressure and found that f was between 0.8~0.88 at 605 K and 825 K. Bourassa, Lazarus and Blackburn [13] measured the effect of pressure on the electrical resistance of Al and yielded $f = 0.625$ at 750 K. The data discussed above, however, were measured at a specific vacancy concentration level.

To complement the experimental studies, atomic modelling provides an effective tool to calculate the f for various materials under different conditions. In the study conducted by Doyama and Cotterill [14], the vacancy volume relaxation factor was found to be 0.83 by computing the locations of the copper atoms surrounding a vacancy. Using the first-principles calculations, Korzhavyi *et al.* [15] obtained f values for Ti, Cu, Ag, Pt and Au in the range of 0.68 to 0.71. Using a pseudopotential theory in the density function theory (DFT), Finnis and Sachdev [16] showed that that f for Al is 0.77. However, Li *et al.* [17] calculated that the f in Al to be 0.94. Most of the simulations mentioned above, however, only considered the atomic volume relaxation at a specific atomic concentration level.

In this chapter, by using an MD simulation in a large-scale atomic model (> 1 million atoms), we calculate the concentration-dependent f values for Al, Cu and Au. A comparison between our results and the data available in the literature are presented. An empirical formula is proposed to calculate f as a function of the vacancy concentration. Moreover, the hydrostatic stress is obtained from the MD simulation under a constrained condition. Lastly, we present an analysis on the relationship between vacancy volume relaxation and the diffusion-induced strain and stress. A new formula for diffusion strain with f is provided. A comparison between our MD results and the commonly accepted stress-vacancy equation is presented.

4.2. Methodology

4.2.1. Basic Equations

Consider a domain of total number of lattice sites, n , with number of vacancies, n_v , as illustrated in Figure 4.1 (a). The total volume of the system is the sum of the volumes occupied by the atoms and vacancies, as given below.

$$V = n_a \Omega_a + n_v \Omega_v, \quad (4.2)$$

where n_a is the number of atoms and $n = n_a + n_v$. If the lattice sites are all occupied by atoms, the total volume of the system would be $V_0 = n \Omega_a$. From Eqs. (4.1) and (4.2), we can obtain the following equation.

$$f = \frac{V - n_a \Omega_a}{n_v \Omega_a} = \frac{V - (n_v + n_a) \Omega_a + n_v \Omega_a}{n_v \Omega_a} = 1 + \frac{V - V_0}{n_v \Omega_a} = 1 + \frac{V - V_0}{V_0} \frac{n}{n_v} \quad (4.3)$$

Eq. (4.3) shows that f can be deduced if the volume change, $V-V_0$, due to the presence of n_v vacancies, is calculated. To investigate the dependency of the vacancy volume relaxation on the atomic/vacancy concentration, the vacancy concentration C_v , atomic concentration C_a and lattice concentration C_{L0} , are defined as follows:

$$C_v = \frac{n_v}{V_0}, \quad (4.4)$$

$$C_a = \frac{n_a}{V_0}, \quad (4.5)$$

$$C_{L0} = \frac{n}{V_0} = \Omega_a^{-1}, \quad (4.6)$$

where $C_v + C_a = C_{v0} + C_{a0} = C_{L0}$. Throughout this manuscript, we use C_{v0} and C_{a0} to denote the initial vacancy and atomic concentrations, respectively. The C_{v0} in solid metals is on the scale of $\sim 10^{-6} C_{L0}$; thus, we can consider C_{a0} as approximately equal to C_{L0} .

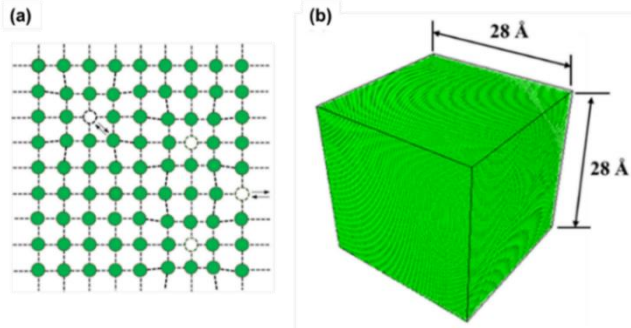


Figure 4.1 (a) Schematic illustration of a crystal structure with vacancies. (b) Al cubic box with ~ 1350000 atoms.

4.2.2 Simulation Method

As mentioned above, for most crystal structures, the C_{v0} is $\sim 10^{-6} C_{L0}$. Thus, we use a cubic model containing ~ 1350000 atoms, as shown in Figure 4.1(b), to accurately capture such a low vacancy concentration level. Furthermore, vacancies are generated by randomly deleting a certain number of atoms in this model. The MD calculations were performed using a large-scale atomic/molecular massively parallel simulator (LAMMPS) [18]. The conventional embedded atom method (EAM) was applied to describe the interactions between atoms [19], which used the potentials for Al atoms (Jacobsen *et al.* [20]), Cu atoms (Adams [21]) and Au

atoms (Foiles *et al.* [22]). In all the simulations, a time step of 0.001 ps was selected for calculation and a periodic boundary condition was applied in the three dimensions. The open visualization tool (OVITO) software was used to visualise our simulation results.

Considering Al as an example, the computational procedures for f are as follows:

- 1) Minimising the potential energy of the initial model: The coordinates of the atoms were iteratively adjusted until the change in energy between iterations was less than 1×10^{-8} or the change in the global force was less than 1×10^{-8} eV/Å. Subsequently, we relaxed the system in a constant NPT ensemble (N is the total number of atoms, P is the pressure and T is the temperature) at 500 K and zero pressure for 200 ps. This relaxation time is sufficiently long to allow the system to reach equilibrium. The temperature and pressure damping parameters were 100 time steps, 0.1 ps. After this procedure, the initial volume of the system, V_0 , and the atomic volume, Ω_a , could be obtained.
- 2) Generating vacancies: Based on the fully relaxed model, we randomly removed a certain number of atoms to generate different vacancy concentrations from 6×10^{22} to $6 \times 10^{27} \text{ m}^{-3}$, corresponding to $10^{-6}C_{L0}$ to $0.1C_{L0}$. Here, three random vacancy distributions were applied at each vacancy concentration level.
- 3) Determining the volume of the system with vacancies: Relaxing the system for 1000 ps, we obtained the volume of the system, V , at different vacancy concentrations.
- 4) Calculating f : Based on Eq. (4.3) and the obtained volumes V and V_0 , the f values at different vacancy concentration levels could be determined.

The same computational procedures were used for calculating f in Cu and Au.

In this study, we also calculated the hydrostatic stress induced by vacancy generation in a fully constrained condition, as described below.

- 1) Minimising the potential energy of the initial model: We relaxed the system in a constant NPT ensemble at 500 K and zero pressure for 200 ps to allow it to reach the equilibrium state.
- 2) Generating vacancies: We randomly removed atoms to create different vacancy concentrations ranging from 6×10^{22} to $6 \times 10^{27} \text{ m}^{-3}$, corresponding to $10^{-6}C_{L0}$ to $0.1C_{L0}$. Three random vacancy distributions were applied at each vacancy

concentration level.

- 3) Calculating the hydrostatic stress: We relaxed the system for 1000 ps under an NVT ensemble (V implies keeping the volume of the model as constant) to attain the equilibrium status at different vacancy concentration levels. Subsequently, we calculated the internal stress using following equation.

$$\sigma_{ij} = \frac{1}{V} \sum_{\alpha} \left[\frac{1}{2} \sum_{\beta=1}^N (R_i^{\beta} - R_i^{\alpha}) F_j^{\alpha\beta} - m^{\alpha} v_i^{\alpha} v_i^{\alpha} \right] \quad (4.7)$$

where V , R , F , m and v represent the volume of the system, position, force, mass and velocity of the atoms, respectively. The subscripts i and j indicate the direction of the stress component and the superscripts α and β indicate the a pair atoms. The hydrostatic stress (σ) is equal to $(\sigma_{11} + \sigma_{22} + \sigma_{33})/3$.

4.3. Results and Discussion

4.3.1 Vacancy Volume Relaxation Factor in Al

Figure 4.2 (a) shows the volume of the system without vacancies at 500 K. The volume can reach the equilibrium at 200 ps. Additionally, Figure 4.2 (b) shows that the volume of the system with vacancies can attain a steady state at 1000 ps. Both figures demonstrated that the relaxation times in our simulations are sufficient.

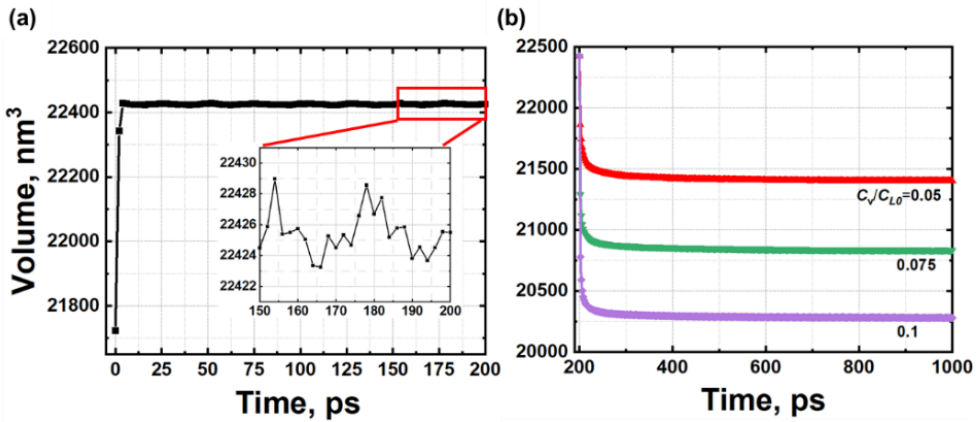


Figure 4.2. Volumes of systems without vacancies (a) and with different levels of vacancy concentration (b).

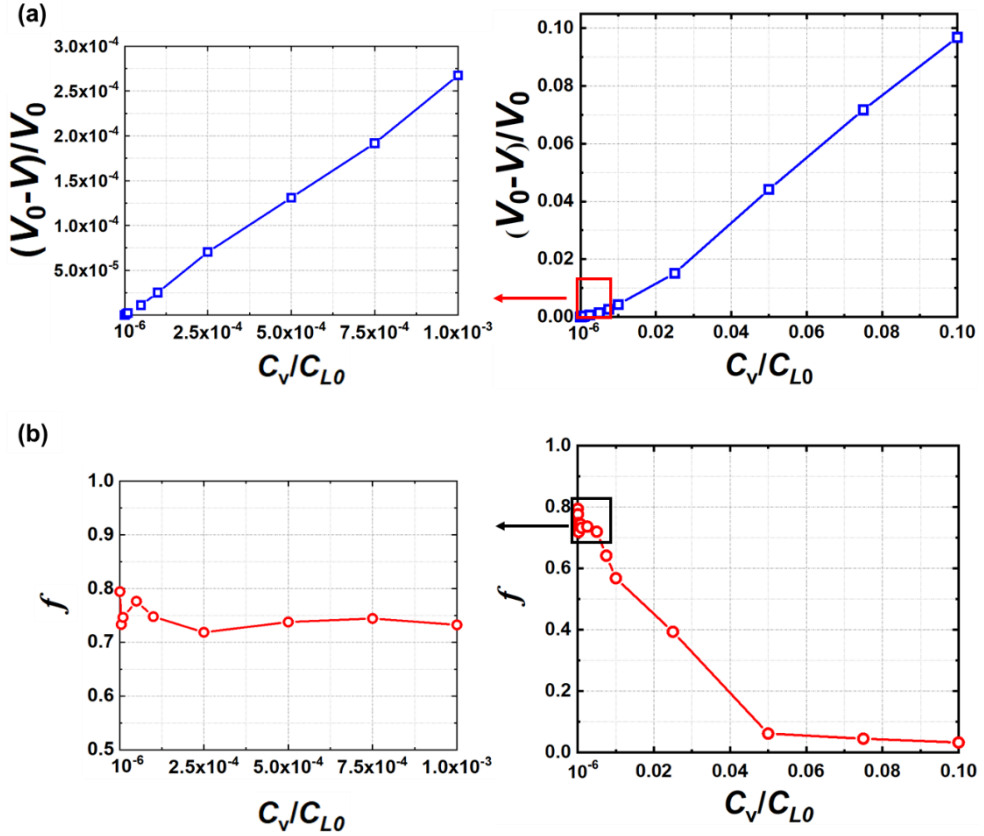


Figure 4.3. (a) Normalized volume change and (b) vacancy volume relaxation factor of Al for various vacancy concentrations levels at 500 K.

Figure 4.3 (a) and (b) respectively shows the normalised volume change and the f for Al with different vacancy concentrations ranging from $10^{-6}C_{L0}$ to $0.1C_{L0}$ at 500 K. When the vacancy concentration remains at a low level, i.e. at the $10^{-6}C_{L0}$ to $10^{-3}C_{L0}$ range, as shown in the enlarged figure in Figure 4.3 (a), f maintains a nearly constant value, varying slightly from 0.79 to 0.7. This implies that a vacancy can retain a large portion of the atomic volume at a low vacancy concentration level. However, with increasing vacancy concentration, the normalised volume change of the system increases significantly. Consequently, f decreases rapidly. When the vacancy concentration reaches $0.05C_{L0}$, f decreases from ~ 0.7 to 0, implying that the volume occupied by vacancies completely collapses – in other words the volume ever occupied by a vacancy is completely filled by surrounding atoms.

To determine the mechanism behind the results, we observe the microstructure in Al at different vacancy concentrations, as plotted in Figure 4.4. In this figure, the green, red and blue regions represent the FCC, HPC and BCC lattice structures, respectively. At a low vacancy concentration level, e.g. at $10^{-3}C_{L0}$, as shown in Figure 4.4 (a), the system is FCC dominated. This implies that the vacancies in Al are isolated from each other. However, with increasing vacancy concentration, the exchanging locations of the atoms and vacancies promote the accumulation of vacancies. Thus, HPC lattice structure clusters appear randomly, as shown in Figure 4.4 (b). When the vacancy concentration increases to $0.1C_{L0}$, massive dislocations are formed, as shown in Figure 4.4 (c). Figure 4.5 is a schematic diagram illustrating how vacancies coalesce into a line imperfection to form a dislocation. On increasing the vacancy concentration further, the coalescence of vacancies appears in the microstructure and reduces f .

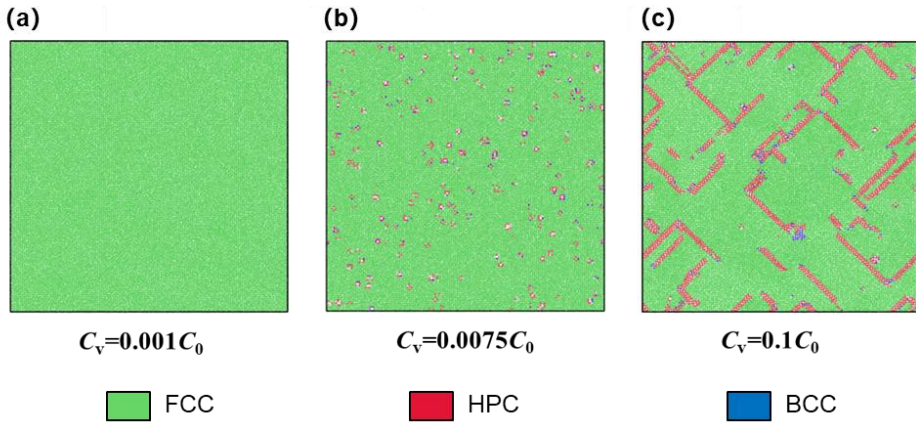


Figure 4.4. Lattice structure for Al at different vacancy concentrations, where the green, red and blue regions represent FCC, HPC and BCC lattice structures, respectively.

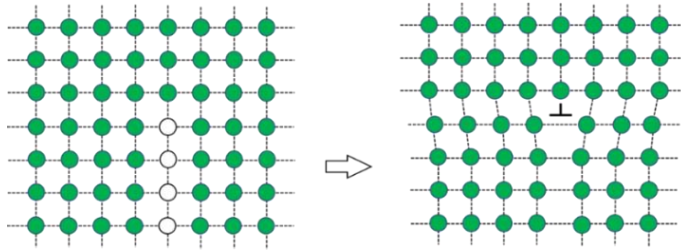


Figure 4.5. Schematic diagram representing the formation of dislocation due to vacancy coalescence.

Figure 4.6 compares our simulation results to the experimental and simulation data for Al available in literature. The baseline shown in Figure 4.6 represents our simulation results at 500 K. Additionally, the simulation results obtained at 605 K, 825 K, 700 K and 750K, are also included at respective concentration levels in this figure for a direct comparison with literature data. Notably, Figure 4.6 is plotted with a logarithmic scale on the x-axis. Our results agree well with the experimental data measured at 605 K and 825 K at a vacancy concentration of approximately $10^{-6}C_{L0}$. The results of Bourassa *et al.* [13] at 750 K with a vacancy concentration in the $10^{-5}C_{L0}$ ~ $10^{-4}C_{L0}$ range are lower than our simulation results. Furthermore, our f at $C_v = 0.001C_0$ is consistent with the simulation results obtained by Finnis [16]. However, Li *et al.* [17] observed a much higher f at $C_v = 10^{-3}C_{L0}$. After careful evaluation, the MD model by Li *et al.* was found to contain only ~1000 atoms. Evidently, erroneous results were obtained with a very small-scale MD model.

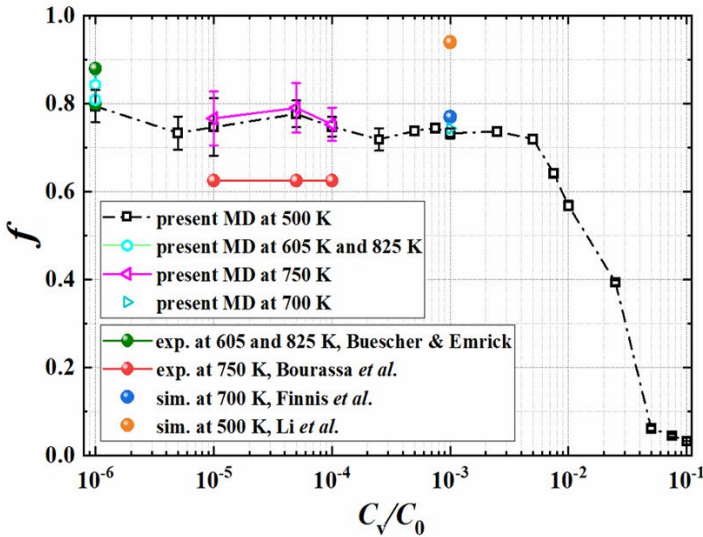


Figure 4.6. Comparison of the vacancy volume relaxation factor in Al with existing experimental and simulation data.

Figure 4.7 displays the results of the hydrostatic stress as a function of vacancy concentration when considering a constrained boundary condition for the studied domain. It shows that when the vacancy concentration is lower than $0.05C_{L0}$, the hydrostatic stress can continually increase because of the accumulation of vacancies. On further increasing the vacancy concentration, the hydrostatic stress reaches a critical value of approximately 3 GPa. Subsequently, the hydrostatic stress decreases rapidly, indicating the failure of the material. The MD simulation results for microstructures at different concentration levels are plotted in

Figure 4.8. When we increase the vacancy concentration from a low level to $0.05C_{L0}$, massive dislocations and small voids are generated in the system. With the continual increase of vacancy concentration, a visible void can be observed at $0.075C_{L0}$.

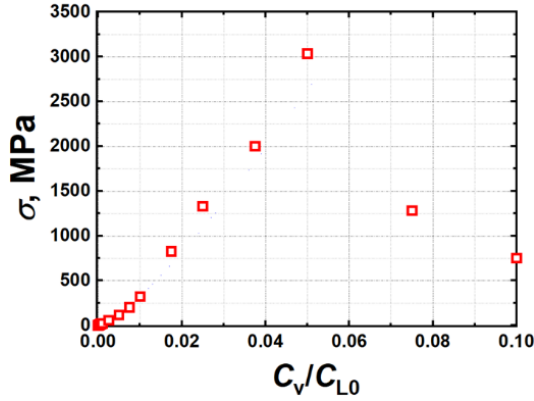


Figure 4.7. MD simulation results for the hydrostatic stress at different vacancy concentration levels under a constrained boundary condition.

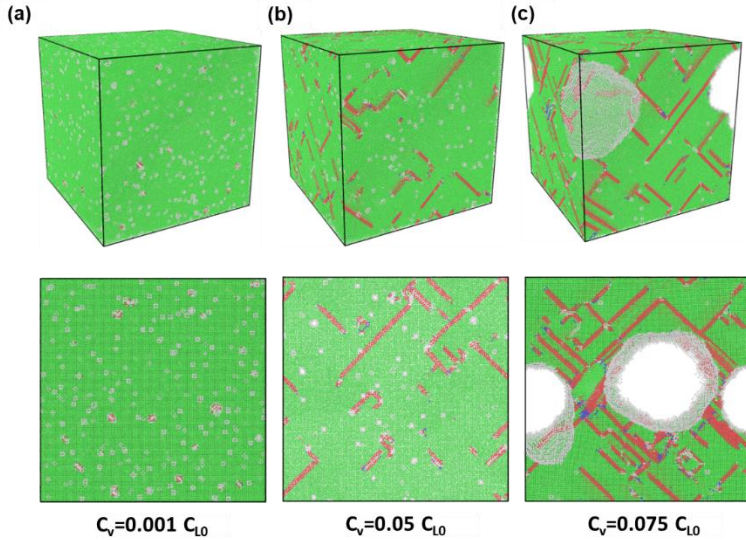


Figure 4.8. Lattice structures in Al with different vacancy concentrations under a constrained boundary condition, the upper images are in three dimensions and the lower ones are the cross-sections.

4.3.2. Empirical Formula of Vacancy Volume Relaxation Factor

Figure 4.9 plots the f values of Al, Cu and Au for different vacancy concentrations at 500 K. Cu and Au show trends in f similar to that of Al, i.e. a nearly constant value at low vacancy

concentrations followed by a rapid decrease at high vacancy concentrations. When the vacancy concentration in Cu changes from $10^{-6}C_{L0}$ to $0.0075C_{L0}$, f remains approximately 0.77. Thus is consistent with the value $f = 0.75$ obtained in experiments [8]. For Au, when the concentration remains at a low level, f is approximately 0.62, which is lower than those in Al and Cu. This suggests an easier volume relaxation in Au owing to vacancy diffusion. At the same vacancy concentration level, i.e. $10^{-5}C_{L0} \sim 10^{-4}C_{L0}$, our results for Au is consistent with $f \sim 0.45$ measured experimentally [13]. Interestingly, for these three metals, the f values all begin to rapidly decrease at $C_v = 0.0075C_{L0}$. An empirical formula is then proposed as follows:

$$f = \begin{cases} f_0, & 10^{-6} \leq \frac{C_v}{C_{L0}} < 0.0075 \\ \alpha \exp\left(\frac{\beta C_v}{C_{L0}}\right), & \frac{C_v}{C_{L0}} \geq 0.0075 \end{cases} \quad (4.8)$$

where values of f_0 and the coefficients α and β for Al, Cu and Au are listed in Table 4.1. At low vacancy concentrations, f is considered a constant. When vacancy concentration increases to $0.0075C_{L0}$, f decreases exponentially.

Table 4.1. Coefficients for the empirical formula in Eq. (8) for f in Al, Cu and Au.

	$\Omega_a (\text{\AA}^3)$	f_0	α	β
Al	16.64	0.73	1.08	-55.30
Cu	12.11	0.77	0.94	-27.38
Au	17.30	0.62	0.84	-29.35

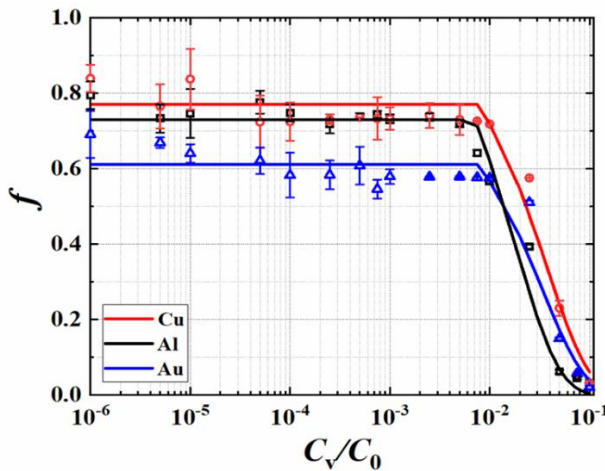


Figure 4.9. MD results and fitting lines using Eq. (4.8) for f of Cu, Al and Au at 500 K.

4.4. Diffusion-Induced Strain and Stress

With the obtained f , the rate form of volumetric strain induced by atomic diffusion can be obtained as follows [5, 23]:

$$d\theta^{diff} = (1 - f) \frac{dC_a}{C_a} \quad (4.9)$$

The accumulated diffusion strain can be obtained via the following integral form.

$$\theta^{diff} = \int_{C_{a0}}^{C_a} (1 - f) \frac{dC_a}{C_a} \quad (4.10)$$

Assuming a constant f , we have

$$\theta^{diff} = (1 - f) \ln \left(\frac{C_a}{C_{a0}} \right) = (1 - f) \ln \left(1 - \frac{C_v}{C_{a0}} \right) \quad (4.11)$$

Using the relationship between C_v , C_a and C_L , as shown in Eqs. (4.4)–(4.6), the diffusion strain can be also written as follows:

$$\theta^{diff} = (1 - f) \ln \left(1 - \frac{C_v}{C_{a0}} \right) = (1 - f) \ln \left(1 - \frac{C_{v0}}{C_{a0}} \frac{C_v}{C_{v0}} \right) \quad (4.12)$$

From the above equations, it can be seen that the vacancy volume relaxation factor plays an important role in determining the diffusion-induced strain. For a system, the total strain is a sum of diffusion strain and mechanical strain. If the system is under a fully constrained configuration, the total strain is zero. We can obtain the following equation,

$$\theta = \theta^{diff} + \theta^m = 0, \quad (4.13)$$

where θ^m is the volumetric mechanical strain, and θ is the total volumetric strain. Based on Hooke's law, the hydrostatic stress induced by concentration variations can be obtained as follows:

$$\sigma = B\theta^m = -B\theta^{diff} = -B \int_{C_{a0}}^{C_a} (1 - f) \frac{dC_a}{C_a}, \quad (4.14)$$

where B is the bulk modulus. Figure 4.10 plots the diffusion strain in Al for different vacancy concentrations, where the black line represents the strain with constant $f = 0.73$, and the red line represents the strain with the concentration-dependent f as described by Eq. (4.10). At high vacancy concentration levels, the variation in f with the vacancy concentration would produce more volumetric strain compared to the strain obtained via a constant f .

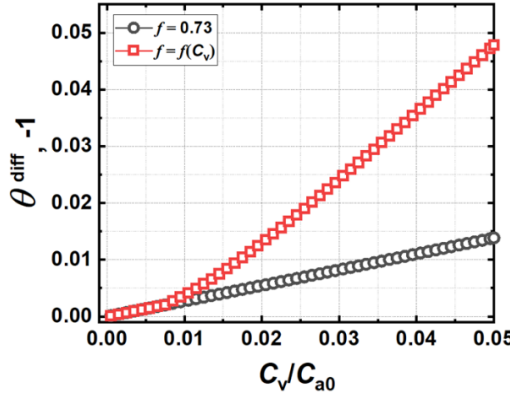


Figure 4.10. Evolution of diffusion strains with vacancy concentrations.

Figure 4.11 plots the hydrostatic stress obtained from the MD simulation and Eq. (4.14) with a bulk modulus of 55 GPa for Al. When the concentration-dependent vacancy relaxation factor is used, an excellent agreement between the MD simulation and Eq. (4.14) is obtained at both low and high vacancy concentration levels. This implies the formula for diffusion strain (Eq. (4.11)) can accurately describe the deformation caused by vacancy concentration variations.

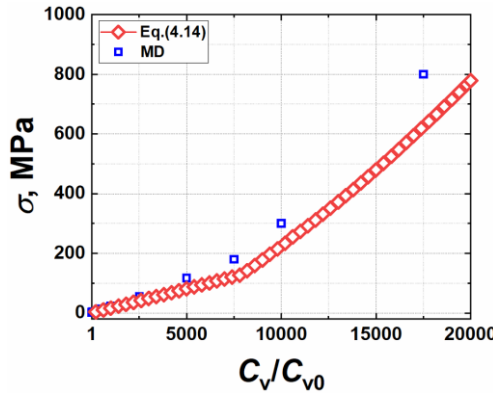


Figure 4.11. Evolution of hydrostatic stress with vacancy concentrations.

Notably, in Figure 4.11, along the x-axis, the vacancy concentration is investigated between C_{v0} and $2 \times 10^4 C_{v0}$. This corresponds to the atomic concentration from C_{a0} to $0.98 C_{a0}$. In previous studies on electromigration [3, 4], the Nabarro–Herring equation, which describes the relationship between hydrostatic stress and vacancy concentration under a fully constrained configuration, is often used as follows:

$$\sigma = \frac{kT}{\Omega_a} \ln \left(\frac{C_v}{C_{v0}} \right) \quad (4.15)$$

From this equation, under a fully fixed boundary condition, we obtained the following formula for diffusion strain as derived in the Eq. (3.12) in Chapter 3.

$$\theta^{\text{diff}} = -\frac{kT}{B\Omega} \ln \left(\frac{C_v}{C_{v0}} \right) \quad (4.16)$$

Using Eq. (4.15), many previous studies [3, 4, 24, 25], including the results in Chapter 3, have determined that the threshold value of the vacancy concentration for electromigration failure is between $1.5 C_{v0}$ to $10 C_{v0}$. This value is only a very small fraction of the scale used in Figure 4.11. For comparison, Figure 4.12 plots the results of hydrostatic stress obtained using Eq. (4.15) with the vacancy concentration only changing from C_{v0} to $10 C_{v0}$. The hydrostatic stress can reach 1 GPa when the vacancy concentration is only $8 C_{v0}$. However, the MD results (see blue dots in Figure 4.12) show a very small hydrostatic stress at $8 C_{v0}$, which is lower than 3 MPa. When the vacancy concentration varies in the range between $2 C_{v0}$ and $10 C_{v0}$, the atomic structure obtained from the MD simulation remains highly FCC controlled (Figure 4.8 (a)). This implies that vacancies at this concentration level are isolated from each other, and no critical failure occurs. Evidently, Eqs. (4.14) and (4.15) present entirely different results.

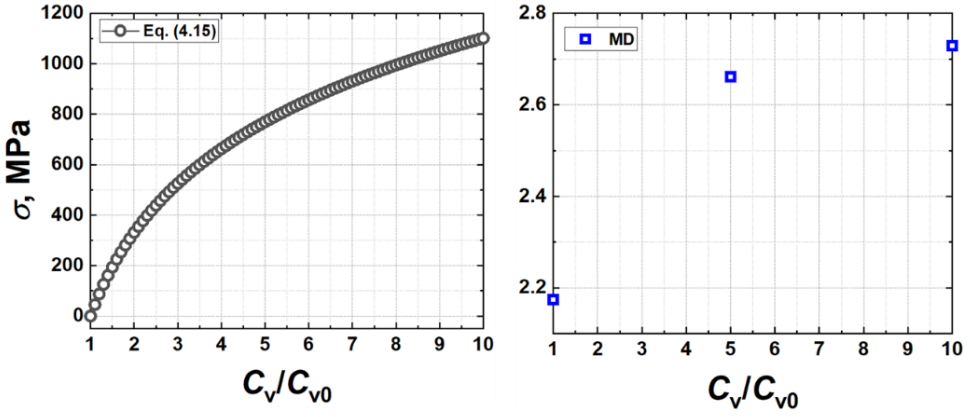


Figure 4.12. Comparison between hydrostatic stresses obtained from Eq. (4.15) and MD simulations.

Figure 4.13 plots the diffusion strains obtained using Eqs. (4.12) and (4.16) when the vacancy concentration changes from C_{v0} to $10C_{v0}$. According to Eq. (4.16), 10 times the initial vacancy concentration can induce a volumetric strain of $\sim 1.5\%$, which is much larger than the strain obtained from Eq. (4.12). It is difficult to imagine that 10 times the initial vacancy concentration can produce such a large strain because 0.2% is commonly measured for the yield strain of metal.

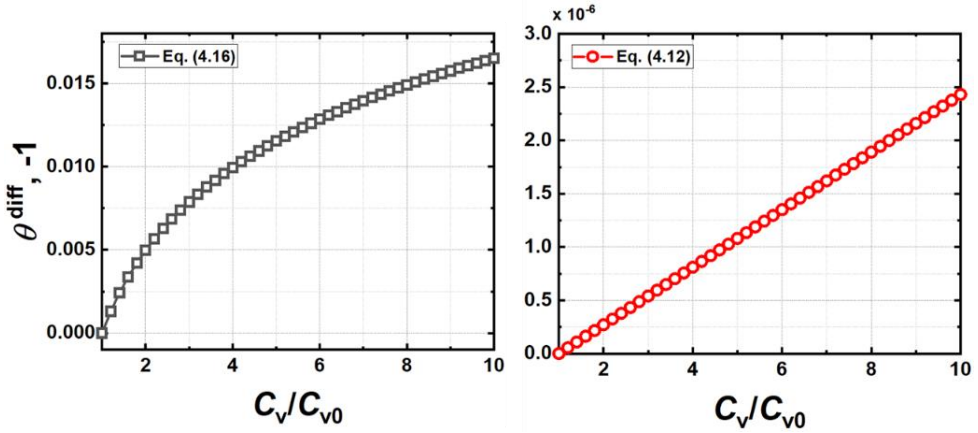


Figure 4.13. Comparison between the diffusion strains obtained from Eqs. (4.16) and (4.12).

Based on above comparison and discussions, we tend to choose the MD-verified Eq. (4.10) as the diffusion strain for our future studies. A fully coupled model with the new MD-verified diffusion strain will be developed and used for modelling electromigration in the studies discussed in Chapters 5 and 6.

4.5. Conclusion

f plays a very important role in determining the diffusion strain and mechanical stress in electromigration. In this study, a large-scale MD simulation is performed to obtain the concentration-dependent f values for Al, Cu and Au. f maintains a nearly constant value at low vacancy concentrations but decreases rapidly once the vacancy concentration exceeds $0.0075C_0$. This implies that the volume occupied by vacancies would completely collapse at high concentration levels. As a validation, our results agree well with both experimental and simulation data available in literature. An empirical equation is obtained to describe f as a function of vacancy concentration. Lastly, we present a new equation for diffusion strain with f . The hydrostatic stress based on this equation is compared to a commonly used stress-vacancy equation in the study of electromigration. This reveals that the threshold values of the vacancy concentration for electromigration failure can be determined at different scales by using different equations for diffusion strain. This new MD-verified diffusion strain equation will be used in a fully coupled theory to be presented in Chapter 5 for our future studies.

References

1. Cui, Z., X. Fan, and G. Zhang, *Molecular dynamic study for concentration-dependent volume relaxation of vacancy*. Microelectronics Reliability, 2021. **120**: p. 114127.
2. Clement, J. and C. Thompson, *Modeling electromigration - induced stress evolution in confined metal lines*. Journal of applied physics, 1995. **78**(2): p. 900-904.
3. Clement, J., *Vacancy supersaturation model for electromigration failure under dc and pulsed dc stress*. Journal of applied physics, 1992. **71**(9): p. 4264-4268.
4. Korhonen, M., et al., *Stress evolution due to electromigration in confined metal lines*. Journal of Applied Physics, 1993. **73**(8): p. 3790-3799.
5. Sukharev, V., E. Zschech, and W.D. Nix, *A model for electromigration-induced degradation mechanisms in dual-inlaid copper interconnects: Effect of microstructure*. Journal of Applied Physics, 2007. **102**(5): p. 053505.
6. Siegel, R., *Vacancy concentrations in metals*. Journal of Nuclear Materials, 1978. **69**: p. 117-146.
7. Kotzurek, J.A., et al., *Direct measurement of vacancy relaxation by dilatometry*. Applied Physics Letters, 2016. **109**(2): p. 021906.

8. Wollenberger, H., *Point Defects in Physical Metallurgy*. Elsevier Science Publisher BV, 1983.
9. Sprengel, W., et al., *Dilatometry: a powerful tool for the study of defects in ultrafine-grained metals*. Journal of Materials Science, 2012. **47**(22): p. 7921-7925.
10. Takamura, J., *Quenched-in vacancies and quenching strains in gold*. Acta metallurgica, 1961. **9**(6): p. 547-557.
11. JE Dickman, R.J., DR Gustafson, *Vacancy formation volume in indium from positron-annihilation measurements*. Physical Review B, 1977. **16**: p. 8.
12. Buescher, B.J. and R. Emrick, *Pressure effect on defect migration in aluminum*. Physical Review B, 1970. **1**(10): p. 3922.
13. PR Bourassa, D.L., DA Blackburn, *Effect of High Pressure on the Thermoelectric Power and Electrical Resistance of Aluminum and Gold*. Physical Review, 1968. **165**(3).
14. Doyama, M. and R. Cotterill, *ENERGIES AND ATOMIC CONFIGURATIONS OF POINT DEFECTS IN FCC METALS*. 1968, Argonne National Lab., Ill.
15. Korzhavyi, P.A., et al., *First-principles calculations of the vacancy formation energy in transition and noble metals*. Physical Review B, 1999. **59**(18): p. 11693.
16. Finnis, M., *Theory of vacancy formation volume*. Journal of Physics F: Metal Physics, 1977. **7**(10): p. 1999.
17. Li, S., et al., *Lattice strain due to an atomic vacancy*. 2009. **10**(6): p. 2798-2808.
18. Plimpton, S., *Fast parallel algorithms for short-range molecular dynamics*. Journal of computational physics, 1995. **117**(1): p. 1-19.
19. Daw, M.S., S.M. Foiles, and M.I. Baskes, *The embedded-atom method: a review of theory and applications*. Materials Science Reports, 1993. **9**(7-8): p. 251-310.
20. Jacobsen, K., J. Norskov, and M.J. Puska, *Interatomic interactions in the effective-medium theory*. Physical Review B, 1987. **35**(14): p. 7423.
21. Adams, J., S. Foiles, and W. Wolfer, *Self-diffusion and impurity diffusion of fee metals using the five-frequency model and the embedded atom method*. Journal of Materials Research, 1989. **4**(1): p. 102-112.
22. Foiles, S., M. Baskes, and M.S. Daw, *Embedded-atom-method functions for the fcc metals Cu, Ag, Au, Ni, Pd, Pt, and their alloys*. Physical review B, 1986. **33**(12): p. 7983.
23. Garikipati, K., L. Bassman, and M. Deal, *A lattice-based micromechanical continuum formulation for stress-driven mass transport in polycrystalline solids*. Journal of the Mechanics Physics of Solids, 2001. **49**(6): p. 1209-1237.

24. Cui, Z., X. Fan, and G. Zhang, *General coupling model for electromigration and one-dimensional numerical solutions*. Journal of Applied Physics, 2019. **125**(10): p. 105101.
25. Cui, Z., X. Fan, and G. Zhang. *Implementation of General Coupling Model of Electromigration in ANSYS*. in *2020 IEEE 70th Electronic Components and Technology Conference (ECTC)*. 2020. IEEE.

5

5

EFFECTS OF MECHANICAL STRESS AND SELF-DIFFUSION: EXPERIMENT AND MODELLING

In this chapter, both experiments and simulations are conducted to investigate the effects of mechanical stress and self-diffusion on electromigration. For the experiments, a full wafer with various electromigration test structures is designed and fabricated. An electromigration measurement setup is established, and several interesting results are obtained. The size effect on electromigration decreases with increasing conductor length. Annealing the conductor can significantly reduce electromigration. Moreover, the oxidation of the conductor tested in air can accelerate the development of electromigration. Importantly, we found that the passivation layer produces different effects on electromigration reduction in the conductor tested in air and vacuum and the annealed conductor tested in vacuum. Moreover, the effects of the sample structure, current density and temperature are also experimentally investigated. In simulations based on the fully coupled electromigration model developed in Chapters 3 and 4, the numerical solutions of a 1D dielectric-covered metal line and stress-free metal line are obtained and compared with experimental data. An exact equation to consider the effect of passivation on the mechanical stress in conductors is derived. Good agreement between the simulation results and the experimental results demonstrates that the atomic concentration gradient plays an important role in electromigration failure. The stress gradient generated in Si_3N_4 -covered conductor can significantly reduce electromigration. Lastly, we can conclude that the second objective of this study is achieved.

5.1. Introduction

For a long time, self-diffusion was considered as a negligible term in electromigration. One popular explanation comes from the comparison between Shatzkes's [1] and Korhonen's models [2]. The Shatzkes model only considers self-diffusion and electromigration itself, resulting in an extremely short lifetime on the scale of seconds. However, a lifetime of several hours is obtained using Korhonen's model when it includes the sink/source term and mechanical stress and neglects self-diffusion. Korhonen's results are more reasonable and similar to experimental results; thus, it is indicated that mechanical stress plays a dominant role in electromigration. Additionally, the failure of the conductor is believed to be caused by mechanical stress. Thereafter, various electromigration models, such as Sarychev's model [3], Suo's model [4] and Sukharev's model [5, 6], were developed to evaluate the stress evolution during electromigration, in which self-diffusion was neglected [4, 7-11]. However, in Chapter 3, we found that the progression of electromigration failure in a stress-free condition is in the same order as that in a totally fixed condition. Self-diffusion plays an important role in balancing the electron wind force. Mechanical stress may not be the decisive parameter in defining electromigration failure. Moreover, the proposed electromigration failure criterion based on the critical vacancy concentration can qualitatively explain the experiments in the literature. To further verify our theory and quantitatively investigate the effects of self-diffusion and mechanical stress on electromigration, extensive experimental data and accurate simulations are required.

In this chapter, experiments and simulations are conducted to investigate the effects of mechanical stress and self-diffusion on electromigration. For our experiments, a mask with various EM test structures is designed and fabricated. Several wafers are fabricated with additional process, such as annealing and passivation. An electromigration measurement setup is established. Various influential factors, such as conductor length, current density, annealing or non-annealing, temperature, passivation condition and sample structure, are experimentally investigated. Electromigration failures are characterised using different methods, such as in-situ resistance monitoring, microscopy, focussed ion beam scanning electron microscopy (FIB-SEM) and energy dispersive X-ray spectroscopy (EDS). In this chapter, a new fully coupled theory is developed. Numerical solutions for a 1D dielectric-covered metal line and a stress-free metal line are obtained to determine the roles of mechanical stress and self-diffusion. Predictions of electromigration failures from void nucleation to void growth are presented and compared with experimental results. Lastly, MD

simulations are conducted to study the microstructure of polycrystalline with and without annealing.

This chapter is organized as follows: Section 5.2 introduces the mask design, sample preparation, and measurement setup. Section 5.3 discusses the electromigration testing results and failure characterisations. Section 5.4 presents the simulation results and comparison with the experimental results. Lastly, this chapter is concluded in Section 5.5.

5.2. Experiment Procedure

5.2.1. Electromigration Testing Wafer Design

Electromigration test structures are designed on a 4-inch full wafer with 52 dies. The layout of the top of a die is shown in Figure 5.1 (a). It includes various types of test structures, such as Blech, SWEAT structures, mixed, two-dimensional (2D), and tapered structures, etc., as illustrated in Figure 5.1 (b). We can use these structures to investigate various influential factors in electromigration.

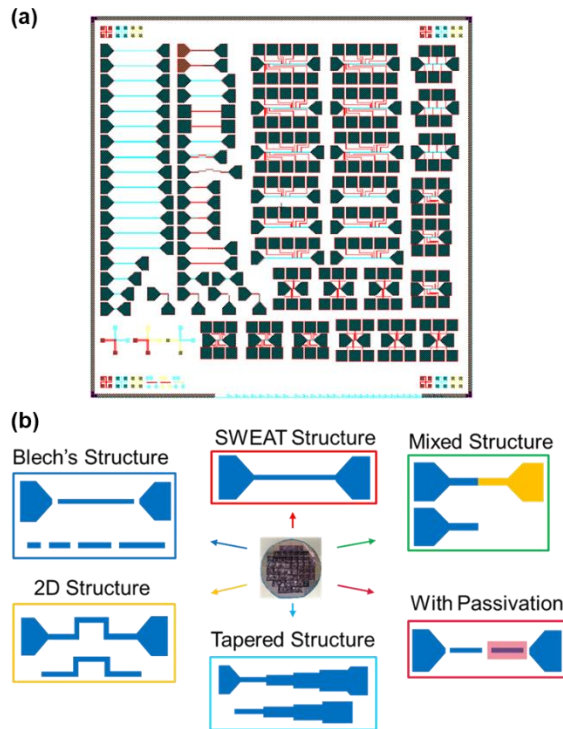


Figure 5.1. (a) Top view of mask design. (b) Schematics for the structures in each die.

5.2.2. Test Sample Preparation and Process

Sample fabrication begins with growing 200 nm-thick SiO_2 by thermal oxidation on a silicon wafer, which is intended as an etching stopping layer and a thermal isolated layer (Figure 5.2 a). After thermal oxidation, a 300 nm-thick titanium nitride (TiN) layer was deposited on the SiO_2 layer by sputtering (Figure 5.2 b). In this process, the reactive gas (N_2) and vapour phase titanium reacted to form TiN in the vacuum chamber. Moreover, the oxidation layer is easily formed on the surface of the TiN layer even in room temperature. Thus, a hot sputter etch (HSE) process was used to remove the oxide layer on TiN. Subsequently, an Al layer was deposited on TiN using reactive sputtering at 300 °C to yield a good quality of metallisation and low contact resistance (Figure 5.2 c). The patterned Al was then etched using wet etching to obtain the required test structures. The etchant used for this step was PES 77-19-04, and the etching rate was approximately 170 nm/min. Furthermore, annealing in a vacuum chamber at 450 °C for 30 min (Figure 5.2 d.2) was carried out on certain wafers. Certain other wafers were deposited with the Si_3N_4 layer on the Al layer as a passivation layer by using plasma enhanced chemical vapour deposition (PECVD) with a mixture of N_2 , SiH_4 and NH_3 at 400 °C (Figure 5.2 f.1). Moreover, certain Si_3N_4 -passivated wafer were annealed at 450 °C for 30 min (Figure 5.2 f.2). After the fabrication process is complete, electromigration wafers with and without passivation and with and without annealing were obtained. Notably, although the Al-based test system is fabricated in this study for electromigration tests, our designed mask can be used for other metals, such as Cu, Au and Ag.

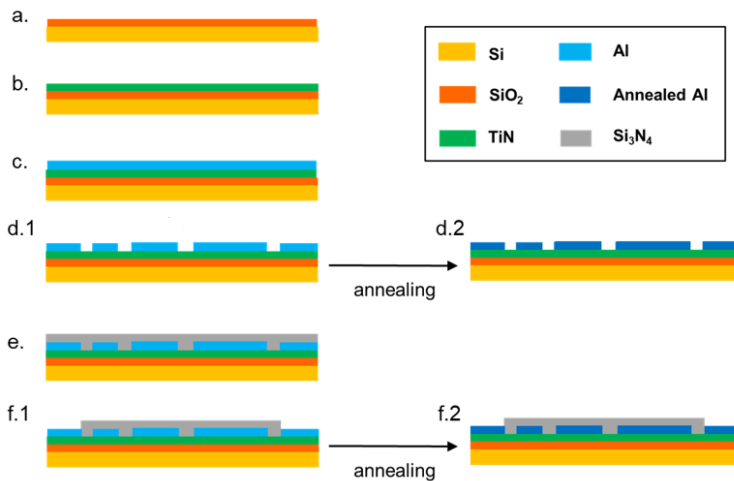


Figure 5.2. Schematic flow diagram of the fabrication process.

Figure 5.3 illustrates test units for annealed, non-annealed, passivated and bare (non-passivated) samples. In electromigration tests, because Al is a better conductor than TiN, the current detours from the former to the latter. This ensures that electromigration occurs in the Al stripes.

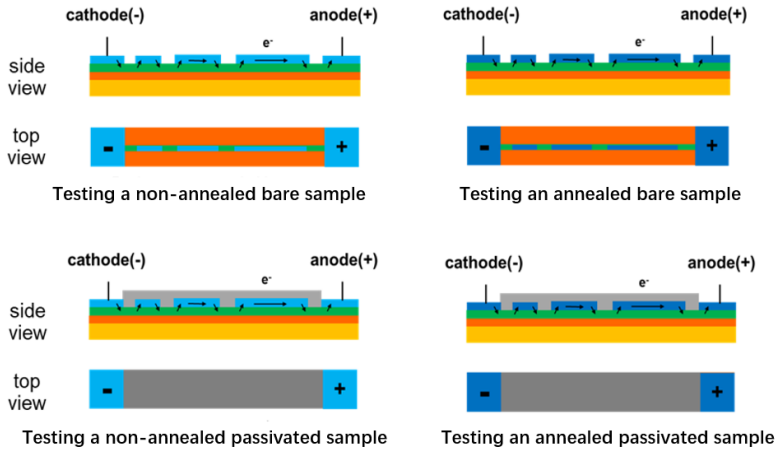


Figure 5.3. Schematic diagrams for the test units.

5.2.3. Electromigration Test Setup

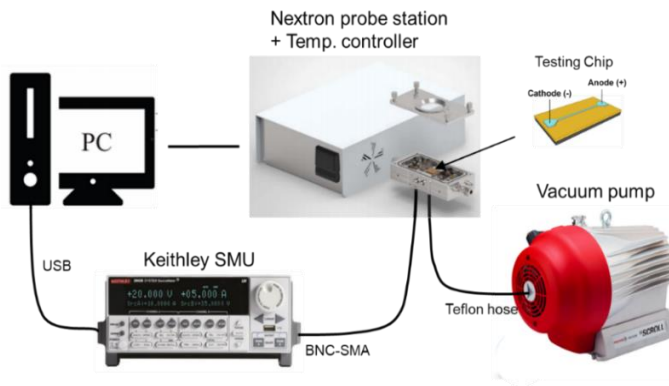


Figure 5.4. Schematic overview of the electromigration measurement setup

Figure 5.4 shows a schematic overview of the measurement setup. The electromigration measurement setup consisted of a Nextron MPS-CHH microprobe chamber with a ceramic chuck. This chamber can be pumped down, while electrical measurements can be performed

using four available probe needles with 20 μm rhodium coated tips. A temperature controller can heat the chamber from 50 $^{\circ}\text{C}$ to 500 $^{\circ}\text{C}$. The vacuum was arranged via a Boc Edwards XDS-10 scroll pump. Current loading was provided, and the resistance was monitored using a Keithley 2612B source measure unit (SMU). The temperature, current loading, and duration of the testing are controlled using a personal computer (PC).

5.2.4. Overview of Testing Plan

In this chapter, extensive electromigration tests with different influential factors are conducted, as illustrated in Figure 5.5.

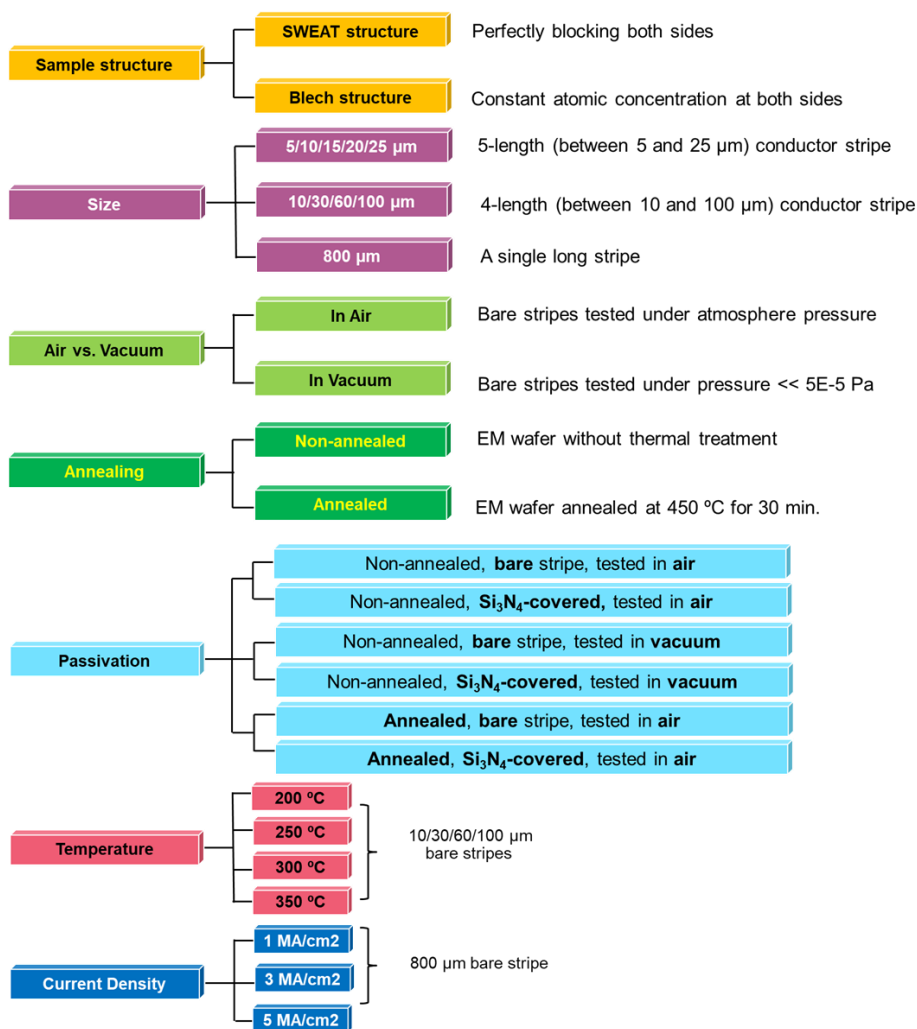


Figure 5.5. Overview of the testing plan

- (1) Sample structure: $800\text{ }\mu\text{m}\times 5\text{ }\mu\text{m}\times 0.2\text{ }\mu\text{m}$ bare Blech and SWEAT structures without annealing were tested under a current density of 1 MA/cm^2 at $250\text{ }^\circ\text{C}$. The Blech and SWEAT structures refer to the narrow Al stripes disconnected and connected with big pads at both sides, respectively.
- (2) Size effect: Bare conductors containing $5/10/15/20/25\text{ }\mu\text{m}$ stripes in the same line, $10/30/60/100\text{ }\mu\text{m}$ stripe in the same line, and a single $800\text{ }\mu\text{m}$ stripe without annealing were tested in vacuum under a current density of 1 MA/cm^2 at $250\text{ }^\circ\text{C}$. All stripes are $5\text{ }\mu\text{m}$ wide and $200\text{ }\mu\text{m}$ thick.
- (3) Air vs. vacuum: $5/10/15/20/25\text{ }\mu\text{m}$ and $10/30/60/100\text{ }\mu\text{m}$ bare stripes without annealing were tested in the air and vacuum conditions. The air condition involves testing the sample in a chamber without using a vacuum pump. Under the vacuum condition, the measurement is performed in a vacuum chamber with pressure lower than $5\text{E-}5\text{ Pa}$. Current loading is 1 MA/cm^2 and the temperature is $250\text{ }^\circ\text{C}$.
- (4) Annealing: $5/10/15/20/25\text{ }\mu\text{m}$ and $10/30/60/100\text{ }\mu\text{m}$ stripes with and without annealing were tested in the vacuum condition under 1 MA/cm^2 at $250\text{ }^\circ\text{C}$.
- (5) Passivation: Under the air condition, non-annealed stripes with and without passivation were tested. In the vacuum condition, non-annealed and annealed stripes with and without passivation were measured. All samples were tested under a current density of 1 MA/cm^2 at $250\text{ }^\circ\text{C}$.
- (6) Temperature: At different temperatures, $10/30/60/100\text{ }\mu\text{m}$ stripes without annealing and passivation were tested in vacuum under a current density of 1 MA/cm^2 .
- (7) Current density: Applying different current loadings, $800\text{ }\mu\text{m}$ stripes without annealing or passivation were tested in vacuum at $250\text{ }^\circ\text{C}$.

5.3. Experimental Results and Discussion

5.3.1. SWEAT vs. Blech Structure

Figure 5.6 shows the electromigration results in $800\text{ }\mu\text{m}$ SWEAT and Blech structures after testing for 20 h. There were no void or hillock formations on both sides of the SWEAT structure because the narrow stripe was connected to the metal pad that served as a reservoir for providing a constant atomic concentration. In the Blech structure, voids and hillocks were observed at the cathode and anode, respectively. This is the typical failure phenomenon for a metal line with perfectly blocking conditions at both ends [12, 13].

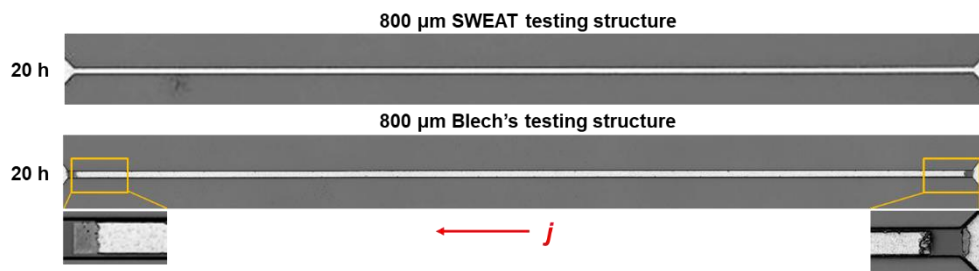


Figure 5.6. Electromigration test results for SWEAT and Blech structures under 1 MA/cm^2 at 20 h.

5.3.2. Size Effects

Figure 5.7 shows the test results of a conductor containing stripes from $5 \mu\text{m}$ to $25 \mu\text{m}$ in the same line, where voids and hillocks at the cathode and anode can be observed. Moreover, the void size increases with the conductor length and time. No voids were observed in the $5 \mu\text{m}$ stripe, and the void in the $10 \mu\text{m}$ stripe was very small. Thus, a critical length of approximately $10 \mu\text{m}$ can be determined for the non-annealed bare Al stripe under 1 MA/cm^2 at 250°C .

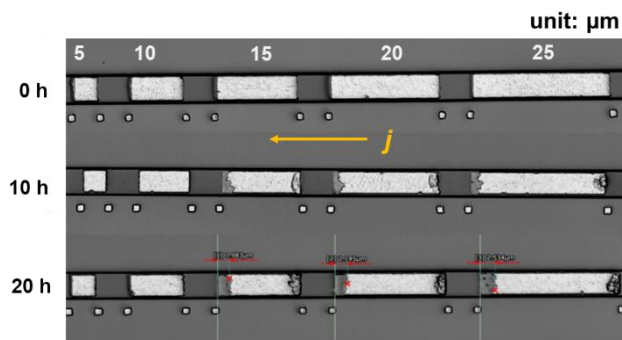


Figure 5.7. Electromigration test results for $5/10/15/20/25 \mu\text{m}$ stripes under 1 MA/cm^2 at 10 h and 20 h.

The electromigration results at different times for a conductor containing $10/30/60/100 \mu\text{m}$ stripes in the same line are shown in Figure 5.8. The void size increases with the stripe length and testing time. Al stripes with $30/60/100 \mu\text{m}$ lengths begin to form voids at approximately 30 min; however, the $10 \mu\text{m}$ stripe begins to form voids at a much later stage, i.e. ~ 10 hours. Moreover, between $30 \mu\text{m}$ and $100 \mu\text{m}$, the void size slightly increases with the increasing stripe length. Figure 5.9 shows the electromigration in $800 \mu\text{m}$ stripe (see Figure 5.9), where the void size at 20 h is similar to that in the $100 \mu\text{m}$ stripe. It appears that the size effect on

the magnitude of electromigration tends to decrease with increasing stripe length and nearly disappears in longer stripes.

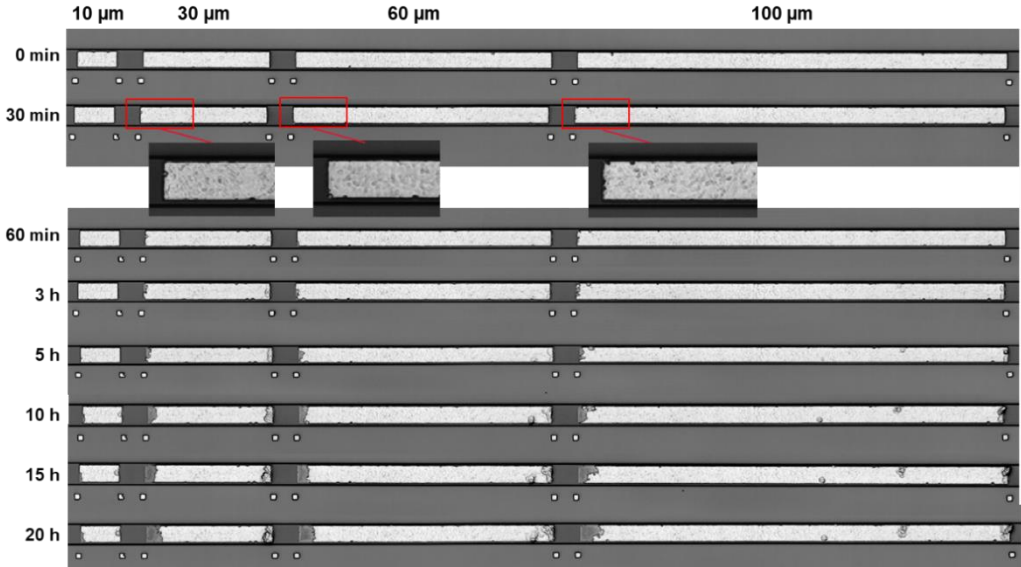


Figure 5.8. Electromigration results for 10/30/60/100 μm stripes under 1 MA/cm^2 at 250 $^{\circ}\text{C}$ from 0 to 20 hours.

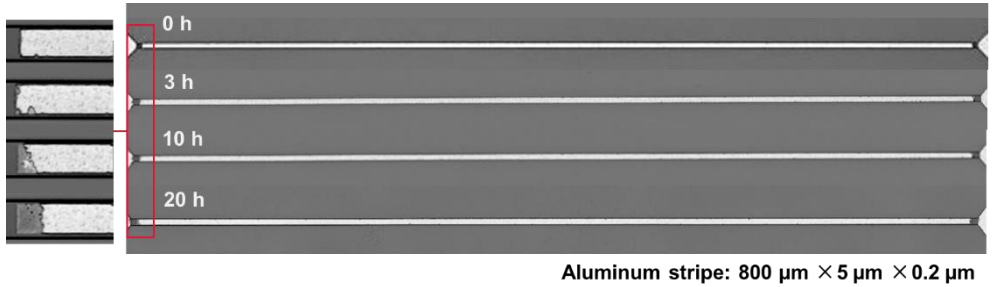


Figure 5.9. Electromigration results for 800 μm stripes under 1 MA/cm^2 at 250 $^{\circ}\text{C}$ from 0 to 20 h.

Figure 5.10 shows the changes in resistances for stripes with different lengths. For the 10 μm stripe, the resistance gradually and slightly increases, indicating a slight electromigration. For the 30/60/100 μm stripes, the resistance continually increases, and it increases rapidly in the longer stripes. However, the difference in the resistance between 60 μm and 100 μm is not noticeable, indicating a similar development of electromigration in the 60 μm to 100 μm stripes. Overall, the resistance change is consistent with the observations of void growth.

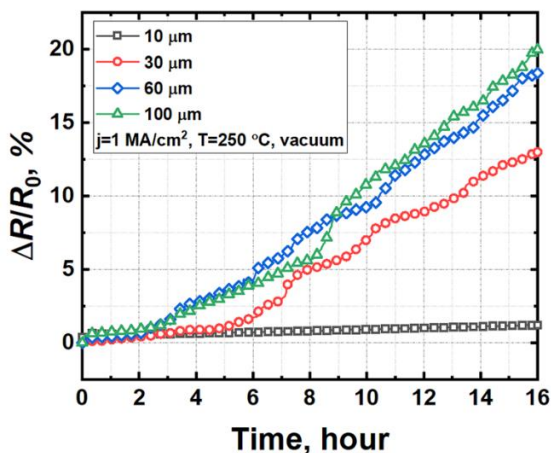


Figure 5.10. In-situ resistance change for 10/30/60/100 μm stripes under 1 MA/cm^2 at 250 $^{\circ}\text{C}$.

5.3.3. In Vacuum vs. In Air

When the bare stripes are exposed to air, electromigration develops much faster than in vacuum, as shown in Figure 5.11. At 10 h, the void sizes for the 30, 60 and 100 μm stripes tested in air were \sim three times longer than those obtained in vacuum. For the 10, 15, 20, 25, 30 μm stripes, the void sizes for the stripes tested in air at 8 h were longer than those tested in vacuum at 10 h. We believe this is because the Al stripes can be oxidized in air at 250 $^{\circ}\text{C}$. The reduction of Al produces a higher current density, leading to an early electromigration failure and a faster void growth.

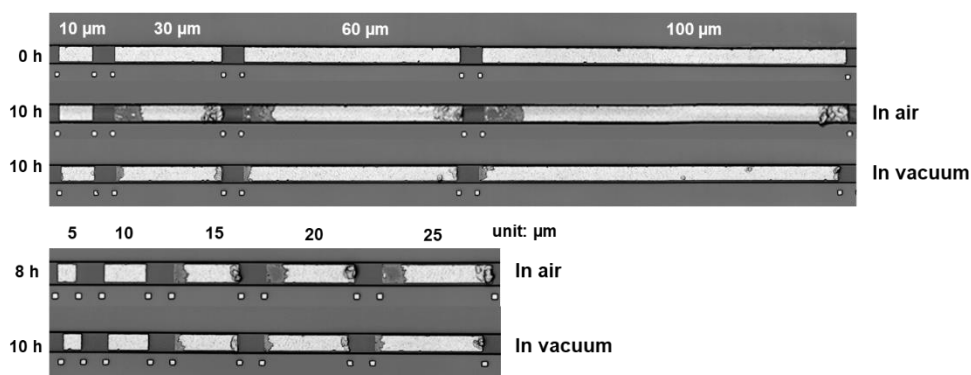


Figure 5.11. Electromigration results for non-annealed bare Al stripes tested in air and the comparison with the measurements in vacuum.

In Figure 5.12, the in-situ measured resistance for the 10 μm stripe in vacuum slightly changed, indicating no electromigration or slight electromigration failure. However, the resistance of the 10 μm stripe exposed to air fast increased over time, which displays a different pattern from the 30 and 60 μm stripes tested in vacuum. These results show that the oxide layer of the Al conductor formed at room temperature cannot protect the conductor from further oxidation at high temperatures.

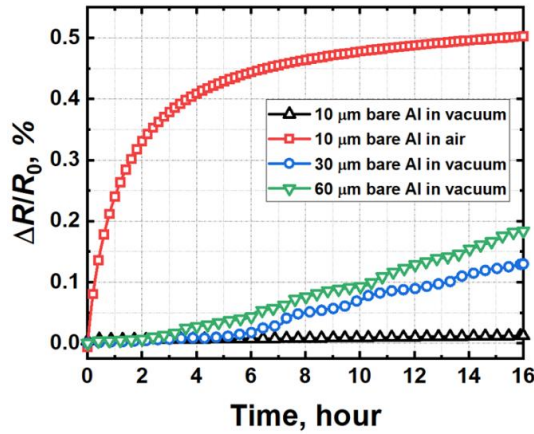


Figure 5.12. In-situ resistance change for the 10 μm stripes tested in air and vacuum.

5.3.4. Effect of Annealing

Figure 5.13 shows the test results for the annealed and non-annealed stripes in vacuum. Comparing with the results of the non-annealed Al stripes, we can identify the following differences.

- Firstly, regarding the surface morphology, the annealed Al stripes had rougher surfaces. Additionally, there were more hillocks in the middle region of the annealed Al stripe.
- Secondly, we can observe that the development of electromigration in the annealed Al stripes occurred later, compared to that in non-annealed Al stripes. Regardless of a longer test duration, the void in the annealed sample was smaller than that in the non-annealed sample.
- Moreover, for the annealed stripes, no voids or hillocks were observed in the 5 and 10 μm stripes. The void and hillock in the 15 μm stripe were very small at 40 h. Thus, the critical length for the annealed stripe is approximately 15 μm , which is longer than that for the non-annealed stripe.

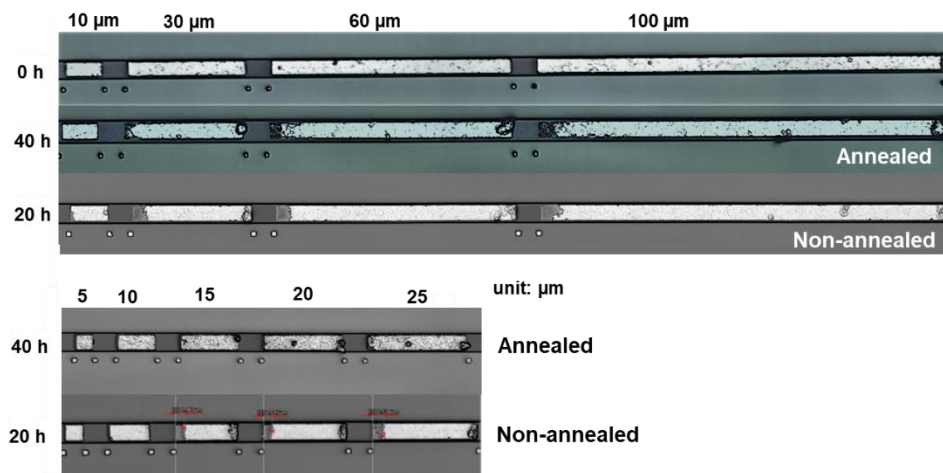


Figure 5.13. Electromigration results for annealed bare stripes under a current density of 1 MA/cm² at 250 °C and comparison with the non-annealed sample.

SEM images shown in Figure 5.14 provide information to understand the different results for the annealed and non-annealed samples. In Figure 5.14 (a), the grain size in the annealed sample is noticeably larger than that in the non-annealed sample. Grain boundaries are fast diffusion paths for mass transport; thus, increasing grain sizes would decrease the effective diffusivity (an extended study using an MD simulation is introduced in Chapter 8), reducing the development of electromigration. Moreover, Figure 5.14 (b) shows that the void in the non-annealed stripe has a clear outline. However, the void in the annealed stripe was unclear and a few Al particles remained in the void region. Meanwhile, we could observe grooves between the grains in the annealed stripe, which proves that mass transport occurs along grain boundaries. These differences indicate that the annealed Al stripe has a more thermodynamically stable microstructure at a high testing temperature (250 °C) compared to the non-annealed Al stripe.

In addition, Figure 5.15 shows the EDS results for the number of Al atoms in certain locations at the cathode, centre and the anode. In the non-annealed sample, the number of atoms slightly changed when moving from the cathode to anode. In the annealed stripe, the number of Al atoms at the cathode was lower than that at the centre or the anode. This indicates that the annealed sample can sustain a lower atomic concentration before void formation compared to the non-annealed sample. This difference also confirms that the annealed Al stripe has a more thermodynamically stable microstructure than the non-annealed Al stripe.

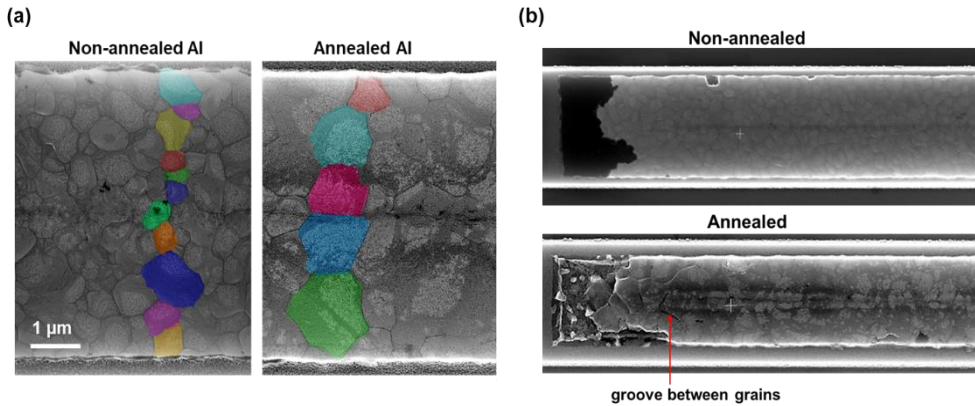


Figure 5.14. SEM images of the (a) microstructures and (b) voids in the annealed and non-annealed stripes.

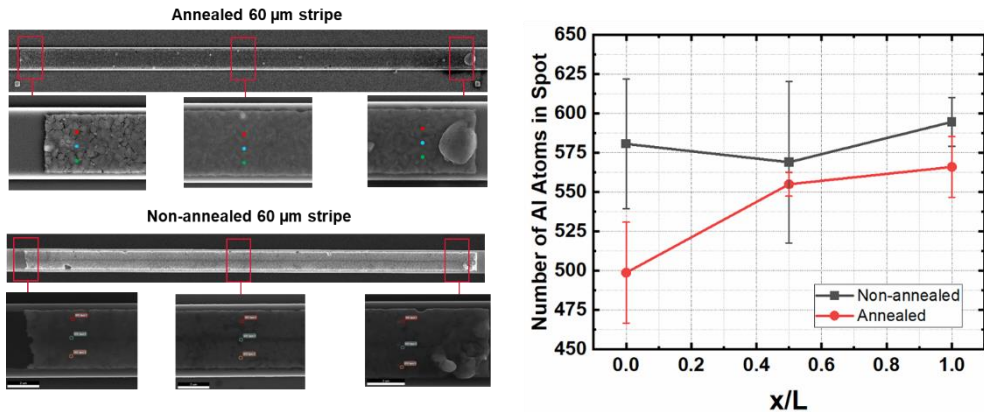


Figure 5.15. EDS results for the number of Al atoms in locations at the cathode, centre and anode for the 60 μm non-annealed and annealed bare stripes. There are three locations at each region.

5.3.5. Effects of Passivation

Bare vs. Si_3N_4 -covered stripes without annealing and tested in air: In the previous section, we have shown that when the Al stripes are exposed to air, electromigration develops very quickly. In Figure 5.16, when the Al stripes are covered by a 300 nm Si_3N_4 layer, electromigration is significantly reduced compared to the bare stripes tested in air. This is because the Si_3N_4 layer can protect the stripe from oxidation. Figure 5.17 shows the changes in the resistances in the 10 μm stripes. When the stripe was bare and exposed to air, its resistance continually increased owing to oxidation. When the stripe was covered by a Si_3N_4

layer or tested in vacuum, the resistance did not change over time. This indicates the absence of oxidation in the Si_3N_4 -covered stripe tested under the air condition.

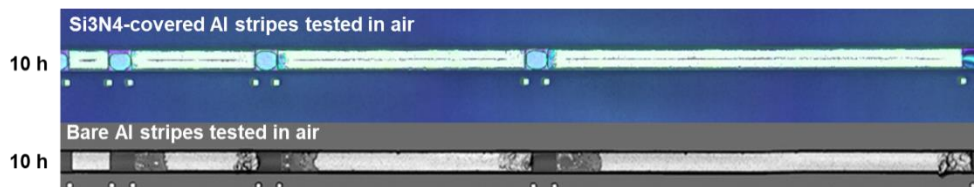


Figure 5.16. Electromigration results for non-annealed stripes with and without passivation tested in air under a current density of 1 MA/cm^2 and 250°C .

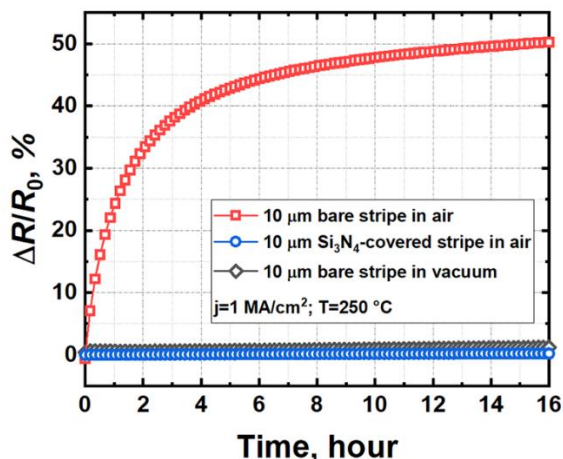


Figure 5.17. In-situ resistance changes in the $10 \mu\text{m}$ bare and passivated stripes tested in air and vacuum.

Bare stripe vs. Si_3N_4 -covered stripes without annealing and tested in vacuum: In Figure 5.18 (a), void formations in both the bare and passivated stripes can be observed at 10 h. Additionally, the void sizes in the passivated and bare stripes were similar, implying that the Si_3N_4 passivation layer does not reduce the electromigration under the vacuum condition for the non-annealed samples. To further confirm this result, a test sample consisting of a $200 \mu\text{m}$ bare stripe and a $200 \mu\text{m}$ Si_3N_4 -covered stripe were tested under the vacuum condition, as shown in Figure 5.18 (b). Interestingly, we observed that the void formation was even larger in the passivated segment, compared to the bare stripe. This again confirms that the Si_3N_4 passivation layer cannot reduce the development of electromigration for the non-annealed sample in vacuum.

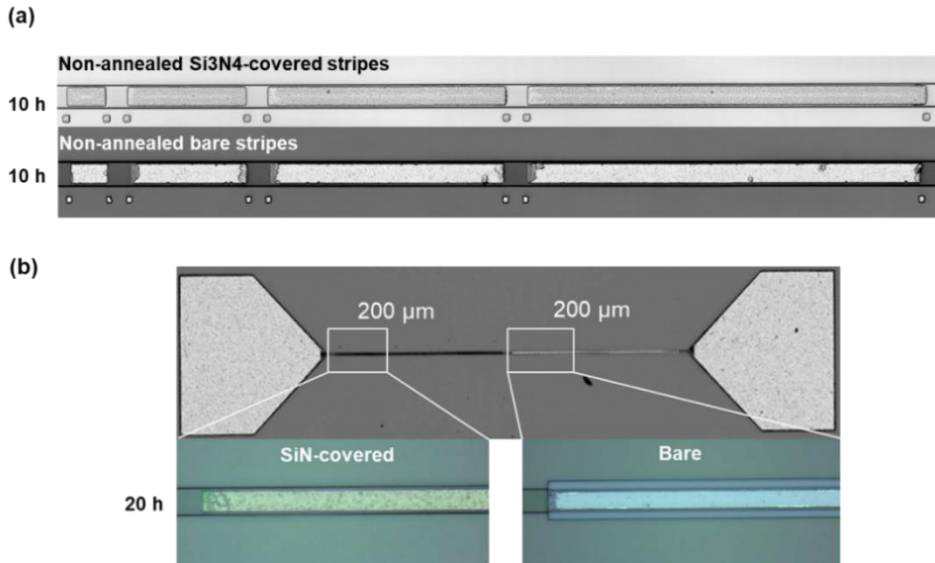


Figure 5.18. Electromigration results for the non-annealed stripes with and without passivation tested in vacuum under a current density of 1 MA/cm^2 and 250°C . (a) Structures containing $10/30/60/100 \mu\text{m}$ stripes in the same line and the Si_3N_4 layer is 900 nm thick. (b) Structure containing a $200 \mu\text{m}$ bare stripe and a $200 \mu\text{m}$ stripe with a 900 nm thick Si_3N_4 layer.

Bare vs. Si_3N_4 -covered stripes with annealing and tested in vacuum: Figure 5.19 shows the effects of passivation on annealed samples. In Figure 5.19 (a), the void size in the Si_3N_4 -covered stripe is noticeably smaller than that in bare stripe. This indicates that Si_3N_4 passivation in the annealed sample can significantly reduce the development of electromigration. To further confirm the results, the same structure with 400 nm thick Al stripes was tested, as shown in Figure 5.19 (b). At 3.5 h , significant void formation could be observed in the bare stripe, while there was nearly no void formation in the Si_3N_4 -covered stripe. Such a noticeable reduction in the development of electromigration indicates that a strong stress gradient was generated in the annealed stripes with passivation. Combining previous characterisations of bare stripes with and without annealing (Figures 5.14 and 5.15), we believe that annealed Al has fewer defects and better coalescence between grains. Thus, the annealed sample can sustain larger mechanical stress compared to the non-annealed sample. As a result, passivation has a positive effect on the annealed sample to reduce electromigration; however, it fails in the non-annealed sample.

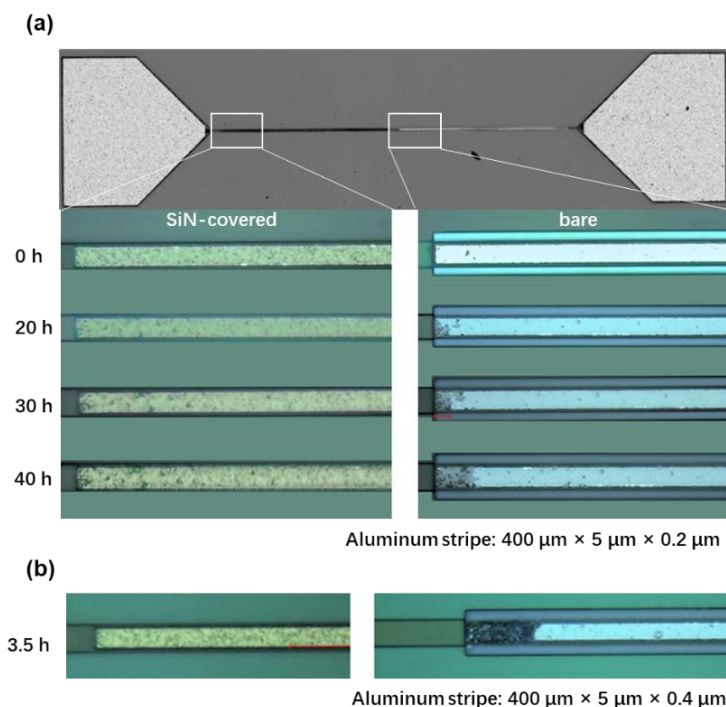


Figure 5.19. Electromigration results for annealed stripes with and without 900 nm Si_3N_4 layer tested in vacuum under a current density of 1 MA/cm^2 and 250°C . Test sample for (a) $400 \mu\text{m} \times 5 \mu\text{m} \times 0.2 \mu\text{m}$ and (b) $400 \mu\text{m} \times 5 \mu\text{m} \times 0.4 \mu\text{m}$ Al stripes.

5.3.6. Effect of Temperature

Figure 5.20 shows the electromigration results for the non-annealed bare stripes at different temperatures under a current density of 1 MA/cm^2 . The void sizes increased with the temperature. Electromigration is essentially an enhanced thermodynamic process; thus, higher temperatures must induce faster atomic diffusion movement. These data are used in Chapter 8 to determine the effective diffusivity in Al.

5.3.7. Effect of Current Density

For $800 \mu\text{m}$ non-annealed bare stripes tested in vacuum, the higher current density induces a larger void at cathode, as shown in Figure 5.21 (a). These data are used for a quantitative comparison with the simulation results. In Figure 5.21 (b), significant void formation was also observed in the pads on the right side. Similarly, hillock formation was also observed in the pads on the left side.

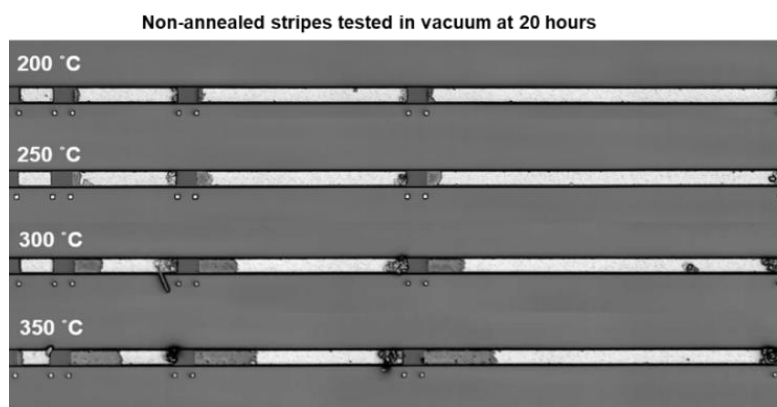


Figure 5.20. EM results for the annealed bare stripes at different temperatures under 1 MA/cm^2 .

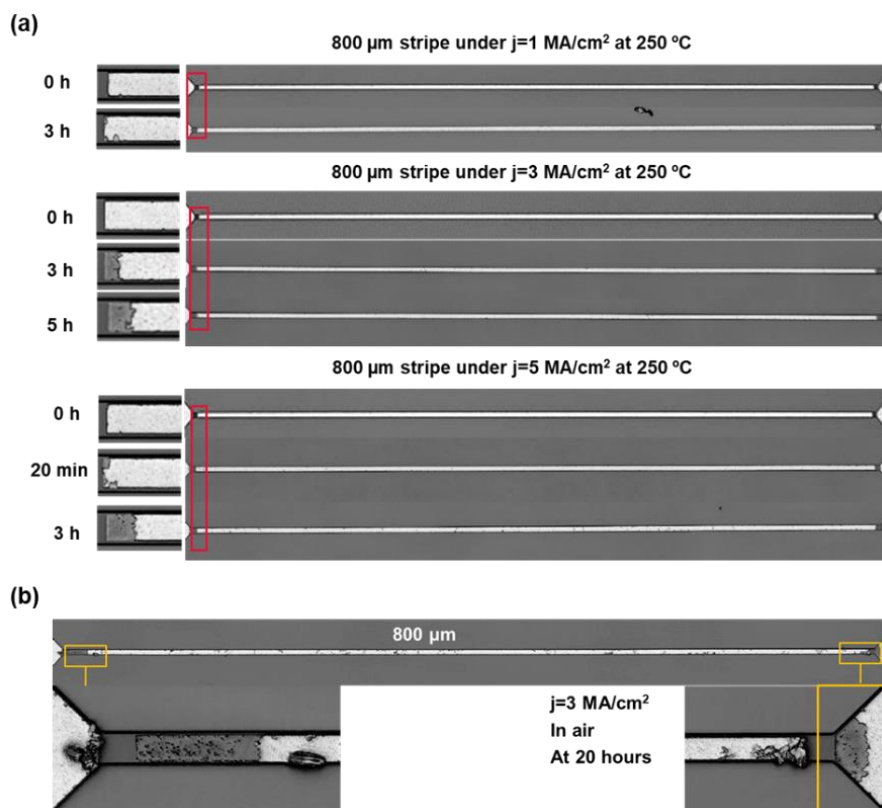


Figure 5.21. EM results for the 800 μm non-annealed bare stripes under different current densities at 250°C .

5.4. Fully-Coupled Theory and Governing Equation

5.4.1. Multi-physics Driven Fully-coupled Model

We developed a general coupling model in Chapter 3 and a MD-verified diffusion-induced strain in Chapter 4. In this section, we combine all the equations for a fully-coupled model based on both the studies in the previous chapters. In the new theory we use atomic concentration C_a to describe the process of electromigration, instead of the C_v used previously in Chapter 3. Consequently, the atomic concentration is employed for failure criterion by electromigration. When the atomic concentration reaches its critical value, void formation takes place. The critical atomic concentration is obtained from experimental data.

A. Transport Equation

$$\frac{\partial \theta}{\partial t} = -\Omega \nabla \cdot \mathbf{J}_a$$

$$\mathbf{J}_a = -D_a \nabla C_a - D_a C_a \frac{Z^* e \rho \mathbf{j}}{k_B T} + D_a C_a \frac{\Omega \nabla \sigma}{k_B T} - D_a C_a \frac{Q^* \nabla T}{k_B T^2}$$

B. Constitutive Equation

$$\theta = tr(\boldsymbol{\varepsilon})$$

$$\boldsymbol{\varepsilon} = \boldsymbol{\varepsilon}^{me} + \boldsymbol{\varepsilon}^{th} + \boldsymbol{\varepsilon}^{diff}$$

$$\boldsymbol{\varepsilon}^{th} = \alpha dT \mathbf{I}$$

$$d\boldsymbol{\varepsilon}^{diff} = \frac{1-f}{3} \frac{dC_a}{C_a} \mathbf{I}$$

$$\boldsymbol{\sigma} = 2G\boldsymbol{\varepsilon} + \lambda tr(\boldsymbol{\varepsilon})\mathbf{I} - Btr(\boldsymbol{\varepsilon})\mathbf{I} - Btr(\boldsymbol{\varepsilon})\mathbf{I}$$

$$\sigma = tr(\boldsymbol{\sigma})/3$$

C. Field Equations

$$\nabla \cdot \boldsymbol{\sigma} + \mathbf{F} = 0$$

$$\boldsymbol{\varepsilon} = \frac{1}{2}(\nabla \mathbf{u} + \mathbf{u} \nabla)$$

$$\nabla \cdot \mathbf{j} = 0$$

$$\mathbf{j} = \frac{\mathbf{E}}{\rho}$$

$$k\nabla^2 T + \mathbf{j} \cdot \mathbf{E} = 0$$

5.4.2. Governing Equation for 1D Case

A. Stress-Free Metal Line

For stripes supported on the TiN substrate without passivation, because there is little constraint from the surrounding material, a 1D stress-free metal line was used to model the bare stripe, as illustrated in Figure 5.23. Under this condition, all stress components were zero, and the atomic flux was blocked at both ends. Moreover, Joule heating was neglected in our simulation, and thus, no temperature gradient exists. Chapter 6 explains why the temperature gradient induced by a 1 MA/cm² current density can be neglected.

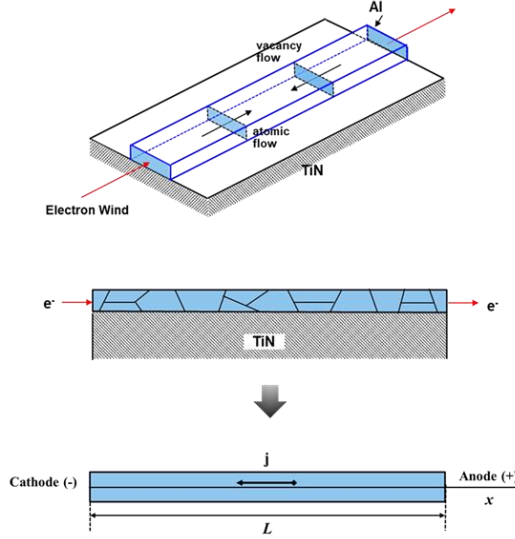


Figure 5.23. Schematic diagram for a 1D stress-free metal line to model the bare stripe.

- Mechanical boundary condition:

$$\sigma_x = \sigma_y = \sigma_z = \sigma_{xy} = \sigma_{yz} = \sigma_{xz} = 0 \quad (5.1)$$

- Temperature:

$$T(x, t) = T_0 \quad (5.2)$$

- Diffusion boundary condition:

$$J_a(0, t) = -\frac{D_a \partial C_a(t, 0)}{\partial x} + \frac{D_a C_a(t, 0) Z^* e \rho j}{k_B T} = 0 \quad (5.3)$$

$$J_a(L, t) = -\frac{D_a \partial C_a(t, L)}{\partial x} + \frac{D_a C_a(t, L) Z^* e \rho j}{k_B T} = 0 \quad (5.4)$$

Applying these conditions to a fully coupled electromigration model, the governing equation for the electromigration in the bare stripe is obtained as follows:

$$\frac{1 - f(C_a)}{C_a} \frac{\partial C_a}{\partial t} = D_a \left(-\frac{Z^* e \rho j}{k_B T} \frac{\partial C_a}{\partial x} + \frac{\partial^2 C_a}{\partial x^2} \right) \quad (5.5)$$

where $f(C_a)$ is the vacancy volume relaxation factor, which changes as a function of the atomic concentration. In Eq. (5.5), although only self-diffusion was considered to balance the electromigration, we will demonstrate that the results obtained from this equation are in excellent agreement with experimental results.

B. Passivated Metal Line

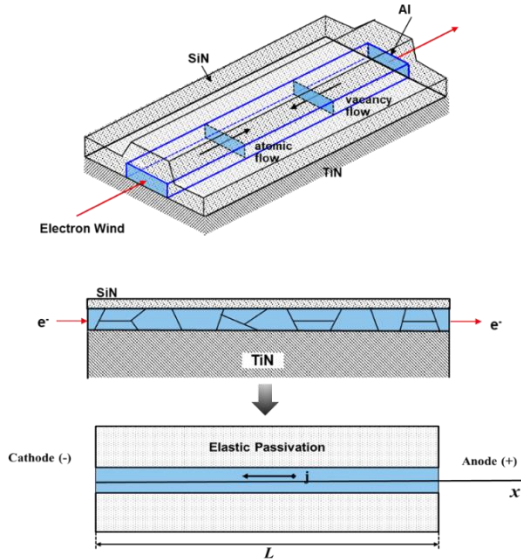


Figure 5.24. Schematic diagram of a 1D metal line embedded in elastic passivation to model the Si_3N_4 -covered stripe.

In contrast to the totally fixed configuration discussed in Chapter 3, this model considers the passivation layer as an elastic material. When Al stripe is covered by a passivation layer, the deformation and stress inside stripe are influenced by both the mechanical properties of the Al stripe and the passivation. Here, we considered the Si_3N_4 -covered Al stripe as a 1D metal line embedded in elastic passivation, as illustrated in Figure 5.24. A modified Eshelby's solution was obtained to consider the effect of passivation on the stress field in the conductor, which are given in details in Appendix A.

- Mechanical boundary conditions: The Al stripe is embedded in Si_3N_4 passivation.
- Diffusion boundary condition:

$$J_a(0, t) = -\frac{D_a \partial C_a(0, t)}{\partial x} + \frac{D_a C_a(0, t) Z^* e \rho j}{k_B T} + \frac{D_a C_a(0, t) \Omega \partial \sigma(0, t)}{k_B T \partial x} = 0 \quad (5.6)$$

$$J_a(L, t) = -\frac{D_a \partial C_a(L, t)}{\partial x} + \frac{D_a C_a(L, t) Z^* e \rho j}{k_B T} + \frac{D_a C_a(L, t) \Omega \partial \sigma(L, t)}{k_B T \partial x} = 0 \quad (5.7)$$

Using Eshelby's solution shown in Appendix A, we can obtain the following coupling relation between C_a and σ .

$$\sigma = -\frac{2E_c(1-f(C_a))}{9[1-v_c+(1+v_m)\varphi]} \int_{C_{a0}}^{C_a} \frac{1-f(C_a)}{C_a} dC_a \quad (5.8)$$

where E_c and v_c are the Young's modulus and Poisson's ratio of Al, respectively. E_m and v_m are the Young's modulus and Poisson's ratio of Si_3N_4 , respectively. φ is the ratio of E_c to E_m ($\varphi=E_c/E_m$). Applying the obtained C_v - σ equation to the fully coupled electromigration model, the governing equation for mass transport in terms of C_a was then obtained as follows:

$$\begin{aligned} & \frac{1+v_c+3(1+v_m)\varphi}{3[1-v_c+(1+v_m)\varphi]} \frac{1-f(C_a)}{C_a} \frac{\partial C_a}{\partial t} \\ &= D_a \left[-\frac{Z^* e \rho j}{k_B T} \frac{\partial C_a}{\partial x} + \frac{\partial^2 C_a}{\partial x^2} + \frac{2E_c \Omega}{9[1-v_c+(1+v_m)\varphi] k_B T} \left[(1 \right. \right. \\ & \quad \left. \left. - f(C_a)) \frac{\partial^2 C_a}{\partial x^2} - \frac{\partial f(C_a)}{\partial C_a} \left(\frac{\partial C_a}{\partial x} \right)^2 \right] \right] \end{aligned} \quad (5.9)$$

C. Equations to Calculate Drift Velocity and Void Length

Based on the obtained numerical solutions, equations to calculate the void size in stress-free and passivated metal lines were developed as follows (the derivation is presented in Appendix B):

For the stress-free metal line:

$$v_{drift} = \frac{D_a}{k_B T} \left(-Z^* e \rho j - \frac{k_B T \Delta C_a}{L - L_{void}} \right) \quad (5.10)$$

$$L_{void} = \int_0^t \frac{D_a}{k_B T} \left[-Z^* e \rho j - \frac{k_B T \Delta C_a}{L - L_{void}} \right] dt \quad (5.11)$$

For the passivated metal line:

$$v_{drift} = \frac{D_a}{k_B T} \left[-Z^* e \rho j - \frac{k_B T \Delta C_a}{L - L_{void}} - \frac{2E_c(1-f)\Delta C_a}{9[1-v_c + (1+v_m)\varphi](L - L_{void})} \right] \quad (5.12)$$

$$L_{void} = \int_0^t \frac{D_a}{k_B T} \left[-Z^* e \rho j - \frac{k_B T \Delta C_a}{L - L_{void}} - \frac{2E_c(1-f)\Delta C_a}{9[1-v_c + (1+v_m)\varphi](L - L_{void})} \right] dt \quad (5.13)$$

where v_{drift} is the drift velocity, L_{void} is the void length, L is the total length of the conductor and t is the testing duration. ΔC_a is the difference between the atomic concentrations at the anode for hillock generation ($C_{a,hillock}$) and at the cathode for void formation ($C_{a,void}$), i.e. $\Delta C_a = C_{a,hillock} - C_{a,void}$.

5.4.3. Overview of the Simulation Procedure

Based on the fully-coupled electromigration model, extensive simulations are presented and compared with experimental results. The simulation procedure is illustrated in Figure 5.22.

- In the first step, combining analytical solutions with several characteristic experimental data, two important parameters, **atomic diffusivity** (D_a) and the **critical atomic concentration for void formation** ($C_{a,void}$), were determined.
- Subsequently, applying the obtained parameters to the governing equations of a simplified 1D model, the numerical solutions for the atomic concentration variation and

stress evolutions can be calculated with different variables, such as conductor length, current density and passivation condition. This procedure was repeated until the critical atomic concentration for **void formation** was reached.

- Once a void is formed, the conductor length and magnitudes of the concentration and stress gradients vary with increasing void size. Equations of drift velocity considering the evolutions of void size were developed, which can be used to predict the **void growth** over time. This procedure was continuously repeated until the conductor length decreased to the critical length with balanced driving forces.

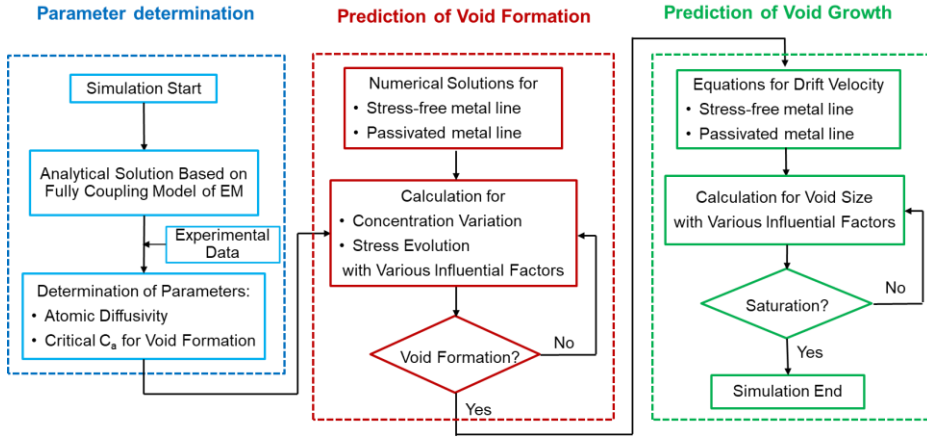


Figure 5.22. Schematic procedure for electromigration simulation.

In this chapter, all numerical results were obtained by using the mode of partial differential equation in Matlab.

5.4.4. Determination of Diffusivity and Critical Atomic Concentration

In Section 5.3.2, we experimentally determined that the critical length was 10 μm for the non-annealed bare stripe under a current density of 1 MA/cm^2 at 250 $^{\circ}\text{C}$. The void length for the 100 μm non-annealed bare stripe at 20 h was 4.4 μm ; thus, the v_{drift} was 0.0608 nm/s . Using these data, we can determine the $D_a^{\text{non-annealed}}$ and $\Delta C_a^{\text{non-annealed}}$ as following steps.

Firstly, applying the critical length to Eq. (5.11), we can determine $\Delta C_a^{\text{non-annealed}}$ via following equation,

$$0 = \int_0^t \frac{D}{k_B T} [Z^* e \rho j - \frac{k_B T \Delta C_a}{L_c}] dt \rightarrow \Delta C_a^{non-annealed} = \frac{Z^* e \rho j L_c}{k_B T} \quad (5.14)$$

Then, based on Eq. (5.10), the atomic diffusivity can be determined via the following equation,

$$D_a^{non-annealed} = v_{drift} k_B T / [-Z^* e \rho j - \frac{k_B T \Delta C_a^{non-annealed}}{L - L_{void}}] \quad (5.15)$$

Using the parameters $Z^*=1$ [12], $e=1.6 \times 10^{-19}$ C, $\rho=2.88 \times 10^{-8}$ Ohm·m, $k=1.38 \times 10^{-23}$ J/K and $T=525$ K, we can obtain $\Delta C_a^{non-annealed}=0.075 C_{a0}$ and $D_a^{non-annealed}=1.03 \times 10^{-14}$ m²/s. Moreover, we assumed that the magnitude of the decreased atomic concentration for void formation was equal to the magnitude of the increased atomic concentration for hillock formation. Thus, the critical atomic concentration for void formation in the non-annealed stripe was $C_{a,void}^{non-annealed}=0.963 C_{a0}$.

In Section 5.3.4, we experimentally determined that the critical length for annealed stripes without passivation was approximately 15 μm under a current density of 1 MA/cm² at 250 °C. The void length for the 100 μm stripe at 40 h was 4.5 μm; thus, the v_{drift} was 0.0313 nm/s. Applying these data to Eqs. (5.10) and (5.11), we can determine the parameters for the annealed sample, $D_a^{annealed}=5.02 \times 10^{-15}$ m²/s, $\Delta C_a^{annealed}=0.105 C_{a0}$ and $C_{a,void}^{annealed}=0.948 C_{a0}$. All the parameters and material properties used in our simulation are listed in Table 5.1.

Table 5.1 Parameters and material properties used in the simulations.

Material properties	Value
Atomic diffusivity for the non-annealed stripe ($D_a^{non-annealed}$)	1×10^{-14} m ² /s
Atomic diffusivity for the annealed stripe ($D_a^{annealed}$)	5.02×10^{-15} m ² /s
Atomic volume for Al (Ω)	1.66×10^{-29} m ³ [14]
Electrical resistivity (ρ)	2.88×10^{-8} Ohm·m [15]
Electric charge (e)	1.6×10^{-19} C
Charge number (Z^*)	1 [12]
Young's modulus of Al (E_m)	70 GPa
Poisson's ratio of Al (ν_m)	0.33
Young's modulus of Si ₃ N ₄ (E_c)	150 GPa
Poisson's ratio of Si ₃ N ₄ (ν_c)	0.23

Vacancy volume relaxation factor of Al (f)	Eq. (4.8) in Chapter 4
Concentration for void formation in the non-annealed stripe ($C_{a,void}^{non-annealed}$)	$0.963 C_{a0}$
Concentration for void formation in the annealed stripe ($C_{a,void}^{annealed}$)	$0.948 C_{a0}$
Critical concentration difference in the non-annealed stripe ($\Delta C_a^{non-annealed}$)	$0.075 C_{a0}$
Critical concentration difference in the annealed stripe ($\Delta C_a^{annealed}$)	$0.105 C_{a0}$

Additionally, we have following relation between atomic concentration, vacancy concentration, and lattice concentration (C_L),

$$C_a + C_v = C_{a0} + C_{v0} = C_L; C_L = \Omega^{-1} \quad (5.16)$$

As $C_{v0}=10^{-6}C_{a0}$, thus,

$$C_{a0} \approx C_L \quad (5.17)$$

5.5. Numerical Results and Comparison with Experiment

5.5.1. Stress-Free Metal Line

Figure 5.25 plots the numerical results for the distributions of normalised atomic concentrations and vacancy concentrations along the 30 μm bare stripe at 10 min, 30 min and 2 h. The atomic concentration decreased at the cathode and increased at the anode, indicating that atomic transport occurs opposite to the direction of the current density. At 30 min, C_a/C_{a0} at the cathode decreased to the threshold condition of void formation, $C_{a,void} = 0.963 C_{a0}$. Moreover, the atomic concentration C_a can be converted to C_v using $C_v/C_{v0}=(1-C_a/C_{a0})10^6$. As a result, $C_{a,void} = 0.963 C_{a0}$ is equivalent to a significantly large vacancy concentration, $\sim 5 \times 10^4 C_v/C_{v0}$. $2 \sim 10 C_v/C_{v0}$ was obtained for the critical vacancy concentration in the literature and in Chapter 3, because the stress-diffusion strain equation (Eq. (2-20), (3-15), or (4-15)) was used. However, when the vacancy concentration varies within the $2C_{v0}$ to $10C_{v0}$ range, as discussed in Chapter 4, the atomic structure obtained from the MD simulation remains highly FCC controlled (Figure 4.8 (a)). This indicates that vacancies at this concentration level ($2 \sim 10 C_v/C_{v0}$) are isolated from each other, and no critical failure occurs. Our new simulation result of $0.96 C_{a0}$ or $\sim 5 \times 10^4 C_{v0}$ provides a more reasonable concentration level for void formation. As a note, all results from now will be presented in terms of C_a (not C_v).

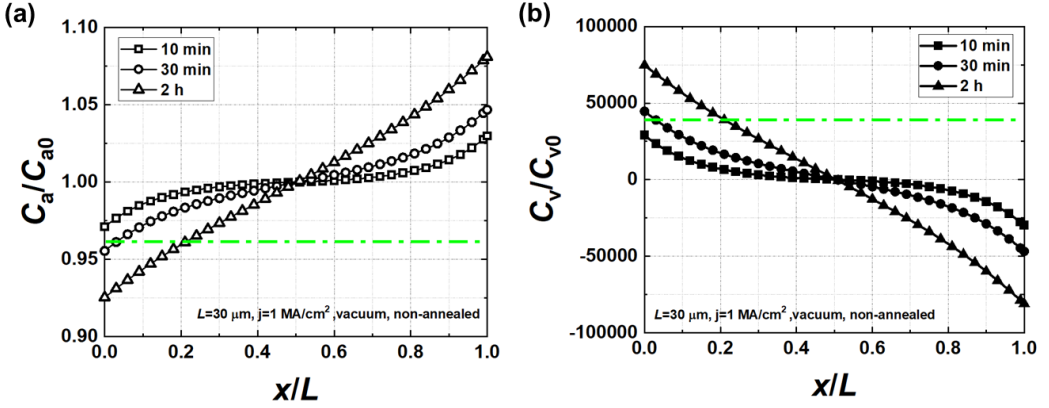


Figure 5.25. Simulation results for the atomic concentration along the 30 μm non-annealed bare stripe at 10 min, 30 min and 2 h.

A. Effect of Conductor Length

Figure 5.26 plots the simulation results for the evolution of atomic concentration at the cathode in the 10, 30, 60 and 100 μm stress-free metal lines. At the early stage ($t < 1 \text{ h}$), atomic concentrations in the 30, 60 and 100 μm lines exhibited the same decreasing trend and reached the threshold value of void formation at 20 min. At the later stage ($t > 2 \text{ h}$), the longer stripe exhibited a more rapid decrease in the atomic concentration. For the 10 μm stripe, the atomic concentration reached saturation at 1 h with $C_a=0.962C_{a0}$, which is equal to the critical concentration for void formation. Thus, slight electromigration failure was indicated for the 10 μm stripe. These simulation results predicting the time to form voids in the non-annealed bare stripes agree with the experimental results shown in Figure 5.8.

After reaching the threshold condition, the void continually grew. Figure 5.27 (a) displays the simulation results for void sizes in the 20, 100 and 800 μm stripes from 20 min to 22 h. The void size almost linearly increased over time, and it grew more rapidly in longer stripes. Moreover, the void size in the 100 μm stripe was noticeably larger than that in the 20 μm stripe. However, the void size in the 800 μm stripe was slightly larger than that in the 100 μm stripe. These simulation results are consistent with the experimental ones. In addition, Figure 5.27 (b) shows the predicted void sizes in the bare stripes with increasing lengths from 5 μm to 130 μm at 10, 20 and 30 h. When the stripe length was less than or equal to 10 μm, the void length was zero. Between 10 μm and 30 μm, void size noticeably increased with the stripe length. When the stripe was longer than 60 μm, the void size slightly increased with

the conductor length. This indicates that the void size in the bare stripe does not linearly increase with the conductor length. Based on Eq. (5.11), the void size in the bare stripe is related to the electron wind and concentration gradient. The magnitude of electron wind remains constant regardless of the stripe length; thus, void size ultimately depends on the magnitude of the concentration gradient that decreases with increasing stripe length. Consequently, the void size in a longer stripe is slightly influenced by the stripe length. These simulation results agree well with experimental observations.

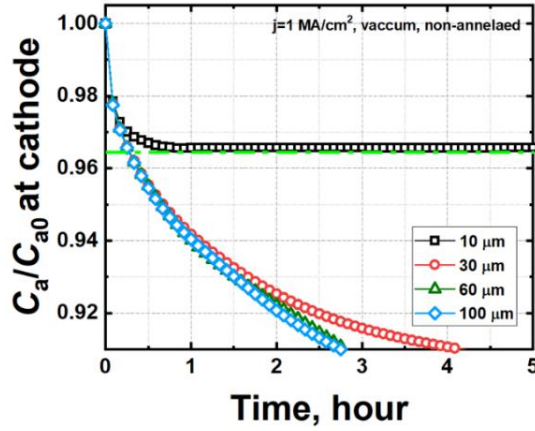


Figure 5.26. Evolution of the atomic concentration at the cathode over time for 10/30/60/100 μm bare stripes.

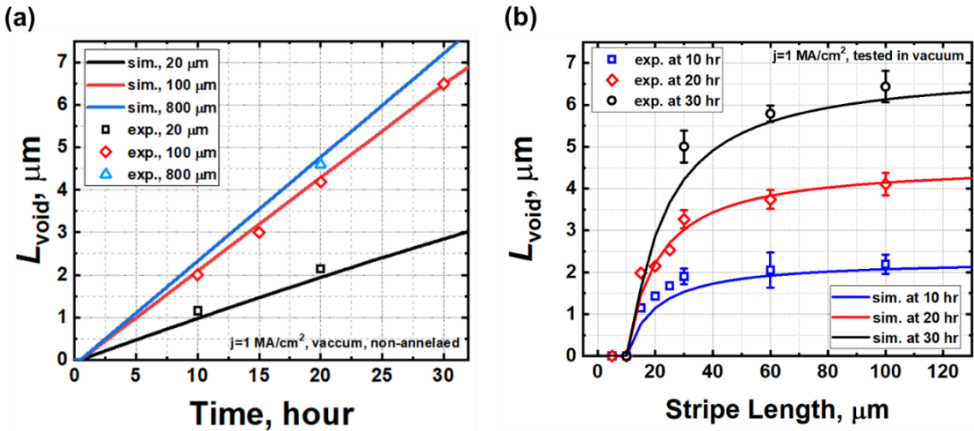


Figure 5.27. Simulation results for the void length in non-annealed bare stripes of different lengths at different times and comparison with experimental data.

B. Effect of Annealing

Figure 5.28 plots the simulation results for the atomic concentrations in the 100 μm annealed and non-annealed stripes under current density of 1 MA/cm^2 . The atomic concentration variations in the annealed stripe were lesser than those in the non-annealed stripe. In the time taken for the C_a/C_{a0} at the cathode in the annealed stripe to reach the threshold condition of void formation at 2 h, the non-annealed stripe had already entered the stage of void growth. Moreover, Figure 5.29 shows the simulation results from void nucleation to void growth, where the upper figure shows the evolution of the atomic concentration at the cathode before void formation and the bottom figure shows the predicted void size after void formation. The 100 μm annealed bare stripe reached the critical concentration at 1.5 h, which took longer than the non-annealed stripe. Additionally, void growth took longer in the annealed stripe than in the non-annealed stripe. At various times, the predicted void size in the annealed and non-annealed stripes agreed well with experiments. Based on the simulation results above, the reduced electromigration in the annealed sample was due to the decreased atomic diffusivity and the lower atomic concentration for void formation.

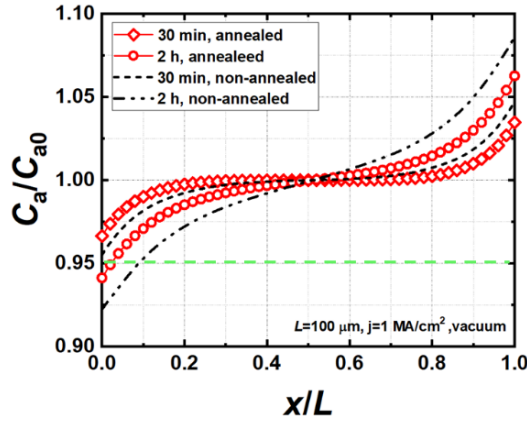


Figure 5.28. Simulation results for the atomic concentration along the 100 μm annealed and non-annealed bare stripes at 30 min and 2 h.

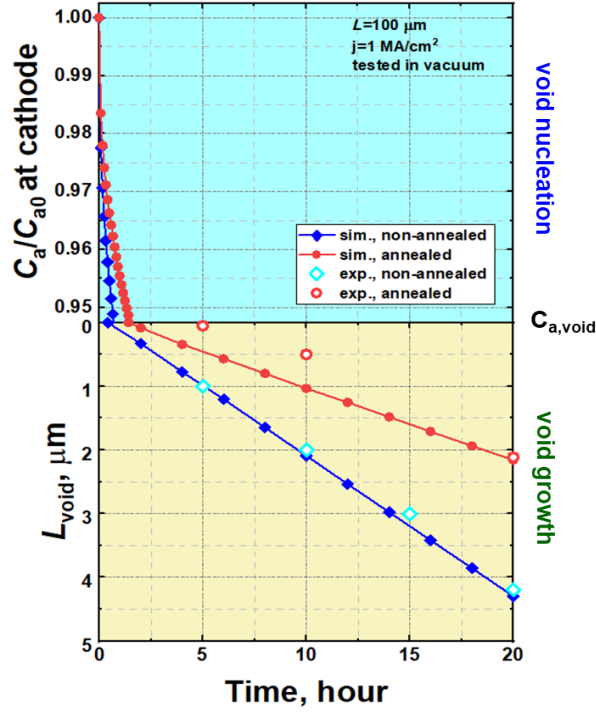


Figure 5.29. Evolution of the atomic concentration at the cathode before reaching the threshold condition of void formation (upper figure) for the 100 μm bare stripes with and without annealing, and the evolution of void size at the cathode after void formation (bottom figure).

C. Effect of Current Density

Simulation results for the 800 μm non-annealed bare stripes under different current densities are plotted in Figure 5.30. With a current density of 1 MA/cm^2 , the stripe reached the threshold condition at ~ 30 min. With increasing current densities of 3 MA/cm^2 and 5 MA/cm^2 , the stripes reached the threshold condition much sooner, i.e. less than 10 min. After entering the stage of void growth, void size linearly increased over time, and the higher current density induces the faster growth of voids. The predicted void size in stripes with 1 MA/cm^2 and 3 MA/cm^2 agree well with the experiments. For the stripe under 5 MA/cm^2 , the predicted void size at 5 h was slightly larger than the experimental result. This error may be due to ignoring the temperature gradient induced by the high current density, which is introduced in Chapter 6.

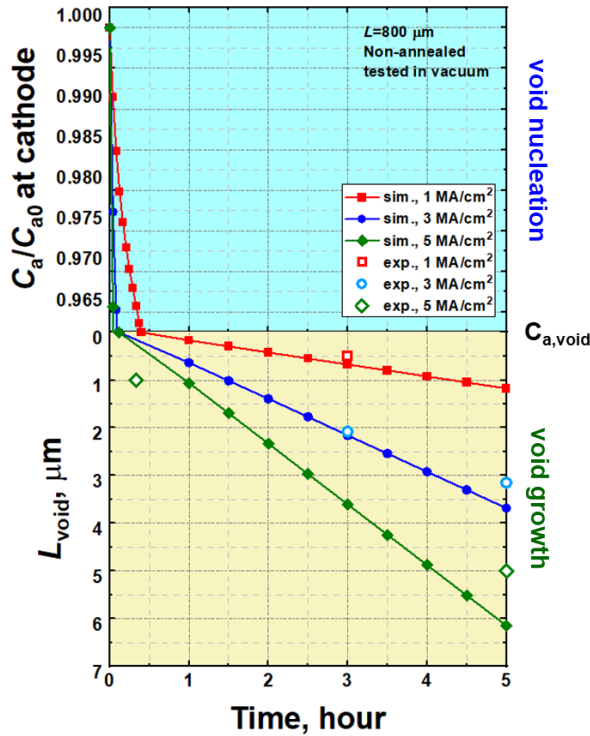


Figure 5.30. Evolution of the atomic concentration at the cathode before reaching the threshold condition of void formation (upper figure) for the 800 μm bare stripes under different current densities, and the evolution of the void size at the cathode after void formation (bottom figure).

5.5.2. Passivated Metal Line

In this section, simulations are conducted based on the experiments conducted on annealed stripes with and without passivation. Figure 5.31 plots the simulation results of the atomic concentration along the 200 μm stripes. At the early stage, e.g. $t = 1.5$ h, electromigration in bare stripe led to void and hillock formation at the cathode and anode, respectively. However, there was no electromigration failure in the Si_3N_4 -covered stripe. This is reflected in Figure 5.31 (b), where C_a/C_{a0} in the passivated metal line slightly varies, but C_a/C_{a0} in the bare stripe sharply increases at the cathode and decreases at the anode. At the late stage, e.g. $t = 20$ h, C_a/C_{a0} in the passivated stripe reached the threshold condition of void formation. However, the electromigration in the bare stripe already produced void growth at the cathode with the much lower C_a/C_{a0} . These simulation results indicate that the passivation layer significantly reduces the depletion of atoms at the cathode and compresses the accumulation of atoms at the anode.

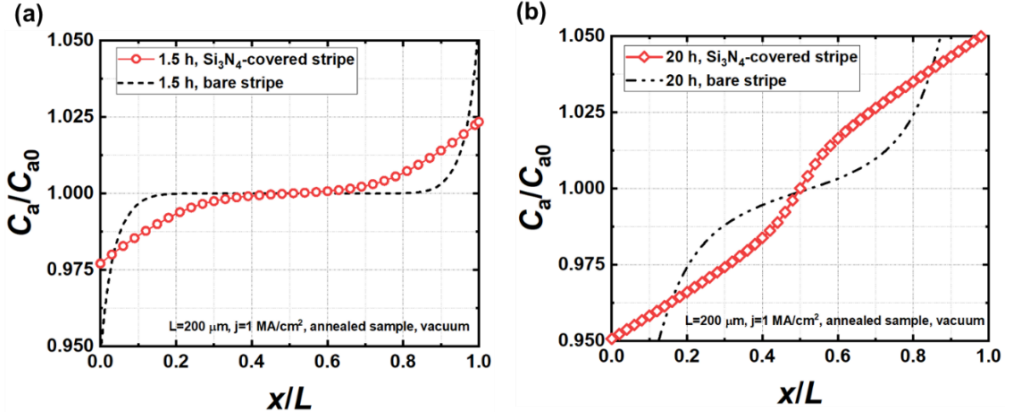


Figure 5.31. Atomic concentration variation in stripes with and without passivation at 1.5 h (a) and 20 h (b).

Figure 5.32 shows the hydrostatic stress in the Si_3N_4 -covered stripe. At 1.5 h, the tensile stress at the cathode was formed because of the depletion of atoms, and the compressive stress was generated at the anode owing to the accumulation of atoms. At 20 h, the development of electromigration causes more atoms diffusing from cathode to anode. As described in Eq. 5.8, increasing C_a could cause higher compressive stress, and decreasing C_a could induce higher tensile stress. As a result, the maximum magnitude of hydrostatic stress reached $\sim 450\text{ MPa}$, leading to a large stress gradient opposite to the direction of electromigration. These results indicate that the stress gradient in the Si_3N_4 -covered stripe causes the reduced electromigration compared to the bare stripe.

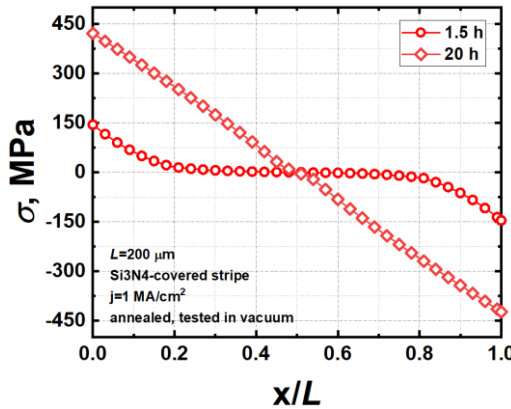


Figure 5.32. Hydrostatic stresses along the $200\text{ }\mu\text{m}$ passivated stripe at 1.5 h and 20 h.

Figure 5.33 shows the simulation results from void nucleation to void growth. The upper figure plots the evolution of atomic concentration at the cathode, where C_a/C_{a0} in the bare stripe decreases more rapidly than that in the passivated stripe. The bare stripe reached the threshold condition at a very early stage (~ 1 h); however, the passivated stripe gradually decreased to the threshold condition at ~ 20 h. After reaching the threshold atomic concentration, the bottom figure shows that the void growth in passivated stripe noticeably occurs later than that in bare stripe. Both phases of void nucleation and growth showed that the development of electromigration in the passivated stripe was reduced. These simulation results agreed well with experimental results.

In our simulations, in the absence of the temperature gradient considered here, there are three flux terms in the passivated stripe.

$$\beta_1 = \frac{F_E(\frac{L}{2}, t)}{F_E(\frac{L}{2}, +\infty)}, \quad \beta_2 = \frac{F_S(\frac{L}{2}, t)}{(\frac{L}{2}, +\infty)}, \quad \beta_3 = \frac{F_C(\frac{L}{2}, t)}{(\frac{L}{2}, +\infty)} \quad (5.18)$$

where

$$F_E = -\frac{Z^* e \rho j}{k_B T} D_a C_a, \quad F_S = \frac{\Omega}{k_B T} \frac{\partial \sigma}{\partial x} D_a C_a, \quad F_C = -D_a \frac{\partial C_v}{\partial x}$$

β_1, β_2 and β_3 represent the normalised fluxes due to electron wind force, stress migration and self-diffusion, respectively. Figure 5.34 shows the evolution of the normalised fluxes at $x = 0.5L$ over time. β_1 consistently remained a positive constant, indicating a constant atomic flux during electromigration. β_2 (the stress gradient) and β_3 (the vacancy concentration gradient) were both negative, implying that both the mechanical stress and vacancy concentration gradients acted as the opposing forces that balanced the electron wind force during electromigration. β_2 and β_3 began at zero at time zero and increased negatively over time. At 14 h, the sum of fluxes induced by the stress and concentration gradients nearly balanced the electric flux. Additionally, the magnitude of the flux due to the stress gradient was significantly larger than that due to self-diffusion. This implied that the stress gradient played a more significant role in counter-balancing electromigration in the Si_3N_4 -covered stripe.

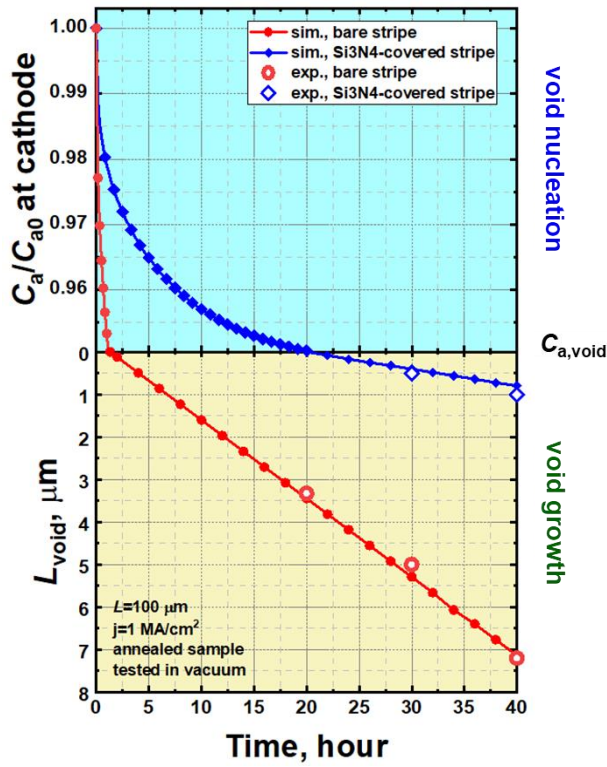


Figure 5.33. Evolution of atomic concentration at the cathode before reaching the threshold condition of void formation (upper figure) for the 200 μm annealed stripes with and without passivation, and the evolution of void size after void formation (bottom figure).

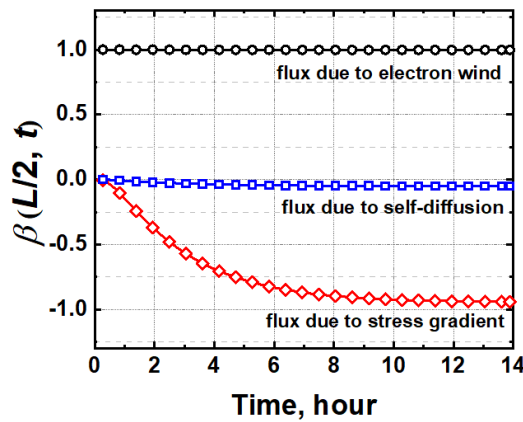


Figure 5.34. Evolutions of normalised fluxes of electromigration, self-diffusion and stress-migration at $x = 0.5L$ over time.

5.5.3. Molecular Dynamic Simulation

MD simulations were performed to investigate the influence of annealing on the Al stripe. Based on the MD study conducted by Zhou *et al* [16], columnar polycrystalline structures were constructed to investigate the coalescence process and the effect of annealing on the microstructure of metal film. The simulation methods are described in Appendix C. Figure 5.35 shows a structure with regularly distributed grains having gaps of at least 18 Å between them. After relaxing the model, under the thermal condition of the deposition process, from 300 °C to 25 °C for 3000 ps, a non-annealed structure was obtained. Two grains on the left were closely attached to the centre grain. Grain C was connected to grain B but separated from grain A. Grain D was completely isolated. The side view of the non-annealed structure shows a large gap between grains A and D. Figure 5.35 (c) demonstrates that the structure is relaxed with additional annealing at 400 °C. Moreover, all the grains coalesced together, and there were no gaps between them. The significant number of HPC and BCC lattice structures in the annealed model implied extensive atomic diffusion among the grains.

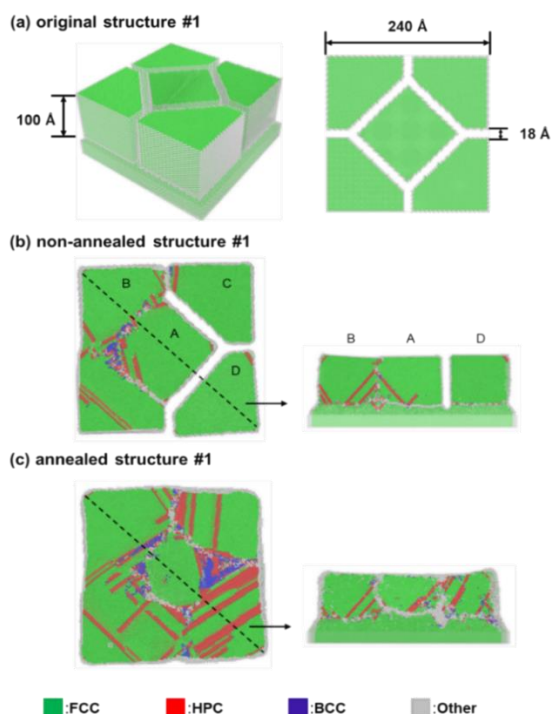


Figure 5.35. (a) 3D and top views of a sketch of the MD model with regularly distributed grains. The total number of atoms in the model is ~1 million. (b) Microstructures from the top and side views after the deposition process (c) Microstructure from the top and side views after the deposition and annealing processes.

Figure 5.36 shows a structure with randomly distributed grains. In the non-annealed structure, small grains coalesced into big grains, and a large gap could be observed between grains A and C. Meanwhile, grain B was not completely attached to grain A and there was a small void at the interface. Moreover, grain D was completely attached to grain A when viewed from the top; however, the cross section at the black dashed line shows that grains B and D simply lean on each other at the surface, leaving an empty hole at the bottom region. In the annealed structure, all the grains coalesced together and there were no gaps, voids or holes at their interfaces. A polycrystalline with fewer defects, better coalescence of grains and a denser structure was obtained after annealing. These simulation results indicated that the annealed Al stripe should have better reliability against electromigration. The voids and holes in the non-annealed sample may have prevented the Al stripe from generating or sustaining large stresses, resulting in the ineffectiveness of the Si_3N_4 layer.

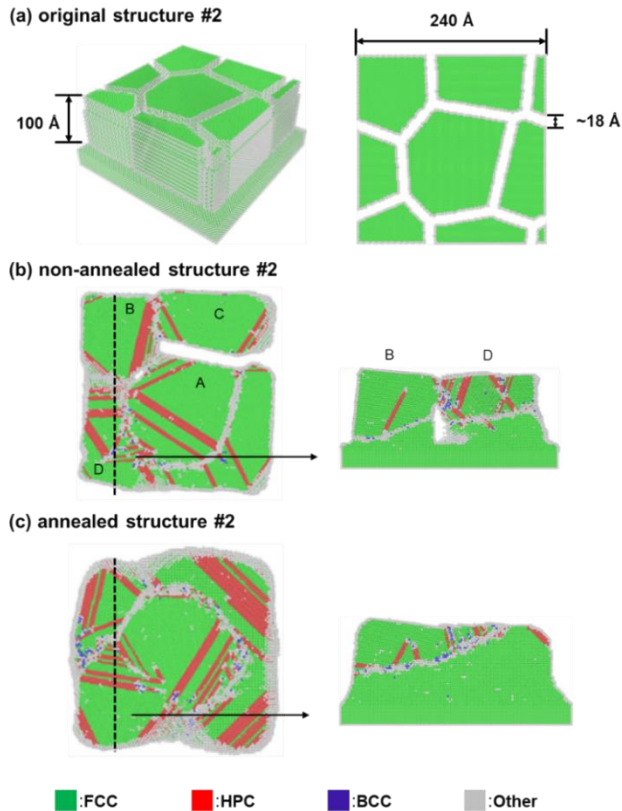


Figure 5.36. (a) 3D and top views of a sketch of the MD model with randomly distributed grains. The total number of atoms in the model is ~1 million. (b) Top and side views of the microstructures after the deposition process (c) Top and side views of the microstructure after the deposition and annealing processes.

5.6. Conclusion

In this chapter, electromigration experiments were performed to investigate the various influential factors in electromigration, such as the conductor length, testing environment, annealing, current density, temperature, passivation and sample structure. Moreover, extensive fully coupled simulations based on the experiments were conducted. The predicted development of electromigration from void nucleation to void growth agree well with experiments.

In our experiments, the void size in the bare stripes increased with the conductor length; however, this size effect on electromigration failure decreased with increasing conductor length. Additionally, when the bare stripes were exposed to air, electromigration failure developed much faster than in vacuum. This is because the Al stripes were oxidized in air, and a higher current density lead to electromigration developing early. Moreover, electromigration in the annealed stripe developed much slower than that in the non-annealed stripe. We found that the grain size in the annealed sample was larger than that in the non-annealed sample, and the decreased material density in the annealed sample was larger than that in the non-annealed ample. These findings indicated that the annealed sample had a better microstructure against electromigration than the non-annealed sample. In addition, in the Si_3N_4 -passivated sample, the passivation layer could protect the Al stripes from oxidation, reducing the development of electromigration. Furthermore, the passivation in the annealed sample could protect the conductor and significantly reduce the electromigration; however, the passivation in the non-annealed sample failed to resist electromigration.

In the simulations, based on the fully coupled model developed in this dissertation, the calculated critical vacancy/atomic concentration for electromigration failure was significantly different from existing solutions in literature. However, the simulation results and predictions were consistent with the experiments, and the determined magnitude of critical atomic concentration was reasonable for void formation. In the simulation of a stress-free metal line, the predicted time to form voids for stripes with different length were consistent with the experiment. The prediction of void growth in stripes with different lengths, current densities and thermal treatment (annealing and non-annealing) agreed well with the experiment. These simulation results also demonstrated the significance of the concentration gradient in electromigration. In spite of zero mechanical stress, the electromigration due to the electron wind force was still affected by the self-diffusion owing to the concentration gradient. Additionally, in the simulation of a metal line embedded in elastic passivation, an

analytical equation was obtained to consider the effect of passivation on mechanical stress in the conductor. The simulation results showed that the stress gradient played a more important role in reducing electromigration in the Si_3N_4 -covered conductor. Ultimately, the MD simulation results showed that annealing could promote the coalescence of grains and reduce the defects in the polycrystalline, producing a more stable microstructure.

Lastly, good agreements between simulations and experiments validated the newly developed coupling theory in this study. Effects of self-diffusion and mechanical stress on electromigration were determined. We can conclude that the second objective listed in Section 1.3 in Chapter 1 is achieved.

References

1. Shatzkes, M. and J. Lloyd, *A model for conductor failure considering diffusion concurrently with electromigration resulting in a current exponent of 2*. Journal of applied physics, 1986. **59**(11): p. 3890-3893.
2. Korhonen, M., et al., *Stress evolution due to electromigration in confined metal lines*. Journal of Applied Physics, 1993. **73**(8): p. 3790-3799.
3. Sarychev, M., et al., *General model for mechanical stress evolution during electromigration*. Journal of Applied Physics, 1999. **86**(6): p. 3068-3075.
4. He, J., et al., *Electromigration lifetime and critical void volume*. Applied Physics Letters, 2004. **85**(20): p. 4639-4641.
5. Sukharev, V. and E. Zschech, *A model for electromigration-induced degradation mechanisms in dual-inlaid copper interconnects: Effect of interface bonding strength*. Journal of Applied Physics, 2004. **96**(11): p. 6337-6343.
6. Sukharev, V., E. Zschech, and W.D. Nix, *A model for electromigration-induced degradation mechanisms in dual-inlaid copper interconnects: Effect of microstructure*. Journal of Applied Physics, 2007. **102**(5): p. 053505.
7. Maniatty, A.M., et al., *Effect of microstructure on electromigration-induced stress*. Journal of Applied Mechanics, 2016. **83**(1).
8. Clement, J., *Vacancy supersaturation model for electromigration failure under dc and pulsed dc stress*. Journal of applied physics, 1992. **71**(9): p. 4264-4268.
9. Clement, J. and C. Thompson, *Modeling electromigration - induced stress evolution in confined metal lines*. Journal of applied physics, 1995. **78**(2): p. 900-904.

10. Pharr, M., et al., *Concurrent electromigration and creep in lead-free solder*. Journal of Applied Physics, 2011. **110**(8): p. 083716.
11. Gleixner, R. and W. Nix, *A physically based model of electromigration and stress-induced void formation in microelectronic interconnects*. Journal of applied physics, 1999. **86**(4): p. 1932-1944.
12. Blech, I.A., *Electromigration in thin aluminum films on titanium nitride*. Journal of applied physics, 1976. **47**(4): p. 1203-1208.
13. Hu, C.K., M. Small, and P. Ho, *Electromigration in Al (Cu) two - level structures: Effect of Cu and kinetics of damage formation*. Journal of applied physics, 1993. **74**(2): p. 969-978.
14. Cui, Z., X. Fan, and G. Zhang, *Molecular dynamic study for concentration-dependent volume relaxation of vacancy*. Microelectronics Reliability, 2021. **120**: p. 114127.
15. Serway, R.A., *Principles of Physics . Fort Worth*. 1998, London: Saunders College Pub: Texas.
16. Zhou, X., et al., *A molecular dynamics study on stress generation during thin film growth*. Applied Surface Science, 2019. **469**: p. 537-552.

6

6

THERMOMIGRATION ACCOMPANYING ELECTROMIGRATION: EXPERIMENT AND MODELLING

In this chapter, thermomigration accompanying electromigration is experimentally and theoretically studied. Several interesting results were observed in our experiments. Firstly, in the Blech structure, electromigration failures spread in the middle region of the conductor with an extended testing duration and increased current density, not only void formation at cathode. Secondly, in the SWEAT structure, voids were observed over a wide range of the entire conductor, and the metal line broke off centre toward the anode side. Unlike the rapid void formation at the cathode in the Blech structure, void formations in the middle of the Blech and SWEAT structures require significantly longer times. Moreover, using various SWEAT structures, it was discovered that the breaking position of the conductor was related to the direction of the current density. In our simulations, the numerical solutions of a 1D metal line with perfectly blocking conditions and constant atomic concentrations at both sides were obtained. Thermomigration was demonstrated to be the primary cause of void formation in the middle region in the Blech and SWEAT structures. The effects of current density and conductor length on electromigration failures were discussed. The predicted resistance based on the numerical solution agreed well with the in-situ resistance measurements. Lastly, an MD simulation was performed to investigate the atomic motion under a temperature gradient.

6.1. Introduction

Owing to Joule heating, electromigration in the interconnect is inevitably accompanied by thermomigration. In the previous chapter, neglecting the effect of thermomigration in the simulation does not imply that it is a minor factor. As early as several decades ago, Jonggook *et al.* [1] had reported that thermomigration may exist in the process of electromigration. They found that the distributions of the hillocks and voids were different from those expected by conventional theories—hillock and void formation at the anode and cathode, respectively. Instead, voids and hillocks were observed at different positions in the conductor. Similar phenomena were also observed in the studies conducted by D’heurle *et al.* [2], Lin *et al.* and Dalleau *et al.* [3]. Researchers believed that the damage in the middle region of the conductor was caused by different atomic diffusivities under a temperature gradient. This is because the temperature in the middle of the metal wire is often higher than that at its edge.

Recently, researchers have found that the temperature gradient caused by Joule heating in solder joints can induce thermomigration comparable to electromigration. [4-10] According to the study conducted by Tu *et al.* [10, 11], for a temperature difference of 1 °C between the two ends of a 10 μm solder joint, the temperature gradient could reach 1000 °C/cm. Under such a temperature gradient, the driving force of thermomigration of Cu atoms in an SnAgCu solder joint is greater than that of electromigration at 150 °C with a current density of 9.7×10^3 A/cm². Moreover, Gu *et al.* [12] found that when the temperature is higher at the cathode than the anode in Sn8Zn3Bi solder joints, void formation was observed on the high temperature side. In the study conducted by Chen *et al.* [5], the failure of a solder joint under a temperature gradient was due to Cu atoms interstitially diffusing in a SnAg solder from the hot end to the cold end. As a result, void formation at the interface between the solder and the hot Cu pad was discovered. These studies mentioned above experimentally showed that thermomigration accompanied with electromigration plays an important role in the failures of interconnects.

As reviewed in Chapter 2, several widely used theoretical models, including Korhonen's model, Kirchheim's model and Sarchev's model, were devoted to evaluating the evolution of mechanical stress during electromigration, ignoring the influence of the temperature gradient. No electromigration model systematically had considered the coupling effect of thermomigration on electromigration. Bassama *et al.* [13] added the effect of thermomigration to Sharchev's model. They then calculated the electromigration in a 2D model through the finite element method. Subsequently, Lin *et al.* [14] extended Bassama's

findings to 3D problems and calculated the influence of temperature on the lifetime of the solder structure. Recently, Sukharev *et al.*[15, 16] established a 3D coupling model of electromigration, considering the impacts from current density, stress gradient, temperature gradient and concentration gradient. However, the studies mentioned above did not reveal the role of thermomigration on electromigration.

In this chapter, the effects of thermomigration on electromigration are investigated through experiments and simulations. In our experiments, the electromigration in both Blech and SWEAT structures under different current densities were analysed. Interesting experimental results were obtained that reflected the effects of current density, conductor length and sample structure on thermomigration. In our simulations, by using the fully coupled electromigration model developed in Chapter 5, the numerical solutions of a 1D metal line with perfectly blocking conditions and constant atomic concentrations at both sides were obtained and compared with the experimental results. The coupling relationship between thermomigration and electromigration and its effect on mass transport, void formation and breaking locations are discussed. Lastly, an MD simulation of atomic diffusion under a temperature gradient was conducted, providing insight into the study of thermomigration.

6.2. Experiment Procedure

The fabrication of test units and the electromigration measurement setup were described in Chapter 5. Here, we mainly introduce the test conditions used.

Test Samples: Figure 6.1 shows the test units used in our tests. All the samples were non-annealed ones without passivation. The test structures were 200 nm thick and their widths and lengths are described as follows:

- SWEAT structure: The narrow Al line was 800 μm long and 5 μm wide. The size of each pad was 300 $\mu\text{m} \times 300 \mu\text{m}$, and both pads were attached to the narrow Al stripe.
- Blech structure: The dimensions of the narrow Al line and the pads were identical to those in the SWEAT structure discussed above, but both pads were disconnected with the narrow Al stripe. Additionally, tests with different lengths of 60 and 100 μm were performed.
- Tapered shape: There were four segments of different widths in the narrow Al line. The total length of all four segments was 400 μm and the widths of the segments were 3/6/12/15 μm going from the left segment to the right.
- 2D shape: Each horizontal and vertical segment was 150 μm and 50 μm long, respectively.

Additionally, the narrow Al stripe was 5 μm wide.

Test Conditions: All tests were performed under the vacuum condition at 250 $^{\circ}\text{C}$. Three different current loadings, 1 MA/cm², 3 MA/cm² and 5 MA/cm², were applied.

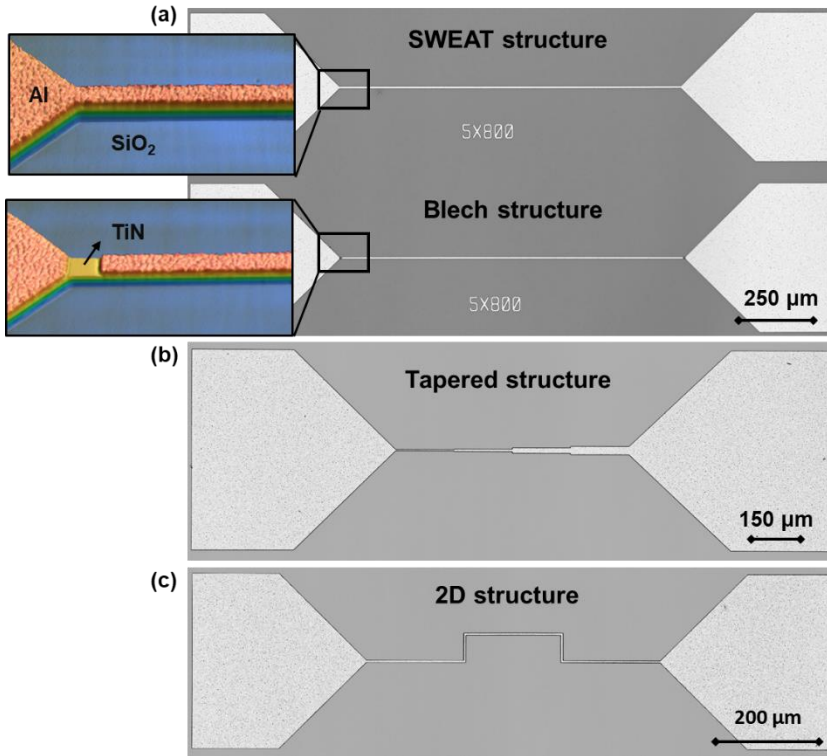


Figure 6.1. (a) SWEAT and Blech structures. (b) Tapered structure. (c) 2D structure.

6.3. Experimental results

6.3.1. Blech Structure

Effect of the Magnitude of Current Density: Figure 6.2 shows the electromigration results in the 800 μm Blech structure under different magnitudes of current densities. In Figure 6.2. (a), void formation at the cathode can be observed at a very early stage (~ 3 h). Apart from this, there were no voids in the other regions of the Al stripe after 20 h of testing. With increasing current density, as shown in Figure 6.2. (b), at the late stage, void formation could be observed in the middle region of the Al stripe. Meanwhile, the void growth in the middle

region was noticeably slower than that at the cathode. When the current density was increased to 5 MA/cm^2 , as shown in Figure 6.2. (c), breaking was observed in the middle region of the conductor at 5 h, which occurred sooner than that under a current density of 3 MA/cm^2 . Additionally, the breaking position was off the middle toward the right.

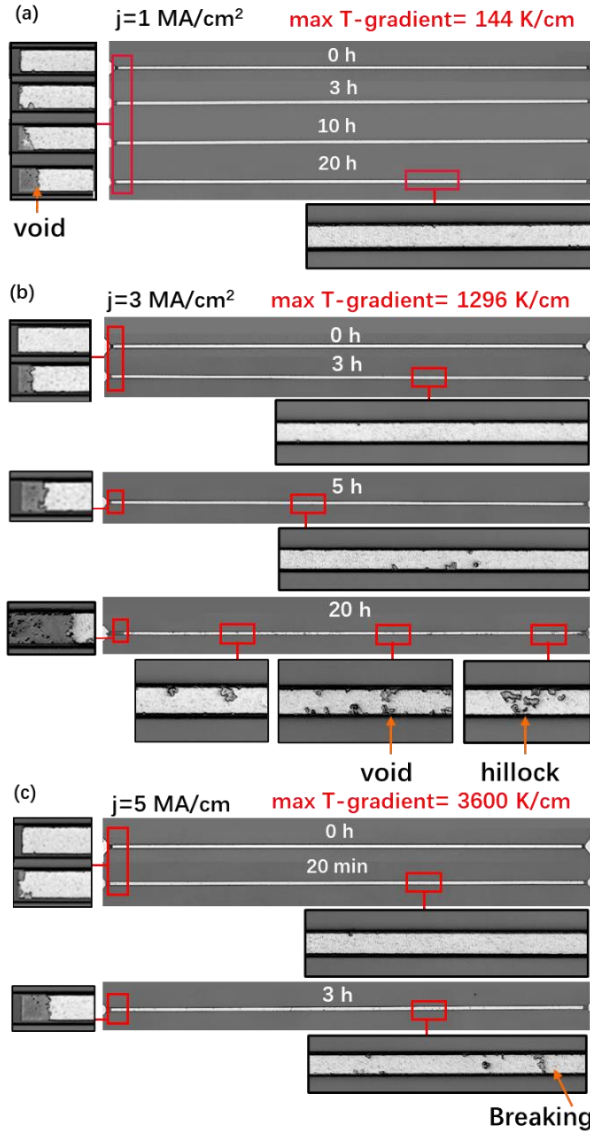


Figure 6.2. Electromigration failures in the $800 \mu\text{m} \times 5 \mu\text{m} \times 200 \text{ nm}$ Al Blech structure at 250°C under current densities of 1 MA/cm^2 (a), 3 MA/cm^2 (b) and 5 MA/cm^2 (c).

Thermomigration is believed to cause the void formation in the middle of the conductor. Increased current density can cause a higher temperature gradient in the Al stripe owing to Joule heating; thus, failures in the middle region were observed under increased current densities of 3 MA/cm² and 5 MA/cm². The numerical solutions presented in Section 6.4 provide more explanations regarding this issue.

Effect of Length: Figure 6.3 shows the failures of the Blech stripes with different lengths under a current density of 3 MA/cm² after 20 h of testing. For the 60 μm and 100 μm Al stripes, no void formation was observed in the middle region, and voids and hillocks were only observed at the cathode and anode, respectively. When the conductor length was increased to 800 μm, apart from large voids and hillocks at the cathode and anode, respectively, we could observe many voids spreading in the middle region of the conductor. Evidently, void formation in the middle region is related to the length of conductor. This is because the increased conductor length can cause a higher temperature gradient in the conductor owing to Joule heating. Consequently, failures in the middle region were observed in longer stripes.

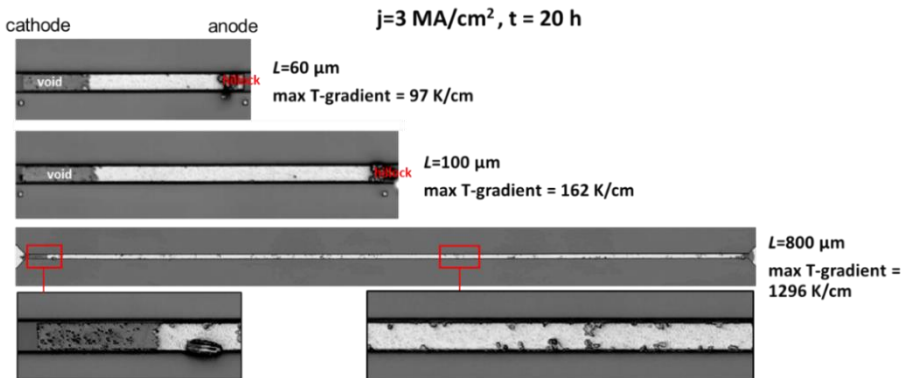


Figure 6.3. Electromigration failures in Al stripes of different lengths after 20 h of testing at 250 °C and a current density of 3 MA/cm²

Void/hillock formation at the cathode and anode was a typical feature due to electromigration in Blech structure in many studies. Blech *et al.* [17-20] performed electromigration tests with 10~115 μm Al stripes under a current density of 0.37 MA/cm² at 350-450 °C. P. Ho *et al.* [21] performed measurements using 10-250 μm Al (Cu) stripes with a 2 MA/cm² current density passed through them at 395 °C. K. N Tu *et al.*[22] investigated electromigration in 3-300 μm

Cu stripes under a 2 MA/cm^2 current density and at 400°C . Somaiah *et al.*[23] tested electromigration in $12 - 100 \mu\text{m}$ Cu stripes by passing a 4 MA/cm^2 current density at 250°C . However, void formation in the middle of the Blech structure was rarely reported in the above-mentioned studies.

6.3.2. SWEAT structure

In the $800 \mu\text{m}$ Al stripe under a current density of 3 MA/cm^2 , voids were observed over a wide range in the middle of the SWEAT structure, as shown in Figure 6.4 (a). At 5 h, several small voids were spreading over a wide range in the middle of the conductor. At 16 h, we could observe a large void toward the right of the centre of the conductor. At 20 h, Al stripe broke off centre toward the right. Unlike void formation at the cathode in the Blech structure, which occurred at a very early stage, that in the SWEAT structure occurred at a later time (at least 10 h) and only in the middle of the conductor. Moreover, with decreasing current density, no voids were observed in the entire SWEAT structure at 20 h.

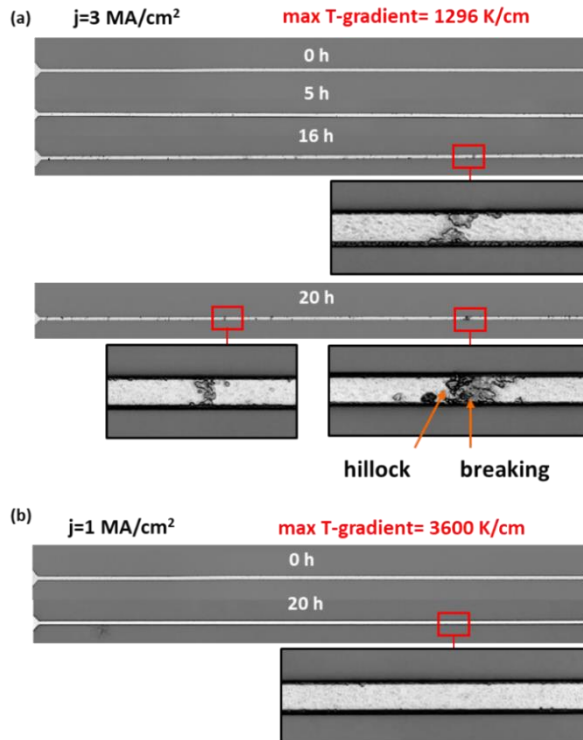


Figure 6.4. Electromigration failures in the $800 \mu\text{m} \times 5 \mu\text{m} \times 200 \text{ nm}$ Al SWEAT structure at 250°C under current densities of 3 MA/cm^2 (a) and 1 MA/cm^2 (b).

Many studies have reported observing voids in the SWEAT structure. In the study conducted by Lloyd *et al.* [24], a $200\text{ }\mu\text{m} \times 5\text{ }\mu\text{m} \times 850\text{ nm}$ Al (Cu) SWEAT type conductor were tested under a current density of 1.8 MA/cm^2 and at $96\sim 265\text{ }^\circ\text{C}$. All the samples failed at the middle of the conductor. The authors believed that the presence of a temperature gradient could lead to a difference in the atomic diffusivity, causing higher mass transport at the hot region than the cold region. This eventually induced failure at the site with a high temperature gradient. Giroux *et al.* [25, 26] investigated electromigration using a SWEAT structure with a $60\text{ }\mu\text{m} \times 3\text{ }\mu\text{m} \times 500\text{ nm}$ Al-0.5% Cu line. They also observed that the failures occurred near the centre of the narrow line. To explain this phenomenon, the authors linked the temperature-dependent diffusivity in the atomic flux and found that the maximum flux divergence was located near the centre of the conductor. In the study conducted by Lee *et al.* [27], the authors suggested that a non-uniform distribution of temperature along the conductor could cause the difference in diffusivity and enhance the flux divergence at the centre of conductor. This resulted in the failure of the conductor. Moreover, in the studies conducted by Pierce [28] and Tan [29], the effect of the temperature gradient on the flux divergence was discussed, emphasizing the importance of temperature in the SWEAT structure. However, the studies mentioned above did not provide mathematical formulation to establish a temperature gradient-induced mass transport to explain the failure of the SWEAT structure.

Effect of Current Flow Direction: Figure 6.5 shows the electromigration in a tapered-shape conductor (SWEAT structure). The four segments had different widths; thus, different magnitudes of current densities passed through the Al stripe. Failure occurred at the narrowest region with the maximum current density at 5 h. Moreover, when the current flowed from the right to the left, the stripe broke off centre to the right in the narrowest line. Additionally, the enlarged SEM image showed small hillocks on the left of the breaking position. However, when the current flowed from the left to the right, the Al stripe broke off centre toward the left in the narrowest line. Moreover, the enlarged image showed the hillock on the right of the breaking position. It is appeared that the breaking position of the conductor was always slightly off middle toward the anode.

2D-shape Unit with SWEAT structure: In the conductor with four right angles in the same plane, we could observe void formations spreading in different sites in each segment, as shown in Figure 6.6. At 5 h, the conductor broke at two different locations: in the middle and right horizontal segments. Additionally, the break on the right was noticeably larger than that in the middle, indicating that the metal line first broke at the middle toward the right.

Moreover, current crowding can occur at corners; however, no obvious voids were observed at these corners.

From the experiments above, we discovered that the breaking position in the middle of the conductor is related to the direction of the current density. In the Blech, SWEAT, tapered and 2D SWEAT structures, the earliest breaks were observed at the middle toward the anode side. Different breaking positions were reported in literature. In the study conducted by Koslova *et al.*[30], a Ni nanowire began to form voids and break in the middle toward the anode end. However, in another study conducted by Koslova *et al.*[31], the breaking of an Au nanowire occurred near the cathode side. Moreover, in the studies conducted by Jeong *et al.*[32] and Stahlmeck *et al.* [33], void formations toward the cathode were also observed. However, regarding the breaking positions in the SWEAT structure, most studies only reported observations. There are no precise explanations regarding the breaking positions. The relationship between the direction of the current density and breaking positions was rarely reported. To resolve this issue, our simulation, discussed in Section 6.4, provides explanations.

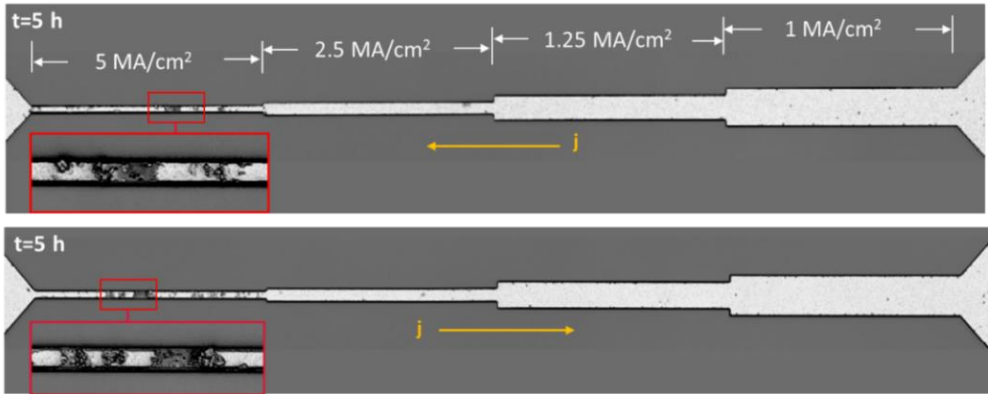


Figure 6.5. Electromigration failures in the tapered SWEAT structure at 250 °C under current densities with opposite directions.

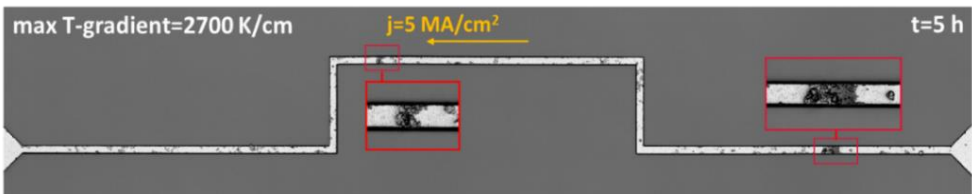


Figure 6.6. Electromigration failures in the 2D SWEAT structure at 250 °C under a current density of 5 MA/cm².

6.4. Numerical Solutions

6.4.1. Governing Equation

In our model, the narrow line was simplified as a 1D metal line with different diffusion boundary conditions, as illustrated in Figure 6.7. In the Blech structure, both ends were perfectly blocked, i.e. $J_a(0) = J_a(L) = 0$. In the SWEAT structure, the atomic concentrations at both ends were constant, i.e. $C_a(0) = C_a(L) = C_{a0}$. Apart from the above conditions, the following assumptions were made.

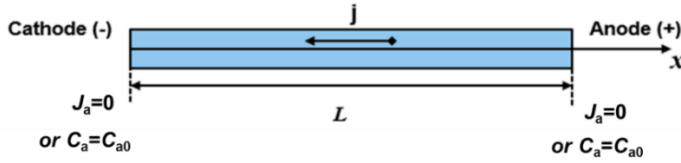


Figure 6.7. Schematic diagram of a 1D metal line.

- The big pads at both ends played the role of a heat sink; thus, the temperature at both ends of the conductor was assumed to be equal to the environment temperature,

$$T(0) = T(L) = T_0$$

- The thermal conductivity is composite of the conductor and the dielectric as follows: $k_T = k_m + (H_d/H_m)k_d$, where k_m and k_d are the thermal conductivities of the Al stripe and the substrate, respectively. H_m and H_d are the thicknesses of the substrate and the Al stripe, respectively. K_T is the effective thermal conductivity of the system.
- In Chapter 5, we had shown that the electromigration in the bare stripes could be accurately simulated using a 1D model with a stress-free condition. In this study, we also assumed the conductor without passivation to be a stress-free metal line. Thus,

$$\sigma_x = \sigma_y = \sigma_z = \sigma_{xy} = \sigma_{yz} = \sigma_{xz} = 0$$

With the above assumptions and conditions, we could obtain the governing equation in terms of the atomic concentration C_a . Additionally, an equation for the temperature distribution along the metal line was also obtained.

$$\begin{aligned} \frac{1 - f(C_a/C_{a0})}{C_a} \frac{\partial C_a}{\partial t} \\ = D_a \left[-\frac{Z^* e \rho j}{k_B T} \frac{\partial C_a}{\partial x} + \frac{\partial^2 C_a}{\partial x^2} - \frac{Q^*}{k_B T^2} \frac{j^2 \rho}{k_T} C_a + \frac{Q^*}{k_B T^2} \left(-\frac{j^2 \rho}{k_T} x \right. \right. \\ \left. \left. + \frac{j^2 \rho L}{2k_T} \right) \frac{\partial C_a}{\partial x} \right] \end{aligned} \quad (5.1)$$

$$T = -\frac{j^2 \rho}{2k_T} x^2 + \frac{j^2 \rho L}{2k_T} x + T_0 \quad (5.2)$$

The diffusion boundary conditions were as follows:

- Blech structure:

$$J_a(0, t) = D_a \left[\frac{\partial C_a(0, t)}{\partial x} - \frac{C_a(0, t) Z^* e \rho j}{k_B T} + \frac{Q^*}{k_B T^2} \frac{\partial T(0, t) C_a(0, t)}{\partial x} \right] = 0 \quad (5.3)$$

$$J_a(L, t) = D_a \left[\frac{\partial C_a(L, t)}{\partial x} - \frac{C_a(L, t) Z^* e \rho j}{k_B T} + \frac{Q^*}{k_B T^2} \frac{\partial T(L, t) C_a(L, t)}{\partial x} \right] = 0 \quad (5.4)$$

- SWEAT structure:

$$C_a(0, t) = C_a(L, t) = C_{a0} \quad (5.5)$$

The initial condition was

$$C_a(x, 0) = C_{a0} \quad (5.6)$$

6.4.2. Numerical Results

The parameters used in our calculations are listed in Table 6.1.

Table 6.1. Parameters used in the calculations.

Material properties	Value
Environment temperature (T_0)	250 °C
Atomic diffusivity (D_a)	$5.01 \times 10^{-9} \exp(-1.21 \text{ eV}/kT) \text{ m}^2/\text{s}$
Atomic volume (Ω)	$1.66 \times 10^{-29} \text{ m}^3$ [34]
Electrical resistivity (ρ)	$2.88 \times 10^{-8} \text{ Ohm}\cdot\text{m}$ [35]
Electrical charge (e)	$1.6 \times 10^{-19} \text{ C}$ [36]
Charge number (Z^*)	1 [17]

Heat of transport (Q^*)	0.3 eV
Boltzmann constant (k)	1.38×10^{-23} J/K
Vacancy volume relaxation factor of Al (f)	Eq. (4.8) in Chapter 4
Thermal conductivity of Al (k_m)	$239 \text{ W} \cdot \text{m}^{-1} \cdot \text{K}^{-1}$ [35]
Thermal conductivity of Si (k_d)	$38 \text{ W} \cdot \text{m}^{-1} \cdot \text{K}^{-1}$ [37]
Thickness of Al conductor (H_d)	200 nm
Thickness of Si substrate (H_d)	400 μm

6.4.2.1. Temperature Profile

Figure 6.8 plots the temperature and the temperature gradient along the 800 μm conductor with a current density of 5 MA/cm². The temperature was at its maximum at the centre of the conductor, and decreased when moving from the centre to either end. The maximum temperature gradient was observed at both the ends but in opposite directions to each other. This implies that the flux due to temperature gradients at both ends had opposite directions, and it was zero at the centre. According to Eqs. (5.7) and (5.8), the maximum temperature is proportional to the square of the product of the current density and the conductor length ($j^2 L^2$). Moreover, the maximum temperature gradient increased with the conductor length (L) and the square of the current density (j^2).

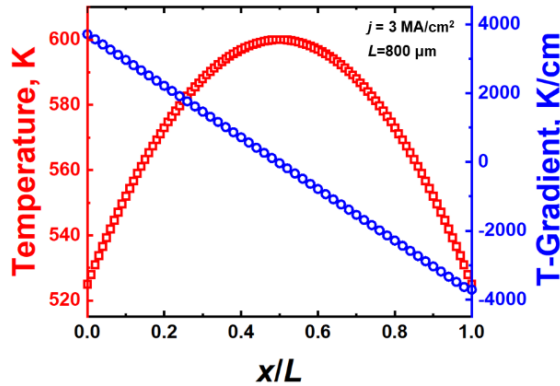


Figure 6.8. Profiles of the temperature and the temperature gradient along the 800 μm conductor under a current density of 5 MA/cm² at 250 °C.

$$T_{max} = T\left(\frac{L}{2}\right) = \frac{j^2 \rho L^2}{8k_T} + T_0 \quad (5.7)$$

$$\left. \frac{dT}{dx} \right|_{max} = \frac{dT(0)}{dx} = -\frac{dT(L)}{dx} = \frac{j^2 \rho L}{2k_T} \quad (5.8)$$

In Figure 6.9 (a), the maximum temperature and the maximum temperature gradient exponentially increase with the current density in the 800 μm conductor. On increasing the current density from 1 MA/cm^2 to 5 MA/cm^2 , the maximum temperature increased from 226 $^\circ\text{C}$ to 600 $^\circ\text{C}$, and the maximum temperature gradient increased from 100 K/cm to 400 K/cm . In Figure 6.9 (b), under 3 MA/cm^2 , the maximum temperature increases squarely with the conductor length, and the maximum temperature gradient increases linearly with the length. Therefore, increasing the current density and the conductor length could significantly induce a high temperature and a temperature gradient in the conductor, and the current density was a more important factor.

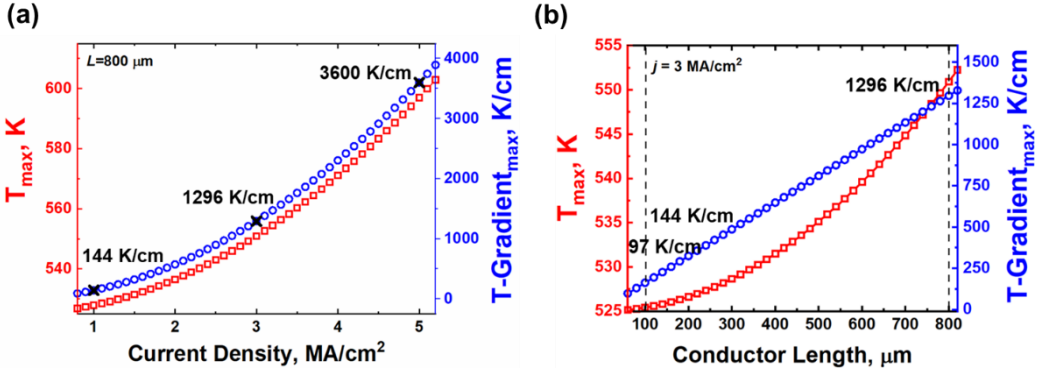


Figure 6.9. (a) Maximum temperature and temperature gradient for an 800 μm conductor with current density increasing from 1 MA/cm^2 to 5 MA/cm^2 . (b) Maximum temperature and temperature gradient for a conductor with its length increasing from 60 μm to 800 μm under 3 MA/cm^2 .

6.4.2.2. Blech Structure

Effect of the Magnitude of Current Density

Figure 6.10 plots the simulation results of the atomic concentration along the 800 μm Blech structure under 1 MA/cm^2 with and without considering thermomigration, in which $C_a=0.963 C_{a0}$ is the critical concentration for void formation and $C_a=1.037 C_{a0}$ is the critical concentration for hillock formation. At the early stage (see Figure 6.10(a)), atomic concentration at cathode reaches critical condition for void formation, and the difference between results with and without considering thermomigration is slight. At the late stage (see Figure 6.10(b)), although the atomic concentration with thermomigration decreases at the

middle region, the atomic concentration is still well above the critical condition for void formation. No failure in the middle region was indicated from the atomic concentration, which was consistent with the experimental observations. These results also demonstrated that all the modeling results in Chapter 5, without considering thermomigration, are valid.

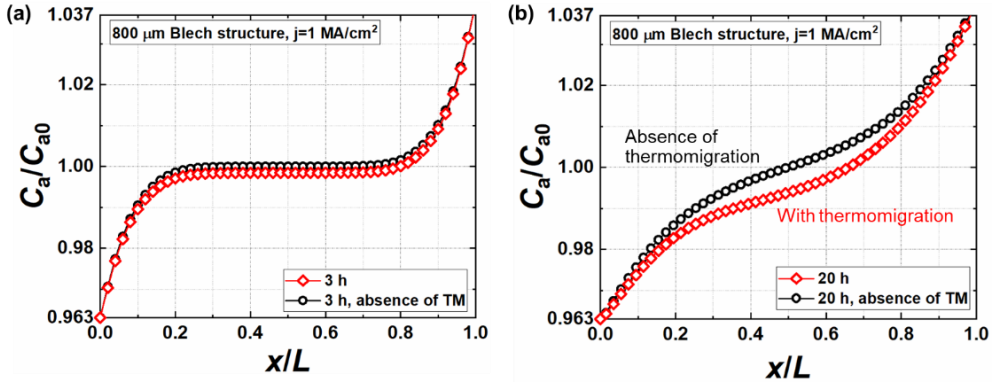


Figure 6.10. Simulation results for the atomic concentration distribution along the 800 μm Blech structure under a current density of 1 MA/cm^2 with and without considering thermomigration at 3 h (a) and 20 h (b).

With increasing current density, Figure 6.11 (a) and (b) shows the distributions of atomic concentrations along the 800 μm Blech structure under 3 MA/cm^2 at 3 h and 15 h, respectively. At the early stage, e.g., $t=3$ h, atomic concentration at both ends first reaches the critical condition for failure. With the consideration of thermomigration, there is an obvious decrease of atomic concentration at middle region, compared to that without considering thermomigration. At the late stage, e.g., $t=15$ h, considering thermomigration produced significantly different results, with C_a/C_{a0} at middle region decreases to the critical value. Electromigration failure is predicted not only at the two ends, but also in the middle region. Moreover, it can be seen that the void formation at the middle region takes longer time, compared to that at both ends. These simulation results were in remarkable agreement with the experimental observations. The main factor causing void formation in the middle region of the Blech structure is thermomigration.

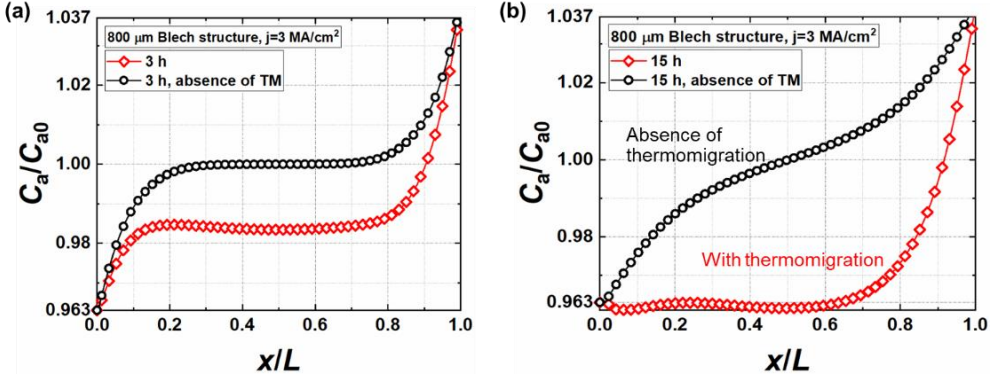


Figure 6.11. Simulation results for the atomic concentration distribution along the 800 μm Blech structure under a current density of 3 MA/cm^2 with and without considering thermomigration at 3 h (a) and 15 h (b).

With further increasing current density, Figure 6.12 plots the numerical results of atomic concentration along the 800 μm Blech structure under 5 MA/cm^2 . Atomic concentration at both ends attains the critical value at an early stage (1 h), but the decreased atomic concentration at the middle region with the consideration of thermomigration is still higher than the critical value. No failure in the middle region was indicated at 1 h. With a longer time, the lowest C_a decreased to the critical value at 3 h, indicating a breaking of conductor. The predicted breaking time (~ 3 h) and position agree well with experimental data.

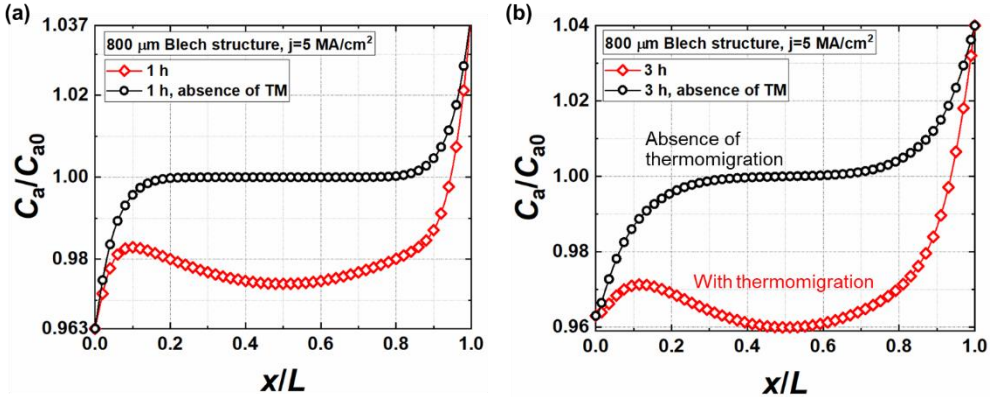


Figure 6.12. Simulation results for the atomic concentration distribution along the 800 μm Blech structure under a current density of 5 MA/cm^2 with and without considering thermomigration at 1 h (a) and 3 h (b).

Effect of Conductor Length

Figure 6.9 (a) has shown that the maximum temperature gradient increases linearly with the conductor length. With $j = 3 \text{ MA/cm}^2$, $L = 60, 100$, and $800 \text{ }\mu\text{m}$, the maximum temperature could increase from 97 K/cm to 1294 K/cm . Here, Figure 6.13 shows the evolutions over time of the atomic concentration at the middle region of conductors ($x = L/2$) with different lengths. With $L = 60$ and $100 \text{ }\mu\text{m}$, the predicted C_a at $x = 0.5 L$ is still well above the critical value, even at 20 h , indicating no void formation. This is consistent with experimental observations. With $L = 800 \text{ }\mu\text{m}$, C_a/C_{a0} at $x = 0.5 L$ decreases gradually below $C_{a,\text{critical}}$ at $\sim 18 \text{ h}$, indicating the void formation. The predicted results agree with experimental data.

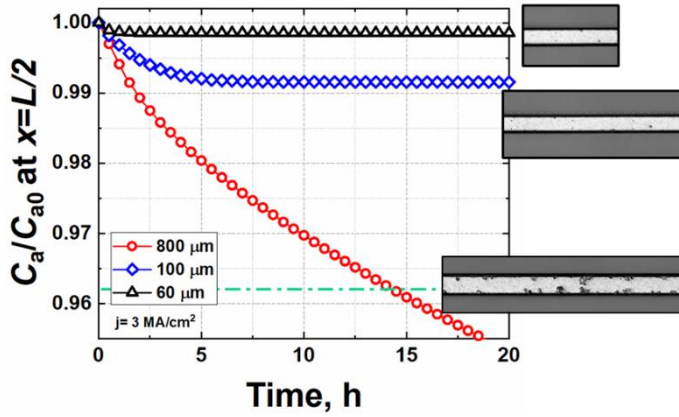


Figure 6.13. Evolution of the atomic concentration at the centre of Blech structure with different lengths.

6.4.2.3. SWEAT Structure

Figure 6.14 shows the simulation results of the atomic concentration along an $800 \text{ }\mu\text{m}$ SWEAT structure. Under current density of 1 MA/cm^2 at 20 h , C_a/C_{a0} along conductor is still well above $C_{a,\text{critical}}$, thus no EM failures are indicated. This is consistent with the experimental observation shown in left figure. Under increased current density, 3 MA/cm^2 , at 5 h , C_a/C_{a0} decreases from both ends to the middle region, and the distribution of the atomic concentration was flat but higher than the threshold condition of void formation. This indicates a tendency of voids spreading in the conductor. At 20 h , the C_a/C_{a0} at the middle region ($x = 0.3\text{--}0.9L$) decreases below the critical concentration. And, the lowest C_a/C_{a0} is off center toward right, indicating an earliest breaking position of conductor. These simulation results agree well with our experimental observations.

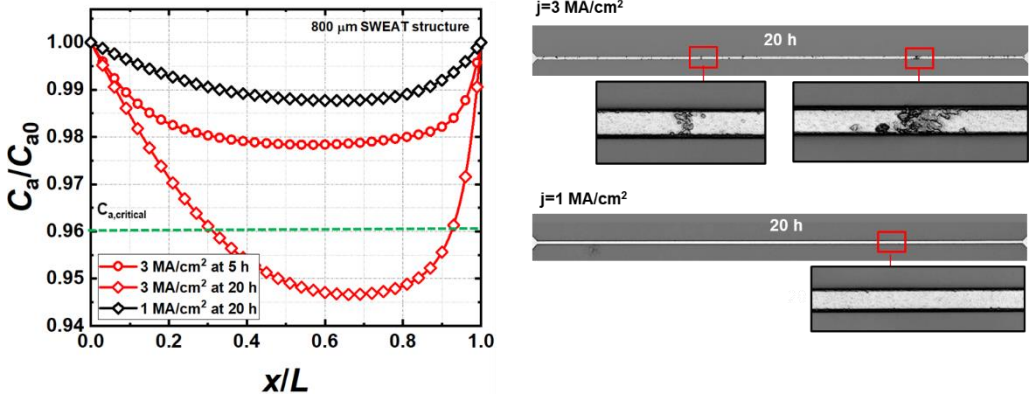


Figure 6.14. Atomic concentration distribution along the 800 μm SWEAT structure under a current density of 3 MA/cm² at 5 and 20 h, compared with the atomic concentration under a current density of 1 MA/cm² at 20 h.

Breaking Positions

As illustrated in Figure 6.15 (a), there are three fluxes in the SWEAT structure. Driven by the electron wind, atoms would diffuse from the cathode to the anode. Moreover, the maximum temperature gradient was observed at both sides, and these gradients were in opposite directions. Thus, the flux due to the temperature gradient could reduce electromigration in the left half; however, it could promote the flux of electromigration in the right half. Furthermore, the self-diffusion could promote electromigration in the left half but reduce it in the right half. The combination of the fluxes induced by electric, temperature and concentration gradients would cause a higher atomic flux at the anode than at the cathode, as plotted in Figure 6.15 (b). This indicated that there were more flux out atoms at the anode than flux-in atoms at the cathode, causing a net reduction of atoms in the conductor. Consequently, the divergence decreased when moving from either side and reached a minimum toward the right of the middle region. This indicated that toward the right of the centre was the location with the fastest rate of reduction in atoms.

Figure 6.16 shows the simulation results of atomic concentration with opposite flowing direction of current. When the current flow from the right to the left, C_a at the middle toward right first reaches the critical concentration ($C_{a,critical}$), indicating a breaking of conductor. However, when the current flow from the left to the right, C_a at the middle toward right first reaches the critical concentration. This indicates that the breaking position of conductor changes from centre toward right to centre toward left. Those simulation results agree well with the experimental observations.

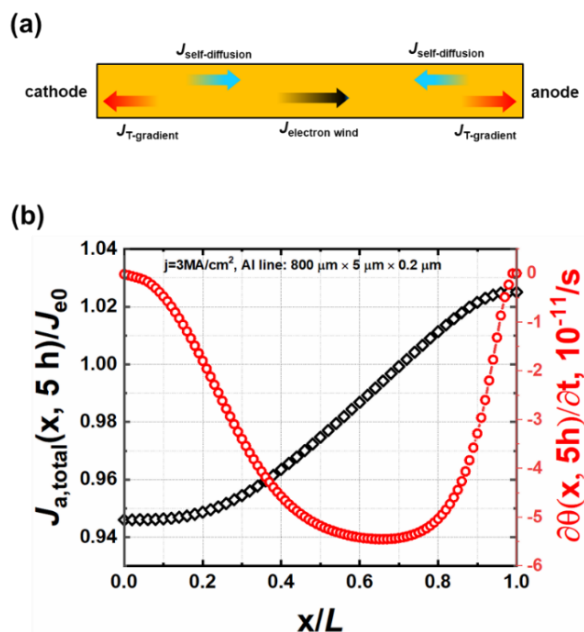


Figure 6.15. (a) Distribution of normalised fluxes of electromigration, self-diffusion and thermomigration at 5 h for the 800 μm SWEAT structure under a 3 MA/cm² current density. (b) Illustration of the directions of the atomic fluxes.

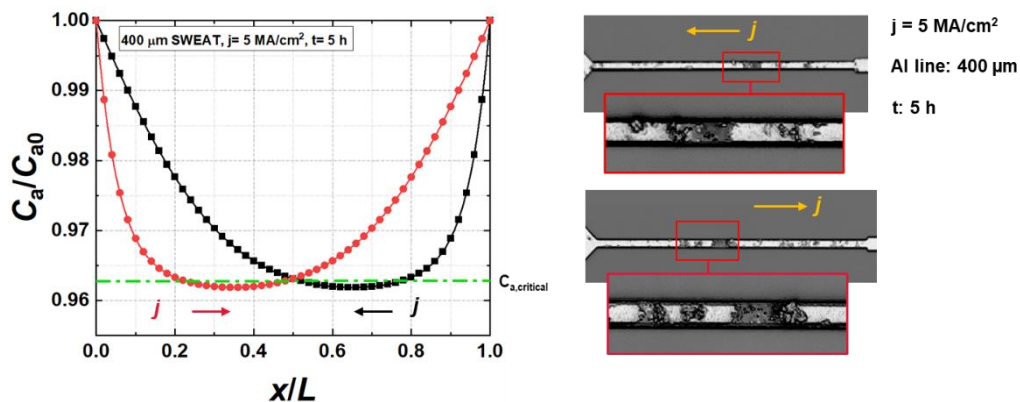


Figure 6.16. Atomic concentration distribution along the 400 μm tapered SWEAT structure under the current density of 5 MA/cm² with different flow direction at 5 h, compared with the experimental results.

Resistance Change in the SWEAT Structure

Electrical resistances in the SWEAT structures under different current densities were measured in-situ, as depicted using solid lines in Figure 6.17. The resistance changed slightly

in the conductor under a current density of 1 MA/cm², indicating a very weak electromigration. With increasing current density, the resistance experienced two stages in the conductor under 3 MA/cm². From 0 to 16 h, the resistance continually increased. Following which, the resistance rapidly increased, exhibiting a nearly vertical growth. According to experimental observations, this turning point indicated the breaking of the conductor. In the conductor under a 5 MA/cm² current density, the resistance experienced two stages with a faster increasing rate and an earlier turning point for the breaking of the conductor.

Additionally, based on our numerical solutions, we could predict the resistance change during electromigration. We assumed the following relationship between the electrical resistivity and atomic concentration.

$$\rho = \rho_0 \frac{C_{a0}}{C_a} \quad (5.9)$$

where ρ is the resistivity of Al and ρ_0 is the initial resistivity. Thus, the initial resistance of the Al conductor was

$$R_0 = \rho_0 AL, \quad (5.10)$$

where A and L are the cross-section area and length of the conductor, respectively. During electromigration, the resistance due to atomic concentration variation was

$$R(t) = \rho_0 A \int_0^L \frac{C_{a0}}{C_a(x, t)} dx \quad (5.11)$$

Thus, the normalised change in resistance could be obtained as follows:

$$\frac{R(t) - R_0}{R_0} = \frac{1}{L} \int_0^L \frac{C_{a0}}{C_a(x, t)} dx - 1 \quad (5.12)$$

where the atomic concentration $C_a(x, t)$ was determined from our numerical solutions. In Figure 6.17, the symbols represent the simulation results for the normalised changes in resistance under different current densities before reaching the critical condition for breaking.

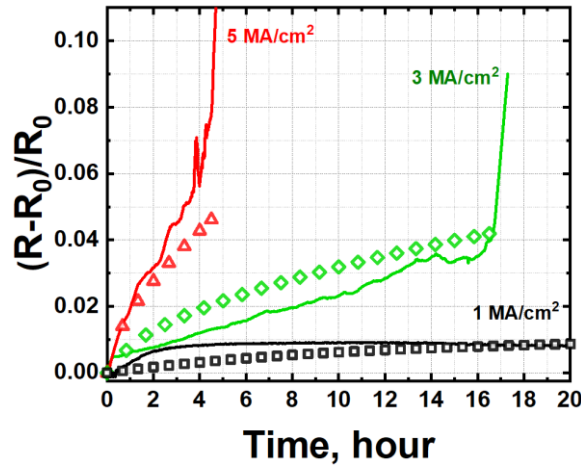


Figure 6.17. Comparison between the resistance changes in the simulation and experiment for the 800 μm SWEAT structures under different current densities. The solid lines represent in-situ resistance measurement results, and the symbols represent the simulation results

6.4.2.4. Blech vs. SWEAT Structure

With the same conductor length ($L=800 \mu\text{m}$) and under the same current density ($j=3 \text{ MA/cm}^2$), Figure 6.18 plots the distribution of atomic concentration in Blech and SWEAT structure. At an early stage (3 h), in Blech structure, void/hillock formation at both ends occurs, and the spreading of voids in the middle of conductor is indicated (see Figure 6.18 (a)). At the same stage (3 h), spreading of voids is also indicated in SWEAT structure, but there is no failure at both ends of SWEAT structure. Moreover, the decrease of concentration at the middle region of Blech and SWEAT structures is similar.

At a significantly delayed time (15 h), at the middle region, atomic concentration in both Blech and SWEAT structure decreases to the critical value, indicating the breaking of conductor. Moreover, Figure 6.18 (b) shows that there is no concentration variation in SWEAT structure without considering the thermomigration, and there is no concentration variation at the middle of Blech structure in the absence of thermomigration. Such a difference before and after considering thermomigration shows that the concentration decreases at the middle of Blech and SWEAT structure is due to the thermomigration.

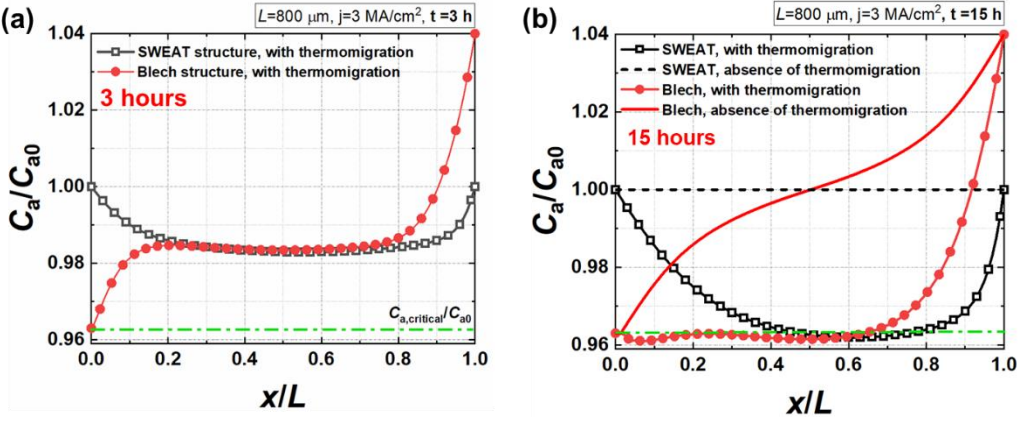


Figure 6.18. Comparison between the simulation results for Blech and SWEAT structure.

6.5. Molecular Dynamic Simulation of Thermomigration

To obtain a more fundamental understanding of the atomic motion during the thermomigration process, direct MD simulations with a temperature gradient were performed (Figure 6.19). The simulation method is discussed in Appendix D. Figure 6.19 (a) shows the dimensions of the MD model. A 20 nm narrow nanowire connected the two large pads at both ends. Figure 6.19 (b) shows the thermomigration of Al atoms. The temperatures at the bottom and top were 900 K and 300 K, respectively. Thus, the magnitude of the temperature gradient in the nanowire was 30 K/nm. From 0 ns to 5 ns, Al atoms tended to diffuse from the hot region to the cold region. Additionally, the enlarged image of the trajectory line shows that the direction of atomic motion was from the bottom to the top. This diffusion direction of thermomigration in Al was consistent with our experiments. Figure 6.19 (c) shows the thermomigration of Sn atoms, where the temperature gradient was 15 K/nm in the nanowire. Based on the displacement contour diagram, most of the Sn atoms in the nanowire moved from the cold region to the hot region. This can be confirmed by the enlarged figure of the trajectory lines. These MD results showed that the Sn atoms tended to diffuse more rapidly from the cold region to the hot region. This diffusion direction of thermomigration in Sn was consistent with the experimental observations in literature [5, 38].

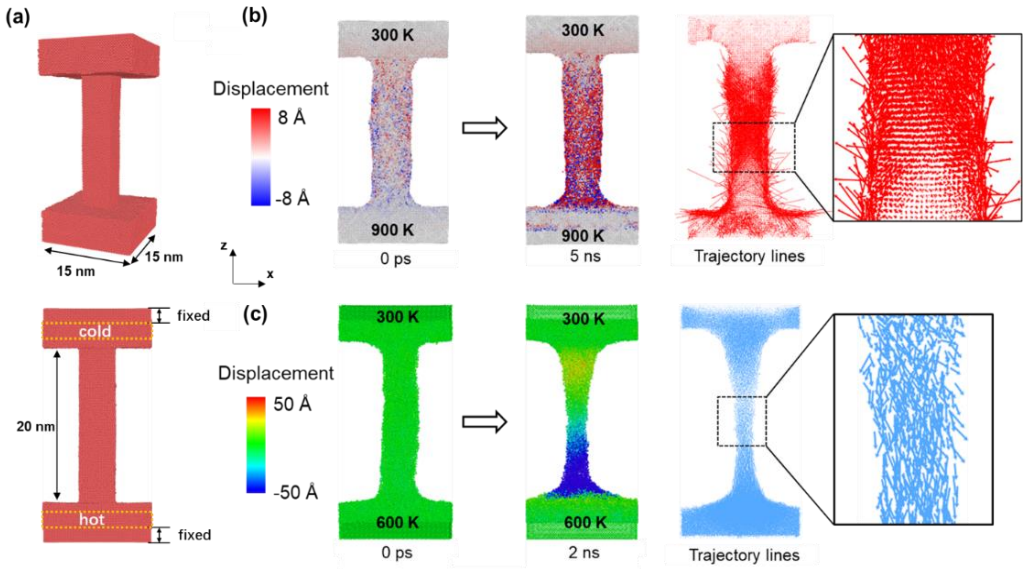


Figure 6.19. Molecular dynamic (MD) simulation results for the motions of Al and Sn atoms under a temperature gradient.

6.6. Conclusions

In this chapter, the effects of thermomigration on electromigration were systematically investigated through experiments and simulations.

During experiments on the Blech structure, we observed electromigration failures spreading in the middle region of the conductor with extended testing durations and increasing current densities. In the SWEAT structure, voids were also observed over a wide range spanning the entire conductor, and the metal line broke off centre toward the anode side. Unlike the early void formation at the cathode in the Blech structure, void formations in the middle regions of the Blech and SWEAT structures required significantly longer times. Moreover, using different SWEAT structures, it was discovered that the breaking position of the conductor is related to the direction of the current flow.

In the simulation, using the simplified 1D model of the Blech and SWEAT structures, our numerical results showed that thermomigration was the primary cause for void formation in the middle region. Moreover, the effects of the magnitude of the current density and the conductor length on the failure of the conductor were revealed. Furthermore, the analysis of

the fluxes in the SWEAT structure indicated that thermomigration would promote electromigration at the anode and reduce it at the cathode and the centre. Thus, the maximum net loss of material must occur in the region between the centre and the anode, causing the breaking of the conductor off centre toward the anode side. Additionally, the predicted resistance change based on numerical solutions was in excellent agreement with the experimental results. It can be concluded that the third objective listed in Section 1.3 in Chapter 1 was achieved.

References

1. Jonggook, K., V. Tyree, and C. Crowell. *Temperature gradient effects in electromigration using an extended transition probability model and temperature gradient free tests. I. Transition probability model*. in *1999 IEEE International Integrated Reliability Workshop Final Report (Cat. No. 99TH8460)*. 1999. IEEE.
2. d'Heurle, F.M., *Electromigration and failure in electronics: An introduction*. Proceedings of the IEEE, 1971. **59**(10): p. 1409-1418.
3. Dalleau, D., *3-D time-depending simulation of void formation in metallization structures*. 2003, Hannover: Universität.
4. Chen, H.-Y., C. Chen, and K.-N. Tu, *Failure induced by thermomigration of interstitial Cu in Pb-free flip chip solder joints*. Applied Physics Letters, 2008. **93**(12): p. 122103.
5. Ouyang, F.-Y. and C.-L. Kao, *In situ observation of thermomigration of Sn atoms to the hot end of 96.5 Sn-3Ag-0.5 Cu flip chip solder joints*. Journal of Applied Physics, 2011. **110**(12): p. 123525.
6. Zhang, P., S. Xue, and J. Wang, *New challenges of miniaturization of electronic devices: Electromigration and thermomigration in lead-free solder joints*. Materials and Design, 2020: p. 108726.
7. Wang, S., et al. *Solder joint reliability under electromigration and thermal-mechanical load*. in *2007 Proceedings 57th Electronic Components and Technology Conference*. 2007. IEEE.
8. Ye, H., C. Basaran, and D. Hopkins, *Thermomigration in Pb–Sn solder joints under joule heating during electric current stressing*. Applied Physics Letters, 2003. **82**(7): p. 1045-1047.
9. Huang, A.T., et al., *Thermomigration in SnPb composite flip chip solder joints*. Applied Physics Letters, 2006. **88**(14): p. 141911.

10. Chen, C., et al., *Thermomigration in solder joints*. Materials Science Engineering: R: Reports, 2012. **73**(9-10): p. 85-100.
11. Tu, K.-N., Y. Liu, and M. Li, *Effect of Joule heating and current crowding on electromigration in mobile technology*. Applied Physics Reviews, 2017. **4**(1): p. 011101.
12. Gu, X., et al., *Thermomigration and electromigration in Sn8Zn3Bi solder joints*. Journal of Materials Science: Materials in Electronics, 2011. **22**(3): p. 217-222.
13. Basaran, C. and M. Lin, *Damage mechanics of electromigration induced failure*. Mechanics of Materials, 2008. **40**(1-2): p. 66-79.
14. Liu, Y., et al., *Prediction of electromigration induced voids and time to failure for solder joint of a wafer level chip scale package*. 2010. **33**(3): p. 544-552.
15. Sukharev, V. and E. Zschech, *A model for electromigration-induced degradation mechanisms in dual-inlaid copper interconnects: Effect of interface bonding strength*. Journal of Applied Physics, 2004. **96**(11): p. 6337-6343.
16. Sukharev, V., E. Zschech, and W.D. Nix, *A model for electromigration-induced degradation mechanisms in dual-inlaid copper interconnects: Effect of microstructure*. Journal of Applied Physics, 2007. **102**(5): p. 053505.
17. Blech, I.A., *Electromigration in thin aluminum films on titanium nitride*. Journal of applied physics, 1976. **47**(4): p. 1203-1208.
18. Blech, I. and E. Kinsbron, *Electromigration in thin gold films on molybdenum surfaces*. Thin Solid Films, 1975. **25**(2): p. 327-334.
19. Blech, I. and K. Tai, *Measurement of stress gradients generated by electromigration*. Applied Physics Letters, 1977. **30**(8): p. 387-389.
20. Blech, I. and C. Herring, *Stress generation by electromigration*. Applied Physics Letters, 1976. **29**(3): p. 131-133.
21. Hu, C.K., M. Small, and P. Ho, *Electromigration in Al (Cu) two - level structures: Effect of Cu and kinetics of damage formation*. Journal of applied physics, 1993. **74**(2): p. 969-978.
22. Lee, K., C. Hu, and K.-N. Tu, *In situ scanning electron microscope comparison studies on electromigration of Cu and Cu (Sn) alloys for advanced chip interconnects*. Journal of applied physics, 1995. **78**(7): p. 4428-4437.
23. Somaiah, N. and P. Kumar, *Inverse Blech Length Phenomenon in Thin-Film Stripes*. Physical Review Applied, 2018. **10**(5): p. 054052.
24. Lloyd, J., *Electromigration in Al-Cu thin films with polyimide passivation*. Thin Solid Films, 1982. **91**(2): p. 175-182.

25. Giroux, F., et al. *Current and temperature distribution impact on electromigration failure location in SWEAT structure*. in *Proceedings of 1994 IEEE International Conference on Microelectronic Test Structures*. 1994. IEEE.
26. Giroux, F., et al. *Wafer-level electromigration tests on NIST and SWEAT structures*. in *Proceedings International Conference on Microelectronic Test Structures*. 1995. IEEE.
27. Lee, T.C., et al. *Comparison of isothermal, constant current and SWEAT wafer level EM testing methods*. in *2001 IEEE International Reliability Physics Symposium Proceedings. 39th Annual (Cat. No. 00CH37167)*. 2001. IEEE.
28. Pierce, D. and P. Brusius, *Electromigration: A review*. Microelectronics Reliability, 1997. **37**(7): p. 1053-1072.
29. Tan, C.M. and A. Roy, *Electromigration in ULSI interconnects*. Materials Science and Engineering: R: Reports, 2007. **58**(1-2): p. 1-75.
30. Kozlova, T. and H.W. Zandbergen. *In situ TEM observation of electromigration in Ni nanobridges*. in *European Microscopy Congress 2016: Proceedings*. 2016. Wiley Online Library.
31. Kozlova, T., *In situ transmission electron microscopy investigations of electromigration in metals*. Doctor thesis, 2015.
32. Jeong, W., et al., *Characterization of nanoscale temperature fields during electromigration of nanowires*. Scientific reports, 2014. **4**(1): p. 1-6.
33. Stahlmecke, B. and G. Dumpich, *Resistance behaviour and morphological changes during electromigration in gold wires*. Journal of Physics: Condensed Matter, 2007. **19**(4): p. 046210.
34. Cui, Z., X. Fan, and G. Zhang, *Molecular dynamic study for concentration-dependent volume relaxation of vacancy*. Microelectronics Reliability, 2021. **120**: p. 114127.
35. Serway, R.A., *Principles of Physics . Fort Worth*. 1998, London: Saunders College Pub: Texas.
36. Cui, Z., X. Fan, and G. Zhang, *General coupling model for electromigration and one-dimensional numerical solutions*. Journal of Applied Physics, 2019. **125**(10): p. 105101.
37. Liu, W. and M. Asheghi, *Thermal conductivity measurements of ultra-thin single crystal silicon layers*. Journal of Heat Transfer, 2006.
38. Zhong, Y., et al., *Coupling effect of thermomigration and cross-interaction on evolution of intermetallic compounds in Cu/Sn/Ni ultrafine interconnects*

undergoing TLP bonding. Journal of Materials Research, 2017. **32**(16): p. 3128-3136.

7

7

IMPLEMENTATION OF THE GENERAL COUPLING MODEL IN ANSYS AND COMSOL

In this chapter, the general coupling model of electromigration is implemented in ANSYS and COMSOL. For implementation in ANSYS, we first identified several errors provided in the ANSYS manual for electromigration modelling. Subsequently, based on the ANSYS build-in multi-physics theory, the implementation method for the general coupling model was presented. We then illustrated the implementation procedures in COMSOL via the weak form PED modulus. The details of the weak expression of the general coupling model and the variable definition required in COMSOL are presented. Lastly, a 1D metal line with a totally fixed and stress-free configuration was provided as benchmark problems, where the finite element solutions from ANSYS and COMSOL were in excellent agreement with the analytical solutions determined in Chapter 3

Parts of this Chapter have been published in IEEE 70th Electronic Components and Technology Conference (ECTC), 2020. [1]

7.1. Introduction

Accurate numerical models of electromigration can complement laboratory testing by predicting the reliability of interconnects in terms of their times-to-failure (TTFs). Although 1D analytical and numerical solutions of vacancy and stress evolution have been used to predict the TTFs of confined Al lines, simulating the damage caused by electromigration in more complex interconnects would require a 3D numerical model. The finite element (FE) method is a natural choice for such models because it can easily handle arbitrary 3D geometries, multiple physics and various loads and boundary conditions.[1]

The FE method has already been applied in the study of electromigration. Sarychev *et al.* [2] proposed a physical model to couple the stress evolution with the vacancy transport, and a sophisticated constitutive model was established. Subsequently, Lin and Basaran [3, 4] implemented this model in a general FE procedure and studied the electromigration in a pure metal line and solder joint. Moreover, Sukharev *et al.* [5, 6] developed a multi-physics model and implemented it in a general commercial FE software. In general, the FE simulations of electromigration in through silicon vias (TSVs) [7], copper dual-damascene structures [8] and SWEAT structures [9] were conducted in different studies. However, none of above-mentioned studies succeed in coupling all important influential factors in electromigration. In Chapter 3, we had developed a fully coupled 3D general coupling model for electromigration, in which all the important physical fields and their effects on electromigration were considered and fully coupled. 1D numerical results were presented and compared to the experimental results and the ones in literature [10].

In this chapter, the general coupling model of electromigration is implemented in ANSYS and COMSOL. We first reviewed the current practice of electromigration modelling in ANSYS, including the tested case studies provided in the ANSYS verification manual, the ANSYS online manual and the paper published by ANSYS. We then presented a method to implement the general coupling model using the current capability of ANSYS multi-physics modelling based on a few approximations. Subsequently, the implementation procedures of the general coupling model in COMSOL via the weak form PED module were presented. Lastly, the 1D metal line with a totally fixed and stress-free configuration was provided as benchmark problems to validate the implementation in ANSYS and COMSOL.

7.2. Implementation of the General Coupling Model in ANSYS

7.2.1. Current Practice of Electromigration Modelling in ANSYS

7.2.1.1. Study Case in the ANSYS Verification Manual

In the test case (VM220) discussed in the ANSYS verification manual, the diffusion and mass transport due to electromigration was presented using a constant current loading on a rectangular conductor with length L and height H . At one end of the conductor ($x = -L$), a constant vacancy concentration was set as the boundary condition. At the other end of the conductor ($x = 0$), a zero-flux boundary condition (blocking diffusion barrier) was applied. To solve this electromigration problem, two approaches are provided. The first approach considered electromigration as a simple diffusion problem, using the diffusion element (PLANE238) and applying the electron wind force as a body load of transport velocity. The second approach used a coupled electric-diffusion element (PLANE223) with KEYOPT(1) = 100001. In both cases, the effects of mechanical stress and temperature gradient were neglected and the sink/source term was set as '0'. Consequently, the two approaches provided the same but incorrect results. As a matter of fact, it has been long recognized that without considering the sink/source term and the effect of stress migration, the time to reach the steady state for electromigration was only ~ 1 s. This is not supported by any experimental data, implying that the tested case VM220 selected an incorrect electromigration model for the verification study.

7.2.1.1. Study Case in the ANSYS Online Manual

In the ANSYS Mechanical APDL 19.1 online manual, two additional examples of electromigration modelling are demonstrated in the 'Coupled-Field Analysis Guide'. This was to show its capability to simultaneously model electromigration, stress-migration and thermomigration induced by current loading as well as mechanical and thermal stresses.

Example 1: Transient stress build-up due to electromigration. (https://ansyshelp.ansys.com/account/secured?returnurl=/Views/Secured/corp/v191/ans_cou/coupsthdldiff.html).

In this example, a constant current loading was applied to a metal line with blocking diffusion conditions at both ends. The temperature of the conductor remained constant. The coupled field element SOLID226 with KEYOPT(1) = 100111 was selected to simultaneously consider the electrical, structural, thermal and diffusion fields. However, there were several errors in this example.

1. The sink/source term was set as '0' in the vacancy transport equation. The study conducted by Shatzkes and Lloyd has shown that the absence of a sink/source term can cause the predicted lifetime of electromigration to have a very short time scale. To prevent this issue, this example incorrectly adjusted the diffusivity to 10% of its normal value. Consequently, the velocity of vacancy migration was decreased and the time to reach the steady state of electromigration was extended. However, for the steady-state results, the obtained maximum hydrostatic stress was only ~ 8 MPa, which was too small to compare with any numerical results published in literature.
2. The values of the vacancy relaxation factor and the coefficient of diffusion strain shown in the APDL file were provided without any basis or literature support. This example attempted to obtain the 'reasonable' numerical results by manipulating a few material properties that did not exist.
3. The mechanical boundary condition shown in APDL file was set as fully fixed at each node in the metal line.

d, all, ux, 0

d, all, uy, 0

d, all, uz, 0

This is not a correct boundary condition setting. It read that each point anywhere is fixed during electromigration. When the electrical current passed through the metal line, the electron wind force caused atomic transport along the electron direction. This could induce displacement along the length of the line.

Example 2: Electromigration and stress-migration in a solder joint.

[https://ansyshelp.ansys.com/account/secured?returnurl=/Views/Secured/corp/v191/ans_cou/coupstelecdiff.html?q=migration model](https://ansyshelp.ansys.com/account/secured?returnurl=/Views/Secured/corp/v191/ans_cou/coupstelecdiff.html?q=migration%20model)).

In this example, a half symmetry model of an SnAgCu (SAC) solder joint sandwiched between two copper plates was studied. The model was meshed with the SOLID227 coupled-field element with KEYOPT(1) = 100101. A constant current load passed through the solder from the bottom plate to the top plate. A uniform temperature of 200 °C was set in the solder ball. Although this example provided a complete process in modelling electromigration in a solder, three errors previously mentioned in Example 1 are also presented here.

7.2.1.3. Electromigration Modelling using ANSYS by [11]

The developers at ANSYS published a paper [11] for electromigration modelling, which provides additional information of the theory in ANSYS using R18.1. For electromigration, the total atomic flux was written as follows:

$$J_v = -D_v \nabla \bar{C}_v + \frac{D_v \bar{C}_v Z^* e}{kT} \mathbf{E} - \frac{D_v \bar{C}_v \Omega}{kT} \nabla \sigma + \frac{D_v \bar{C}_v Q^*}{kT^2} \nabla T \quad (7.1)$$

where D_v is the atomic diffusivity (m^2/s), \bar{C}_v is the normalised atomic concentration (m^{-3}), Z^* is the effective charge number, e is the elementary charge (C), \mathbf{E} is the electric field (V/m), k is Boltzmann's constant, T is the absolute temperature (K), Ω is the atomic volume (m^3), Q^* is the heat of vacancy transport (kJ/mol) and σ is the hydrostatic stress.

The governing equation of mass transport was

$$\frac{\partial \bar{C}_v}{\partial t} + \nabla \cdot \mathbf{J}_v = G \quad (7.2)$$

where G is the rate of vacancy generation/annihilation per unit volume that can be used to define the sink/source term. Applying Eq. (7.1) to the Eq. (7.2) and omitting the G term, we could obtain the following governing equation.

$$\frac{\partial \bar{C}_v}{\partial t} = -D_v \nabla \cdot \left(-\nabla \bar{C}_v + \frac{Z^* e \bar{C}_v \mathbf{E}}{kT} - \frac{\Omega}{kT} \bar{C}_v \nabla \sigma + \frac{Q^*}{kT^2} \bar{C}_v \nabla T \right) \quad (7.3)$$

In the ANSYS coupled-field analysis, the total strain relevant to the process of electromigration was a sum of the elastic strain $\boldsymbol{\varepsilon}^{el}$, thermal strain $\boldsymbol{\varepsilon}^{th}$ and diffusion expansion strain $\boldsymbol{\varepsilon}^{diff}$ as follows:

$$\boldsymbol{\varepsilon} = \boldsymbol{\varepsilon}^{el} + \boldsymbol{\varepsilon}^{th} + \boldsymbol{\varepsilon}^{diff} \quad (7.4)$$

The diffusion expansion strain was defined as follows:

$$\boldsymbol{\varepsilon}^{diff} = \beta (\bar{C} - C_{ref}) \mathbf{I} \quad (7.5)$$

where β is the coefficient of diffusion expansion and C_{ref} is the reference concentration.

To illustrate ANSYS's capabilities for modelling the distributions and evolutions of concentration and stress, a 1D model of electromigration in a pure metal line was developed in this study. As shown in [11], the coefficient of diffusion strain was set as $\beta = -0.05$ to obtain a 'reasonable' hydrostatic stress value at the steady state (~ 350 MPa). However, this value of β was provided without any reference or basis. This study attempted to obtain the 'reasonable' numerical results by manipulating a few material properties that did not exist.

In the following, we briefly introduce the general coupling model of electromigration. The difference between the general coupling model and the ANSYS build-in theory is also identified. Subsequently, we demonstrate how to use the capability of the current ANSYS coupled-field modelling to correctly simulate electromigration behaviour.

7.2.2. General Coupling Model

The details and complete equations of the general coupling model were presented in Chapter 3. Here, we highlight a few key equations. In the general coupling model, the transport equation of electromigration was written as follows:

$$\frac{\partial \theta}{\partial t} = \Omega \nabla \cdot \mathbf{J}_v \quad (7.6)$$

where θ is the trace of the total strain, which is the sum of $\boldsymbol{\varepsilon}^{el}$, $\boldsymbol{\varepsilon}^{th}$ and $\boldsymbol{\varepsilon}^{diff}$. If we neglect the thermal effects, the transport equation can be rewritten as follows:

$$\frac{\partial \varepsilon_{kk}^{diff}}{\partial t} + \frac{\partial \varepsilon_{kk}^{el}}{\partial t} = \Omega \nabla \cdot \mathbf{J}_v \quad (7.7)$$

The formulation of electromigration induced strain was written as the following equation, which can be linearised.

$$\boldsymbol{\varepsilon}^{diff} = -\frac{A}{3} \ln\left(\frac{C_v}{C_{v0}}\right) \mathbf{I} \approx -\frac{A}{3} \left(\frac{C_v}{C_{v0}} - 1\right) \mathbf{I} \quad (7.8)$$

where A is the coefficient of diffusion strain. Comparing Eqs. (7.8) and (7.5), the linear form of the diffusion strain corresponded to the formulation of diffusion strain in ANSYS. Applying Eq. (7.8) to Eq. (7.7), we could obtain the following expanded transport equation.

$$-\frac{A}{C_{v0}} \frac{\partial C_v}{\partial t} + \frac{\partial \varepsilon_{kk}^{el}}{\partial t} = \Omega \nabla \cdot J_v \quad (7.9)$$

To implement the general coupling theory in ANSYS, certain approximations were required. Here, we assumed the following relationship between the volumetric elastic strain and the electromigration strain.

$$\varepsilon_{kk}^{el} = K \varepsilon_{kk}^{diff} \quad (7.10)$$

where the coefficient K may be determined through the material properties, geometry features of the interconnects and the mechanical boundary condition. For a 1D metal line, if there is no constraint on the metal line (stress-free configuration), its elastic deformation is zero. For a metal line embedded in a rigid passivation layer, the metal line is totally fixed. Thus, K can be approximately obtained as follows [25]:

$$K = 0 \quad (\text{stress-free condition}), \quad (7.11)$$

$$K = -\frac{2(1-2\nu)}{3(1-\nu)} \quad (\text{rigid passivation layer}), \quad (7.12)$$

where ν is the Poisson's ratio of the conductor. K changed within the range between '0' to $^{-2(1-2\nu)/(3(1-\nu))}$.

Applying Eq. (7.10) to Eq. (7.9), the mass transport equation using the general coupling model can be rewritten as the following equation.

$$\frac{\partial \bar{C}_v}{\partial t} = -D_{eff,v} \nabla \cdot (-\nabla \bar{C}_v + \frac{Z^* e \bar{C}_v \mathbf{E}}{kT} - \frac{\Omega}{kT} \bar{C}_v \nabla \sigma + \frac{Q^*}{kT^2} \bar{C}_v \nabla T) \quad (7.13)$$

where:

$$D_{eff,v} = \frac{C_{v0} \Omega}{(1+K)A} D_v \quad (7.14)$$

Comparing Eq. (7.3) with Eq. (7.13), the governing equation using the general coupling model was identical to the mass transport equation in ANSYS, apart from the atomic diffusivity. Notably, the sink/source term is not shown in the governing equation (7.13); however, its

effect on the time scale of electromigration was considered via the effective diffusivity as shown in Eq. (7.14).

7.2.3. Method of Implementation in ANSYS

As summarised in Table I, there are two differences between the general coupling model and the ANSYS build-in theory.

- The **diffusion strain** in the general coupling model was approximately equal to the diffusion strain defined in ANSYS for small variations in the vacancy concentration. Thus, the coefficient of diffusion expansion strain β was set based on the coefficient of diffusion strain ($-A/3$) and C_{ref} was set as '1'.
- For the **governing equation of mass transport**, the sole difference between Eq. (7.13) and Eq. (7.3) was the diffusivity D_v . Thus, D_v in ANSYS was set as the effective diffusivity $D_{eff, v}$ based on Eq. (7.14).

Using the two above-mentioned modifications, the general coupling model can be implemented using the ANSYS build-in theory.

Table 7.1. Differences between the general coupling model and the ANSYS build-in theory and implementation method.

Term	General Coupling Model	ANSYS build-in theory
Diffusion strain	Eq. (7.8)	Eq. (7.5)
	By setting $\beta = -A/3$ and $C_{ref} = 1$	
Transport equation	Eq. (7.13)	Eq. (7.3)
	By setting $D_v = D_{eff, v}$	

7.3. Implementation of the General Coupling Model in COMSOL

7.3.1. Weak Form of the General Coupling Model

COMSOL Multiphysics provides strong solvers and user-friendly interfaces to solve any form of PDEs using weak form modelling. Users only need to input weak expressions for the PDEs to be solved. Subsequently, COMSOL would perform a numerical integration

$\iiint (\text{weak expression}) dV = 0$ to obtain the solution. For our general coupling model, the weak forms of the mass conservation equation and field equations are given as follows:

A. Mass Conservation Equation:

$$\frac{\partial \theta}{\partial t} = -\Omega \nabla \cdot \mathbf{J}_a \quad (7.15)$$

The weak form is:

$$\int_{\Phi} t(C) \frac{\partial \theta}{\partial t} dV + \int_{\Phi} \Omega \left(\frac{\partial t(C)}{\partial x} J_{ax} + \frac{\partial t(C)}{\partial y} J_{ay} + \frac{\partial t(C)}{\partial z} J_{az} \right) dV - \int_{\partial \Phi} \Omega t(C) (J_{ax} + J_{ax}) d\Gamma = 0, \quad (7.16)$$

where $t(C)$ is the test function of vacancy concentration. Φ is the 3D domain and $\partial \Phi$ is its boundary.

B. Stress Equilibrium Equation:

$$\begin{aligned} \nabla \cdot \sigma_x + f_x &= 0 \\ \nabla \cdot \sigma_y + f_y &= 0 \\ \nabla \cdot \sigma_z + f_z &= 0 \end{aligned} \quad (7.17)$$

The weak forms in the x, y and z directions were

$$\begin{aligned} \int_{\Phi} \left[\frac{\partial t(u)}{\partial x} \left(C_{1111} \frac{\partial u}{\partial x} + C_{1122} \frac{\partial v}{\partial y} + C_{1133} \frac{\partial w}{\partial z} \right) + \frac{\partial t(u)}{\partial y} C_{1212} \left(\frac{\partial u}{\partial y} + \frac{\partial v}{\partial x} \right) + \frac{\partial t(u)}{\partial z} C_{1313} \left(\frac{\partial w}{\partial x} + \frac{\partial u}{\partial z} \right) \right] dV + \int_{\Phi} t(u) f_x dV - \int_{\partial \Phi} t_x t(u) d\Gamma &= 0, \\ \int_{\Phi} \left[\frac{\partial t(v)}{\partial y} \left(C_{2211} \frac{\partial u}{\partial x} + C_{2222} \frac{\partial v}{\partial y} + C_{2233} \frac{\partial w}{\partial z} \right) + \frac{\partial t(v)}{\partial x} C_{1212} \left(\frac{\partial u}{\partial y} + \frac{\partial v}{\partial x} \right) + \frac{\partial t(v)}{\partial z} C_{2323} \left(\frac{\partial w}{\partial y} + \frac{\partial v}{\partial z} \right) \right] dV + \int_{\Phi} t(v) f_y dV - \int_{\partial \Phi} t_y t(v) d\Gamma &= 0, \\ \int_{\Phi} \left[\frac{\partial t(w)}{\partial z} \left(C_{3311} \frac{\partial u}{\partial x} + C_{3322} \frac{\partial v}{\partial y} + C_{3333} \frac{\partial w}{\partial z} \right) + \frac{\partial t(w)}{\partial y} C_{2323} \left(\frac{\partial w}{\partial y} + \frac{\partial v}{\partial z} \right) + \frac{\partial t(w)}{\partial x} C_{1313} \left(\frac{\partial w}{\partial x} + \frac{\partial u}{\partial z} \right) \right] dV + \int_{\Phi} t(w) f_z dV - \int_{\partial \Phi} t_z t(w) d\Gamma &= 0, \end{aligned} \quad (7.18)$$

where u , v and w were displacements in the x, y and z directions, respectively. Additionally, $t(u)$, $t(v)$ and $t(w)$ were the corresponding test functions.

C. Heat Transfer Equation:

$$k\nabla^2 T + j^2 \rho = 0 \quad (7.19)$$

The weak form was

$$\begin{aligned} \int_{\Phi} t(T) j^2 \rho dV + \int_{\Phi} k \left(\frac{\partial t(T)}{\partial x} \frac{\partial T}{\partial x} + \frac{\partial t(T)}{\partial y} \frac{\partial T}{\partial y} + \frac{\partial t(T)}{\partial z} \frac{\partial T}{\partial z} \right) dV \\ - \int_{\partial\Phi} k t(T) \left(\frac{\partial T}{\partial x} + \frac{\partial T}{\partial y} + \frac{\partial T}{\partial z} \right) d\Gamma = 0 \end{aligned} \quad (7.20)$$

where $t(T)$ is the test function of temperature.

D. Electrical Conduction Equation:

$$\nabla \cdot \left(\frac{\partial V}{\partial x} + \frac{\partial V}{\partial y} + \frac{\partial V}{\partial z} \right) = 0 \quad (7.21)$$

The weak form is

$$\int_{\Phi} \frac{1}{\rho} \left(\frac{\partial t(V)}{\partial x} \frac{\partial V}{\partial x} + \frac{\partial t(V)}{\partial y} \frac{\partial V}{\partial y} + \frac{\partial t(V)}{\partial z} \frac{\partial V}{\partial z} \right) dV + \int_{\partial\Phi} t(V) \frac{1}{\rho} \left(\frac{\partial V}{\partial x} + \frac{\partial V}{\partial y} + \frac{\partial V}{\partial z} \right) d\Gamma = 0, \quad (7.22)$$

where $t(V)$ is the testing function of electrical voltage.

7.3.2. Method of Implementation in COMSOL

Before implementation in COMSOL, we must know the **writing format** of mathematical formulas in COMSOL. Take the displacement u as an example,

- the 1st derivatives are u_x , u_y and u_z
- the 2nd derivatives are u_{xx} , u_{xy} , and u_{yz}
- the time derivatives are: u_t and u_{tt}
- the mixed derivatives are: u_{xt} and u_{ytt}

Key steps for implementation are listed below.

Step#1: Define DOFs, C for concentration, F for voltage, T for temperature, u for displacement in x , v for displacement in y , and w for displacement in z .

Step#2: Define the material properties and unit of DOFs as global variables as listed in Table 7.2.

Step#3: Define the dependent variables as shown in the following table, Table 7.3.

Step#4: Input the weak expressions of the mass conservation equation (Eq. (7.16)) and field equations (Eqs. (7.18), (7.20) and (7.22)), as shown in Table 7.4.

Table 7.2. Global variables in COMSOL

Name	Description
D	Vacancy diffusivity
Ze	Effective charge number
e	Elementary charge
kB	Boltzmann's constant
p	Electrical resistivity
k	Thermal conductivity
Ql	Heat of transfer
Tl	Environment temperature
E	Young's modulus
mu	Poisson's ratio
P_modulus	P_wave modulus
lame	Lame constant
Shear_modulus	Shear modulus
V	Volume per atom
K	Bulk modulus
alfa	Coefficient of thermal expansion
A	Coefficient of diffusion strain
C0	Unit of concentration
T0	Unit of temperature
F0	Unit of voltage
u0	Unit of displacement in x
v0	Unit of displacement in y
w0	Unit of displacement in z

Table 7.3. Dependent variables in COMSOL

Name	Expression	unit	Description
Dependent variables in the electric field			
Ex	$-F_x \cdot F_0$	V/m	Electrical field in x
Ey	$-F_y \cdot F_0$	V/m	Electrical field in y
Ez	$-F_z \cdot F_0$	V/m	Electrical field in z
jx	E_x / ρ	A/m ²	Current density in x
jy	E_y / ρ	A/m ²	Current density in y
jz	E_z / ρ	A/m ²	Current density in z
EW_x	$Z e^* e^* p^* j_x / (k_B \cdot T_0)$	1/m	Electron wind in x
EW_y	$Z e^* e^* p^* j_y / (k_B \cdot T_0)$	1/m	Electron wind in y
EW_z	$Z e^* e^* p^* j_z / (k_B \cdot T_0)$	1/m	Electron wind in z
Dependent variables in the temperature field			
Q	$(j_x^2 + j_y^2 + j_z^2) \cdot \rho$	W/m ³	Heat source
GT_x	$T_x \cdot T_0$	K/m	T_gradient in x
GT_y	$T_y \cdot T_0$	K/m	T_gradient in y
GT_z	$T_z \cdot T_0$	K/m	T_gradient in z
TW_x	$Q_1 \cdot GT_x / (k_B \cdot T^2 \cdot T_0)$	J/m	Driving force of T_gradient in x
TW_y	$Q_1 \cdot GT_y / (k_B \cdot T^2 \cdot T_0)$	J/m	Driving force of T_gradient in y
TW_z	$Q_1 \cdot GT_z / (k_B \cdot T^2 \cdot T_0)$	J/m	Driving force of T_gradient in z
Dependent variables in the strain field			
exx	$U_x \cdot u_0$		Total strain in x
eyy	$V_y \cdot v_0$		Total strain in y
ezz	$W_z \cdot w_0$		Total strain in z
exy	$0.5 \cdot (u_y + v_x) \cdot$		Total strain in xy
exz	$0.5 \cdot (u_z + w_x)$		Total strain in xz
eyz	$0.5 \cdot (v_z + w_y)$		Total strain in yz
etxx	$\alpha \cdot (T - T_0 - T_1)$		Thermal strain in x
etyy	$\alpha \cdot (T - T_0 - T_1)$		Thermal strain in y
etzz	$\alpha \cdot (T - T_0)$		Thermal strain in z
edxx	$(1-f) \cdot \log(C)/3$		Diffusion strain in x

edxx	$(1-f)*\log(C)/3$		Diffusion strain in x
edxx	$(1-f)*\log(C)/3$		Diffusion strain in x
emx	$exx-etxx-edxx$		Mechanical strain in x
emy	$eyy-etyy-edyy$		Mechanical strain in y
emz	$ezz-etzz-edzz$		Mechanical strain in z
Dependent variables in the stress field			
Sx	$p_modulus*emx+lame*emy+lame*emz$	N/m^2	Normal stress in x
Sy	$Lame*emx+p_modulus*emy+lame*emz$	N/m^2	Normal stress in y
Sz	$Lame*emx+lame*emy+p_modulus*emz$	N/m^2	Normal stress in z
SHy	$(Sx+Sy+Sz)/3$	N/m^2	Hydrostatic stress
Gx_SHy	$d(SHy,x)$	N/m^3	Hydrostatic stress gradient in x
Gy_SHy	$d(SHy,y)$	N/m^3	Hydrostatic stress gradient in y
Gz_SHy	$d(SHy,z)$	N/m^3	Hydrostatic stress gradient in z
SW_x	$-Gx_SHy*V/(kB*T0)$	$1/m$	Driving force of stress-migration in x
SW_y	$-Gx_SHy*V/(kB*T0)$	$1/m$	Driving force of stress-migration in y
SW_z	$-Gx_SHy*V/(kB*T0)$	$1/m$	Driving force of stress-migration in z

Table 7.4. Input format of the weak form of governing equations

Mass conservation equation	$Test(C)*A*Ct+test(C)*(u0*uxt+v0*vyt+w0*wzt) -D*test(Cy)*(-Cy+EW_y*C+TW_x*C-SW_y*C) - D*test(Cx)*(-Cx+EW_x*C+TW_x*C-SW_x*C) -D*test(Cz)*(-Cz+EW_z*C+TW_z*C-SW_z*C)$
Electrical conduction equation	$p^{-1}*test(Fx)*Fx+p^{-1}*test(Fy)*Fy+p^{-1}*test(Fz)*Fz$
Heat transfer equation	$k*T0*test(Tx)*Tx+k*T0*test(Ty)*Ty+k*T0*test(Tz)*Tz-Q*test(T)$

Stress equilibrium equation in x	$p_modulus*test(ux)*emx+lame*test(ux)*emy+lame*test(ux)*emz$ $+shear_modulus*test(uy)*(exy)+shear_modulus*test(uz)*(exz)$
Stress equilibrium equation in y	$Lame*test(vy)*emx+p_modulus*test(vy)*emy+lame*test(vy)*emz$ $+shear_modulus*test(vx)*exy+shear_modulus*test(vz)*eyz$
Stress equilibrium equation in z	$Lame*test(wz)*emx+lame*test(wz)*emy+p_modulus*test(wz)*emz$ $+shear_modulus*test(wx)*exz+shear_modulus*test(wy)*eyz$

Through the above-mentioned four steps, the general coupling theory can be completely implemented in COMSOL. We have defined independent variables for six DOFs (concentration, temperature, voltage and displacement in x, y and z), global variables for material properties, dependent variables for different fields and weak expressions for governing equations.

7.4. Case Study

7.4.1. Totally Fixed Metal Line

A 1D totally confined metal line with a perfectly blocking condition was studied as a benchmark problem, as shown in Figure 7.1. For simplicity, Joule heating was neglected in this study; thus, there are no temperature gradients in the entire model. The following initial and boundary conditions were implied.

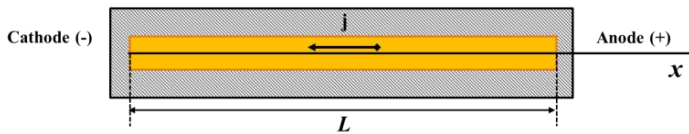


Figure 7.1. Benchmark problem for a metal line embedded in a rigid passivation layer.

- Initial condition: $C_v(x) = C_{v0}$ and $T = 500$ K.
- Diffusion boundary condition: the vacancy flux was blocked at both sides of the metal line, $J_v(0) = J_v(L) = 0$.
- Mechanical boundary condition: the metal line was embedded in a rigid passivation layer, $v = w = 0$ and $u(0) = u(L) = 0$.

To verify our implementations in ANSYS and COMSOL, the analytical solution of this 1D problem was used to compare with the FEA results. Details of the analytical solutions are described in Chapter 3. Table 7.5 shows the material properties used in our simulations.

Table 7.5. Parameters used in the calculations.

Material properties	Value
Length of the metal line (L)	50 μm
Young's modulus (E)	70 GPa
Poisson's ratio (ν)	0.3
Atomic diffusivity (D_a)	$3.0 \times 10^{-16} \text{ m}^2/\text{s}$
Atomic volume (Ω)	$1.66 \times 10^{-29} \text{ m}^3$
Electrical resistivity (ρ)	$4.88 \times 10^{-8} \text{ Ohm} \cdot \text{m}$
Current density (j)	$1.0 \times 10^{10} \text{ A/m}^2$
Elementary charge (e)	$1.6 \times 10^{-19} \text{ C}$
Charge number (Z^*)	3.5
Boltzmann constant (k)	$1.38 \times 10^{-23} \text{ J/K}$
Coefficient of diffusion strain	-0.0071

Figure 7.2 (a) plots the normalised vacancy concentration (C_v) along the length of the metal line, in which vacancies accumulated at the cathode side and decreased at the anode side. This indicates that atomic transport was along the direction opposite to the current density. Figure 7.2 (b) shows the tensile stress on the cathode side due to the depletion of atoms, and the compressive stress on the anode side. At the steady state, the FEA results obtained from ANSYS and COMSOL were in excellent agreement with the analytical solutions. Moreover, the transient-state results of the FEA were consistent with the results of analytical solutions, as shown in Figures 7.3 (a) and (b). We selected the FE model in COMSOL as an example to show the contour of vacancy concentration and hydrostatic stress, as shown in Figures 7.4 and 7.5.

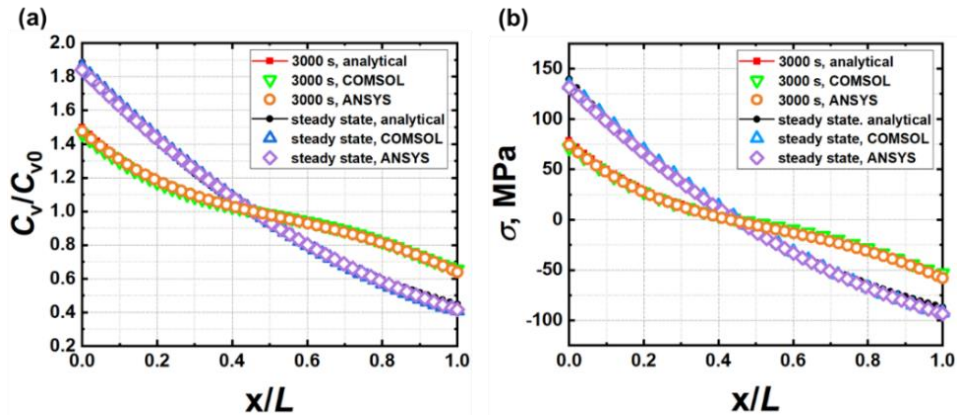


Figure 7.2. (a) Distribution of vacancy concentration along the length of the conductor. (b) Distribution of hydrostatic stress along the length of the conductor.

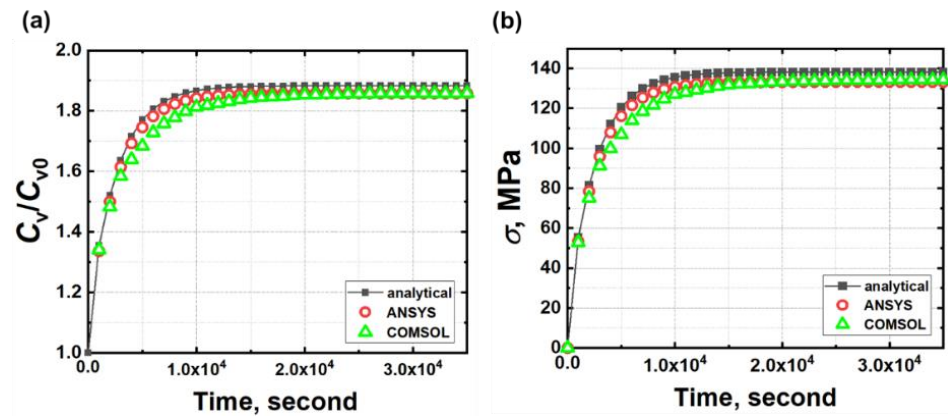


Figure 7.3. (a) Vacancy concentration and (b) hydrostatic stress build-up over time at $x = 0$.

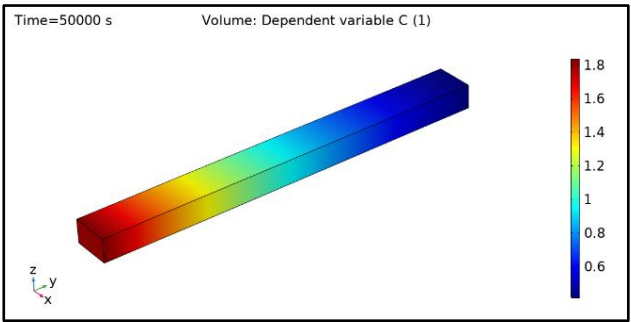


Figure 7.4. Contour plot of atomic concentration at 10^5 s for a totally fixed metal line from COMSOL.

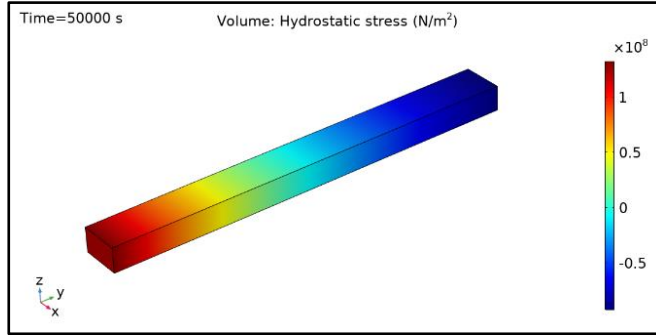


Figure 7.5. Contour plot of of hydrostatic stress at 10^5 s for a totally fixed metal line from COMSOL.

7.4.2. Stress-Free Metal Line

Here, we consider a metal line under the stress-free condition, as shown in Figure 7.6 (a). For simplicity, Joule heating was neglected in this study. Thus, no temperature gradient exists for the entire model. The analytical solution for this problem was used to compare with the FEA results (details are presented in Chapter 3). The initial and diffusion boundary conditions were identical to those of Case 1. For FE modelling, the constraints shown in Figure 7.6 (b) were applied to remove the rigid displacement of the metal line.

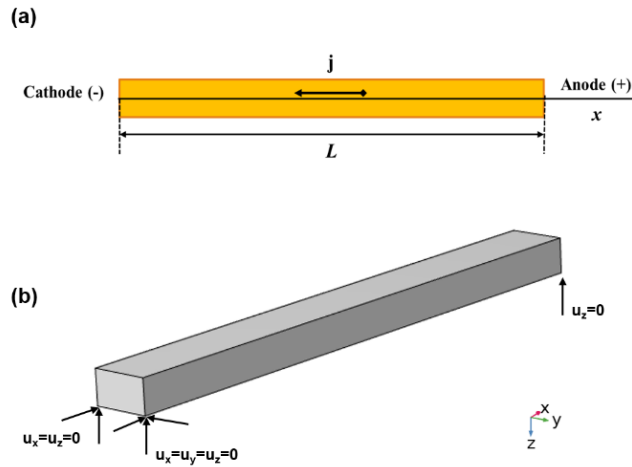


Figure 7.6. (a) Schematic diagram for the stress-free metal line. (b) Applied constraints to remove rigid displacement in FE simulations.

Figure 7.7 (a) plots the vacancy concentration distribution along the metal line. At the steady state, the FEA results from COMSOL and ANSYS were nearly identical to the analytical solution. Figure 7.7 (b) plots the evolution of the vacancy concentration at the cathode over time. The FEA results were consistent with the analytical solution at the transient state. The FE model in ANSYS was selected as an example to demonstrate the contour of vacancy concentration and hydrostatic stress (as shown in Figures 7.8 and 7.9). The stress in the conductor varied at a very low level, i.e. -1 to 3 MPa.

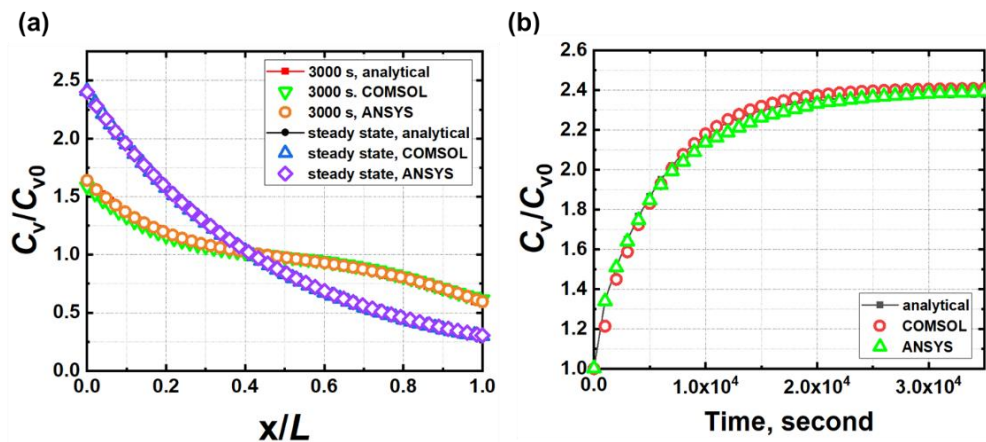


Figure 7.7. (a) Distribution of vacancy concentration along the length of the conductor. (b) Vacancy concentration build-up over time at $x = 0$.

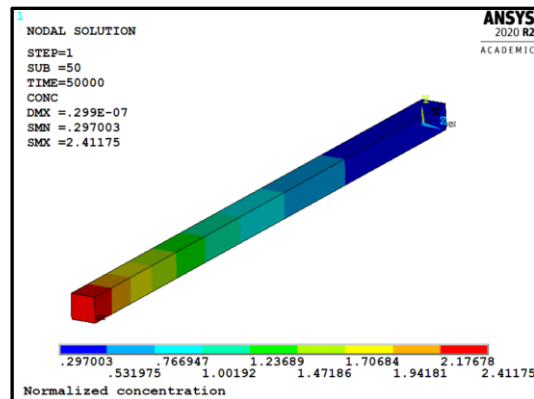


Figure 7.8. Contour of normalised vacancy concentration at 10^5 s for a stress-free metal line from ANSYS.

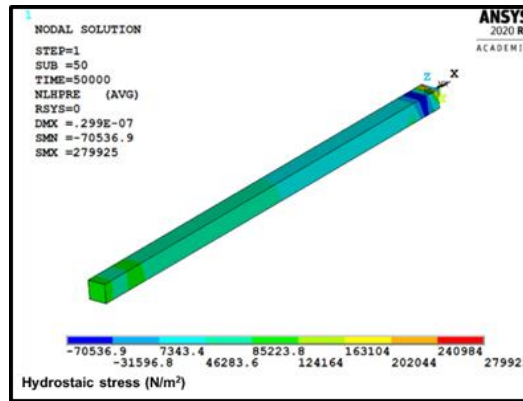


Figure 7.9. Contour of hydrostatic stress at 10^5 s for a stress-free metal line from ANSYS.

7.5. Conclusions

In this chapter, the general coupling model for electromigration was implemented in ANSYS and COMSOL using the ANSYS build-in coupled-field theory and the COMSOL weak form PDE module, respectively. Several incorrect settings in the ANSYS manuals were identified and corrected. The details of the implementation of the general coupling model in ANSYS were presented. The weak form of the general coupling model was derived, and the implementation procedure in COMSOL was described. The obtained 1D FEA results were in excellent agreement with the analytical solutions, which acted as validation. Using the developed FEA method, the developed general coupling model could be conveniently used in predicting electromigration in complex 3D interconnects. As a next step, we will apply the same procedures to implement the fully coupled theory we presented in Chapter 5 and 6 into ANSYS and COMSOL.

References

1. Cui, Z., X. Fan, and G. Zhang. Implementation of General Coupling Model of Electromigration in ANSYS. in 2020 IEEE 70th Electronic Components and Technology Conference (ECTC). 2020. IEEE.
2. Sarychev, M., et al., General model for mechanical stress evolution during electromigration. Journal of Applied Physics, 1999. 86(6): p. 3068-3075.
3. Basaran, C. and M. Lin, Damage mechanics of electromigration induced failure. Mechanics of Materials, 2008. 40(1-2): p. 66-79.

4. Lin, M. and C. Basaran, Electromigration induced stress analysis using fully coupled mechanical–diffusion equations with nonlinear material properties. *Computational Materials Science*, 2005. 34(1): p. 82-98.
5. Sukharev, V. and E. Zschech, A model for electromigration-induced degradation mechanisms in dual-inlaid copper interconnects: Effect of interface bonding strength. *Journal of Applied Physics*, 2004. 96(11): p. 6337-6343.
6. Sukharev, V., E. Zschech, and W.D. Nix, A model for electromigration-induced degradation mechanisms in dual-inlaid copper interconnects: Effect of microstructure. *Journal of Applied Physics*, 2007. 102(5): p. 053505.
7. Pak, J., et al. Modeling of electromigration in through-silicon-via based 3D IC. in 2011 IEEE 61st Electronic Components and Technology Conference (ECTC). 2011. IEEE.
8. Hou, Y. and C.M. Tan, Comparison of stress-induced voiding phenomena in copper line–via structures with different dielectric materials. *Semiconductor science technology*, 2009. 24(8): p. 085014.
9. Jing, J., L. Liang, and G. Meng, Electromigration simulation for metal lines. *Journal of Electronic Packaging*, 2010. 132(1).
10. Korhonen, M., et al., Stress evolution due to electromigration in confined metal lines. *Journal of Applied Physics*, 1993. 73(8): p. 3790-3799.
11. Antonova, E.E. and D.C. Looman. Finite elements for electromigration analysis. in 2017 IEEE 67th Electronic Components and Technology Conference (ECTC). 2017. IEEE.

8

CALCULATION OF ATOMIC DIFFUSIVITY IN POLYCRYSTALLINE METAL

Understanding the atomic diffusion features in metallic conductors is significant to explaining certain phenomenon in electromigration. Moreover, one of the applications of electromigration is the determination of the atomic diffusivity in metallisation, which is necessary for the prediction not only for electromigration but also the creep, nanoparticle sintering and film deposition. In this chapter, using electromigration experiments and MD simulations, we study the atomic diffusion features in polycrystal metal and propose an MD-based methodology to calculate the effective diffusivity in polycrystal metals. The effects of grain size and temperature on the diffusion behaviours of polycrystals were explored. The Arrhenius equation of the diffusivity of grain boundaries (GBs) and the empirical formula of its thickness at various temperatures were obtained. The effective diffusivity of polycrystals was then calculated and correlated to the GB's diffusivity and the volume fraction of atoms in grain boundaries. Based on these simulation results, we proposed an MD-based diffusion model that could be used to calculate the effective diffusivity in polycrystal metals. Additionally, electromigration tests were conducted to determine the effective diffusivity experimentally. The good agreement between the calculated and experimental results demonstrated that the proposed approach can calculate the effective diffusivity accurately.

8.1. Introduction

Electromigration is essentially a physical process of mass transport. To predict electromigration failure accurately, a reliable parameter of atomic diffusivity is necessary. Moreover, this parameter is also important for the analysis and prediction of Coble creep, nanoparticle sintering, film deposition, etc. Thus, numerous experimental studies have been conducted to determine the diffusivity in metals; however, different values of diffusivity were reported in literature. Considering Al as an example, Seeger *et al.* [1] investigated the temperature dependence of the diffusivity in Al by using tracer and nuclear magnetic resonance techniques. They determined an Arrhenius equation with the pre-exponential $D_0 = 0.047 \text{ cm}^2/\text{s}$ and activation energy $Q = 1.26 \text{ eV}$. Lundy and Murdock [2] determined the activation energy of self-diffusion in Al as 1.49 eV using radioactive Al^{26} . However, in the study conducted by Demmel *et al.* [3], the activation energy of self-diffusion in Al was determined with the coherent quasielastic neutron scattering technique to be 0.274 eV.

For the atomic diffusion in polycrystals, grain boundaries (GBs) provide a fast-diffusion path [4, 5]. In the study conducted by Cho and Thompson [6], the mass transport during electromigration can be noticeably reduced in the Al line with large grains but accelerated in Al with small grains. This indicates that GBs play an important role in atomic diffusion in polycrystalline Al. Typically, the atomic diffusivity along GBs (D_{GBs}) is determined via indirect means [7, 8]. For example, in the study conducted Wang *et al.*, [9] an ‘average’ diffusivity for an Al polycrystal, also called effective diffusivity (D_{eff}), was experimentally determined. Subsequently, the diffusivity along GBs was estimated via a simple equation correlating D_{eff} and D_{GBs} . Surholt and Herzig [10] experimentally determined a volume diffusion coefficient in Cu and then calculated the product of the diffusivity and thickness of GBs using the Suzuoka solution of the GB diffusion equation.

MD simulation is an effective tool to investigate material properties at the atomic level, providing insight into understanding diffusion features along GBs. Suzuki and Mishin [11] investigated the atomic diffusion along Cu GBs and identified that vacancies migrate along GBs by exchanging position with individual atoms. In the study conducted by Sorensen *et al.* [12], the atomic diffusivity along Cu GB $\Sigma = 5(210)$ was discovered to follow the Arrhenius law quite accurately over a wide range of temperatures. Additionally, the diffusivity along GBs was discovered to be much higher than that in the grains. Furthermore, in the study conducted by Sellers *et al.* [13], the effective diffusivity of a Sn bicrystal was significantly

affected by atomic diffusivity along GBs. Moreover, the low energy GB exhibited a low activation energy of diffusion along GBs.

In this chapter, combining the MD simulation and our experiments, we investigate the atomic diffusion features in polycrystalline and develop an MD-based diffusivity model for polycrystal metals. Key parameters, such as the activation energy in GBs and their thicknesses as a function of temperature, were determined by the MD simulation. The averaged grain size could be determined experimentally. Additionally, the electromigration test was conducted to obtain the effective diffusivity, which was then compared to the predictions from our model. This chapter is organized as follows. Section 8.2 describes an overview of the proposed methodology and simulation details. Section 8.3 presents the simulation results for atomic diffusion in polycrystals with different grain sizes and temperatures. A simulation-based model for calculating the effective diffusivity was proposed. In Section 8.4, the experimental results of the effective diffusivity in polycrystals and the validation of the proposed methodology are presented. Section 8.5 concludes this chapter.

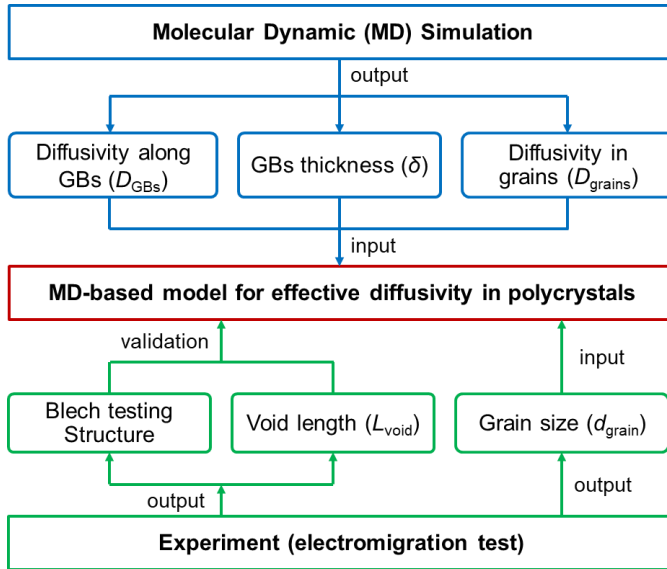


Figure 8.1. Overview of the proposed methodology.

8.2. Methodology

Figure 8.1 illustrates an overview of the proposed methodology for determining the effective diffusivity in polycrystals. Firstly, extensive MD simulations were performed to investigate the diffusion behaviours in GBs and grains. A few key parameters were identified, such as the atomic diffusivity along GBs (D_{GBs}) and their thicknesses (δ). Subsequently, an MD-based effective diffusivity model was proposed. To validate this model, an electromigration test to obtain the void length and to determine the effective diffusivity experimentally was conducted using a Blech structure. The average grain size (d_{grain}) of the actual metal in experiments was measured. Lastly, combining the parameters obtained from both simulations and experiments (D_{GBs} , δ and d_{grain}) with the proposed diffusion model, we could predict the effective diffusivity for polycrystal metals.

8.2.1. Molecular Dynamic Simulation Details

Using the Voronoi method [14, 15], we constructed the MD model for polycrystal Al with four different grain sizes, as shown in Figures 8.2 (a)–(d). Three random polycrystalline structures were constructed for each grain size. The dimensions of the model along the x , y and z directions were 400 Å, 400 Å, and 100 Å, respectively. The total number of atoms in each model was approximately one million.

In this study, the diffusion behaviours for the atoms in grains, GBs, and the entire polycrystal were investigated. Figure 8.3 (a) illustrates a representative polycrystal model after equilibrium. The enlarged figure inside the grain in Figure 8.3 (a) shows that the atoms in it had an intact FCC lattice structure. Figure 8.3 (b) shows only the atoms along the GBs, from which the diffusivity in GBs can be obtained.

Our MD simulations were conducted using the large-scale atomic/molecular massively parallel simulator (LAMMPS). The embedded-atom method (EAM) with a potential file developed by Voter was used to calculate the interaction between Al atoms [16]. Newton's equation of motion was integrated with the Verlet algorithm. The open visualization tool (OVITO) software was used to visualise our simulation results [17]. A time step of 2 fs was selected for the calculations, and the periodic boundary condition was applied in the three dimensions.

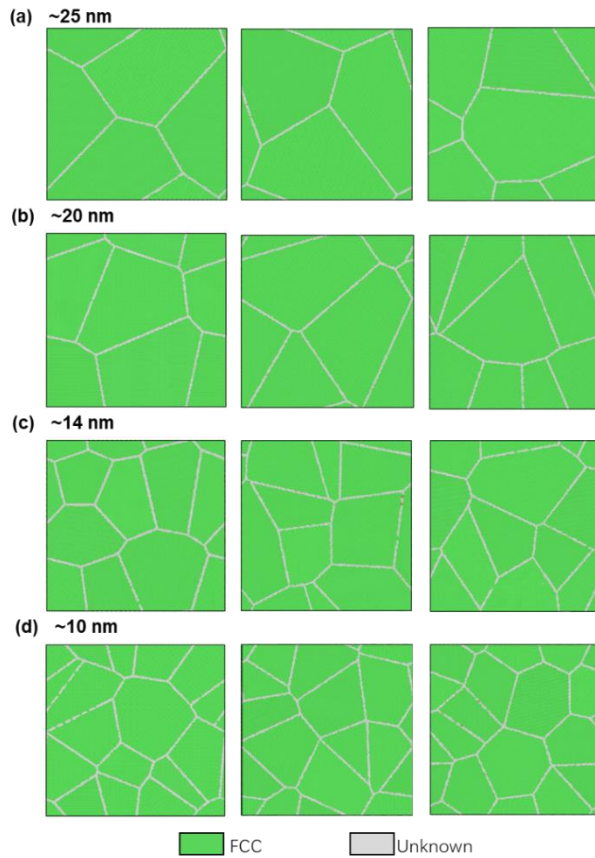


Figure 8.2. MD models for polycrystal Al with grain sizes of (a) 25 nm, (b) 20 nm, (c) 14 nm and (d) 10 nm. The green region represents the atoms in the grains with FCC lattice structures, and the grey region represents the atoms in the GBs with irregular lattice structures.

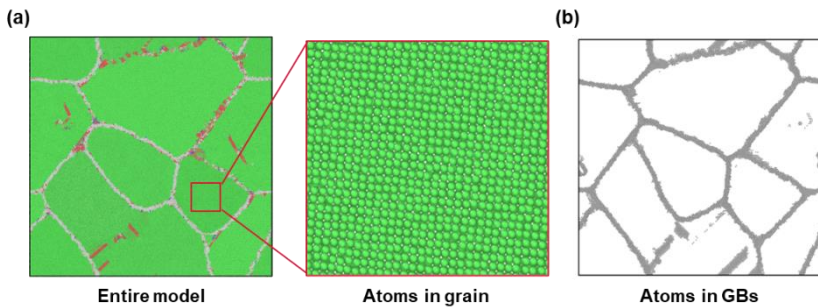


Figure 8.3. Illustrations for the objects of study: entire polycrystalline, atoms in grains and atoms in GBs.

The simulation procedure can be divided into three steps: (1) The system energy was minimised; the coordinates of the atoms were iteratively adjusted until the change in energy between the outer iteration was less than 1×10^{-8} eV/Å. Subsequently, the system was relaxed for 1500 ps in the NPT ensemble with the target temperature (300 K, 400 K, 500 K, 600 K, 700 K) and zero pressure to obtain a stable polycrystal structure and reach the equilibrium state. (2) Based on the fully relaxed structure, polyhedral template matching (PTM) was computed to identify the different lattice structures in polycrystals. In particular, the atoms with unknown lattice structures were defined as atoms in the GBs, as shown in Figure 8.3 (b). (3) Subsequently, we continually relaxed the system for 2000 ps to calculate the mean-squared displacement (MSD) and diffusivities for atoms in the GBs, grains and the entire polycrystal. Here, the MSD was computed using the following equation [13, 18, 19].

$$MSD_{GBs} = \frac{1}{N_{GBs}} \sum_{i=1}^N [r_i(t) - r_i(0)]^2, \quad (8.1)$$

$$MSD_{grain} = \frac{1}{N_{grain}} \sum_{i=1}^N [r_i(t) - r_i(0)]^2, \quad (8.2)$$

$$MSD_{eff} = \frac{1}{N_{eff}} \sum_{i=1}^N [r_i(t) - r_i(0)]^2, \quad (8.3)$$

where N_{GBs} , N_{grain} and N_{all} represent the number of atoms in the GBs, grains and the entire model, respectively. $r_i(t)$ and $r_i(0)$ are respectively the locations of atom i at time t and 0. Based on the calculated MSD, the diffusivity in the solid material could be calculated via the Einstein relation [13, 20, 21].

$$D_{GBs} = \lim_{t \rightarrow \infty} \frac{1}{2n} \frac{dMSD_{GBs}}{dt}, \quad (8.4)$$

$$D_{grain} = \lim_{t \rightarrow \infty} \frac{1}{2n} \frac{dMSD_{grain}}{dt}, \quad (8.5)$$

$$D_{eff} = \lim_{t \rightarrow \infty} \frac{1}{2n} \frac{dMSD_{eff}}{dt}, \quad (8.6)$$

where D_{GBs} , D_{grain} and D_{eff} are the diffusivities for GBs, grains and the entire polycrystalline, respectively. n is the dimension of the simulation structure. Although the period used in the MD calculation of diffusivity was only a few nanoseconds, existing studies [13, 21, 22] have proven that an MD simulation can calculate the atomic diffusivity accurately.

8.2.2. Experiment to Estimate Diffusivity

The mass transport induced by electromigration was used to estimate the effective diffusivity in Al. During electromigration, atoms tended to diffuse from the cathode to the anode, causing void growth at the former and hillock formation at the latter. Based on the study conducted by Blech *et al.* [23], the drift velocity of a metal film could be experimentally determined using the following equation.

$$v = \frac{L_{void}}{t}, \quad (8.7)$$

where L_{void} is the void length induced by electromigration and t is the test time. Additionally, based on the Nernst-Einstein equation [24], the drift velocity can be expressed as follows:

$$v = D_{eff} \frac{F}{kT}, \quad (8.8)$$

where D_{eff} is the effective diffusivity of the Al film and F is the driving force. For an Al film without dielectric passivation layer, F is equal to the sum of the electron wind force and the driving force of self-diffusion, as shown below.

$$F = Z^* e \rho j - \frac{kT}{C_v} \frac{\partial C_v}{\partial x} \quad (8.9)$$

We have shown that for a conductor longer than 60 μm , the effect of self-diffusion on electromigration is very small. Thus, the drift velocity for bare and long Al stripes can be expressed as follows:

$$v = D_{eff} \frac{Z^* e \rho j}{kT} \quad (8.10)$$

Using Eqs. (7) and (8), the effective diffusivity can be expressed using the following equation.

$$D_{eff} = \frac{L_{void} kT}{t} (Z^* e \rho j)^{-1} \quad (8.11)$$

In this study, 100 μm long, 5 μm wide and 0.2 μm thick non-annealed Al stripes were used for electromigration tests at 200 °C, 250 °C, 300 °C, 350 °C in vacuum.

8.3. Results and Discussion

Firstly, we considered a polycrystal with 10 nm grains at 600 K as an example to illustrate the diffusion features in grains and GBs, as plotted in Figure 8.4. After relaxing the model for 1500 ps, the microstructure in Figure 8.4 (a) shows that atoms in the grains retain the FCC lattice structure. However, a few atoms in the GBs change to an HPC lattice structure, which indicates the formation of dislocations near the GBs. Figure 8.4 (b) plots the trajectory lines for atom movements, in which the lines in the grains and GBs have apparent differences. Trajectory lines in the GBs were dense and irregular, connecting different sites. However, trajectory lines in the grains were loose and regular, isolated at different sites, as shown in the enlarged figure. The visual difference between grain A and grains B and C was due to different crystal orientations. In fact, their diffusion features are nearly identical. This indicates that atoms in grains only slightly vibrate around their lattice site, without much diffusion occurring. However, the trajectories in the GBs indicate that the atoms in them can irregularly jump between different sites, diffusing along the GBs. To quantitatively investigate the difference between GB diffusion and lattice diffusion in grains, we calculate the MSD and diffusivity for atoms in GBs and grains, respectively, in the following parts of the manuscript.

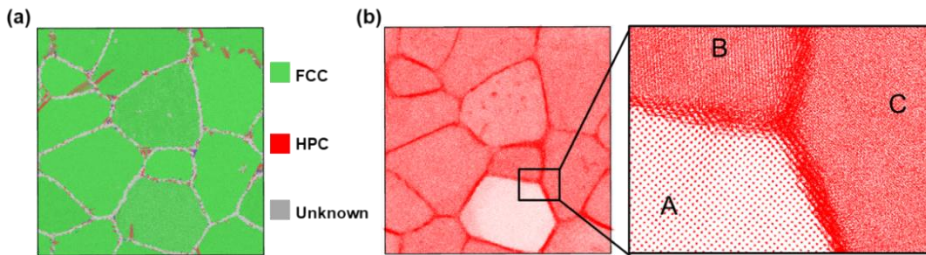


Figure 8.4. (a) Microstructure of the polycrystal with ~ 10 nm grains at 600 K. (b) Trajectory lines for atomic movements.

8.3.1. Atomic Diffusion along the Grain Boundary

Let us focus on the atomic diffusion at GBs. Figure 8.5 plots the MSD_{GBs} at different temperatures for polycrystals with different grain sizes, in which the averaged results with an error bar, based on the three random MD models shown in Figure 8.2, are reported. Regardless of the grain sizes, MSD_{GBs} was larger at higher temperatures. Although the MSD_{GBs} with different grain sizes at the same temperature have different error bars, the average MSD_{GBs} changes at the same level were slightly different from each other. The MSD,

as defined in Eqs. (8.1)–(8.3), represented the average distance for atomic movement. Thus, the MSD_{GBs} values in Figure 8.5 indicated that increasing temperatures could significantly promote atomic diffusion along GBs; however, grain sizes have little effect on the values of MSD_{GBs} .

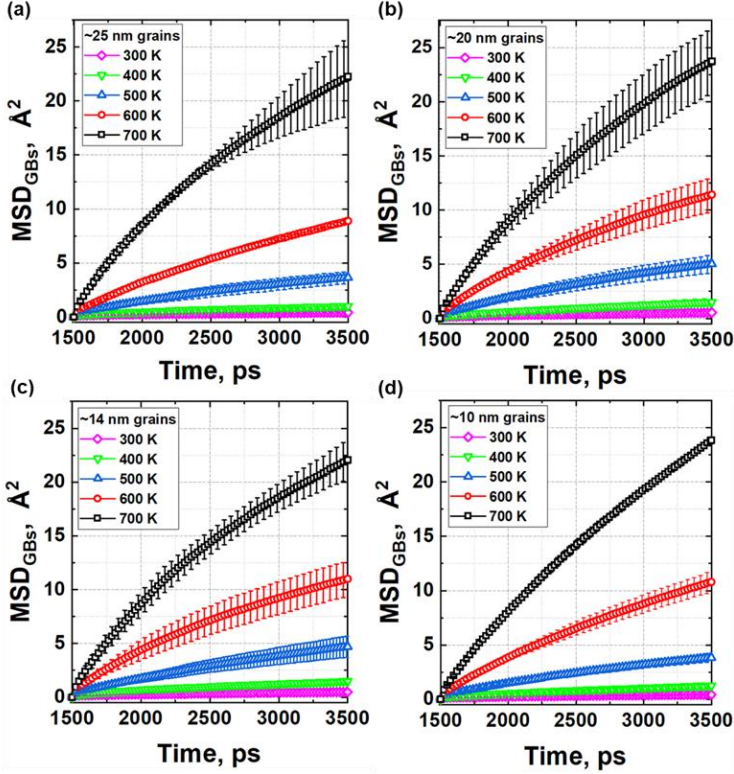


Figure 8.5. MSD_{GBs} at different temperatures for polycrystals of different grain sizes.

Based on Eq. (8.4), we obtained the diffusivity of the GBs (D_{GBs}) by calculating the rate of MSD_{GBs} in the 2500 ps to 3500 ps range, as shown in Figure 8.6. As expected, at the same temperature, the magnitudes of D_{GBs} with different grain sizes were significantly close to each other. Additionally, it was evident that the D_{GBs} changed as a function of temperature. Through an Arrhenius equation fit, we obtained the Arrhenius equation for D_{GBs} as follows:

$$D_{GBs} = 5.982 \times 10^{-10} \exp\left(-\frac{0.235 \text{ eV}}{kT}\right) \text{ m}^2/\text{s} \quad (8.12)$$

where $5.982 \times 10^{-10} \text{ m}^2/\text{s}$ is the pre-coefficient ($D_{\text{GBs},0}$) and 0.235 eV is the activation energy (Q) for GB diffusion.

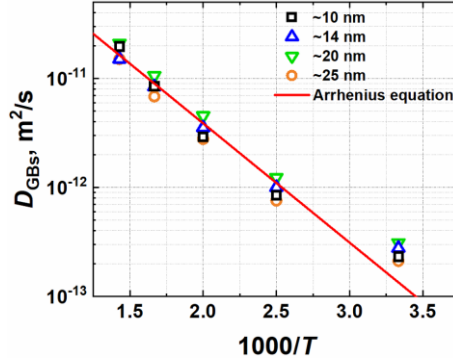


Figure 8.6. D_{GBs} values at different temperatures for polycrystals with different grain sizes and Arrhenius equations.

Moreover, based on the trajectory lines of the movements of the atoms, the thickness of the GB at different temperatures could be identified, as plotted in Figure 8.7. At a low temperature (300 K), the trajectory lines along the GBs were slight and unclear, and their thickness was approximately 2.1 Å. When the temperature increased to 500 K, the trajectories along the GBs became visible. At 700 K, the outlines of the trajectories along the GBs grew thicker, and the thickness of the GBs increased to ~8.81 Å. This varying trend in the GBs indicated that increasing temperatures could induce more atoms near the GBs to participate in the irregular movements, resulting in a thicker GB.

Figure 8.8 plots the average thickness of the GBs with different grain sizes at different temperatures. The thickness of the GBs increased linearly with temperature, and the grain size had little effect on this thickness. Thus, the thickness of GBs in polycrystals could be fitted as a function of temperature as follows:

$$\delta(T) = 0.015(T - 300 \text{ K}) + 2, \quad (8.13)$$

where the unit of the thickness of GBs is Å.

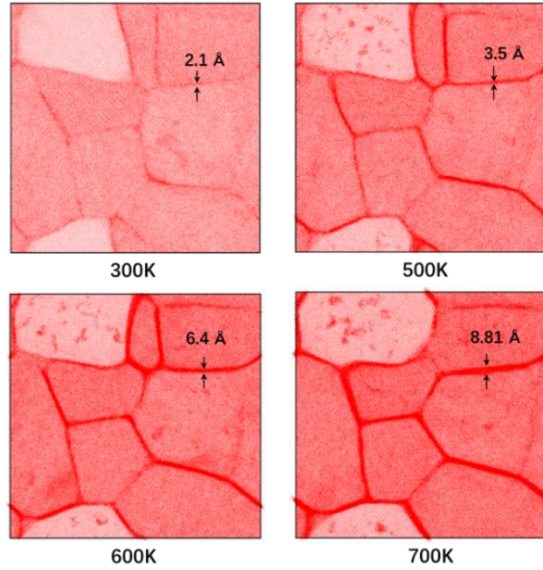


Figure 8.7. Trajectory lines of atomic movements at different temperatures for polycrystals with ~ 14 nm grains.

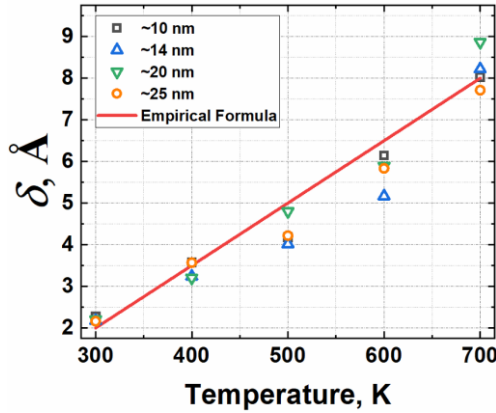


Figure 8.8. Thickness of GBs at different temperatures for different grain sizes.

8.3.2. Atomic Diffusion in Grains

In this section, we focus on the atomic diffusion in grains. Figure 8.9 plots the MSD_{grains} with ~ 10 nm grains at low (300 K), medium (500 K) and high (700 K) temperatures. The figure shows that the MSD_{grains} is larger at 700 K. However, the magnitudes of MSD_{grains} at 300 K and 500 K remained nearly constant after equilibrium. The flat curves at 300 K and 500 K indicated that atoms in grains tended to vibrate around their own lattice site, with no diffusion in the grains. The increasing MSD_{grains} at 700 K suggested that the atoms could jump at

different sites, causing atomic diffusion in grains. These results were consistent with the information reflected in Figure 8.7, in which the trajectories in grains at 300 K were isolated to each other. However, when the temperature increased to 700 K, there were a few trajectories connecting different sites in grains. This difference is because atoms remain at a low energy level at medium and low temperatures, and it is difficult to overcome the energy barrier to diffuse between different sites. However, at high temperatures, atoms tend to contain sufficient energy to exchange locations with their neighbours, migrating at different sites.

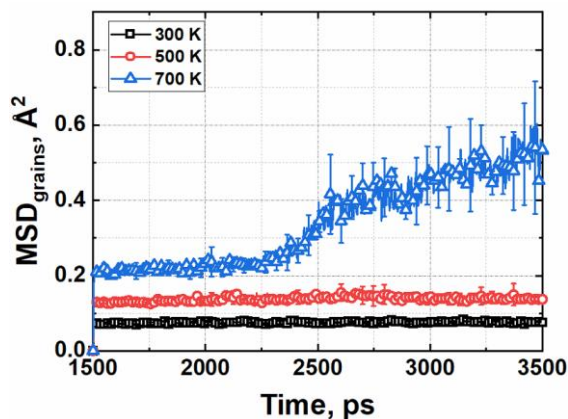


Figure 8.9. MSD_{grains} at 300K, 500K and 700K for polycrystals with ~ 10 nm grains.

Additionally, compared to the MSD of GBs shown in Figure 8.8, we could find that at the same temperature, MSD_{grains} was much lower than MSD_{GBs} . Even at 700K, the MSD_{grains} at 3500 ns was 50 times lower than MSD_{GBs} . These differences between MSD_{grains} and MSD_{GBs} were consistent with our former analysis of Figure 8.6. Here, although we only plotted the MSD_{grains} for a polycrystal with 10 nm grains, the results for the other grain sizes exhibited a similar changing trend. As the diffusivity in the MD calculation was the rate of MSD over time, it was expected that the diffusivity for atoms in grains was negligible compared to the D_{GBs} .

8.3.3. Effective Diffusivity of Polycrystals

Figure 8.10 plots the MSD_{eff} at 300 K, 500 K 700 K for polycrystals with different grain sizes. The figure shows that at the same temperature, the MSD_{eff} with smaller grains is larger. Meanwhile, we could determine that the MSD_{eff} at higher temperatures tended to be higher. These results indicated that both grain size and temperature played important roles in the

overall diffusion of polycrystals. The increasing temperature could promote atomic diffusion in polycrystals; however, the increasing grain size tended to decrease the overall diffusion rate of polycrystals.

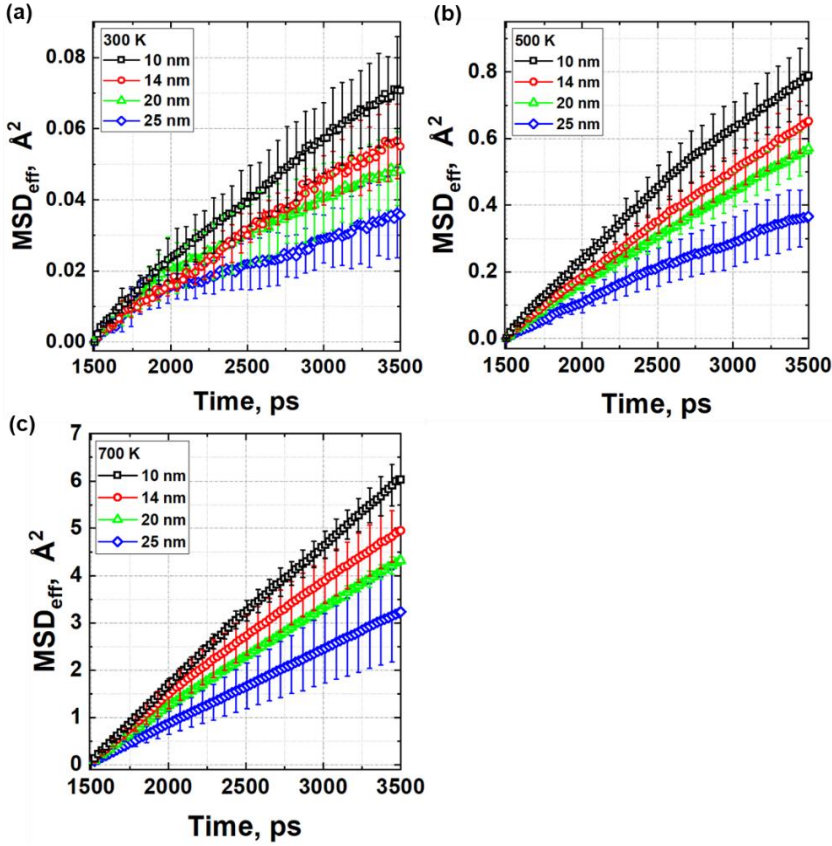


Figure 8.10. MSD_{GBs} at 300K, 500K and 700K for polycrystals with different grain sizes.

Based on the MSD_{eff} data, the effective diffusivities of polycrystals at different temperature were obtained, as plotted in Figure 8.11. It clearly showed that the magnitude of effective diffusivity was related to the temperature and grain size. For a polycrystal with the same grain size, the D_{eff} at higher temperatures was higher. From 300K to 500 K and then to 700 K, the effective diffusivities varied at three different levels, increasing from a scale of $10^{-14} \text{ m}^2/\text{s}$ to $10^{-13} \text{ m}^2/\text{s}$ and then to $10^{-12} \text{ m}^2/\text{s}$. Moreover, for polycrystals at the same temperature, D_{eff} exhibited a decreasing trend with increasing grain size. In contrast to the diffusivity of GBs, the magnitude of effective diffusivity depended on the grain size.

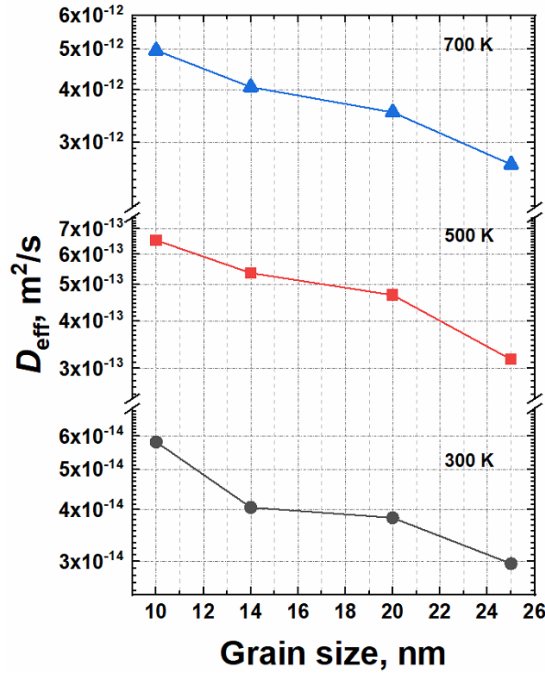


Figure 8.11. D_{eff} for the model with different grain sizes at 300 K, 500 K and 700 K.

To investigate the mechanism behind these results, we used the equation proposed by Hart [25] to describe the relationship between D_{eff} , D_{GBs} and D_{grains} as follows:

$$D_{eff} = \varphi_{GBs} D_{GBs} + (1 - \varphi_{GBs}) D_{grain}, \quad (8.14)$$

where φ_{GBs} and $1 - \varphi_{GBs}$ are the volume fractions of atoms in the GBs and grains, respectively. [26] According to our simulation results, the D_{Grain} below melting temperature was negligible compared to D_{GBs} ($D_{Grain} \ll D_{GBs}$). Thus, the second term on the right side of Eq. (8.14) can be neglected, and Eq. (8.14) can be approximately written as follows:

$$D_{eff} = \varphi_{GBs} D_{GBs} \quad (8.15)$$

Eq. (8.15) shows that the effective diffusivity can be approximately expressed as the product of atomic diffusivity along the GBs and the volume fraction of atoms in the GBs. Although D_{GBs} was independent of grain size, the volume fraction of atoms in the GBs, φ_{GBs} , depended on the grain size. A decreased grain size implies an increased GB length, which could increase the volume proportion of the GB (φ_{GBs}).

8.3.4 MD-Based Model for Effective Diffusivity

In Eq. (8.15), the effective diffusivity is expressed as the product of D_{GBs} and ϕ_{GBs} . Based on the study conducted by Thorvaldsen [27, 28], ϕ_{GBs} can be expressed using the following equation:

$$\phi_{GBs} = H_{GBs} \frac{\delta}{d_{grains}}, \quad (8.16)$$

where δ is thickness of the GBs, d_{grains} is the average diameter of the grain, and H_{GBs} is a dimensionless numerical factor that depends on the grain shape and grain size distribution, varying between 2.5 and 3.0. For example, the values of H_{GBs} for three common space-filling polycrystals, tetrakaidecahedra, Johnson-Mehl grains and Voronoi polyhedral are 2.6575, 2.5715 and 2.9105, respectively [26, 27]. Applying Eq. (8.16) to Eq. (8.17), we can rewrite the effective diffusivity as follows:

$$D_{eff} = D_{GBs,0} \exp \left(-\frac{Q}{kT} \right) \frac{H_{GBs} \delta(T)}{d_{grains}}, \quad (8.17)$$

where $D_{GBs,0}$ and Q are the pre-coefficient and activation energy for the D_{GBs} , respectively, which could be determined from Eq. (8.12). Additionally, $\delta(T)$ can be determined from Eq. (8.13). Once the average grain size (d_{Grain}) was known, we could calculate the D_{eff} based on Eq. (8.17).

8.4. Experimental Results and Comparison

The Al film used for the electromigration test is found to have a columnar polycrystal microstructure, as shown in Figure 8.12. From the top view of non-annealed (Figure 8.12 (a)), a polycrystal microstructure can be observed and average grain size is ~ 454.4 nm. From the side view (Figure 8.12 (b)), the cross-section prepared by focused ion beam (FIB) shows a single grain in the thickness direction.

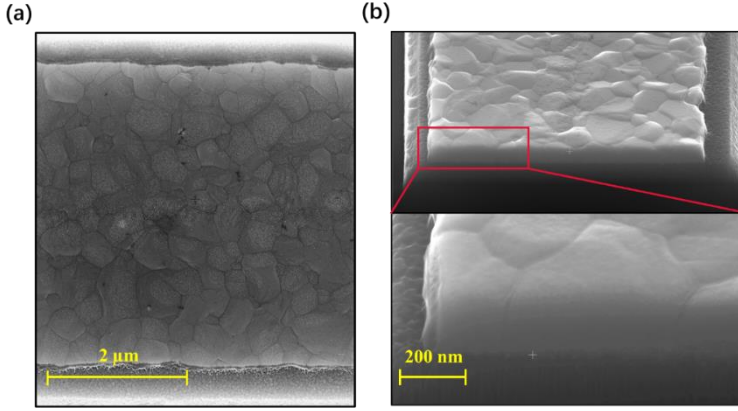


Figure 8.12. (a) SEM image of the Al film from the top view. (b) SEM image of the cross-section of the Al film from the side view.

Figure 8.13 shows the electromigration results at different temperatures at testing time of 20 h. The void at the left side and hillock at the right side can be observed. And the Al line tested at the higher temperature shows a longer void length. In the present test, we tested three samples at each temperature level; corresponding results of void length are listed in Table 1. Based on Eq. (8.11), we can determine the D_{eff} at different temperatures experimentally. Here, $Z^*=1$ [29], $e=1.6 \times 10^{-19}$ C, $\rho=2.82 \times 10^{-8}$ $\Omega \cdot \text{m}$ [30], $j=1 \times 10^{10}$ A/m², $k=1.38 \times 10^{-23}$ J/K, and $L=100$ μm are used. Figure 14 plots the effective diffusivity obtained from experiments. The corresponding Arrhenius equation for effective diffusivity is $5.01 \times 10^{-9} \exp(-1.21 \text{ eV}/kT)$ m²/s.

In Figure 8.14, the calculated diffusivity based on Equation (8.17) is also included, as shown in the solid line. The $d_{\text{grains}} = 450$ nm obtained from experiment and $H_{\text{GBs}} = 2.91$ are used. From Figure 8.14, a very good agreement between the diffusivity obtained from electromigration test and the predicted ones is obtained. Traditionally, there is a gap between MD predicted diffusivity and experimental results, as the MD simulations with a very large grain size, such as 450 nm, are prohibited due to the huge size of the MD model. In the present study, we treat the diffusion in polycrystal as a composite of diffusion in GBs and grains. The effects of temperature and grain size on diffusivity are taken into account in Eq. (8.17) by combining the Arrhenius equation and Hart equation. Then, the average diffusivity of polycrystal can be determined via calculating the key parameters. The good agreement between calculation and experimental result demonstrates that the proposed methodology has

the capability to calculate the effective diffusivity accurately. And this approach can be used to calculate the diffusivity for the other polycrystal metals.

Table 8.1. Void lengths for the Al lines after electromigration tests

Temperature (°C)	Void length (μm)		
	#1	#2	#3
200	2.1	1.8	2.5
250	3.7	3.5	3.3
300	8.2	12.4	10.5
350	17.3	21.2	18.5

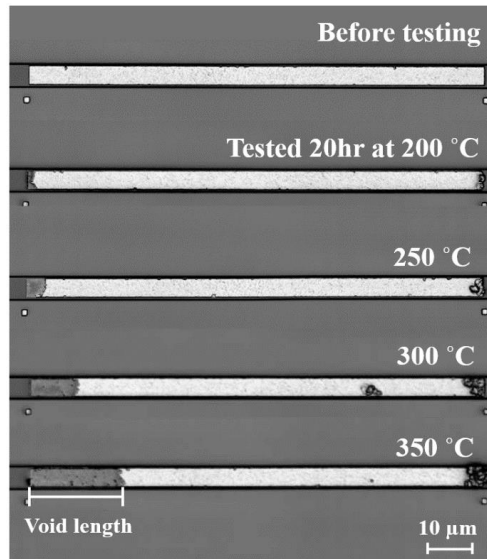


Figure 8.13. Optical microscope images for the Al stripe before and after electromigration tests at 200, 250, 300 and 350 °C for 20 h.

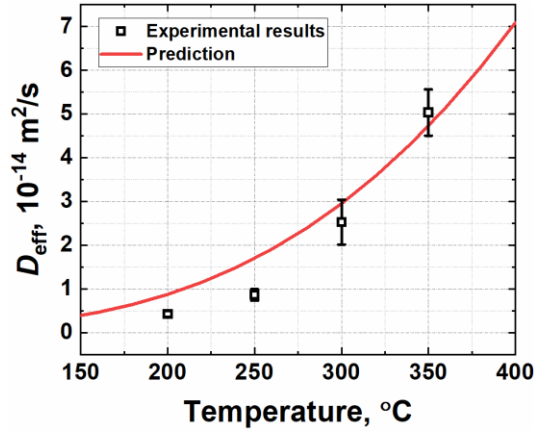


Figure 8.14. Markers represent the D_{eff} determined from electromigration experiments. The solid line represents the D_{eff} calculated using our model.

8.5. Conclusions

In this chapter, an experimentally validated approach that relies on the MD simulation for calculating effective diffusivity was developed. Firstly, the MD simulations were performed to determine the parameters used for the calculation of effective diffusivity. The atomic diffusivity along GBs could be expressed as an Arrhenius equation and the GB's thickness could be given as an empirical equation of temperatures. Additionally, the atomic diffusivity along GBs was at least several orders higher than that in the grains. Combining the results of effective diffusivity with the atomic diffusion features in grains and GBs, we find that the effects of grain size on overall diffusivity are through the volume fraction of atoms in grain boundaries. Then, based on these MD results, we propose a simulation-based diffusion model that can be used to predict effective diffusivity. Finally, the effective diffusivities from the calculation are compared to the experimental results determined using electromigration testing method. The good agreement between calculation and experiment provides validation for the present methodology. Henceforth, the approach developed in this paper can be used to determine the diffusivity in various polycrystalline metals.

References

1. Seeger, A., D. Wolf, and H. Mehrer, Analysis of tracer and nuclear magnetic resonance measurements of self - diffusion in aluminium. *Physica status solidi*, 1971. 48(2): p. 481-496.
2. Lundy, T. and J. Murdock, Diffusion of Al²⁶ and Mn⁵⁴ in aluminum. *Journal of Applied Physics*, 1962. 33(5): p. 1671-1673.
3. Demmel, F., et al., Diffusion in liquid aluminium probed by quasielastic neutron scattering. *Physical Review B*, 2011. 84(1): p. 014307.
4. Peterson, N., Grain-boundary diffusion in metals. *International metals reviews*, 1983. 28(1): p. 65-91.
5. Preis, W. and W. Sitte, Fast grain boundary diffusion and rate-limiting surface exchange reactions in polycrystalline materials. *Journal of applied physics*, 2005. 97(9): p. 093504.
6. Cho, J. and C. Thompson, Grain size dependence of electromigration - induced failures in narrow interconnects. *Applied Physics Letters*, 1989. 54(25): p. 2577-2579.
7. Budke, E., et al., Tracer diffusion of Au and Cu in a series of near $\Sigma=5$ (310)[001] symmetrical Cu tilt grain boundaries. *Acta materialia*, 1999. 47(2): p. 385-395.
8. Ma, Q. and R. Balluffi, Diffusion along [001] tilt boundaries in the Au/Ag system—I. Experimental results. *Acta metallurgica et materialia*, 1993. 41(1): p. 133-141.
9. Wang, P.-C., et al., Electromigration-induced stress in aluminum conductor lines measured by x-ray microdiffraction. *Applied Physics Letters*, 1998. 72(11): p. 1296-1298.
10. Surholt, T. and C. Herzig, Grain boundary self-diffusion in Cu polycrystals of different purity. *Acta materialia*, 1997. 45(9): p. 3817-3823.
11. Suzuki, A. and Y. Mishin, Atomic mechanisms of grain boundary diffusion: Low versus high temperatures. *Journal of materials science*, 2005. 40(12): p. 3155-3161.
12. Sørensen, M.R., Y. Mishin, and A.F. Voter, Diffusion mechanisms in Cu grain boundaries. *Physical Review B*, 2000. 62(6): p. 3658.
13. Sellers, M.S., et al., β -Sn grain-boundary structure and self-diffusivity via molecular dynamics simulations. *Physical Review B*, 2010. 81(13): p. 134111.
14. Brostow, W., J.-P. Dussault, and B.L. Fox, Construction of Voronoi polyhedra. *Journal of Computational Physics*, 1978. 29(1): p. 81-92.
15. Finney, J., A procedure for the construction of Voronoi polyhedra. *Journal of computational physics*, 1979. 32(1): p. 137-143.

16. Voter, A.F., Embedded atom method potentials for seven fcc metals: Ni, Pd, Pt, Cu, Ag, Au, and Al. Los Alamos Unclassified Technical Report# LA-UR, 1993: p. 93-3901.
17. Stukowski, A., Visualization and analysis of atomistic simulation data with OVITO—the Open Visualization Tool. *Modelling and Simulation in Materials Science Engineering*, 2009. 18(1): p. 015012.
18. Hu, D., et al., Thermal kinetic and mechanical behaviors of pressure-assisted Cu nanoparticles sintering: A molecular dynamics study. *Results in Physics*, 2020: p. 103486.
19. Naeiji, P., F. Varaminian, and M. Rahmati, The kinetic modeling of methane hydrate growth by using molecular dynamic simulations. *International Journal of Heat and Mass Transfer*, 2019. 142: p. 118356.
20. Rao, Z., S. Wang, and F. Peng, Self diffusion and heat capacity of n-alkanes based phase change materials: A molecular dynamics study. *International Journal of heat mass transfer*, 2013. 64: p. 581-589.
21. Annamareddy, A., et al., Mechanisms of bulk and surface diffusion in metallic glasses determined from molecular dynamics simulations. *Acta Materialia*, 2021: p. 116794.
22. Pun, G.P. and Y. Mishin, A molecular dynamics study of self-diffusion in the cores of screw and edge dislocations in aluminum. *Acta Materialia*, 2009. 57(18): p. 5531-5542.
23. Blech, I., Diffusional back flows during electromigration. *Acta Materialia*, 1998. 46(11): p. 3717-3723.
24. Tan, C.M. and A. Roy, Electromigration in ULSI interconnects. *Materials Science and Engineering: R: Reports*, 2007. 58(1-2): p. 1-75.
25. Hart, E., On the role of dislocations in bulk diffusion. *Acta Metallurgica*, 1957. 5(10): p. 597.
26. Chen, Y. and C.A. Schuh, Geometric considerations for diffusion in polycrystalline solids. *Journal of Applied Physics*, 2007. 101(6): p. 063524.
27. Thorvaldsen, A., The intercept method—1. Evaluation of grain shape. *Acta materialia*, 1997. 45(2): p. 587-594.
28. Thorvaldsen, A., The intercept method—2. Determination of spatial grain size. *Acta materialia*, 1997. 45(2): p. 595-600.
29. Blech, I.A., Electromigration in thin aluminum films on titanium nitride. *Journal of applied physics*, 1976. 47(4): p. 1203-1208.

30. Serway, R.A., Principles of Physics . Fort Worth, Texas; London: Saunders College Pub. 1998, ISBN 0-03-020457-7.

9

9

CONCLUSIONS AND RECOMMENDATIONS

This chapter summarises the main conclusion that can be derived from this dissertation, while considering the objective as postulated in Section 1.3.

9.1. Conclusion

A comprehensive and integrated study of electromigration in microelectronics was conducted, including the theory development, numerical simulation, and experimental study. The multi-physics-driven continuum theory was used to couple different physical causes during electromigration. The vacancy volume relaxation and atomic diffusion features were systematically studied by using MD simulations. Moreover, extensive experimental studies, from testing wafer/die design and fabrication, sample preparation and process, to the measurement setup and characterization, were carried out. By combining experiments with simulations, the effects of self-diffusion, mechanical stress, and thermomigration on electromigration were investigated. The major conclusions in this dissertation are summarised as follows.

9.1.1. Fully Coupled Multi-Physics-Driven Model of Electromigration

In this study, several long-standing problems and questions in the formulation of electromigration were addressed. A fully coupled and self-consistent electromigration theory was developed. Some key contributions are summarized as follows:

- 1) The mass conservation equation in terms of the total strain can describe the diffusion process, which is driven by interacting driving forces, such as electron wind, gradients of atomic concentration, temperature, and mechanical stress.
- 2) A new diffusion-induced strain equation using the vacancy volume relaxation factor,

based on MD simulations, was applied.

- 3) The exact relationship between hydrostatic stress and vacancy concentration was developed.
- 4) An electromigration failure criterion based on the critical atomic or vacancy concentration was proposed.

9.1.2. Experiment and Simulation

For the experimental study in this dissertation, electromigration testing dies in 4-inch full wafer, with more than 3000 testing samples, including various testing structures per wafer, were designed and fabricated. Different factors influencing electromigration were considered in the design of experiment. The in-situ resistance monitoring and microstructure analysis using SEM and EDS were performed to understand failure mechanisms. Meanwhile, extensive fully coupled simulations using parameters set in experiments were conducted. Synergetic and cohesive analyses between the simulation and experiment are provided. The following conclusions and understandings of electromigration are presented.

Effect of Self-diffusion on Electromigration: First, it was theoretically determined that the progression of electromigration failure under a zero mechanical stress condition is comparable with electromigration failure under a totally confined condition. Second, the steady state solution for threshold product of jL under the stress-free condition is consistent with the experimental results reported in the literature. These indicate that the self-diffusion can independently counter-balance electron wind force, and the vacancy concentration can be used as a decisive parameter to define electromigration failure. Moreover, in Chapter 5, by simulating the bare stripes tested in the experiments as stress-free metal lines, the predicted electromigration failures were shown to be in excellent agreement with the experimental observations for void formation to void growth. This confirms again that self-diffusion plays an important role in balancing electromigration. Therefore, to accurately predict electromigration failures, it is necessary to consider the coupling effect of self-diffusion on electromigration.

Mechanical Stress on Electromigration: In this study, an exact hydrostatic stress-vacancy concentration ($\sigma-C_v$) equation was derived, which satisfies both the equilibrium equation and the mechanical boundary condition. The effect of passivation on the $\sigma-C_v$ equation was also considered by using Eshelby's solution. The experimental study showed that the Si_3N_4 passivation layer can significantly reduce the electromigration development in the annealed

conductor compared with the annealed conductor without passivation. Based on the fully coupled theory with exact σ - C_v relation, simulation results agree well with experimental observations. Additionally, the analytical solution showed that the mechanical stress gradient plays a more important role in balancing electromigration than the self-diffusion.

Coupling Effect of Thermomigration on Electromigration: In this study, thermomigration accompanying electromigration was studied by using Blech's and SWEAT structures. In Blech's structure, with the increasing current density and conductor length, it was observed that voids are spreading throughout the middle region of the conductor. In the SWEAT structure, voids were observed in a wide range of the entire conductor, and the metal line breaks off centre toward the anode side. Unlike the rapid void formation at the cathode in Blech's structure, void formations in the middle of Blech's and SWEAT structures require significantly more time. Based on the fully coupled electromigration model, the numerical results and theoretical predictions were remarkably consistent with the experimental results. Additionally, it was revealed that the temperature gradient, related to the current density and conductor length, was the cause for void formations at the middle region and breaking off centre toward the anode.

Other Contributions from Experiments: In this study, environmental factors, such as air vs. vacuum and temperature, and process factors, such as annealing and passivation layer, were experimentally investigated. It was found that the annealing of the sample in vacuum can significantly reduce the electromigration, and the oxidation of a conductor tested in air can accelerate electromigration development. Importantly, we found that the passivation layer could prevent the oxidation of Al stripes to reduce electromigration development. Moreover, the passivation in annealed sample could protect the conductor and significantly reduce the electromigration; however, the passivation in the non-annealed sample failed to reduce electromigration.

9.1.3. Atomistic Modelling on Electromigration Study

In this study, by using large-scale MD simulation, the concentration-dependent vacancy volume relaxation factors for Al, Cu, and Au were calculated. A uniform empirical equation was developed to express the vacancy volume relaxation factor as a function of the vacancy concentration. Meanwhile, the hydrostatic stress was also calculated using MD simulations. Based on the MD simulation results, a new diffusion-induced strain equation using the vacancy volume relaxation factor was presented. Furthermore, the atomistic modelling

method was also used to explain the phenomenon observed in the experiments. In Chapter 5, the MD simulation showed that thermal annealing can reduce the defects in polycrystalline and promote the coalescence of grains, explaining why the annealed Al stripe could have better reliability against electromigration. In Chapter 6, the MD simulations of thermomigration was presented, where the movement directions of Al and Sn atoms under temperature gradient were consistent with the experimental observations reported in literature. In addition, in Chapter 8, the developed MD-based diffusion was presented and used to determine the effective diffusivity in polycrystal metals. The activation energy for the Arrhenius equation, volume fraction of atoms in grain boundaries, and the grain boundary thickness were determined from the MD results. The predicted effective diffusivity based on the MD simulation was consistent with the diffusivity determined from the electromigration experiments.

These studies adequately show that atomistic modelling has great potential in the study of electromigration. It can be used to determine critical parameters related to electromigration modelling, explain failure mechanisms for electromigration experiments, and predict the diffusion behaviours in various metallic systems.

9.1.4. Numerical Implementation with Finite Element Method

In this study, the general coupling model of electromigration was implemented in ANSYS and COMSOL. A 1-D metal line with a totally fixed configuration and stress-free configuration was given as benchmark problem. The finite element solutions from ANSYS and COMSOL were in excellent agreement with the analytical solutions. These works provide easy implementation of the present study in practical applications.

9.2. Recommendations for Future Work

1. The MD calculation of the vacancy volume relaxation factor (f) in this study was conducted under 500 K, without considering the influence of different temperatures. Further calculations of f with various temperatures should be conducted to update the empirical equation of f as a function of the vacancy concentration and temperature. Furthermore, the determination of the effective charge number Z^* by using atomistic modelling is also suggested for future studies.

2. Although the present study investigated the effect of microstructures on electromigration developments through experimental characterization and MD simulations, simulations based

on continuum theory did not consider the effect of microstructure on void formation and evolution. To further understand electromigration failures, electromigration simulation in a conductor should be performed with real microstructures. The micro-structure enriched finite element simulation with mesoscale calculation is a possible candidate to achieve this.

3. Currently, although it is not available for industry engineers for correctly performing fully coupled modelling through commercial software, present works provide a good basis. General coupling model was implemented in ANSYS and COMSOL. As an update, the implementation of new diffusion strain in ANSYS and COMSOL is not difficult. Implementation in ABAQUS is planned in the future study, and some preparation work has been done.

4. Entropy-based damage model will be a more comprehensive description of electromigration failure compared with the critical atomic/vacancy concentrations proposed in this work. Irreversible entropy production from mass diffusion, viscoplastic deformation, and joule heating can be used to characterize material degradation due to electromigration. The threshold entropy can be used to determine the MTTF.

5. Nowadays, electromigration accompanied by thermomigration in solder joints is a major reliability concern. A comprehensive understanding of electromigration in solder joints is urgent. (1) The developed fully coupled model assumes that the atoms diffuse in metallic systems via substitutional diffusion, which is dominated by the diffusion mechanism in pure metal. However, for the electromigration in solder, atoms interstitially diffuse in composite materials, and chemical reactions may occur during electromigration in solder, which is an entirely different failure mechanism from void and hillock formations. Therefore, a new coupling model and failure criterion are necessary for describing electromigration in solder. (2) In this thesis, we established a complete electromigration measurement setup, which can be applied to the experimental study of solder. It is recommended to design an experiment to investigate the thermomigration in solder without electromigration, and the in-situ SEM observation is suggested for observing the failure process in the solder joint.

6. The application temperature in SiC-based devices is at least 300 °C. Thus, the temperature used in the accelerated tests of electromigration actually is the working temperature of SiC-based devices. Moreover, the SiC die attach and interconnect is moving away from solders and wire bonds towards sintered silver or copper structure. As sintered structure is a kind of porous material, thus the electromigration behaviour may be different from the copper interconnect and solder. More research about it will be valuable.

Appendix A

Eshelby's Solution

Eshelby solution

The metal line covered by Si_3N_4 layer is simplified as following structure,

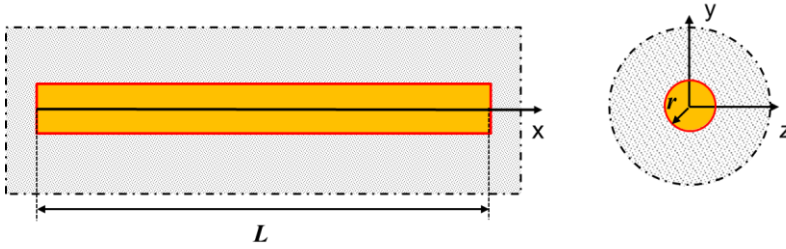


Figure A1. Schematic for the structure of metal line covered by passivation layer.

We make following assumptions,

1. Metal line is assumed as a circle cylinder inclusion with $L \gg r$.
2. Metal line is embedded in an infinity dielectric matrix.
3. Both metal line and dielectric matrix are considered as elastic materials, E_c and ν_c for conductor, E_m and ν_m for dielectric matrix.

For the metal line with eigenvalue ε_{ij}^* ,

$$\varepsilon_{ij}^* = \varepsilon^* \delta_{ij} \quad (\text{A1})$$

where ε^* can be diffusion strain or thermal strain. Based on the Hooke's law, the stress-strain relationship with eigenvalue can be written as follows,

$$\begin{aligned} \sigma_x &= 2G(\varepsilon_x - \varepsilon^*) + \lambda(\varepsilon_{kk} - 3\varepsilon^*) \\ \sigma_y &= 2G(\varepsilon_y - \varepsilon^*) + \lambda(\varepsilon_{kk} - 3\varepsilon^*) \\ \sigma_z &= 2G(\varepsilon_z - \varepsilon^*) + \lambda(\varepsilon_{kk} - 3\varepsilon^*) \end{aligned} \quad (\text{A2})$$

where G and λ are Lamé's constants, $G = \frac{E_c}{2(1+\nu_c)}$ and $\lambda = \frac{E_c \nu_c}{(1+\nu_c)(1-2\nu_c)}$. Above equation can be equivalently rewritten as follows,

$$\begin{aligned} 0 &= 2G[\varepsilon_x - (\varepsilon^* + \frac{\sigma_x}{E})] + \lambda[\varepsilon_{kk} - (3\varepsilon^* + \frac{\sigma_x}{E} - \frac{2\nu\sigma_x}{E})] \\ \sigma_y &= 2G[\varepsilon_y - (\varepsilon^* - \frac{\nu\sigma_x}{E})] + \lambda[\varepsilon_{kk} - (3\varepsilon^* + \frac{\sigma_x}{E} - \frac{2\nu\sigma_x}{E})] \\ \sigma_z &= 2G[\varepsilon_z - (\varepsilon^* - \frac{\nu\sigma_x}{E})] + \lambda[\varepsilon_{kk} - (3\varepsilon^* + \frac{\sigma_x}{E} - \frac{2\nu\sigma_x}{E})] \end{aligned} \quad (A3)$$

As the transformation from Equation (A2) to (A3), present problem can be considered as a plane stress problem with new eigenvalue ε'_{ij} ,

$$\varepsilon'_x = \varepsilon^* + \frac{\sigma_x}{E_c}, \varepsilon'_y = \varepsilon'_z = \varepsilon^* - \frac{\nu_c \sigma_x}{E_c} \quad (A4)$$

To obtain a complete stress-strain relation as shown in Equations (A3), we still need a relation between ε'_{ij} and ε_{ij} . Based on the Eshelby's theory, this relation can be expressed as follows,

$$\varepsilon_{ij} = S'_{ijkl} \varepsilon'_{kl} \quad (A5)$$

where the plane-stress inhomogeneity Eshelby's tensor (S'_{ijkl}) is,

$$S'_{ijkl} = \begin{bmatrix} 1 & A + \frac{\nu_m}{2}(B+C) & A + \frac{\nu_m}{2}(B+C) \\ 0 & \frac{5+\nu_m}{8}B + \frac{3\nu_m-1}{8}C & \frac{5+\nu_m}{8}C + \frac{3\nu_m-1}{8}B \\ 0 & \frac{5+\nu_m}{8}C + \frac{3\nu_m-1}{8}B & \frac{5+\nu_m}{8}B + \frac{3\nu_m-1}{8}C \end{bmatrix},$$

and:

$$A = -\frac{E_c \nu_m - E_m \nu_c}{E_c + E_m + E_c \nu_m - E_m \nu_c},$$

$$B = \frac{E_c(5E_c + 3E_m + E_c \nu_m - E_m \nu_c)}{-E_c^2 \nu_m^2 + 2E_c^2 \nu_m + 3E_c^2 + 2E_c E_m \nu_c \nu_m - 2E_c E_m \nu_c + 4E_c E_m - E_m^2 \nu_c^2 + E_m^2},$$

$$C = \frac{E_c(E_c - E_m - 3E_c v_m + 3E_m v_c)}{-E_c^2 v_m^2 + 2E_c^2 v_m + 3E_c^2 + 2E_c E_m v_c v_m - 2E_c E_m v_c + 4E_c E_m - E_m^2 v_c^2 + E_m^2}.$$

Applying the Equation (A4) to Equation (A5), we can obtain the ε_{ij} as follows,

$$\begin{aligned}\varepsilon_x &= \frac{(1+v_c)(1-2v_c)+\varphi(1+v_m)}{E_c(1+\varphi-v_c+\varphi v_m)} \sigma_x + \frac{1+\varphi+\varphi v_m+v_c}{1+\varphi+\varphi v_m-v_c} \varepsilon^* \\ \varepsilon_y &= \frac{(1+v_m)\varphi}{1-v_c+\varphi+\varphi v_m} \left(\varepsilon^* - \frac{v_c \sigma_x}{E_c} \right) \\ \varepsilon_z &= \frac{(1+v_m)\varphi}{1-v_c+\varphi+\varphi v_m} \left(\varepsilon^* - \frac{v_c \sigma_x}{E_c} \right)\end{aligned}\quad (A6)$$

where $\varphi=E_c/E_m$. Applying Eqs. (A6) to Eqs. (A3), we can obtain σ_y and σ_z as follows,

$$\begin{aligned}\sigma_y &= -\frac{E_c}{1-v_c+\varphi+\varphi v_m} \varepsilon^* + \frac{v_c}{1-v_c+\varphi+\varphi v_m} \sigma_x \\ \sigma_z &= -\frac{E_c}{1-v_c+\varphi+\varphi v_m} \varepsilon^* + \frac{v_c}{1-v_c+\varphi+\varphi v_m} \sigma_x\end{aligned}\quad (A7)$$

From Equations (A6) and (A7), it can be seen that the strain and stress become the functions of ε_{ij}^* and σ_x .

Case 1: Metal Line Laterally Confined in Elastic Matrix



Figure A2. Schematic for the structure of metal line laterally confined in elastic matrix.

When the metal line is laterally confined in dielectric matrix and both ends of conductor are stress free, as shown in Figure A2, we have the following mechanical boundary conditions,

$$\begin{aligned}
 \sigma_x(t, 0) &= \sigma_x(t, L) = 0 \\
 \varepsilon_{xy} &= \varepsilon_{xz} = \varepsilon_{yz} = 0 \\
 \sigma_{xy} &= \sigma_{xz} = \sigma_{yz} = 0
 \end{aligned} \tag{A8}$$

Based on the equilibrium equation $\frac{\partial \sigma_x}{\partial x} = 0$ and above mechanical condition, we have,

$$\sigma_x(t, x) = 0 \tag{A9}$$

Applying it to Equation (A6) and (A7), we can obtain the strain and stress as follows,

$$\begin{aligned}
 \varepsilon_x &= \frac{1+\varphi+\varphi v_m+v_c}{1-v_c+(1+v_m)\varphi} \varepsilon^*, \\
 \varepsilon_y &= \varepsilon_z = \frac{(1+v_m)\varphi}{1-v_c+(1+v_m)\varphi} \varepsilon^* \\
 \sigma_y &= \sigma_z = -\frac{E_c}{1-v_c+(1+v_m)\varphi} \varepsilon^*.
 \end{aligned} \tag{A10}$$

The volumetric strain and hydrostatic stress are,

$$\begin{aligned}
 \theta &= \frac{1+v_c+3(1+v_m)\varphi}{1-v_c+(1+v_m)\varphi} \varepsilon^* \\
 \sigma &= \frac{\sigma_x+\sigma_y+\sigma_z}{3} = -\frac{2E_c}{3[1-v_c+(1+v_m)\varphi]} \varepsilon^*
 \end{aligned} \tag{A11}$$

Case 2: Metal Line Fully Confined in Elastic Matrix

When the metal line is laterally confined in dielectric matrix and both ends of conductor are fixed, as shown in Figure A3, we have the following mechanical boundary conditions,

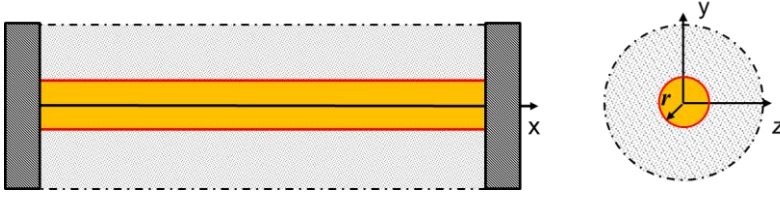


Figure A3. Schematic for the structure of metal line fully confined in elastic matrix.

$$\begin{aligned}
 u_x(t, 0) &= u_x(t, L) = 0 \\
 \varepsilon_{xy} &= \varepsilon_{xz} = \varepsilon_{yz} = 0 \\
 \sigma_{xy} &= \sigma_{xz} = \sigma_{yz} = 0
 \end{aligned} \tag{A12}$$

Based on the equilibrium equation, we have,

$$\frac{\partial \sigma_x}{\partial x} = 0 \rightarrow \sigma_x = \text{cons.} \tag{A13}$$

Applying Equations (A12) and (A13) to Equation (A6), we obtain σ_x ,

$$\sigma_x = -\frac{E_c(1+\varphi+\varphi v_m+v_c)}{[(1+v_c)(1-2v_c)+\varphi(1+v_m)]L} \int_0^L \varepsilon^* dx \tag{A14}$$

Then, the other strain and stress can be determined as follows,

$$\begin{aligned}
 \varepsilon_x &= \frac{1+\varphi+\varphi v_m+v_c}{1+\varphi+\varphi v_m-v_c} (\varepsilon^* - \int_0^L \varepsilon^* dx) \\
 \varepsilon_y = \varepsilon_z &= \frac{(1+v_m)\varphi}{1-v_c+\varphi+\varphi v_m} (\varepsilon^* + \frac{v_c(1+v_c+\varphi+\varphi v_m)}{[(1+v_c)(1-2v_c)+\varphi(1+v_m)]L} \int_0^L \varepsilon^* dx) \\
 \sigma_y = \sigma_z &= -\frac{E_c}{1-v_c+\varphi+\varphi v_m} (\varepsilon^* + \frac{v_c(1+v_c+\varphi+\varphi v_m)}{[(1+v_c)(1-2v_c)+\varphi(1+v_m)]L} \int_0^L \varepsilon^* dx)
 \end{aligned} \tag{A15}$$

Case 3: Metal Line Fully Confined in Matrix with $E_m = +\infty$

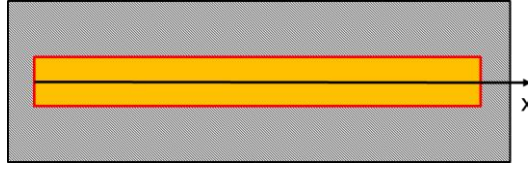


Figure A4. Schematic for the structure of metal line fully confined in rigid layer.

When the matrix has an infinity large Young's modulus and both ends of conductor are fixed, the solution can be obtained based on the solution of case#2. The infinity large Young's modulus means,

$$\varphi = \frac{E_c}{E_m} \xrightarrow{E_m = +\infty} \varphi = 0, \quad (\text{A16})$$

Applying it to Equations (C14) and (C15), we can obtain the strain and stress as follows,

$$\begin{aligned} \sigma_x &= -\frac{E_c}{(1-2\nu_c)} \int_0^L \varepsilon^* dx \\ \varepsilon_x &= \frac{1+\nu_c}{1-\nu_c} \left(\varepsilon^* - \frac{1}{L} \int_0^L \varepsilon^* dx \right) \\ \varepsilon_y &= \varepsilon_z = 0 \\ \sigma_y = \sigma_z &= -\frac{E_c}{1-\nu_c} \left(\varepsilon^* - \frac{\nu_c}{1-2\nu_c} \frac{1}{L} \int_0^L \varepsilon^* dx \right) \end{aligned} \quad (\text{A17})$$

And, the volumetric strain and hydrostatic stress are,

$$\begin{aligned} \theta &= \frac{1+\nu_c}{1-\nu_c} \left(\varepsilon^* - \frac{1}{L} \int_0^L \varepsilon^* dx \right) \\ \sigma &= \frac{\sigma_x + \sigma_y + \sigma_z}{3} = -\frac{2E}{3(1-\nu_c)} \left[\varepsilon^* + \frac{1+\nu_c}{2(1-2\nu_c)L} \int_0^L \varepsilon^* dx \right] \end{aligned} \quad (\text{A18})$$

These results are same to the stress and strain obtained for the metal line under total confinement.

Appendix B

Method to Calculate the Void Length

B1. Drift Velocity:

Based on Nernst-Einstein equation, the drift velocity is given as following equation,

$$v = D_a \frac{F}{kT} \quad (B1)$$

where D_a is the atomic diffusion coefficient and F is the driving force of atomic diffusion. In Blech's study, the net drift velocity during electromigration is,

$$v = v_{EM} + v_s \quad (B2)$$

where v_{EM} is the drift velocity induced by electron wind, and v_s is the drift velocity induced by stress gradient. Actually, a complete formulation of drift velocity should also consider the contribution from self-diffusion and thermomigration, as shown in following equation,

$$v = v_{EM} + v_s + v_C + v_T \quad (B3)$$

where v_C is the drift velocity induced by concentration gradient and v_T is the drift velocity induced by temperature gradient. In present study, as a uniform temperature condition is applied, thus the net drift velocity is,

$$v = v_{EM} + v_s + v_C \quad (B4)$$

Equation (B4) can be further extended as,

Appendix B

$$v = \frac{D_a}{kT} \left(-Z^* e \rho j - \frac{kT \Delta C}{\Delta l} + \frac{\Delta \sigma}{\Delta l} \right) \quad (B5)$$

where Z^* is the effective charge, e the electronic charge, ρ the resistivity, j the current density.

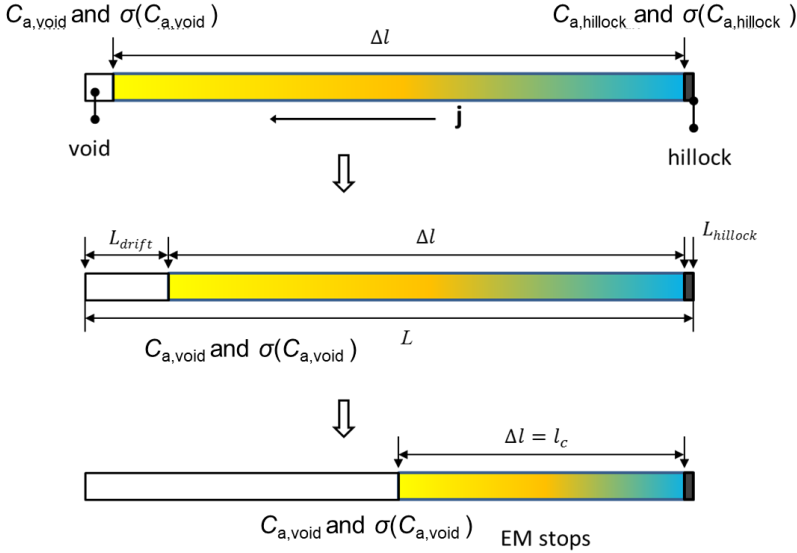


Figure B1 The schematic for the electromigration

As illustrated in Figure B1, ΔC is the difference of atomic concentration at both ends, and its maximum value is,

$$\Delta C_a = C_{a,hillock} - C_{a,void} \quad (B6)$$

where $C_{a,hillock}$ means saturation atomic concentration to form hillock and $C_{a,void}$ means the saturation atomic concentration to form void. Δl is the distance between $C_{a,hillock}$ and $C_{a,void}$. $\Delta \sigma$ is the difference of hydrostatic stresses that depends on the concentration, $\sigma(C_{a,hillock})$ and $\sigma(C_{a,void})$. Thus, Equation (B5) can be rewritten as follows,

$$v = \frac{D}{kT} \left[-Z^* e \rho j - \frac{kT(C_{a,hillock} - C_{a,void})}{\Delta l} + \frac{\sigma(C_{a,hillock}) - \sigma(C_{a,void})}{\Delta l} \right] \quad (B7)$$

If we assume that the saturation concentration to form hillock $C_{a,hillock}$ and saturation concentration to form void $C_{a,void}$ do not change during EM, when the drift length (length of

void) expands during EM, as illustrated in Figure B1, the Δl will decrease and leads to the increases of driving forces of stress gradient and self-diffusion. When Δl decreases to the critical length, electron wind force can be fully balanced by self-diffusion and stress-migration,

$$Z^*e\rho j = -\frac{kT(C_{a,hillock}-C_{a,void})}{l_c} + \frac{\sigma(C_{a,hillock})-(C_{a,void})}{l_c} \quad (B8)$$

And, the net drift velocity becomes zero ($v=0$).

B2. Determination of critical concentration and atomic diffusion coefficients

In the present study, we did the EM test under stress-free configuration, the drift velocity can be expressed as follows,

$$v = \frac{D_a}{kT} \left[-Z^*e\rho j - \frac{kT(C_{a,hillock}-C_{a,void})}{\Delta l} \right] \quad (B9)$$

As we observed that the critical length is $L_c=10 \mu\text{m}$ in measurement, thus the critical concentration difference can be determined via following equation,

$$Z^*e\rho j = -kT \frac{kT(C_{a,hillock}-C_{a,void})}{L_c} \quad (B10)$$

Using the parameters shown in Table. B1, we calculate the critical atomic concentration difference is $C_{a,hillock} - C_{a,void} = 0.1C_{a0}$.

Furthermore, as we have tested the drift length for 100 μm stripe at 10 hours is 2.19 μm , thus the drift velocity is 0.0608 nm/s and $\Delta l = 97.81 \mu\text{m}$. Applying those value and critical concentration to Equation (B9), we can determine the atomic diffusion coefficients via following equation,

$$D_a = vkT / \left[-Z^*e\rho j - \frac{kT\Delta C_c}{\Delta l} \right] \quad (B11)$$

As a result, $D_a = 1.025 \times 10^{-15} \text{m}^2/\text{s}$.

Table B1. The parameters for Aluminum

Effective charge number (Z^*)	1
Elementary charge (e)	1.6×10^{-19} C
Electrical resistivity (ρ)	2.88×10^{-8} Ohm·m
Boltzmann constant (k)	1.38×10^{-23} J/K
Temperature (T)	550 K

B3. Calculation of drift length

Therefore, the drift velocity under stress free configuration can be expressed as,

$$v(t) = \frac{D_a}{kT} \left[-Z^* e \rho j - \frac{kT \Delta C_c}{\Delta l(t)} \right] \quad (B12)$$

The drift length is the integral of drift velocity over testing time t ,

$$L_{drift} = \int_0^t v(t) dt \quad (B13)$$

As the total length of stripe is the sum of L_{drift} , Δl and $L_{hillock}$, and experiment shows that the $L_{hillock}$ only occupies a small part of total length. Thus, the total length of strip can be approximately expressed as follows,

$$L \approx L_{drift} + \Delta l \quad (B14)$$

Applying this relation to Equation (B13), we can obtain the following equation,

$$L_{drift} = \int_0^t \frac{D}{kT} \left[-Z^* e \rho j - \frac{kT \Delta C_c}{L - L_{drift}} \right] dt \quad (B15)$$

Then, the numerical solution is calculated by using Matlab.

For the Al strip covered by SiN layer, the effect of stress on EM is considered. In our theory, we have coupled the hydrostatic stress with atomic concentration as follows,

$$\sigma(C_a) = -\frac{2E_c(1-f)}{9[1-v_c+(1+v_m)\varphi]} \ln(C_a) \quad (B16)$$

Thus, the difference of hydrostatic stress at two sides can be obtained,

$$\Delta\sigma_c = -\frac{2E_c(1-f)}{9[1-v_c+(1+v_m)\varphi]} \ln\left(\frac{C_{a,hillock}}{C_{a,void}}\right) \quad (B17)$$

Applying this relation to Equation (B7), we can obtain the net drift velocity under confined configuration,

$$v(t) = \frac{D}{kT} \left[-Z^* e \rho j - \frac{kT \Delta C_c}{\Delta l(t)} - \frac{2E_c(1-f)}{9[1-v_c+(1+v_m)\varphi] \Delta l(t)} \ln\left(\frac{C_{a,hillock}}{C_{a,void}}\right) \right] \quad (B18)$$

Then, combining Equations (B19) with (B14) and (B15), the drift length can be calculated via following equation,

$$L_{drift} = \int_0^t \frac{D}{kT} \left[-Z^* e \rho j - \frac{kT \Delta C_c}{L-L_{drift}} - \frac{2E_c(1-f)}{9[1-v_c+(1+v_m)\varphi](L-L_{drift})} \ln\left(\frac{C_{a,hillock}}{C_{a,void}}\right) \right] dt \quad (B19)$$

Finally, the numerical solution can be calculated by using Matlab.

Appendix C

Molecular Dynamic Simulation of Thermal Annealing on Al

C1. Growth Modes in Thin Metal Film

During the deposition process, adatoms are not able to achieve their fully relaxed locations. Three growth modes have been identified as illustrated in Figure C1: (1) Frank-van de Merwe (FM) mode also known as layer-by-layer growth; (2) Volmer-Weber (VM) also known as island growth and (3) Stranski-Krastanov (SK) which incorporates both the layer-by-layer and island nucleation mechanisms. Although each type of growth mode is important to a particular type of film deposition technology, we will focus on the VW mode, which is commonly observed in many sputter-deposited films with polycolumnar type microstructure.

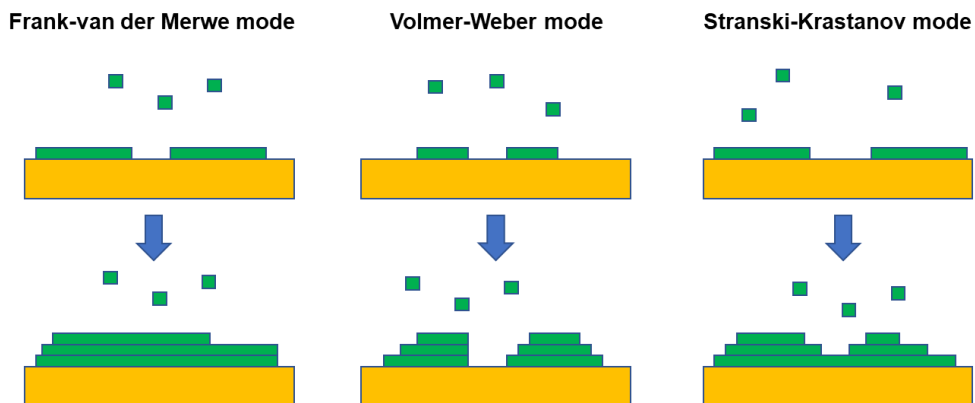


Figure C1. Schematic illustration for growth modes for thin metal film.

According to the studies of Hoffman, and Nix and Clement, the islands formed in early stage of deposition tend to impinge with each other, reducing the gap between adjacent islands to form a complete film.

B2. Model Construction

According to the VM mode of growth, the Al polycrystalline columnar grain structures are constructed, one for regular distributed grains (see Figure C2 (a)) and the other one for randomly distributed grains (see Figure C2 (b)). Total atoms for each model are $\sim 500,000$ atoms. And Each grains have different crystal orientations. The constructed models are consistent with the microstructure observed in this work (see Figure 8.12). Dimensions of present model are labeled in Figure B2. For entire simulation, the bottom three atomic layers are fixed and left structure is free.

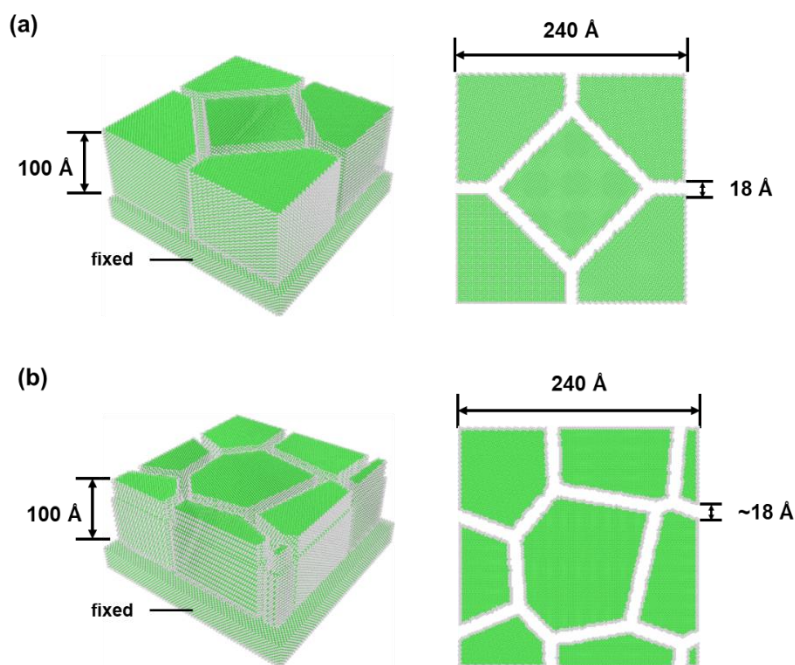


Figure C2. (a) A sketch of the MD model with regularly distributed grains in 3D view and top view. (b) (a) A sketch of the MD model with randomly distributed grains

C3. Simulation Details

The molecular dynamic calculations are performed by using the Large-scale Atomic/Molecular Massively Parallel Simulator (LAMMPS). The classical Embedded Atom Methods (EAM) is applied to describe the interactions between atoms, in which the potential for Al atoms developed by Jacobsen et al. was used. In all simulations, a timestep of 0.001

ps is chosen for calculation and the periodic boundary condition is applied in the three dimensions. And the NVT ensemble is used for entire simulation. The Open Visualization Tool (OVITO) software is used to visualize our simulation results.

The computational procedure for non-annealed structure is:

- 1) Minimizing the potential energy of the system: The coordinates of the atoms are iteratively adjusted until the change in energy between iterations is less than 1×10^{-8} or the change of global force is less than 1×10^{-8} eV/Å. After that, we cool down the system under NVT ensemble from 675 K to 300 K within 100 ps.
- 2) Relaxing structure: Continually relax the system at 300 K for 3000 ps, to reach the equilibrium.

Temperature profile for this non-annealed sample is shown in Figure C3.

The computational procedure for annealed structure is:

- 1) Minimizing the potential energy of the system: same to the first step shown in non-annealed sample.
- 2) Relax the system at 300 K for 1000 ps.
- 3) Annealing structure: Increase the temperature of system from 300 K to 700 K within 100 ps. Then, keep the temperature at 700 K for 1000 ps to relax the structure at annealing condition. After that, the system is cooled down to 300 K again within 100 ps.
- 4) Relax the annealed structure at 300 K to 3000 ps totally.

Temperature profile for this annealing simulation is shown in Figure C3.

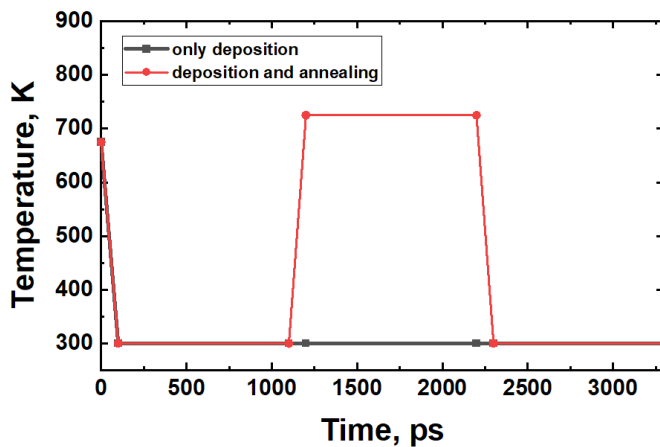


Figure C3. Temperature profile for simulation.

Appendix D

Molecular Dynamic Simulation of Thermomigration

D1. Model Construction

Nanowire connected with two big pads is constructure for simulate the motion of atoms under temperature gradient, as shown in Figure D1. Total 171564 atoms for Al model and 81995 atoms for Sn model. Atoms at the top and bottom are fixed to avoid the rotation and bending during simulation.

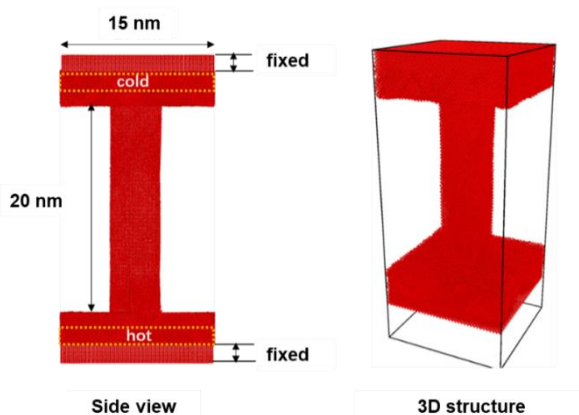


Figure D1. Initial structure for the MD simulation of thermomigration.

D2. Simulation Details

The molecular dynamic simulation with temperature gradient is performed by using the Large-scale Atomic/Molecular Massively Parallel Simulator (LAMMPS). The classical Embedded Atom Methods (EAM) is applied to describe the interactions between atoms in which the potentials for Al and Sn atoms developed by Jacobsen and Sn atoms developed by Tuna were used. In all simulations, a timestep of 0.001 ps is chosen for calculation and the periodic boundary condition is applied in the three dimensions. The Open Visualization Tool

(OVITO) software is used to visualize our simulation results. Simulation procedures are listed below:

- 1) Relaxing model without temperature gradient: Minimizing the potential energy of the system. The coordinates of the atoms are iteratively adjusted until the change in energy between iterations is less than 1×10^{-8} or the change of global force is less than 1×10^{-8} eV/Å. After that, relax system under NVT ensemble at temperature of 450 K for 100 ps, reaching equilibrium.
- 2) Creating temperature gradient: Under ensemble of NVE, we increase the temperature at the region “hot” to 600 K by using the Langevin thermostat within 50 ps. Meanwhile, we decrease the temperature at region “cold” to 300 K within 50 ps.
- 3) Relaxing the system with temperature gradient: Under ensemble of NVE, the temperature at “hot” region is kept as 600 K and temperature at “cold” region is kept as 300 K for 1000 ps.

D3. Temperature Distributions

After we set different temperatures at both ends of nanowire, 250 ps are required to form a stable temperature gradient along the nanowire, as shown in Figure D2. Then, temperature at hot end linearly decreases to cold end.

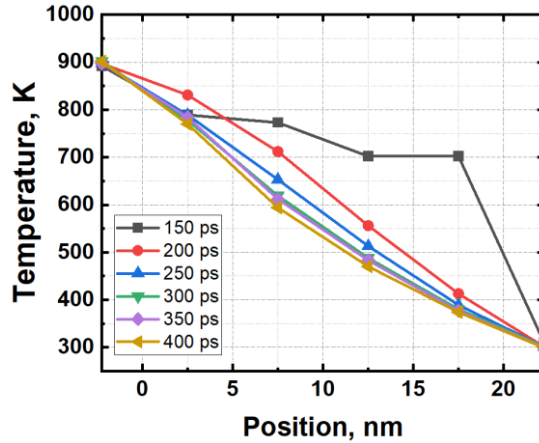


Figure D2. Temperature profile along nanowire at different time.

SUMMARY

This dissertation presents a comprehensive and integrated study, including theory development, numerical simulation and experiment, for multi-physics driven electromigration in microelectronics. Multi-scale methodologies from atomistic modeling to continuum theory-based simulation have been developed. Moreover, extensive experimental testing, from testing wafer/die design and fabrication, sample preparation and process, to the measurement setup and characterization, has been conducted. The dissertation also provides synergetic and cohesive analysis between simulation and experiment. The simulation predictions and results have been well validated by experimental data.

Chapter 1 describes the background of electromigration phenomenon in the field of microelectronics and the outline of the dissertation. In Chapter 2, a comprehensive literature review on the history of electromigration theory and the state-of-the-art development of important electromigration models is presented, in which the gaps and the lacking in knowledge are addressed. Chapter 3 presents a new 3D general coupling model for electromigration. In this model, the diffusion-induced strain (or electromigration-induced strain), derived from the widely accepted stress-vacancy equation, is fully coupled with other governing equations and field equations. Additionally, the mass conservation equation in terms of the total strain is used to describe the diffusion process, which is driven by multi-physics, including electrical field, temperature field, deformation field, and self-diffusion. In this Chapter, one-dimensional numerical solutions of a metal line, with both totally fixed and stress-free configurations, are obtained. Steady-state analytical solutions for these two configurations are also obtained. The new formulas for the threshold product of jL (current density and conductor length) represent a major departure from the well-known Blech's theory, as the new solutions consider not only the effect of mechanical stress gradient but also the concentration gradient. Although the general coupling model is a fully coupled 3D model, and the results are overall consistent with the existing experimental observations, the scale of critical vacancy concentration to induce electromigration failure seems to be unreasonable.

In order to develop a fundamental understanding of the vacancy volume relaxation that is related to the critical vacancy concentration, Chapter 4 investigates the vacancy volume

relaxation using molecular dynamics (MD) simulation. Large-scale molecular dynamic (MD) simulation is performed to investigate the concentration-dependent vacancy volume relaxation in Al, Cu, and Au, respectively. The vacancy volume relaxation factor is calculated and correlated to the microstructure change based on MD results. A uniform empirical equation is developed to obtain the vacancy volume relaxation factor as a function of vacancy concentration. Furthermore, the hydrostatic stress is also calculated using MD simulations. Based on the MD simulation results, we present a new diffusion-induced strain equation using the vacancy volume relaxation factor. This new diffusion strain equation is used in the subsequent chapters for fully-coupled electromigration modeling.

Chapter 5 presents a comprehensive and integrated study including experiment and numerical simulation to further investigate the effects of mechanical stress and self-diffusion during electromigration. Electromigration testing dies in 4-in full wafer, with more than 3000 testing samples including various testing structures per wafer were designed and fabricated. Both Blech's testing structure with perfectly blocking conditions at both ends, and SWEAT (standard wafer-level electromigration acceleration test) testing structure with metal pad connected at both ends, are applied. In our experimental study, environmental factors, such as air vs. vacuum and temperature; process factors, such as annealing and passivation layer; as well as geometrical and loading factors, such as conductor length and current density, are taken into considerations in the design of the experiment. Through the measurement setup, the in-situ resistance change can be monitored. Microstructure analysis using SEM, and EDS are performed on some samples to understand the failure mechanisms. Furthermore, we have conducted extensive fully-coupled simulations using parameters set in experiments. The simulation results are now fundamentally different from the results presented in Chapter 3, because the MD-based diffusion strain constitutive equation developed in Chapter 4 has been adopted. The failure criterion is based on the critical atomic concentration, which shows differences in orders with major literature results. However, the new simulation results have been well validated by experimental results presented in this Chapter. additionally, an analytical solution considering the effect of passivation is also derived and developed. In the end, molecular dynamic simulations show that annealing process can reduce the defects in metal film and promote coalescences of grains, causing better microstructures in polycrystals.

In Chapter 6, the thermomigration accompanying electromigration is studied experimentally and theoretically. To accurately assess the effect of thermomigration under the elevated current density, the conventional design of the accelerated electromigration tests is not

adequate, as the failure locations and time due to electromigration accompanied by thermomigration are not previously known. Using Blech's structure, we have observed the failures that are spreading throughout the mid-segment, due to the effect of high temperature gradient, in the extended testing hours. In SWEAT structure, voids are observed at a wide range of the entire conductor, and the metal line breaks off center toward the anode side. Unlike the fast void formation at cathode in Blech's structure, void formations in the middle of Blech's and SWEAT structures need significantly longer time. Moreover, we have observed electromigration failure, mainly due to thermomigration in the tapered and 2-D structures as well. In simulations, the numerical results and theoretical predictions, based on our fully coupled model, are remarkably consistent with the experimental results. Temperature gradient (that is related to current density) and conductor length are two important factors for the contributions from thermomigration. Furthermore, molecular dynamic simulation of thermomigration is performed, in which the movement directions of Al and Sn atoms under temperature gradient are consistent with experimental observations.

Chapter 7 describes the implementation of the general coupling model (Chapter 3) in ANSYS and COMSOL. In the general coupling model, the diffusion equation (mass conservation equation) is not a standard form of diffusion equation in built-in multi-physics theory in ANSYS. Therefore, the effective diffusivity concept has been derived and introduced. Additionally, the diffusion strain equation must be linearized in order to use the standard form of ANSYS built-in equation. To implement the general coupling model into COMSOL, we have developed the weak form of the governing equations. Then, by using the Weak Form PDE modulus, the general coupling model can be fully implemented in COMSOL. We have presented the numerical results, both from ANSYS and COMSOL, for a 1-D metal line benchmark problem. It is not difficult to implement the fully coupled electromigration model with the new diffusion strain equation presented in Chapter 4. This work will be carried out in the future.

In Chapter 8, atomic diffusion behaviors in polycrystalline is systematically investigated using molecular dynamics simulation and experimental data collected in Chapter 6. A MD-based diffusion model to determine the effective diffusivity in polycrystal metals is developed. Based on MD simulation, the activation energy for the Arrhenius equation, volume fraction of atoms in grain boundaries, and the grain boundary thickness can be obtained. Through experiment, the average grain size can be determined. Through the proposed formula, the effective diffusivity in polycrystal metals can be obtained. In this Chapter, the predicted

effective diffusivity is compared with the diffusivity determined from electromigration experiments, which demonstrates that the proposed approach is able to calculate the effective diffusivity accurately.

SAMENVATTING

Dit proefschrift presenteert een uitgebreide en geïntegreerde studie, inclusief theorieontwikkeling, numerieke simulatie en experiment, voor multi-fysica gedreven elektromigratie in micro-elektronica. Er zijn meerschallige methodologieën ontwikkeld, van atomistische modellering tot op continuümtheorie gebaseerde simulatie. Bovendien zijn uitgebreide experimentele tests uitgevoerd, van het testen van wafer/die-ontwerp en fabricage, monstervoorbereiding en -proces tot de meetopstelling en karakterisering. Het proefschrift biedt ook synergetische en samenhangende analyse tussen simulatie en experiment. De simulatievoorspellingen en resultaten zijn goed gevalideerd door experimentele gegevens.

Hoofdstuk 1 beschrijft de achtergrond van het fenomeen van elektromigratie op het gebied van micro-elektronica en de contouren van het proefschrift. In Hoofdstukken 2 wordt een uitgebreid literatuuroverzicht van de geschiedenis van de elektromigratietheorie en de state-of-the-art ontwikkeling van belangrijke elektromigratiemodellen gepresenteerd, waarin de hiaten en het gebrek aan kennis worden aangepakt. Hoofdstuk 3 presenteert een nieuw 3D algemeen koppelingsmodel voor elektromigratie. In dit model is de door diffusie geïnduceerde rek (of door elektromigratie geïnduceerde rek), afgeleid van de algemeen aanvaarde spanning-vacature-vergelijking, volledig gekoppeld aan andere heersende vergelijkingen en veldvergelijkingen. Bovendien wordt de vergelijking voor massabehoud in termen van de totale spanning gebruikt om het diffusieproces te beschrijven, dat wordt aangedreven door multifysica, waaronder elektrisch veld, temperatuurveld, vervormingsveld en zelfdiffusie. In dit hoofdstuk worden eendimensionale numerieke oplossingen van een metalen lijn verkregen, met zowel volledig vaste als spanningsvrije configuraties. Steady-state analytische oplossingen voor deze twee configuraties worden ook verkregen. De nieuwe formules voor het drempelproduct van jL (stroomdichtheid en geleiderlengte) vormen een belangrijke afwijking van de bekende Blech-theorie, aangezien de nieuwe oplossingen niet alleen rekening houden met het effect van de mechanische spanningsgradiënt maar ook met de concentratiegradiënt. Hoewel het algemene koppelingsmodel een volledig gekoppeld 3D-model is en de resultaten over het algemeen consistent zijn met de bestaande experimentele waarnemingen, lijkt de schaal van kritische leegstandsconcentratie om het falen van elektromigratie te veroorzaken onredelijk.

Om een fundamenteel begrip te krijgen van de leegstandsvolumerelaxatie die gerelateerd is aan de kritische leegstandsconcentratie, onderzoekt Hoofdstuk 4 de leegstandsvolumerelaxatie met behulp van moleculaire dynamica (MD) simulatie. Grootschalige moleculaire dynamische (MD) simulatie wordt uitgevoerd om de concentratieafhankelijke leegstandsvolumerelaxatie in respectievelijk Al, Cu en Au te onderzoeken. De relaxatiefactor van het leegstandsvolume wordt berekend en gecorreleerd aan de microstructuurverandering op basis van MD-resultaten. Er is een uniforme empirische vergelijking ontwikkeld om de leegstandsvolume-relaxatiefactor als functie van de leegstandsconcentratie te verkrijgen. Verder wordt de hydrostatische spanning ook berekend met behulp van MD-simulaties. Op basis van de MD-simulatiere resultaten presenteren we een nieuwe diffusie-geïnduceerde spanningsvergelijking met behulp van de leegstandsvolumerelaxatiefactor. Deze nieuwe diffusie-rekvergelijking wordt in de volgende hoofdstukken gebruikt voor volledig gekoppelde elektromigratiemodellering.

Hoofdstuk 5 presenteert een uitgebreide en geïntegreerde studie inclusief experiment en numerieke simulatie om de effecten van mechanische stress en zelfdiffusie tijdens elektromigratie verder te onderzoeken. werden ontworpen en vervaardigd. Zowel de teststructuur van Blech met perfect blokkerende omstandigheden aan beide uiteinden, als de SWEAT-teststructuur (standaard wafer-level electromigration acceleratietest) met aan beide uiteinden verbonden metalen pad, worden toegepast. In onze experimentele studie, omgevingsfactoren, zoals lucht versus vacuüm en temperatuur; procesfactoren, zoals gloei- en passiveringslaag; evenals geometrische en belastingsfactoren, zoals geleiderlengte en stroomdichtheid, worden in aanmerking genomen bij het ontwerp van het experiment. Via de meetopstelling kan de in-situ weerstandsverandering worden gevolgd. Microstructuuranalyse met behulp van SEM en EDS wordt op sommige monsters uitgevoerd om de faalmechanismen te begrijpen. Verder hebben we uitgebreide volledig gekoppelde simulaties uitgevoerd met behulp van parameters die in experimenten zijn ingesteld. De simulatiere resultaten zijn nu fundamenteel verschillend van de resultaten gepresenteerd in Hoofdstuk 3, omdat de MD-gebaseerde constitutieve vergelijking van de diffusiestam, ontwikkeld in Hoofdstuk 4, is overgenomen. Het faalcriterium is gebaseerd op de kritische atoomconcentratie, die verschillen in volgorde laat zien met belangrijke literatuurre sultaten. De nieuwe simulatiere resultaten zijn echter goed gevalideerd door de experimentele resultaten die in dit hoofdstuk worden gepresenteerd. In dit hoofdstuk wordt ook een analytische oplossing afgeleid die rekening houdt met het effect van passivering

In Hoofdstuk 6 wordt de thermomigratie die gepaard gaat met elektromigratie experimenteel en theoretisch bestudeerd. Om het effect van thermomigratie onder de verhoogde stroomdichtheid nauwkeurig te beoordelen, is het conventionele ontwerp van de versnelde elektromigratietests niet voldoende, omdat de faallocaties en tijd als gevolg van elektromigratie vergezeld van thermomigratie niet eerder bekend zijn. Met behulp van de structuur van Blech hebben we de storingen waargenomen die zich tijdens de langere testuren door het middensegment verspreiden als gevolg van het effect van een hoge temperatuurgradiënt. In de SWEAT-structuur worden holtes waargenomen over een breed bereik van de gehele geleider en breekt de metalen lijn uit het midden naar de anodezijde. In tegenstelling tot de snelle vorming van lege ruimten aan de kathode in de structuur van Blech, hebben de vorming van lege ruimten in het midden van de structuren van Blech en SWEAT aanzienlijk meer tijd nodig. Bovendien hebben we het falen van elektromigratie waargenomen, voornamelijk als gevolg van thermomigratie in de taps toelopende en 2-D-structuren. In simulaties zijn de numerieke resultaten en theoretische voorspellingen, gebaseerd op ons volledig gekoppelde model, opmerkelijk consistent met de experimentele resultaten. Temperatuurgradiënt (dat is gerelateerd aan stroomdichtheid) en geleiderlengte zijn twee belangrijke factoren voor de bijdragen van thermomigratie. Verder wordt moleculair dynamische simulatie van thermomigratie uitgevoerd, waarbij de bewegingsrichtingen van Al- en Sn-atomen onder temperatuurgradiënt consistent zijn met experimentele waarnemingen.

Hoofdstuk 7 beschrijft de implementatie van het algemene koppelingsmodel (hoofdstuk 3) in ANSYS en COMSOL. In het algemene koppelingsmodel is de diffusievergelijking (massabehoudvergelijking) geen standaardvorm van diffusievergelijking in de ingebouwde multifysica-theorie in ANSYS. Daarom is het concept van effectieve diffusiviteit afgeleid en geïntroduceerd. Bovendien moet de diffusie-rekvergelijking worden gelineariseerd om de standaardvorm van de ingebouwde ANSYS-vergelijking te gebruiken. Om het algemene koppelingsmodel in COMSOL te implementeren, hebben we de zwakke vorm van de heersende vergelijkingen ontwikkeld. Vervolgens kan door gebruik te maken van de Weak Form PDE-modulus het algemene koppelingsmodel volledig worden geïmplementeerd in COMSOL. We hebben de numerieke resultaten gepresenteerd, zowel van ANSYS als COMSOL, voor een 1-D metalen lijnbenchmarkprobleem. Het is niet moeilijk om het volledig gekoppelde elektromigratiemodel te implementeren met de nieuwe diffusie-rekvergelijking die in hoofdstuk 4 wordt gepresenteerd. Dit werk zal in de toekomst worden uitgevoerd.

In Hoofdstuk 8 wordt atomaire diffusiegedrag in polykristallijne metalen systematisch onderzocht met behulp van moleculaire dynamische simulatie en experimentele data verzameld in Hoofdstuk 6. Een MD-gebaseerd diffusiemodel om de effectieve diffusie in polykristallijne metalen te bepalen is ontwikkeld. Op basis van MD-simulatie kunnen de activeringsenergie voor de Arrhenius-vergelijking, de volumefractie van atomen in korrelgrenzen en de korrelgrensdikte worden verkregen. Door middel van experimenten kan de gemiddelde korrelgrootte worden bepaald. Door de voorgestelde formule kan de effectieve diffusie in polykristallijne metalen worden verkregen. In dit hoofdstuk wordt de voorspelde effectieve diffusiviteit vergeleken met de diffusiviteit bepaald uit elektromigratie-experimenten, wat aantoont dat de voorgestelde aanpak in staat is om de effectieve diffusiviteit nauwkeurig te berekenen

ACKNOWLEDGEMENT

Ph.D. is a memorable and challenging journey that cannot be accomplished by just individual effort. I believe I am fortunate to arrive at the endpoint of this journey. It is not just my own achievements, but the result of the collaboration of many wonderful people who I would like to thank here.

First, I would like to express my most profound appreciation to my promotor Prof. Dr. Guoqi Zhang for giving me the opportunity to pursue my Ph.D. at TU Delft. His patience, motivation, and immense knowledge helped me achieve each goal in my Ph.D. study. His passion and determination in scientific research will continually encourage me in my future career.

I would like to dedicate my sincere gratitude to my other promotor, Prof. Dr. Xuejun Fan, who has the attitude and the substance of a true academic researcher. He continually and convincingly conveys a rigorous and pragmatic spirit for research. He was always available for discussion regardless of the time, location, and distance. Without his guidance and persistent help, this dissertation would not have been possible. Moreover, his noble nature toward family, friends, and the young generation has taught me a lot. He was not only a supervisor, but also a role model in my life. It is my honour to have had the chance to study under his supervision.

I am grateful to my co-promotor, Dr. Sten Vollebregt for the realization of the electromigration measurements. His assistance with the mask design, sample fabrication, measurement setup, characterisations, and feedback during the writing and publishing phase was very helpful. I really enjoyed working with him.

I would like to thank Yaqian Zhang for her excellent work in the electromigration experiments. Her learning attitude and adaptability impressed me a lot. Our experiments were finished during the most severe time of the COVID-19 pandemic. Yaqian's spirit and patience inspired me. The tough time we experienced when solving unknown issues in the experiments is unforgettable. I would like to thank Dong Hu for his assistance with the experimental characterization. He taught me the basic knowledge of SEM, EDX, and FIB, and I taught him molecular dynamic simulation. I was very happy to cooperate with him. I also would like to

thank Prof. dr. Jiajie Fan from the Fudan University for his valuable suggestions and comments on writing and publishing scientific papers. Dr. Jiajie's cooperation in establishing the reliability of the phosphor material was impressive. I am looking forward to our next collaboration.

It was my pleasure to work with my brilliant colleagues from ECTM and EKL: Prof. dr. Lina Sarro, Dr. Willem van Driel, Dr. Rene Poelma, Dr. Jianhuang Lin, Dr. Hongyu Tang, Dr. Fengze Hou, Dr. Jianwen Sun, Dr. Hao Zhang, Dr. Daniel Yi, Dr. Boyao Zhang, Dr. Bo Sun, Dr. Amir Mirza, Dr. Leandro Sacco, Dr. Lucas Middelburg, Dr. Aleksandar Jovic, Ziqiao Huang, Jiarui Mo, Hande Aydogmus, Milica Dostanic, Tianyi Jing, Leo Guo, Paul Motreuil-Ragot, Joost van Ginkel, Zichuan Li, Hongzhi Du, Xinrui Ji, Joost Romijn. I would like to thank all other professors, PhDs, post-docs, master students, and technicians inside or outside our department for their presentations, feedback, cooperation, help, and friendship.

I would also like to thank my wife, Tao Sun, who appeared in my life when I needed her most. Her support, tolerance, encouragement, patience, and unwavering love are the unshakable bedrocks of my life. In the period of writing this dissertation, our baby was just two months old. My wife independently took care of the baby during the day and had many sleepless nights to support my work. To our family, her contribution has been ten times more than mine. Moreover, I would like to thank my parents for supporting me spiritually throughout my life. Whenever I encounter any trouble, they come over first to support me and encourage me. I thank them for their unconditional support during this Ph.D. phase and on the entire journey until this moment.

CURRICULUM VITAE

Zhen Cui

16-11-1990 Born in Taiyuan, Shanxi Province, China

EDUCATION

2009-2013 Bachelor in Engineering Mechanics,
Taiyuan University of Technology, Shanxi, China
Thesis “Response of Dynamic Loading in Truss Structure”

2014-2017 Master in Solid Mechanics,
Tianjin University, Tianjin, China
Thesis “Theoretical Investigations of Interfacial Sliding and Buckling
of Graphene on a Flexible Substrate”

2018-2021 PhD in Microelectronics
Delft University of Technology, Delft, the Netherlands
Dissertation “Multi-Physics Driven Study of Electromigration: Multi-
Scale Modeling and Experiment”
Promotor: Prof.dr. G.Q. Zhang
 Prof.dr. X.J. Fan
Copromotor: Dr. S. Vollebregt

LIST OF PUBLICATIONS

JOURNAL PAPERS

1. **Zhen Cui**, Yaqian Zhang, Dong Hu, Sten Vollebregt, Xuejun Fan, Guoqi Zhang, Electromigration and thermomigration-induced void formations and breaking in various micro-interconnect, in preparation.
2. **Zhen Cui**, Yaqian Zhang, Dong Hu, Sten Vollebregt, Xuejun Fan, Guoqi Zhang, Effect of mechanical confinement and annealing on electromigration: Experimental study and theoretical modeling, in preparation.
3. **Zhen Cui**, Yaqian Zhang, Dong Hu, Sten Vollebregt, Jiajie Fan, Xuejun Fan, Guoqi Zhang, Calculation of atomic diffusivity in polycrystal metal: molecular dynamic simulation and experimental study, under review.
4. Wei Chen, Ye Chen, Yixin Cao, **Zhen Cui**, Xuejun Fan, Guoqi Zhang and Jiajie Fan, Sulfur-rich ageing mechanism of silicone encapsulant used in LED packaging: An experimental and molecular dynamic simulation study, under review.
5. **Zhen Cui**, Xuejun Fan, Guoqi Zhang, Molecular dynamic study for concentration-dependent volume relaxation of vacancy, Microelectronics Reliability, 120, 114127, 2021.
6. Dong Hu, **Zhen Cui**, Jiajie Fan, Xuejun Fan, Guoqi Zhang, Thermal kinetic and mechanical behaviors of pressure-assisted Cu nanoparticles sintering: A molecular dynamics study, Results in Physics, 19, 103486, 2020. Co-first author.
7. **Zhen Cui**, Jiajie Fan, Hendrik Joost van Ginkel, Xuejun Fan, Guoqi Zhang. The interface adhesion of $\text{CaAlSiN}_3\text{:Eu}^{2+}$ phosphor/silicone used in light-emitting diode packaging: a first principles study, Applied Surface Science, 510, 145251, 2020.
8. Hongyu Tang, Dong Hu, **Zhen Cui**, Huaiyu Ye, Guoqi Zhang, Effects of defect and temperature on the mechanical performance of WS₂: A multiscale Analysis, Journal of Physics and Chemistry C, 2021, 15, 4, 2680-2690.
9. **Zhen Cui**, Xuejun Fan, Guoqi Zhang, General coupling model for electromigration and one-dimensional numerical solutions, Journal of Applied Physics, 125, 105101, 2019.

-
10. Jiajie Fan, **Zhen Cui**, Ling Zhou, Xuejun Fan, Guoqi Zhang, Hydrolysis kinetic study of CaAlSiN_3 : Eu^{2+} red phosphor with both water immersion test and first-principles calculation, *Journal of Luminescence*, 219, 116874, 2019.
 11. Yu Zhang, Pengli Zhu, Gang Li, **Zhen Cui**, Chengqiang Cui, Kai Zhang, Jian Gao, Xin Chen, Guoqi Zhang, Rong Sun, Chingping Wong. PVP-mediated galvanic replacement synthesis of smart elliptic Cu–Ag nanoflakes for electrically conductive pastes, *ACS applied materials & interfaces*, 11,8, 2019.

CONFERENCE PAPERS

1. **Zhen Cui**, Xuejun Fan, Guoqi Zhang, Implementation of general coupling model of electromigration in Ansys, 2020 70th Electronic Components and Technology Conference (ECTC), online, IEEE.
2. **Zhen Cui**; Xianping Chen; Xuejun Fan; GuoQi Zhang, Interfacial properties of Cu/SiO_2 using a multiscale modelling approach in electronic packages, 2018 19th International Conference on Thermal, Mechanical and Multi-Physics Simulation and Experiments in Microelectronics and Microsystems (EuroSimE), Toulouse, France, IEEE.
3. **Zhen Cui**; Yingying Zhang; Qun Yang; GuoQi Zhang; Xianping Chen; Interfacial Failure Characterization of Electronic Packaging Component Using a Multiscale Modelling Approach, 2018 2nd Electron Devices Technology and Manufacturing Conference (EDTM), Kobe, Japan.
